SLAC-R-678

Evidence of Light-by-Light Scattering with Real Photons*

Steven John Boege

Stanford Linear Accelerator Center
Stanford University
Stanford, CA 94309

SLAC-Report-678

Prepared for the Department of Energy
under contract number DE-AC03-76SF00515

Printed in the United States of America. Available from the National Technical Information Service, U.S. Department of Commerce, 5285 Port Royal Road, Springfield, VA 22161.

* Ph.D. thesis, University of Rochester, Rochester, New York.

Evidence of Light-by-Light Scattering with Real Photons

by
Steven John Boege

Submitted in Partial Fulfillment
of the
Requirements for the Degree
Doctor of Philosophy

Supervised by
Professor Adrian C. Melissinos

Department of Physics and Astronomy
The College
Arts and Sciences

The University of Rochester
Rochester, New York

1996

For my many teachers, especially my parents...

Curriculum Vitae

Steven John Boege was born in Coon Rapids, MN on the Twentieth of July, 1969. He attended Hamline University from 1987 to 1991, and graduated with a Bachelor of Arts degree in 1991. He came to the University of Rochester in the Fall of 1991 and began graduate studies in Physics. He received the Master of Arts degree in 1993, and then pursued his research at the Stanford Linear Accelerator Center under the direction of Professor Adrian C. Melissinos.

Acknowledgments

My doctoral research was facilitated by a number of people. Kathy Fatyga, Kristin Kurz, and Michael Simon helped me through coursework and The Prelim by sharing both knowledge and frustration. Alan Fry and Phillip Koehn provided reassurance and humor that got me through many dark, cold Winter nights. Without the support of these friends, I would not have completed classes, much less a earned a degree.

Pat Borrelli and Wolfram Ragg helped keep the lab well equipped and the laser system's performance "rock steady". Charlie Bamber had many clever ideas, his intuition helped solve many problems. Glenn Horton-Smith and Christian Bula were extremely patient in dealing with my incessant computing questions. Theofilos Kotseroglou worked hard to improve the laser system and performed extensive data analysis. Kirk McDonald, David Burke, Bill Bugg, Steve Berridge, and many other people are responsible for the existence and success of E-144. David D. Meyerhofer invested a great deal of time and effort in and provided crucial laser expertise to E-144. His family was generous in allowing him so much time away from Rochester.

The support of my family was unflagging. I want to thank my sister Kate for everything she did to lift my spirits. I want to thank my parents for each and every time they encouraged me to stick to my guns, to finish what I started, to do my personal best.

I owe the most to Adrian C. Melissinos. Before I had even applied to The University of Rochester his enthusiasm surrounded me, it has been inspirational to me. I feel incredibly fortunate and grateful to have enjoyed his guidance and encouragement during coursework, examinations, lab crises and triumphs, data analysis, and thesis preparation.

This work was supported by the United States Department of Energy under Contract Number DE-FG02-91ER-40685.

Abstract

In a new experiment at the Stanford Linear Accelerator Center, heretofore untested aspects of high field strength Quantum Electrodynamics were probed. Bunches of 46.6 GeV electrons available in the Final Focus Test Beam line were brought into collision with terawatt pulses of either 1.17 eV or 2.34 eV photons from a Nd:Glass laser system. Several physical process were investigated. This thesis describes the production of electron-positron pairs in photon-photon collisions. This is particularly interesting since it represents the generation of massive particles from massless particles.

The bunch/pulse trajectories are approximately antiparallel. Due to the head-on nature of the collisions, the electrons see, in their rest frame, a transformed laser pulse electric field amplitude $\overline{\mathcal{E}_0} = 2\gamma\mathcal{E}_0$, and so a lab frame field $\mathcal{E}_0 \sim 1.0 \times 10^{11}$ V/cm corresponds to a 46.6 GeV electron rest frame field $\overline{\mathcal{E}_0} \sim 1.8 \times 10^{16}$ V/cm. For electric field amplitudes of this magnitude, perturbative QED is of limited validity. Multiphoton processes dominate collision results.

The geometry of the experiments was such that any pairs produced came into existence in the midst of the electron/photon collision region. The electron from a produced pair was indistinguishable from the recoil electrons generated via other processes in collisions. Detecting the positron, then, was the only way to observe pair production. In data accumulated during the September 1994 Final Focus Test Beam run, positrons in excess of background were detected.

Positron signals were extracted from an ensemble of data collected during electron bunch/laser pulse collisions. Calorimeter readings were used to measure the energy, and reconstruct the transverse displacement of positrons propagating downstream from the bunch/pulse collision region. Field maps of permanent magnets located downstream of the collision region but upstream of the calorimeter were used in implementing a cut of off-momentum background positrons.

Effects of various cuts and the characteristics of the detected positrons are presented. Statistically significant positron production above background is reported. The rate for e^+ production is calculated, and the energy spectrum of the candidates is shown. The agreement of simulation results with these observations is described.

Contents

1 Physics Motivation **1**
1.1 Cross Sections & Rates 2

2 Experimental Setup and Detection System **15**
2.1 The e^- Beam 16
2.2 The Detectors 16
2.2.1 Collecting Scattered Positrons 16
2.2.2 Shower Measurement 21
2.2.3 Shower Simulation 24
2.3 The Data Acquisition System 27

3 The Laser System **34**
3.1 Introduction 35
3.2 Design Principles 35
3.2.1 CPA 36
3.2.2 Slab Geometry Amplifiers 40
3.2.3 Spatial and Temporal Overlap 41
3.3 Operation 42
3.3.1 The Oscillator 42
3.3.2 The Regenerative Amplifier 44
3.3.3 The Rod Preamplifier 44
3.3.4 The Slab Amplifier 46
3.4 Diagnostics 55
3.4.1 Energy 55
3.4.2 Pulse Duration 56
3.4.3 Spot Size 58
3.5 Laser Performance 65
3.6 Second Harmonic Generation 70
3.6.1 Motivation 70
3.6.2 Conversion Efficiencies 72
3.7 Synchronization 72

4 Data Analysis **77**
4.1 Introduction 78
4.2 Calibration Data 78
4.3 The Processing of Raw Data 79
4.4 The Minimization of Calorimeter Fluctuations 81
4.5 Position Reconstruction 88
4.5.1 The Selection of Single Peak Showers 92
4.6 The Development of "Hit" Constraints 101

5 Results and Conclusions **113**
5.1 Collision Quality Control 114
5.2 Laser Pulse - Beam Bunch Collision Data 115
5.3 dN/dE of Positrons: Experiment and Theory 138
5.3.1 Relative Rate 138
5.4 Statistical Significance 139
5.5 dN/dE: Observed and Theoretical 140
5.5.1 Absolute Rate 145

Bibliography **152**

A Positron Production in Al **159**

B Event Simulation **163**

List of Figures

1.1 Collision Region Layout. 3
1.2 Single Incident Photon (Linear) Compton Scattering. 3
1.3 Multiple Incident Photon (Nonlinear) Compton Scattering. 7
1.4 e^-/ω_0 Collision Gamma Spectra. 8
1.5 Elastic Photon/Photon Scattering. 9
1.6 Inelastic Photon/Photon Scattering. 10
1.7 Multiphoton Breit-Wheeler Pair Production Yield. 11
1.8 Total Multiphoton Breit-Wheeler Pair Production Rate versus Υ. 12
1.9 Multiphoton Breit-Wheeler Pair Production Rate versus e^+ Energy: Several Υs. 13

2.1 The Stanford Linear Accelerator Center. 17
2.2 SLAC Beamline Overview. 18
2.3 Mapped e^+ and e^- Trajectories from IP1 to the calorimeters. . . . 19
2.4 PCAL Schematic. 23
2.5 Calorimeter Calibration. 25
2.6 Simulated Shower Profiles. 26
2.7 The Data Acquisition System. 29
2.8 FFTB wire scan. 31
2.9 Beam Parameters for Run 9083. 32

3.1 Pulse Formation and Amplification Sequence. 37
3.2 Physical Layout of Laser System. 38
3.3 The Synchronization Scheme. 43
3.4 Oscillator Pulse Train. 45
3.5 Chirped Pulse Spectrum. 45
3.6 Regenerative Amplifier Pulse Train. 46
3.7 Photograph: Anamorphic Beam Expander and Slab Amplifier. . . 47
3.8 Slab Output Energy versus PFN Voltage. 49
3.9 Slab Gain versus PFN Energy. 50
3.10 Photograph: The Third Optical Table. 51
3.11 Layout of Beam Transport. 52
3.12 Photograph: Beam Transport and Interaction Point. 53

3.13 Detail Drawing of Interaction Point. 54
3.14 Single Shot Autocorrelation Schematic. 57
3.15 Laser Pulse Autocorrelation Trace. 59
3.16 Equivalent Target Plane Measurement Setup. 60
3.17 Laser Pulse Intensity Profile. 63
3.18 Horizontal Waist Scan. 64
3.19 Vertical Waist Scan. 66
3.20 Spot Size Scan. 67
3.21 Run Averaged: Green, IR, η_{SHG} ≡Green/IR, and η_{SHG} versus IR. 68
3.22 Run Averaged: area (A_L), pulsewidth (τ_L). 69
3.23 Run Averaged: η, Υ. 71
3.24 Scattering Rate versus Optical Delay. 75
3.25 XT Scan. 76

4.1 Raw PCAL Pedestals. 80
4.2 PCAL Schematic. 82
4.3 Calorimeter Coherent Noise: $E_{i,j}^{CC}$ versus $E_{i,j}^{OC}$, row f, segment 1. . 83
4.4 The Coherent Noise Parameterization Process. 86
4.5 Corrected Calorimeter Signals: OC Energy versus CC Energy − 0.99OC Energy − 0.22. 87
4.6 $y_0 - y_R$: Fractional and Logarithmic Weighting Schemes. 91
4.7 Reconstruction Algorithm Applied to Simulated Shower. 93
4.8 Foil Data: s0+s1, rows a-f, columns 0-4, "hitless". 96
4.9 Foil Data: s0+s1, rows a-f, columns 0-4, "multihit". 97
4.10 Foil Data: s0+s1, rows a-f, columns 0-4, "hit". 98
4.11 The transverse profile of a single incident positron's shower. . . . 99
4.12 $y_0 - y_R$: Logarithmic Weighting, Varied W_0. 100
4.13 Foil Data: y_R, Logarithmic Weighting, Varied W_0. 102
4.14 Foil Data: y_R, Logarithmic Weighting, Varied W_0. 103
4.15 Foil Data: y_R and x_R. 104
4.16 Foil Data: 0 <NHIT < 5. 105
4.17 Foil Data: 0.5 <NHIT < 1.5. 106
4.18 Foil Data: Cluster energy versus reconstructed y position. 107
4.19 Mean NHIT $\pm\sigma$ versus reconstructed y position. 108
4.20 Cluster energy versus reconstructed y position 109
4.21 Foil Data: Δy_R and Δx_R. 111
4.22 Foil Data: Shower Sharing. 112

5.1 Run Data: Run 9077 Control Plot. 117
5.2 Run Data: Run 9079 Control Plot. 118
5.3 Run Data: Run 9081 Control Plot. 119
5.4 Run Data: Run 9082 Control Plot. 120
5.5 Run Data: Run 9083 Control Plot. 121

5.6 Run Data: Run 9089 Control Plot. 122
5.7 Run Data: Run 9090 Control Plot. 123
5.8 Run Data: Cluster energy versus reconstructed vertical deflection, y_R. 128
5.9 e^-/ω_0 Collision Data: The distribution of NHIT 129
5.10 e^-/ω_0 Collision Data: The distribution of y 130
5.11 e^-/ω_0 Collision Data:The distribution of x 131
5.12 e^-/ω_0 Collision Data: The distribution of Δy. 132
5.13 e^-/ω_0 Collision Data: The distribution of Δx. 133
5.14 e^-/ω_0 Collision Data: The distribution of S0%. 134
5.15 e^-/ω_0 Collision Data: The distribution of S1%. 135
5.16 Joint Probability Density Function $P(m' = 20|n \geq 13; X)$. 141
5.17 Joint Probability Density Function $P(m' = 50|n \geq 17; X)$. 142
5.18 dN_e/dE_e: Runs 9077–9083. 143
5.19 dN_e/dE_e: Runs 9077–9090. 144
5.20 Υ Distribution. 148
5.21 Cut Efficiencies: Δx_R, Δy_R, S0%, S1%. 149
5.22 Cut Efficiencies: x_R, nhit. 150

A.1 $d\sigma_{\hbar\gamma}$ versus $\hbar\gamma$ for e^+ production in Al. 160
A.2 dN/dE versus E for e^+ production in Al 161

List of Tables

2.1 Beam Parameter Cuts for Run 9083. 33

4.1 Slopes and Offsets for Removal of Coherent Noise. 88
4.2 Cell Characteristics, September 1994. 95
4.3 Cell Characteristics, March 1994. 101

5.1 The 9000s: Triggers 116
5.2 Cut Results: NHIT 126
5.3 Cut Results: Δy. 136
5.4 Cut Results: Δx. 136
5.5 Cut Results: x. 137
5.6 Cut Results: S0%≡ECLS0/ECL. 137
5.7 Cut Results: S1%≡ECLS1/ECL. 138
5.8 Cut Results: Individual Runs 139
5.9 Parameters for Average Rate Calculation. 147
5.10 Average Rate Calculation Results. 147
5.11 Absolute Rate: Observed and Predicted. 151

Chapter 1

Physics Motivation

Experiment 144 (E–144) at the Stanford Linear Accelerator Center (SLAC) is a study of high field strength Quantum Electrodynamics (QED).[1] High intensity laser photon (ω_0) pulses produced at a rate available from few other laser systems are brought into collision with high energy electron (e^-) bunches available only in the Final Focus Test Beam (FFTB) line of SLAC. The ω_0 pulse is directed along a path that is approximately antiparallel to that of the e^- bunch. This geometry exploits the extremely relativistic nature of the electrons. The Lorentz transformation of the pulse's lab frame electric field yields, in the e^- rest frame, a field strength on the order of $\sim 10^{16}$V/cm, an amplitude otherwise unattainable in a laboratory setting.

The multiphoton Breit-Wheeler process (MBWP) is one facet of QED investigated by E-144.[2] It is the simplest manifestation of light-by-light scattering involving only real photons. In our probe of this process,

$$n\omega_0 + \gamma \rightarrow e^+e^-. \tag{1.1}$$

A high energy photon (γ) collides with n low energy laser photons (ω_0), forming e^+e^- pairs.[3] Figure 1.1 shows a schematic overview of the experimental setup. As the pulse and bunch cross, Compton scattering of e^-s occurs. In the setup depicted, very energetic γs are produced when e^-s interact with $m \geq 1$ laser photons. These γs propagate downstream with the unscattered and recoil electrons. The γs generated within the laser pulse can subsequently collide with $n \geq 3$ laser photons, forming e^+e^- pairs. . This thesis reports the first evidence of Multiphoton Breit-Wheeler pair production. Positrons in excess of background have been observed with $> 99\%$ confidence.

1.1 Cross Sections & Rates

There are two steps considered in our study of Multiphoton Breit-Wheeler pair production. In the first step, a high energy γ is created in a $n \geq 1$ Compton scattering process. Linear Compton scattering (LCS), depicted in Figure 1.2 is the process in which an e^- absorbs a single ω_0 of energy E_ω and emits a photon of energy E_γ[4] In the rest frame of the e^-, the energy of the emitted photon

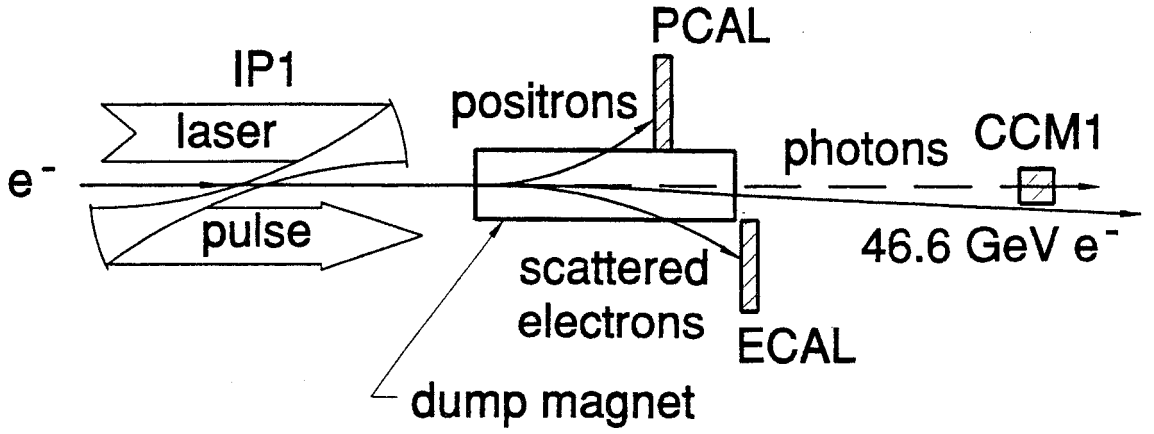

Figure 1.1: Collision Region Layout.

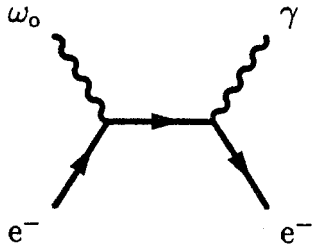

Figure 1.2: Single Incident Photon (Linear) Compton Scattering.

$\overline{E_\gamma}$ is given by

$$\overline{E_\gamma} = \frac{\overline{E_\omega} m_e c^2}{m_e c^2 + \overline{E_\omega}\left(1 - \cos\overline{\theta}\right)}, \tag{1.2}$$

where $\overline{\theta}$ is the angle between the incident photon and the scattered photon and $\overline{E_\omega}$ is the energy of the incident photon, both measured in the e^-'s rest frame. For a highly relativistic e^- of total energy, E_e,

$$\gamma \sim \frac{E_e}{m_e c^2} = \frac{46.6 \text{ GeV}}{0.511\text{MeV}} \sim 9.10 \times 10^4. \tag{1.3}$$

The e^- rest frame laser photon energy $\overline{E_\omega}$ is

$$\overline{E_\omega} = \gamma E_\omega \left(1 - \beta \cos\alpha\right), \tag{1.4}$$

where α is the angle of the laser pulses' propagation relative to that of the e^- bunches, viewed in the lab frame. Figure 1.1 shows the geometry of the interaction region; the crossing angle $180° - \alpha = 17°$. Using the approximations $\beta \sim 1$, and $\cos 163° \sim -1$,

$$\overline{E_\omega} \sim 2\gamma E_\omega. \tag{1.5}$$

In the lab frame, the energy of the backscattered γ is given by

$$E_\gamma = E_\omega \frac{4\gamma^2}{1 + 2\gamma^2\left(1 - \cos\theta\right) + \left(2\gamma\hbar\omega_0/m_e c^2\right)\left(1 + \cos\theta\right)}. \tag{1.6}$$

The highest energy γs are produced when $\theta = 0°$. This corresponds to maximal momentum transfer,[5] and in the lab frame

$$E_\gamma = \frac{4\gamma^2 m_e c^2}{m_e c^2 + 4\gamma E_\omega} E_\omega. \tag{1.7}$$

For laser photons of wavelength $\lambda = 0.527$ μm, E_γ can reach up to 29.2 GeV. For laser photons of wavelength $\lambda = 1.053$ μm, E_γ can reach up to 21.3 GeV.

For the $n = 1$ case, the differential cross section is given by the Klein-Nishina Formula [6],

$$\frac{d\sigma}{dy} = \frac{2\pi r_e^2}{x}\left[(1-y) + \frac{1}{(1-y)} - \frac{4y}{x\left(1-y\right)} + \frac{4y^2}{x^2\left(1-y\right)^2}\right], \tag{1.8}$$

where

$$x = \frac{4\hbar\omega_0 E_e}{m_e^2 c^4}, \tag{1.9}$$

$$y = \frac{E_\gamma}{E_e} \leq y_{max} = \frac{x}{1+x}. \tag{1.10}$$

Equations 1.7 and 1.8 do not take intense field effects into account. Multiphoton absorption is not included. Electrons and positrons propagating through an intense electromagnetic field undergo acceleration. In the case of a circularly polarized, high intensity laser pulse, the transverse motion of an e^- is a circle of radius r. In strong enough fields, the transverse motion becomes relativistic and we must write

$$q_e \mathcal{E}_{rms} = \gamma_\perp m_e \omega_0^2 r = \gamma_\perp \beta_\perp m_e \omega_0 c, \tag{1.11}$$

where

$$\beta_\perp = \frac{v_\perp}{c} = \frac{\omega_0 r}{c}, \tag{1.12}$$

and

$$\gamma_\perp = \frac{1}{\sqrt{(1-\beta_\perp^2)}}. \tag{1.13}$$

Here $\mathcal{E}_{rms}$ denotes the rms electric field in the pulse. For describing electron motion, it is convenient to define the field strength parameter η

$$\eta \equiv \frac{q_e \mathcal{E}_{rms}}{\omega_0 mc} = \gamma_\perp \beta_\perp \tag{1.14}$$

The relativistic mass shift due to the transverse motion of the e^-s and e^+s is given by

$$\overline{m} = \gamma_\perp m_e. \tag{1.15}$$

Written in terms of η, the "effective mass" $\overline{m}$, is given by

$$\overline{m}^2 = m_e^2 \left(1+\eta^2\right). \tag{1.16}$$

The laser pulse intensity I is defined as the radiant energy per unit time transported through unit area. It is the product of the energy density stored in

an electromagnetic wave and the wave's speed of propagation. In vacuum,

$$I = c\langle U\rangle \text{ and } \langle U\rangle = \frac{1}{2}\left\langle \epsilon_0 E_0^2 + \frac{1}{\mu_0} B_0^2 \right\rangle. \tag{1.17}$$

Since

$$B_0^2 = \frac{1}{c^2}\mu_0\epsilon_0 E_0^2,\ U = \frac{\epsilon_0}{2}E_0^2,\ \text{and } I = \frac{c\epsilon_0}{2}E_0^2 = c\epsilon_0\mathcal{E}_{rms}^2 \tag{1.18}$$

The relationship between I and $\mathcal{E}_{rms}$ can be inverted. Since we can measure the energy, duration, and area of the laser pulse, we can calculate I, and thus $\mathcal{E}_{rms}$.

$$\mathcal{E}_{rms}^2\left(\frac{\mathrm{V}^2}{\mathrm{cm}^2}\right) = \frac{1}{c\epsilon_0}I = \sqrt{\frac{\mu_0}{\epsilon_0}}I = Z_0 I = (377\Omega)\, I\left(\frac{\mathrm{W}}{\mathrm{cm}^2}\right) \tag{1.19}$$

For describing QED effects, it is convenient to introduce the parameter Υ, given by [7]

$$\Upsilon \equiv \frac{2\gamma q_e \mathcal{E}_{rms}\hbar}{m_e^2 c^3} = \frac{2\gamma\hbar\omega_0}{m_e c^2}\eta \tag{1.20}$$

When the intensity of the laser pulse reaches $I \sim 7\times 10^{18}\mathrm{W/cm}^2$, the Lorentz invariant ratio of the electric field seen by the e^- to the Schwinger critical field, Υ, approaches unity. The critical field $\mathcal{E}_c$ is an electromagnetic field in which the potential energy difference across a Compton wavelength is an electron rest mass. Klein's paradox becomes important in such a field, pairs can tunnel out of the vacuum.[8] Its amplitude is given by

$$\mathcal{E}_c \equiv \frac{m_e^2 c^3}{q_e\hbar} = 1.3\times 10^{16}\mathrm{V/cm} = 4.4\times 10^{13}\mathrm{Gauss}. \tag{1.21}$$

In this region, perturbative QED is of limited validity,[9] and one expects copious production of e^+e^-pairs[10] and the dominance of multiphoton effects.[11, 12]

The effective mass shifts the kinematic (Compton) edge for single and multiple photon ($n \geq 1$) collisions.[13] Such "nonlinear" Compton scattering (NLCS) is depicted in Figure 1.3.

The cross section for the absorption of n ω_0s in the case of high circularly

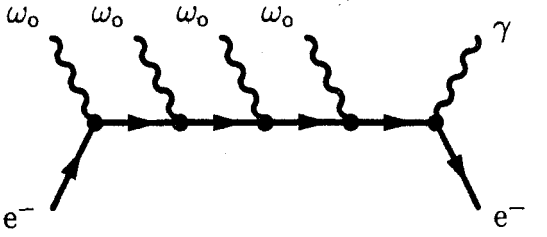

Figure 1.3: Multiple Incident Photon (Nonlinear) Compton Scattering.

polarized photon density, is given by [14].

$$\frac{d\sigma_n}{dy} = \frac{2\pi r_e^2}{x}\left[-\frac{4}{\eta^2}J_n^2(z) + \left(2 + \frac{u^2}{1+u}\left(J_{n-1}^2(z) + J_{n+1}^2(z) - 2J_n^2(z)\right)\right)\right] \quad (1.22)$$

Here

$$u \simeq \frac{y}{1-y}, \quad (1.23)$$

$$y_{max} = \frac{nx}{1+\eta^2+nx}, \text{ and} \quad (1.24)$$

$$z = \frac{2\eta}{x}\sqrt{1+\eta^2}\sqrt{u\left(\frac{nx}{1+\eta^2} - u\right)} \quad (1.25)$$

Figure 1.4 is a plot of dN_γ/dE_γ versus E_γ for green photons back-scattered by 46.6 GeV e^-s . Note the $n = 1$ kinematic threshold, above which the cross section drops rapidly. This threshold is given by [7]

$$\text{Max}(E_\gamma) = \frac{4n\gamma^2\hbar\omega_0}{1 + 4n\gamma\hbar\omega_0/m_e c^2 + \eta^2}. \quad (1.26)$$

Consider the case where $\eta = .4$. For $\lambda = 1.053\mu$m, $\text{Max}(E_\gamma) = 19.5$ GeV. For $\lambda = 0.527\mu$m, $\text{Max}(E_\gamma) = 27.5$ GeV. Compton scattering produces the desirable high energy γs at a high rate. This effect is enhanced when the γs produced in the multiphoton Compton scattering are included. That is, the nonlinear Comptons, not the double scatters. When an electron absorbs more than one laser photon before emitting a γ, the kinematic edge for γs is shifted upwards. The contributions from n=2,3, and 4 are discernible as "shoulders" in the dN_γ/dE_γ plot.

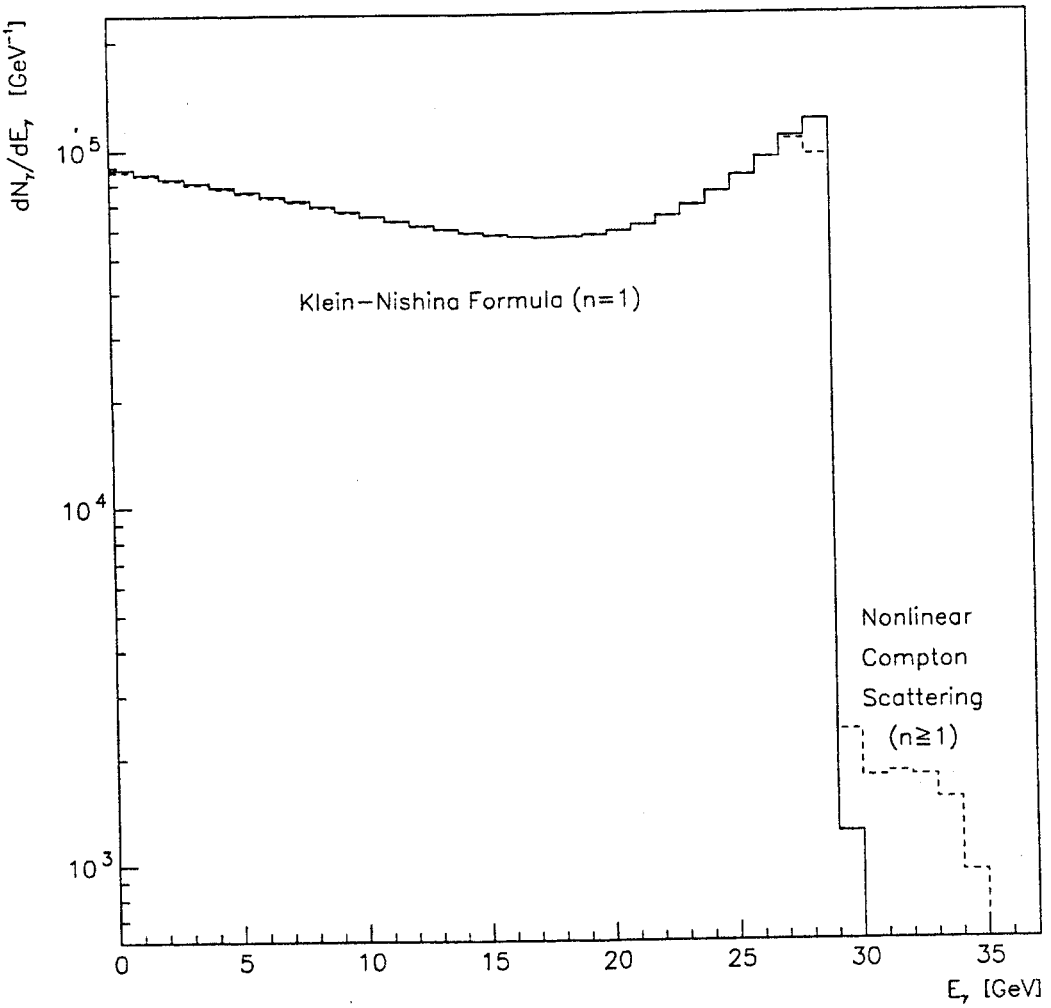

Figure 1.4: e^-/ω_0 Gamma Spectra.
The solid line represents the γ production rate given by the Klein-Nishina formula from Equation 1.8. The dashed line represents the γ production given by the nonlinear Compton scattering formula from Equation 1.22. Note the "rounding" in the NLCS case of the edge at 29.3 GeV in the LCS case, and the "shoulder" due to multiphoton effects.

These γs , though low in number, are much more likely to produce a pair. Their high energy makes it so they need to absorb fewer photons to satisfy kinematic requirements. Increasing E_γ decreases $n_{\min}$. This reduces the number of steps in the process, reducing the number of vertex factors in the cross section! They thus make significant contributions to the overall Breit-Wheeler pair production cross section. Figure 1.7 is a plot of dN_e/dE_e versus outgoing e^+ or e^- energy.

In the second step, the γ collides with several laser photons and an e^+e^- pair is produced. Photon/Photon scattering is depicted in Figures 1.5 and 1.6. The cross section for the the multiphoton Breit-Wheeler process was derived in [14]. Neglecting crossing angle, the cross section for the case of circularly polarized light is given by

$$\frac{d\sigma_n}{dy} = \frac{2\pi r_e^2}{x}\left\{\frac{4}{\eta^2}J_n^2(z) + (u-2)\left[J_{n-1}^2(z) + J_{n+1}^2(z) - 2J_n^2(z)\right]\right\}, \tag{1.27}$$

where (for $nE_\omega \ll E_\gamma$)

$$x = \frac{4E_\omega E_\gamma}{m_e^2 c^4}, \tag{1.28}$$

$$y = \frac{E_e}{E_\gamma}, \tag{1.29}$$

$$u = \frac{1}{y(1-y)}, \tag{1.30}$$

and

$$z = \eta\sqrt{1+\eta^2}\,\frac{2}{x}\sqrt{u\left(\frac{nx}{1+\eta^2} - u\right)} \tag{1.31}$$

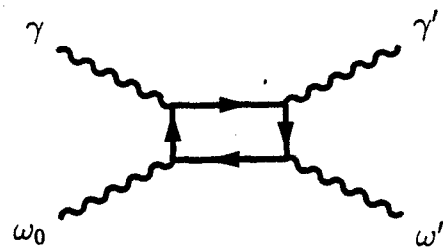

Figure 1.5: Elastic Photon/Photon Scattering.

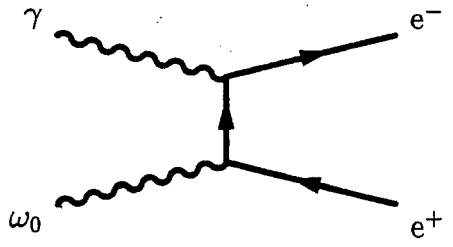

Figure 1.6: Inelastic Photon/Photon Scattering.

The cross section described by Equation 1.31 has kinematic cutoffs. For each n, there is an E_γ below which energy and momentum conservation disallow pair production. The cross section is only defined for E_γ such that

$$(\mid \vec{p_\gamma} \mid + n \mid \vec{p_\omega} \mid)^2 - (\vec{p_\gamma} + n\vec{p_\omega}) \cdot (\vec{p_\gamma} + n\vec{p_\omega}) \geq (2\overline{m}c)^2 . \tag{1.32}$$

We can write

$$E_\gamma \geq \frac{m_e^2(1+\eta^2)c^4}{nE_\omega} = \frac{\overline{m}^2c^4}{nE_\omega}, \tag{1.33}$$

and solve for n,

$$n_{\min} = \frac{\overline{m}^2c^4}{E_\gamma E_\omega}, \tag{1.34}$$

where $n_{\min}$ is rounded up to the nearest integer number of photons. For $\lambda = 1.053\mu$m, the γ must collide with 12 or more ω_0s to produce a pair. For $\lambda = 0.527\mu$m, the γ must collide with 5 or more ω_0s to produce a pair. Since $n_{\min}$ decreases as E_γ increases, even small fluxes of high energy γs contribute significantly to the cross section.

The expected rate of positron production was calculated. The software used laser pulse, e^- bunch, and geometrical parameters to simulate a bunch–pulse collision. The total rate for positrons produced per pulse was one quantity calculated. Figure 1.8 illustrates the Υ dependence of the total rate.

$r_e \equiv q_e^2/4\pi\epsilon_0 m_e^2 c^2 = 2.818 \times 10^{-13}$ cm. The classical electron radius.

m_e $0.5110 \times \mathrm{MeV/c^2}$. The electron rest mass.

q_e 1.602×10^{-19}C. The electron charge.

λ_{IR} 1.053μm. The wavelength of the Infrared laser pulse ω_0s.

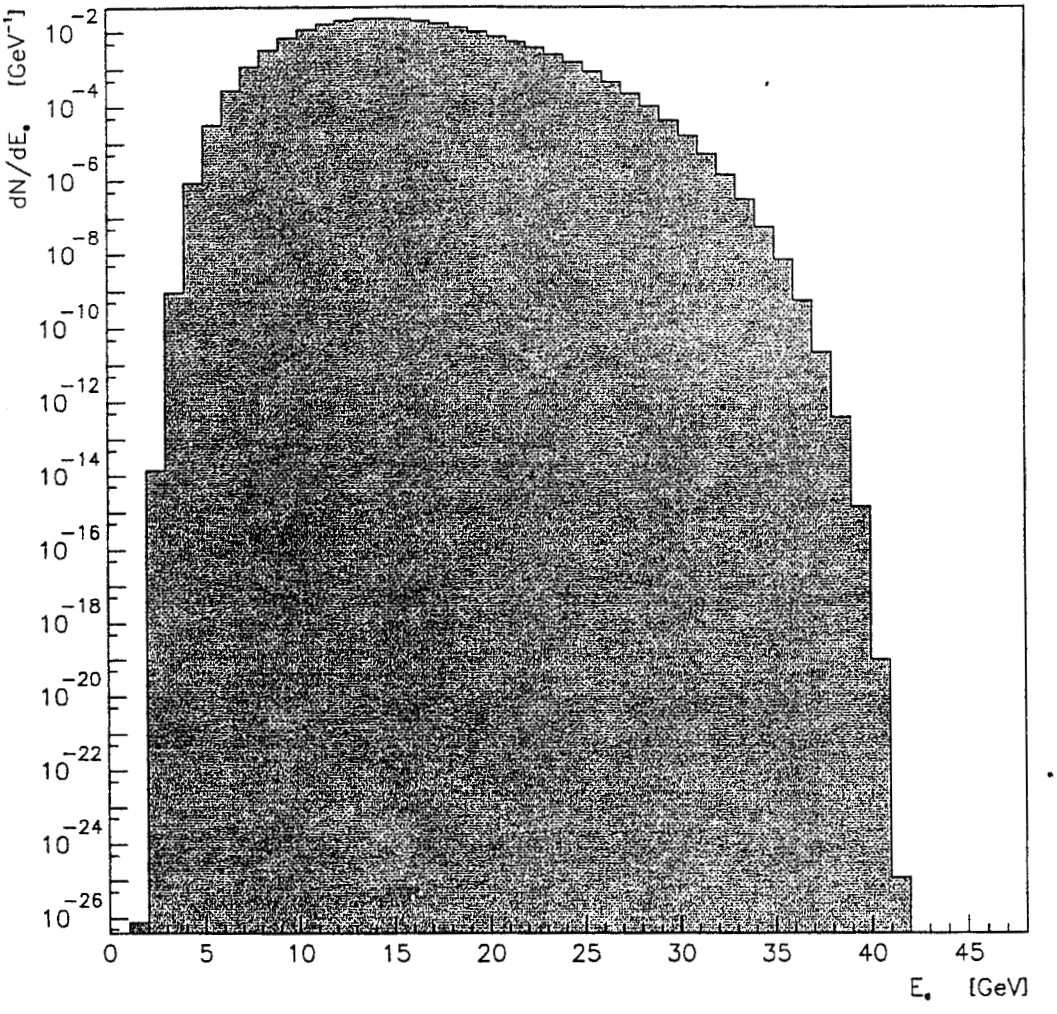

Figure 1.7: Multiphoton Breit-Wheeler Pair Production Yield.
This spectrum is for 46.6 GeV electrons colliding with Green ($\lambda = 0.527\mu$m) laser photons. The simulation treated the electron bunch as having a 30×100 μm^2 transverse area, and a 5 ps pulselength. The simulation treated the laser pulse as having a 2.5 ps pulselength, a 14.5 μm^2 spot size, and an energy of 867 mJ.

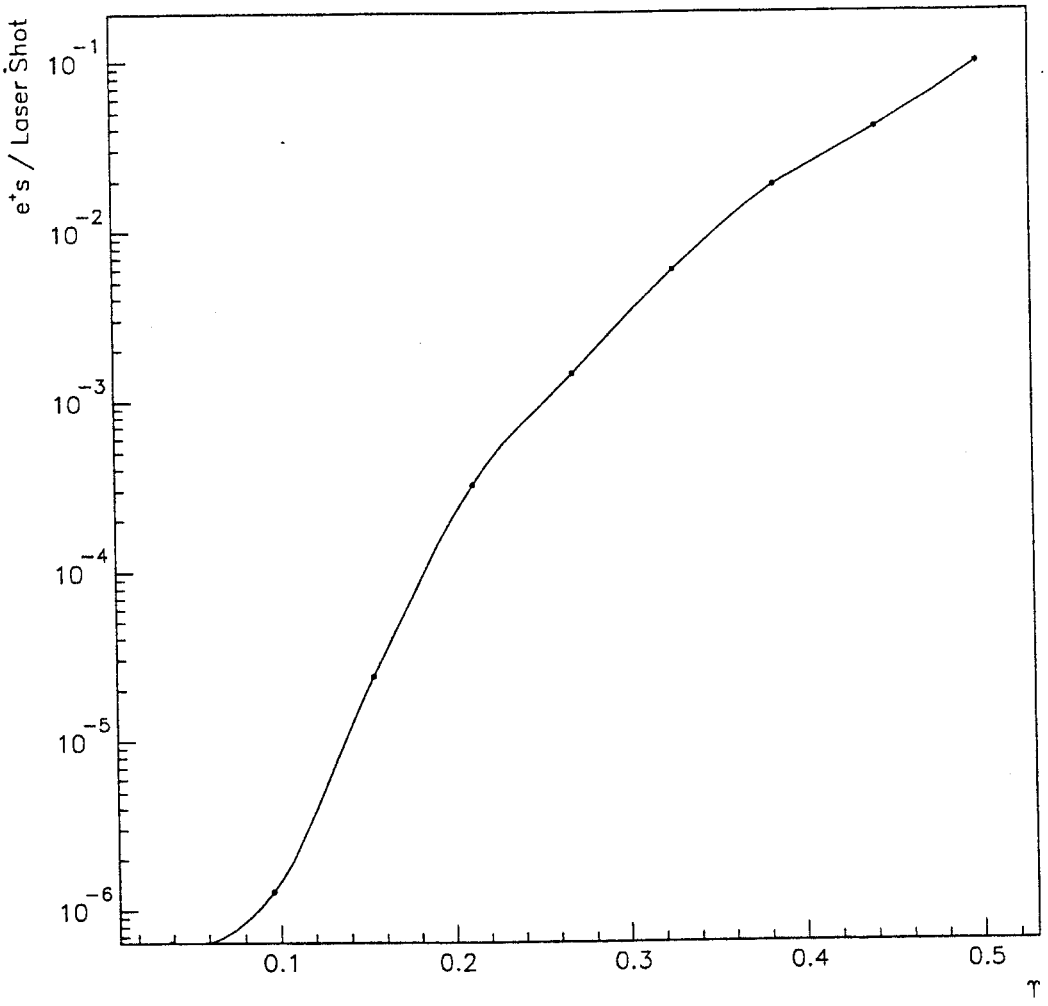

Figure 1.8: Total Multiphoton Breit-Wheeler Pair Production Rate versus Υ. This plot represents the total Multiphoton Breit-Wheeler Pair Production rate integrated over outgoing particle energy as a function of Υ for Green ($\lambda = 0.527\mu$m) laser photons and 46.6 GeV incident electrons.

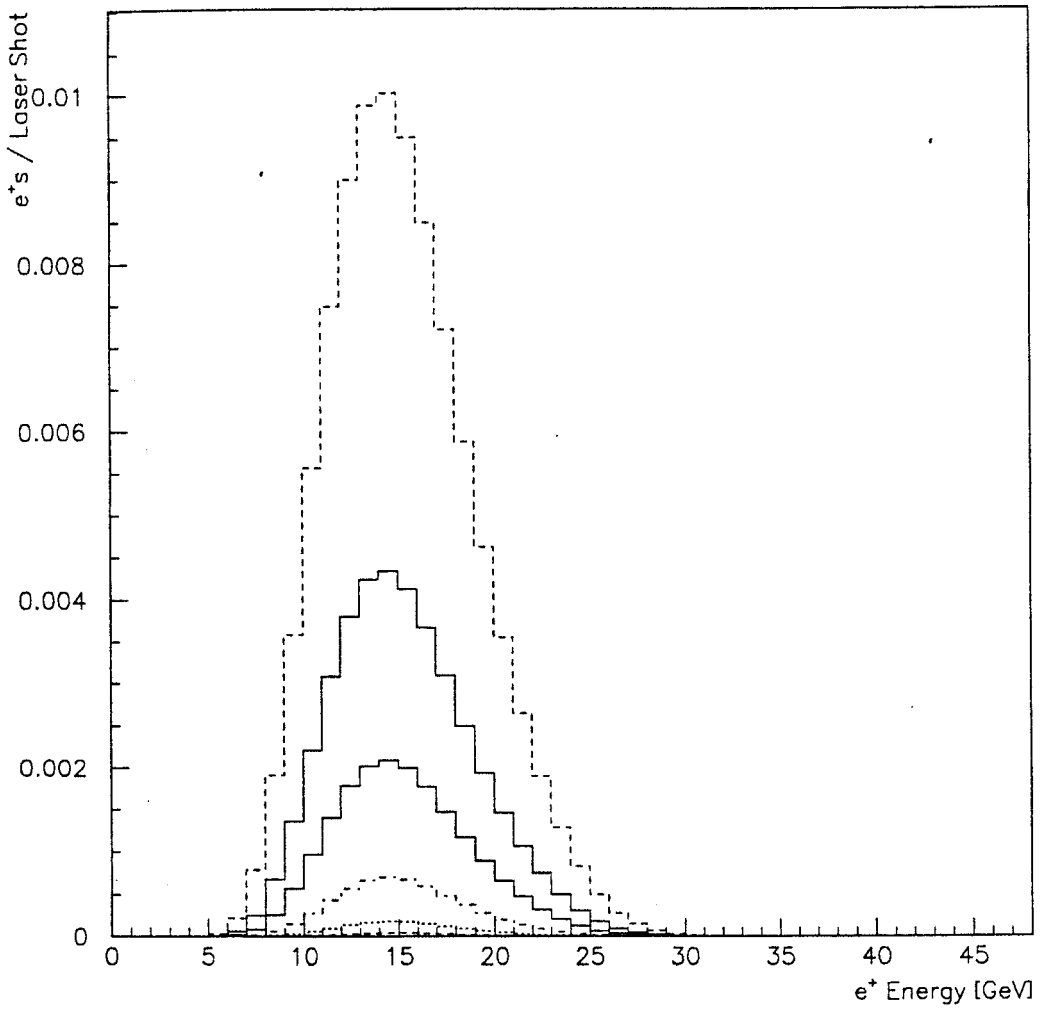

Figure 1.9: Multiphoton Breit-Wheeler Pair Production Rate versus e^+ Energy: Several Υs.
The traces correspond to five different values of Υ. Starting with the top trace,
$\Upsilon = 0.50$ ($I \sim 3.5 \times 10^{18}\mathrm{W/cm^2}$),
$\Upsilon = 0.44$ ($I \sim 2.7 \times 10^{18}\mathrm{W/cm^2}$),
$\Upsilon = 0.39$ ($I \sim 2.1 \times 10^{18}\mathrm{W/cm^2}$),
$\Upsilon = 0.33$ ($I \sim 1.5 \times 10^{18}\mathrm{W/cm^2}$), and
$\Upsilon = 0.27$ ($I \sim 9.8 \times 10^{17}\mathrm{W/cm^2}$).

$\hbar\omega_{IR}$ 1.18 eV. The energy of the Infrared laser pulse ω_0s.

λ_{Green} 0.527 μm. The wavelength of the Green laser pulse ω_0s.

$\hbar\omega_{Green}$ 2.36 eV. The energy of the Green laser pulse ω_0s.

$\gamma_{\|}$ 9.12×10^4. The longitudinal Lorentz transformation factor between the lab and e^- bunch rest frames.

Chapter 2

Experimental Setup and Detection System

2.1 The e^- Beam

The SLAC linac (Linear Accelerator) shown in Figure 2.1 produces a beam of high energy electron bunches. Electrons are launched from a cathode and accelerated in a straight line by radiofrequency (rf) electric fields synchronized to the electrons' passage. The compressed e^- bunches are accelerated by standing waves as they traverse a series of coupled s-band rf cavities. A repeating train of such bunches is usually referred to as a "beam." The klystrons which power the cavities are each driven with a unique phase relative to the SLAC master rf. In traversing the linac, the electrons are accelerated to 46.6 GeV. Upon reaching the end of the linac, they are coupled into the Final Focus Test Beam (FFTB) line and steered downstream to the point where they collide with the laser pulses.

Figure 2.2 gives an overview of the SLAC beam lines. The bunches start at (1), are accelerated along the entire length of (5), and are steered into (22).[15] Magnetic fields are used to steer and focus the electron beam. In the FFTB, the e^- beam is focusable down to very small transverse dimensions. This experiment was performed at SLAC specifically because of the beam characteristics attainable in the FFTB.[16, 17] We attain the large electric field amplitudes by tightly focusing the laser pulse. The spot size of the focussed pulse is $\sim 50\ \mu m^2$. To establish effective collisions it is necessary for the transverse profile of the electron bunch to be of similar dimensions. For both the laser pulses and the e^- beam bunches, the smallest possible dimensions are desirable: the higher the photon and electron density, the higher the scattering rate.

2.2 The Detectors

2.2.1 Collecting Scattered Positrons

Collisions occurred in the region of overlap of the e^- bunch and ω_0 pulse designated IP1. Figure 2.3 is a scaled schematic representation of the section of beam line stretching from IP1 to the the e^+ detector (PCAL). As can be seen in Figure 2.3, there are a set of permanent magnets downstream from IP1 that are used to deflect the e^- bunches down into an underground beam dump. We make use of these magnets, they effectively transform the momentum spectrum, $dN/d\vec{p}$ of e^-s and e^+s into a vertical spatial profile, dN/dy.

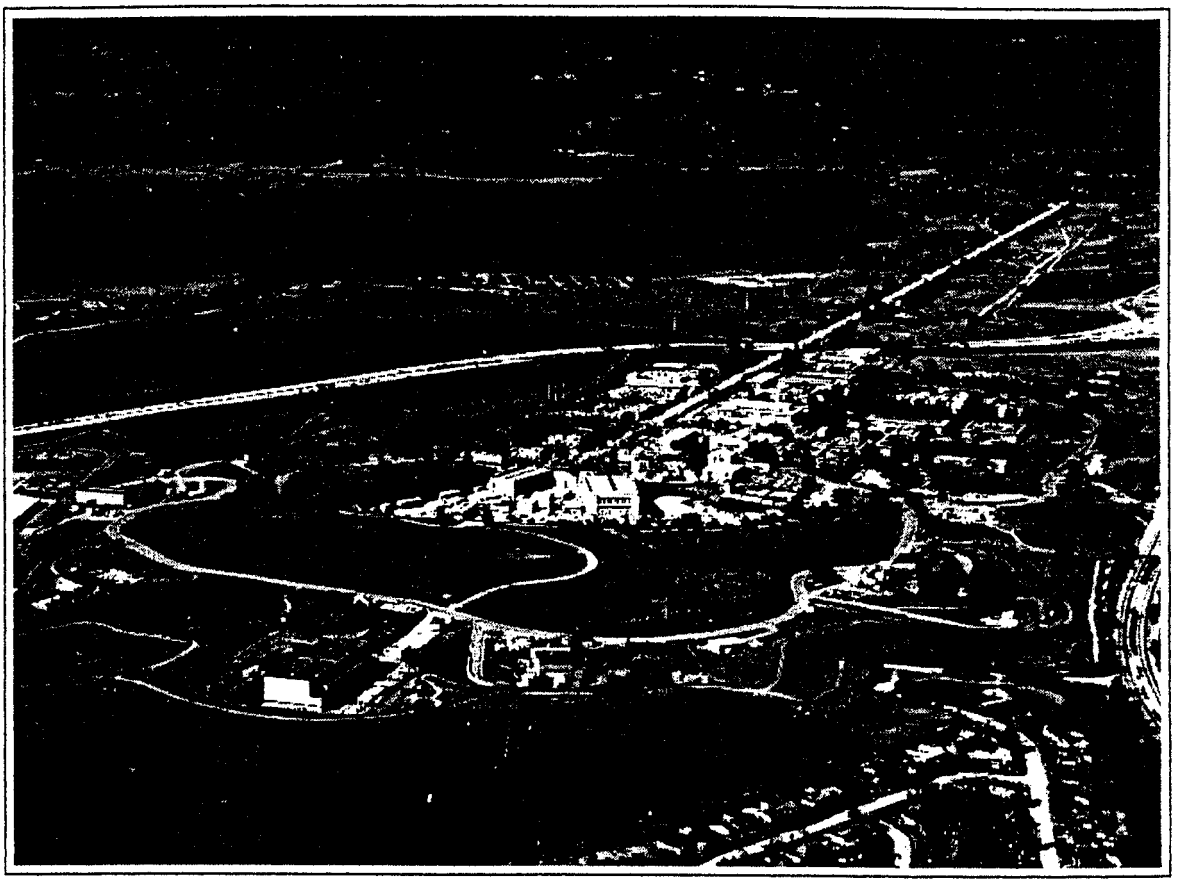

Figure 2.1: The Stanford Linear Accelerator Center.

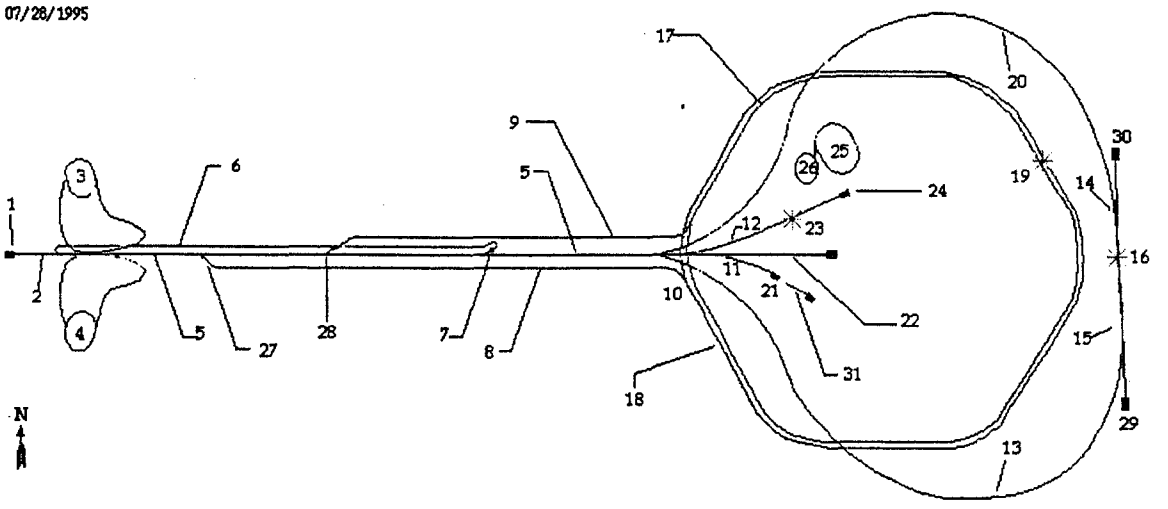

Figure 2.2: SLAC Beamline Overview.[15]

1	electron-gun	17	PEP II Low Energy Ring [3.1 GeV]
2	200 MeV injector	18	PEP II High Energy Ring [9 GeV]
3	North damping ring [1.15 GeV]	19	PEP II IR-2 detector
4	South damping ring [1.15 GeV]	20	SLC north arc [45 GeV]
5	Linac	21	End Station B
6	Positron return line	22	Final Focus Test Beam
7	Positron source	23	End Station A
8	PEP II High Energy Bypass	24	Beam Dump East
9	PEP II Low Energy Bypass	25	SSRL SPEAR [3 GeV]
10	Beam Switch Yard	26	SSRL Booster
11	B-Line	27	Sector-4 PEP II e+ injector
12	A-Line [50 GeV]	28	Sector-10 PEP II e- injector
13	SLC south arc [45 GeV]	29	Positron dump
14	North final focus	30	Electron dump
15	South final focus	31	Next Linear Collider Test Accelerator
16	Collider Experimenter Hall		

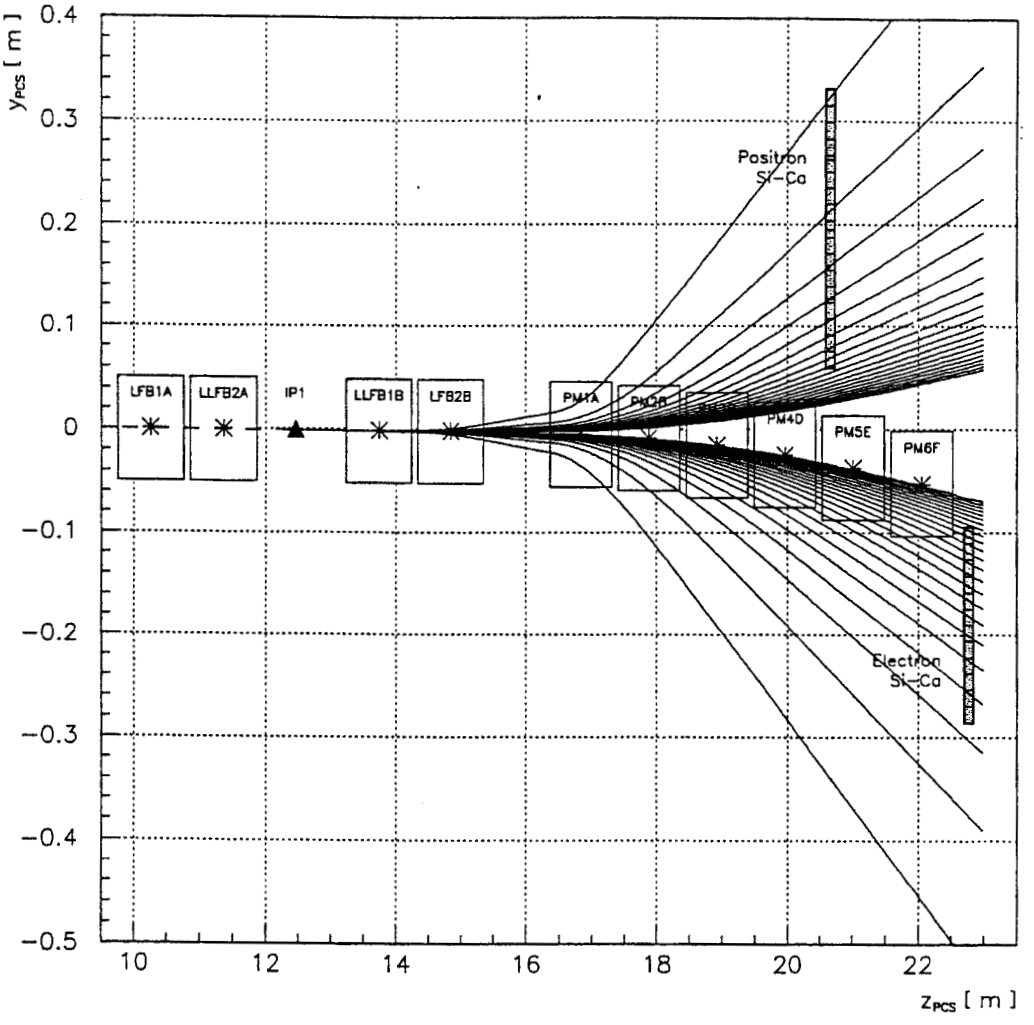

Figure 2.3: Mapped e^+ and e^- Trajectories from IP1 to the calorimeters.
The lines fanning out from IP1 represent particles with energies equally spaced in the range going from 2–20 GeV. Cartesian axis are defined in the following way: $+\hat{z}$ pointed downstream along the FFTB (from left to right in the plot), $+\hat{y}$ pointed vertically out of the earth (from the bottom to the top in the plot), and $+\hat{x}$ obeyed right-handed convention (into the page in the plot).

Magnetic deflection is commonly used to measure charged particle momentum.[18] The trajectory of an e^- of momentum $\vec{p} = p_0\hat{z}$ sent through a uniform magnetic field $\vec{B} = -B_0\hat{x}$ will be helical. In the case where the particle momentum is orthogonal to $\vec{B}$, the equations of motion simplify. The force on an electron moving in a uniform magnetic field is given by

$$\frac{d\vec{p}}{dt} = \dot{\vec{p}} = \frac{q_e}{c}\vec{v}\times\vec{B}. \tag{2.1}$$

The solutions to these 3 coupled differential equations, are given by Reference [19].

$$\vec{v}(t) = v_x\hat{x} + \frac{q_e c B_0}{E}\rho(\hat{y} - i\hat{z})\exp\left(-i\frac{q_e c B_0}{E}t\right), \tag{2.2}$$

where ρ is the radius of curvature of the e^-s . For B in Gauss, $\mid \vec{p_0} \mid$ in MeV/c, and q_e in Coulombs, ρ in cm is given by [20]

$$\rho = \frac{3333 \mid \vec{p_0} \mid}{q_e B}. \tag{2.3}$$

A numerical integration program was used to map the momentum to deflection transformation by calculating the trajectories of e^+s and e^-s traversing the center of the beam/pulse crossing region in IP1. This trajectory map was used in the candidate identification process. The positron flux into the detector was low enough to allow the identification of single particles, and the reconstruction of their points of impact. Each particle trajectory depended upon momentum $\vec{p_0}$ and initial location $\vec{r_0} = x_0\hat{x} + y_0\hat{y} + z_0\hat{z}$. We constructed a look-up table, giving $y(\vec{p_0}, \vec{r_0})$ for $x = x_0$, $z = z_0 + 8.078$ m. The look-up table produced had 0.5 mm resolution in y. EMAP(y) is the energy that a positron would have to have had in order to arrive at $(x_0, y, z_0 + 8.078$ m). Showers, centered at y_R, containing energy far greater or less than EMAP(y_R) were cut; the e^+s impacting the calorimeter in these cases did not originate at IP1. Such positrons are subsequently referred to as "off-momentum background positrons."

Detectors well suited to measure the vertical spatial profile of deflected e^+s and e^-s were installed above and below the beam line. These detectors were

Silicon/Tungsten (Si)/(W) electromagnetic calorimeters designed and built by The University of Tennessee.[21, 22] The calorimeter above the beam line (PCAL) measured incident e^+ characteristics.

In the bunch/pulse collisions, the e^-s from produced pairs were indiscernible from Compton and nonlinear Compton scattered e^-s . Thus, to measure pair production rates, positrons had to be counted. A later phase of this experiment plans to bring the γ cone into collision with a fraction of the original laser pulse after the dump magnets have separated the electrons from the γs. In this running mode, both members of the pair will be detectable, and track reconstruction will be used to measure the mass spectrum of the pairs thus produced.[7]

2.2.2 Shower Measurement

In PCAL itself, an alternating series of W alloy and Si layers was used to create and measure the energy of electromagnetic showers caused by incident e^+s . Positrons traversing the W alloy caused a shower of γs and e^- e^+ pairs. When such showers propagate into Si spanned by an electric field, the e^+s and e^-s ,

> ...deposit ionization energy and dislodge e^-s , which in turn produce secondary ionization. This causes a separation of the e^-s and holes in the semiconductor, which then separate due to the presence of an electric field. They collect at the electrodes, giving a signal proportional to the deposited energy.[23]

The probability of showering is parameterized by the radiation length, X_0. X_0 is the average distance it takes a high energy e^- to lose all but 1/e of its energy by bremsstrahlung. Its value can be approximated by[24]

$$X_0 = \frac{A\ 716.4\ \text{g cm}^{-2}}{Z(Z+1)\ln(287/\sqrt{Z})}. \tag{2.4}$$

The critical energy

$$E_C = \frac{610\text{MeV}}{\text{Z} + 1.24} \tag{2.5}$$

of a material is the energy above which bremsstrahlung replaces ionization as the chief mechanism of e^- energy loss. The Moliere Radius,

$$M_R \sim \frac{X_0\,(21\text{MeV})}{E_C} \tag{2.6}$$

is a parameter that describes the transverse development of an electromagnetic shower in a material.

The rectangular geometry of PCAL is represented in Figure 2.4. Sixteen square Si cells (also known as "pads") were grouped on $6.4 \times 6.4\text{cm}^2$ wafers. These 300μm thick wafers (Si: $X_0 = 9.36$cm) were interleaved with 3.5 mm radiator plates composed of an alloy of tungsten, copper, and nickel (W90Cu6Ni4: $X_0 = 0.41$cm). Each radiator layer was 0.85 radiation lengths thick. There were 23 layers of Si. The beam line was orthogonal to the planes of the layers. There were 16 rows and 4 columns in each layer. The pad located in row i and column k of each layer had its own electrodes. Pads with matching transverse coordinates (row and column indices) but differing longitudinal coordinates (layer number) were "ganged together" by wiring their electrodes in parallel, summing the layers' signals. These collections of layers were referred to as a "longitudinal segments." PCAL had two segments. Segment 0 has signals from the first nine layers, Segment 1 has signals from the remaining 14. This configuration, depicted in Figure 2.6 was selected so that half of the total shower energy was deposited in each segment.

Each 16×16 mm pad provided signal. Ganged signals were read out by custom charge integration amplifier modules originally built as part of the Redundant Analog Bus-Based Information Transfer (Rabbit) system electronics from E-706 at Fermilab. The rows of PCAL were numbered from zero to fifteen, rows ten through fifteen were often expressed in hexadecimal notation. The columns of PCAL were numbered from zero to three. The e^+'s deflection was vertical. Which row a particle struck was a function of its energy. Row f was closest to the beam line, the highest energy e^+s impacted there. The lower energy e^+s were deflected further up, into rows e through 0.

The E-144 calorimeters underwent several calibrations. They were removed from the FFTB tunnel and placed directly in the path of low flux e^- bunches.

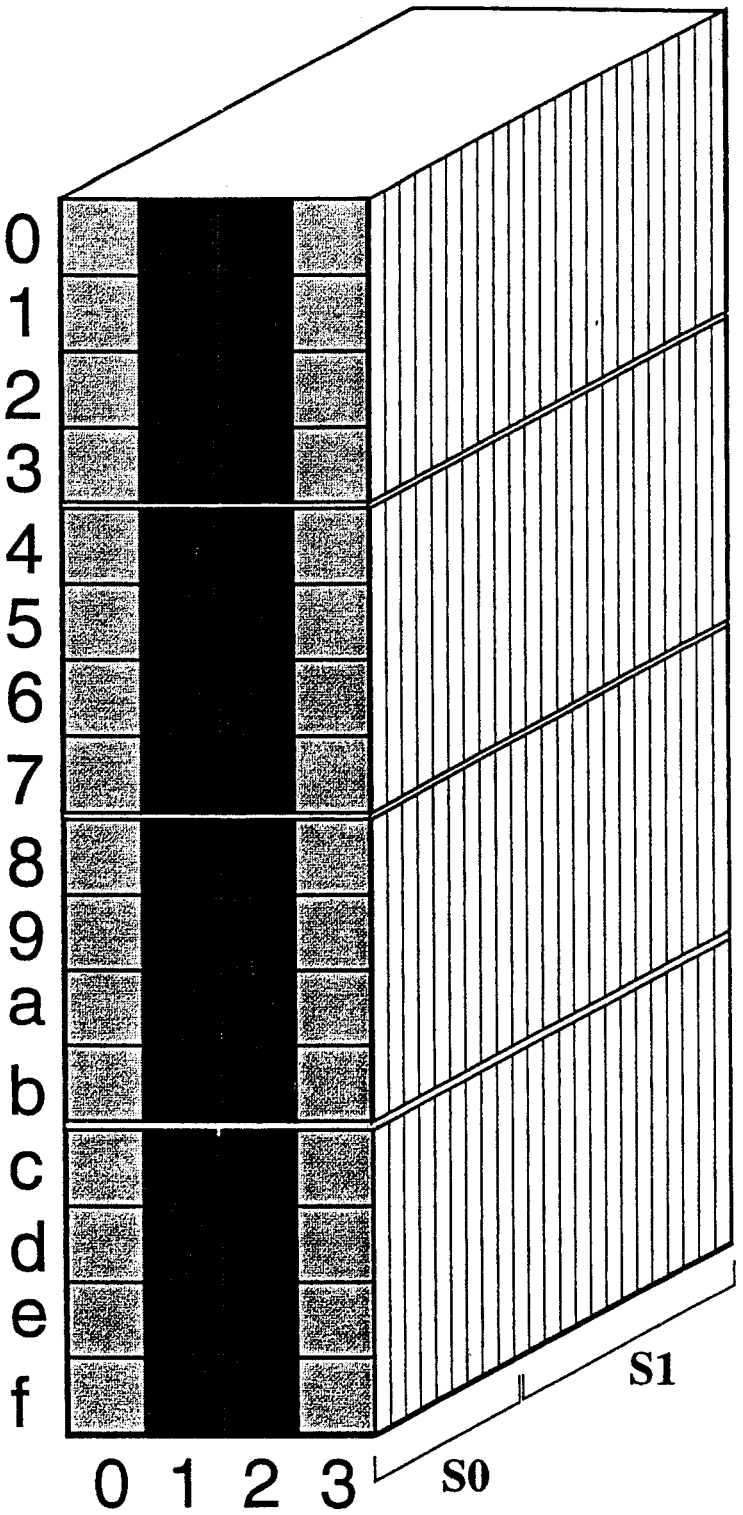

Figure 2.4: PCAL Schematic.
There are 16 rows of 4 columns. There are twenty three layers. Signals from the front 9 layers are summed and referred to Segment 0 or S0. Signals from the remaining 14 layer are summed and referred to as Segment 1 or S1.

Since the energy of the e⁻s was well defined, the voltage sampled and digitized at the output of the amplifiers could be converted into "counts per GeV." Once PCAL was returned to the FFTB , its output could be converted from counts to GeV. Figure 2.5 shows data acquired during a calibrations run. Peaks corresponding to 0–6 electron hits per cell per event are shown.

2.2.3 Shower Simulation

The showers created in and measured by PCAL have both longitudinal and transverse components. These components may be modeled. Accounting for PCAL geometry, a positron of energy E_0 will initiate a shower

$$S_{\perp}(r) = E_0 \left(\frac{\delta}{2\beta_1} \exp\left(-\frac{|\, r - r_0 \,|}{\beta_1} \right) + \frac{(1-\delta)}{2\beta_2} \exp\left(-\frac{|\, r - r_0 \,|}{\beta_2} \right) \right), \qquad (2.7)$$

where $\beta_1 = 3.0$ mm, $\beta_2 = 10.7$ mm, $\delta = \frac{2}{3}$, $r^2 = x^2 + y^2$, and $r_0^2 = x_0^2 + y_0^2$. The βs are material and detector specific parameters related to the Moliere Radius. W is an excellent radiator substance, inasmuch as its transverse shower profiles are very narrow, allowing their origin to be reconstructed with greater precision and accuracy. The longitudinal profile generally obeys

$$S_{\parallel}(z) = \varepsilon_0 t^a \exp(-bt), \qquad (2.8)$$

where, $t = z/X_0$, $a \simeq 3.2 + .3 \ln(E_0)$, $b \simeq .75 - 0.05 \ln(E_0)$, and $\varepsilon_0 \simeq 2.2 + 1.5 \ln(E_0)$.[26] Figure 2.6 depicts simulated shower profiles. The longitudinal shower plot is a simulation of 20 GeV particles.[27] The solid curve in the transverse shower plot represents the shower shape. The dashed line represents the energy measured by the cell found by integrating Equation 2.7 between cell boundaries.

The energy resolution associated with calorimeters describes the spread of measurements ΔE about the the actual value of E. For Si-W calorimeters ,

$$\frac{\Delta E}{E} \simeq 20\% \frac{X}{\sqrt{E}}, \qquad (2.9)$$

where X is the sampling length in units of radiation length and E is measured in GeV.

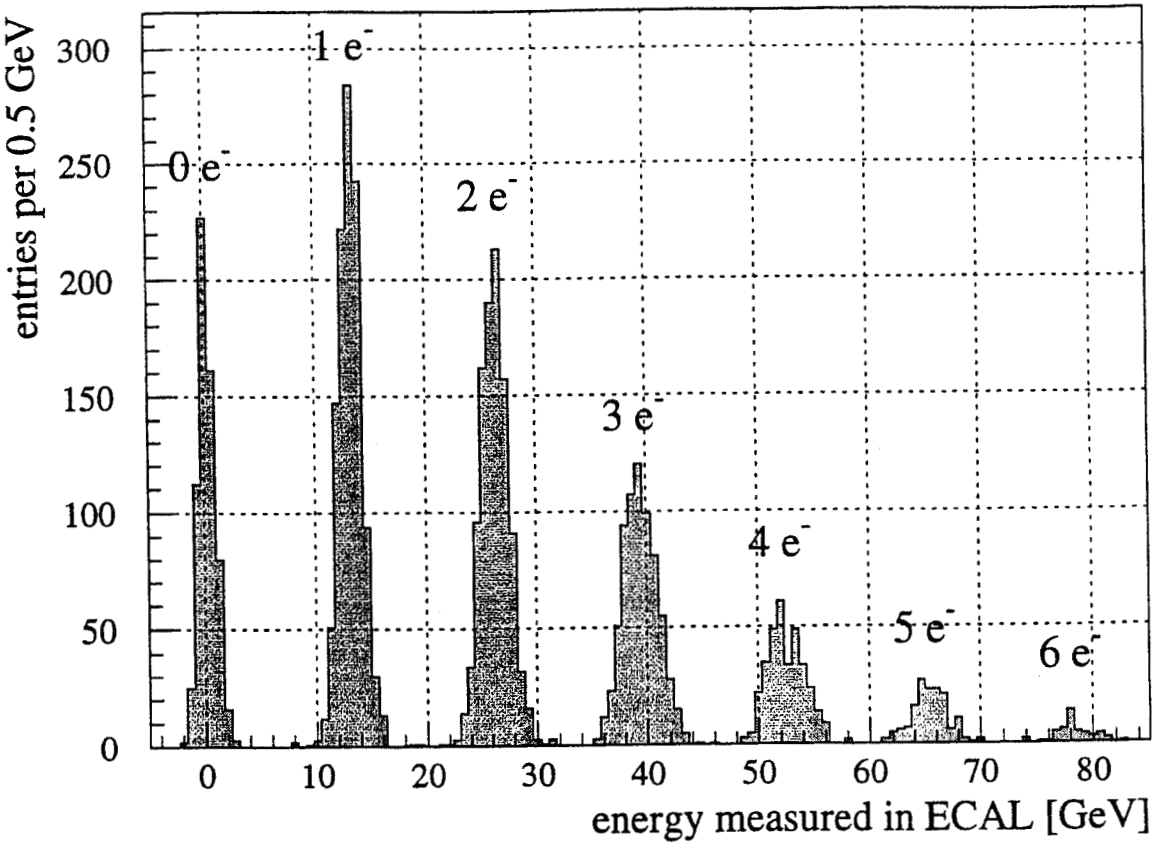

Figure 2.5: Calorimeter Calibration.
This plot shows the ECAL response to a 13 GeV calibration beam.[25]

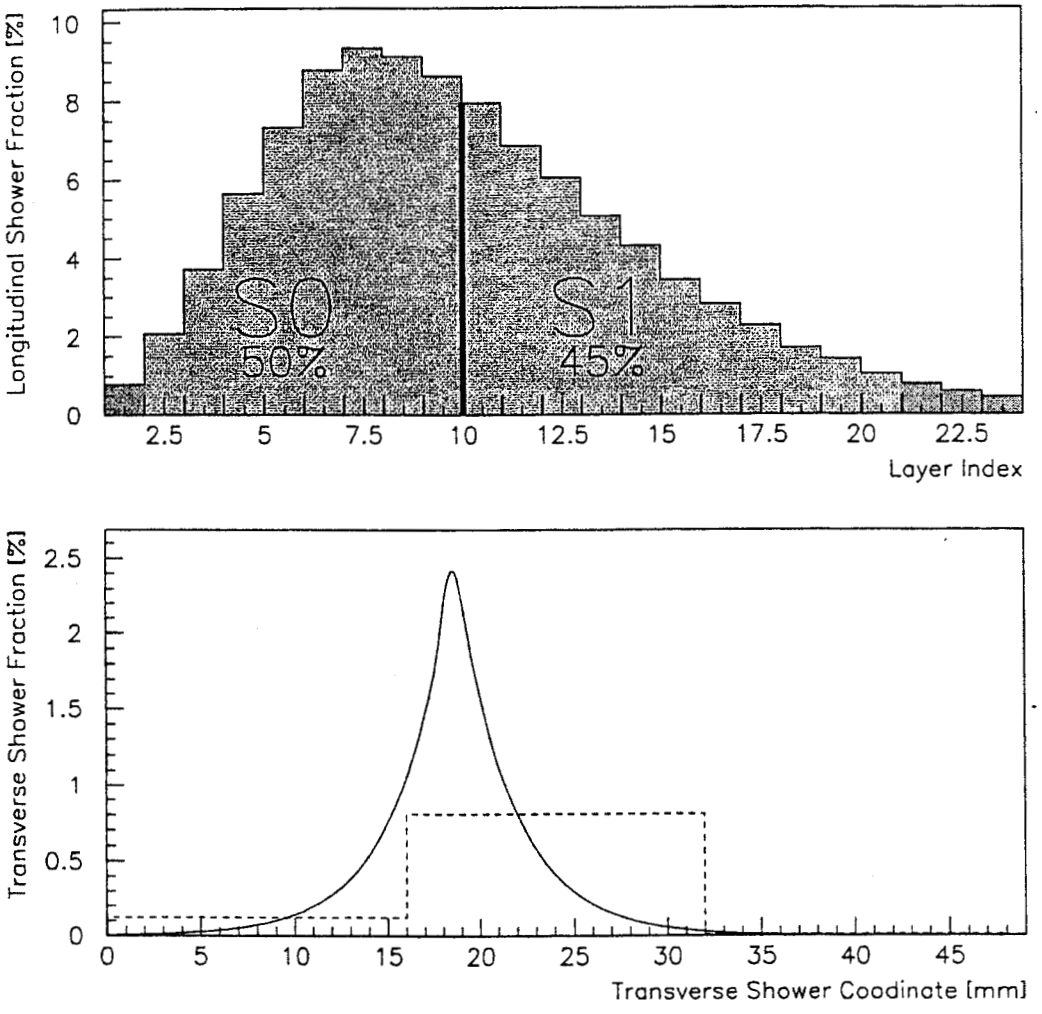

Figure 2.6: Simulated Shower Profiles.
The top plot represents the longitudinal profile of the electromagnetic shower caused by incident positrons. The bottom plot represents the transverse extent of the cascade. The solid line is the shower profile. The dashed line is the calorimeter cell response to the solid line. Each cell measures the shower energy it receives, the output is proportional to the integral of the shower profile over the extent of the cell.

2.3 The Data Acquisition System

The data acquisition system (DAQ) for E-144 was operated over an Ethernet network of IBM PC compatible computers (PCs). One master (Back End, or BE) PC ordered actions by a varying number of slave (Front End, or FE) PCs. In most cases, the FEs were ordered to report back readings from various detectors. When in acquisition mode, the FEs read out detectors upon being "triggered" by timing signals (triggers) derived from the SLAC Master Pattern Generator (MPG). An adjustable "mask" was superimposed on the MPG output via the SLAC control program (SCP), or "skip". This mask selected which MPG signals were presented to the E-144 PCs. The MPG signals occurred with fixed timing relative to the arrival of e^- bunches at IP1.

The data acquisition system's design called for calorimeter readout whenever a SLAC trigger was seen. The triggers were of 4 varieties:

E1L0 An event was a "Laser Off" event if there was an e^- bunch and there was not a laser pulse at IP1.

E0L0 An event was a "Laser Off Pedestal" event if there was neither an e^- bunch nor a laser pulse at IP1.

E1L1 An event was a "Laser On" event if there was an e^- bunch and there was a laser pulse at IP1.

E0L1 An event was a "Laser On Pedestal" event if there was not an e^- bunch but there was a laser pulse at IP1.

The bit following **E** represents the state of the e^- bunch, 1 indicates the presence of an e^- bunch, 0 indicates the absence of an e^- bunch, and X indicates either or both. The bit following **L** represents the state of the laser pulse, 1 indicates the presence of a ω_0 pulse, 0 indicates the absence of a ω_0 pulse, and X indicates either or both.

There have been two different but similar trigger schemes. Prior to the March 1995 run, there were 4 E1L0s for every E1L1. The timing was simple: E1L0, 200μs, E1L0, 200μs, E1L1, 600μs, E1L0, 200μs, E1L0, 200μs. Every 24th

E1L0 event, a "kicker" magnet located in the linac was energized, dumping the e^- bunch, making E1L0 → E0L0. Every 8th E1L1 event, the kicker was fired, making E1L1 → E0L1. Starting in March, a different scheme was used. The nominal trigger ratio was reduced form 4:1 to 2:1. The new timing was: E1L0, 200μs, E1L1, 1600μs, E1L0, 200μs. Every 32nd E1L0 → E0L0. Every 64th E1L1 → E0L1. Every trigger causing the Back End to acquire data was referred to as an "Event." A succession of events, for which collected data is gathered into a single file, is referred to as a "Run."

During runs, the BE waited for triggers. Upon observing a trigger, it ordered action from each of the FEs, blocking further triggers until all PCs reported their assigned tasks complete. This helped to maintain the synchronization of the readout cycle. When acquiring data, the BE ordered the FEs to send it their event data blocks. It made several synchronization checks, and, when satisfied, it combined the equipment data block extracted from each FE's event data block into a run event data block, subsequently writing it to a data file residing on a hard disk and broadcasting it over the Ethernet.

The detectors and diagnostic equipment read out by the FEs were myriad. Figure 2.7 provides an overview of the DAQ, listing some of the measurements made by the FEs. The Rabbit electronics described in were read out by SICA1. Three calorimeters were involved, one to detect e^+s , another to detect recoil e^-s , and a third to detect the forward γs produced in ω_0–e^- collisions. The e^- beam diagnostics were read out by BEAM1. Quantities recorded included beam polarization (when defined), toroid signals, beam positions, a variety of Cerenkov counter readings, and the trigger word for the signals that caused detector readout. The optical delay line was adjusted by LASER1. A digital scope that measured either laser energy at two points or laser energy and pulselength was read out by LASER2. A CCD camera imaging the intensity profile of the laser focus was read out by LASER3.

The tasks of the Front End PCs were myriad. Laser2 was the PC responsible for readout of a HP 546001A Oscilloscope, 2 channels of which were digitized per trigger. One channel was dedicated to measuring the peak voltage attained by the output of a Molectron J50-LP pyroelectric Joulemeter

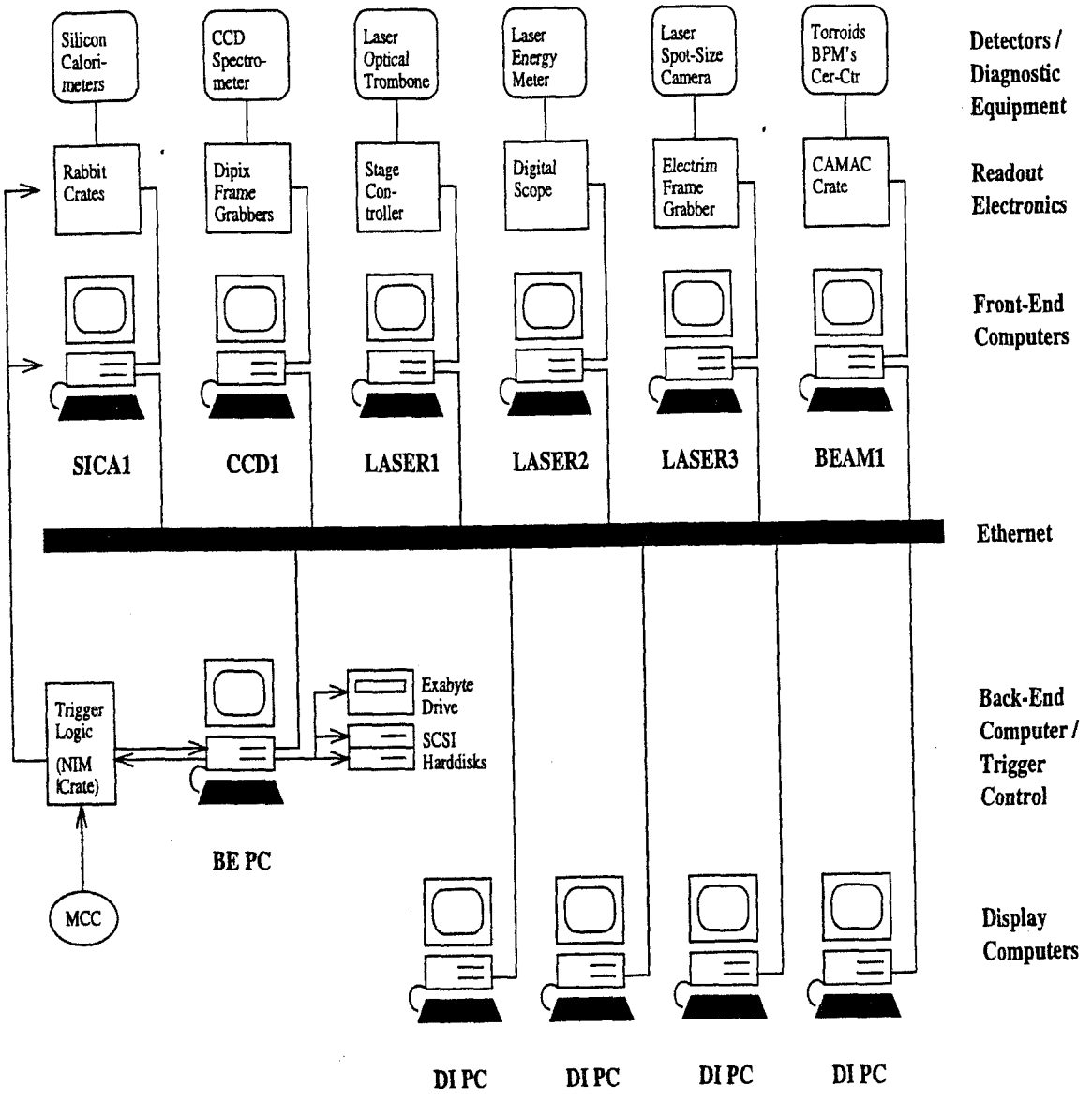

Figure 2.7: The Data Acquisition System.
The Back End PC orchestrated readout of detectors, rastering of collision parameters, and archival of data.

illuminated by some fraction of a laser pulse. The other channel was used either to measure the output of a second Joulemeter or to digitize the output of an EG&G Reticon S Series Solid State Line Scanner (512 25μm wide pixels) used to image the single-shot autocorrelators pulsewidth-dependent intensity profile. Beam1 was the PC responsible for monitoring beam parameters and talking to the SLC Control System.

There were a variety of run types supported by the BE, including "Timing Scans," "Pedestal Runs," "X-T Scans," "X Scans," "Y Scans," and "Physics Runs." A "Physics Run" is one during which beam bunch/laser pulse collisions occur. In one of the "Scan" runs, one or two of the overlap parameters was rastered through a range of values selected to map out the scattering rates' dependence on bunch/pulse average overlap. In Physics Runs, overlap parameters were not rastered. Variations of these parameters came only in the form of instantaneous jitter and long term drift.

For "e^+ Runs", the electron beam was tuned so as to minimize its area while maintaining minimal background. Figure 2.8 is a plot of a wire scan performed while the "e^+ " configuration of FFTB magnet strengths was loaded. The wire was scanned in a plane transverse to the beam line. The scan path crossed the center of the beam line and bisected the angle between the $\hat{x}$ and $\hat{y}$ axes. The radius is given by

$$r_u^2 = \sqrt{\frac{r_x^2 + r_y^2}{2}}. \tag{2.10}$$

For every event, 6 beam parameters were measured: charge (BMCH), x-position(BMX), x-angle(BMXP), y-position(BMY), y-angle(BMYP), and energy(BMDE). For each run, gaussian fits were made to the distributions of parameter measurements. In all subsequent analysis, events with one or more parameter outside of the range $[\mu - 3\sigma, \mu + 3\sigma]$ were automatically cut.

A toroid downstream from IP1 in the FFTB beam line, installed to monitor beam charge for beam containment purposes, was used to measure BMCH. This toroid was installed as part of the protection system, excessive charge can trip beam interlocks. Our sample of the signal is fed into a GADC read out by the

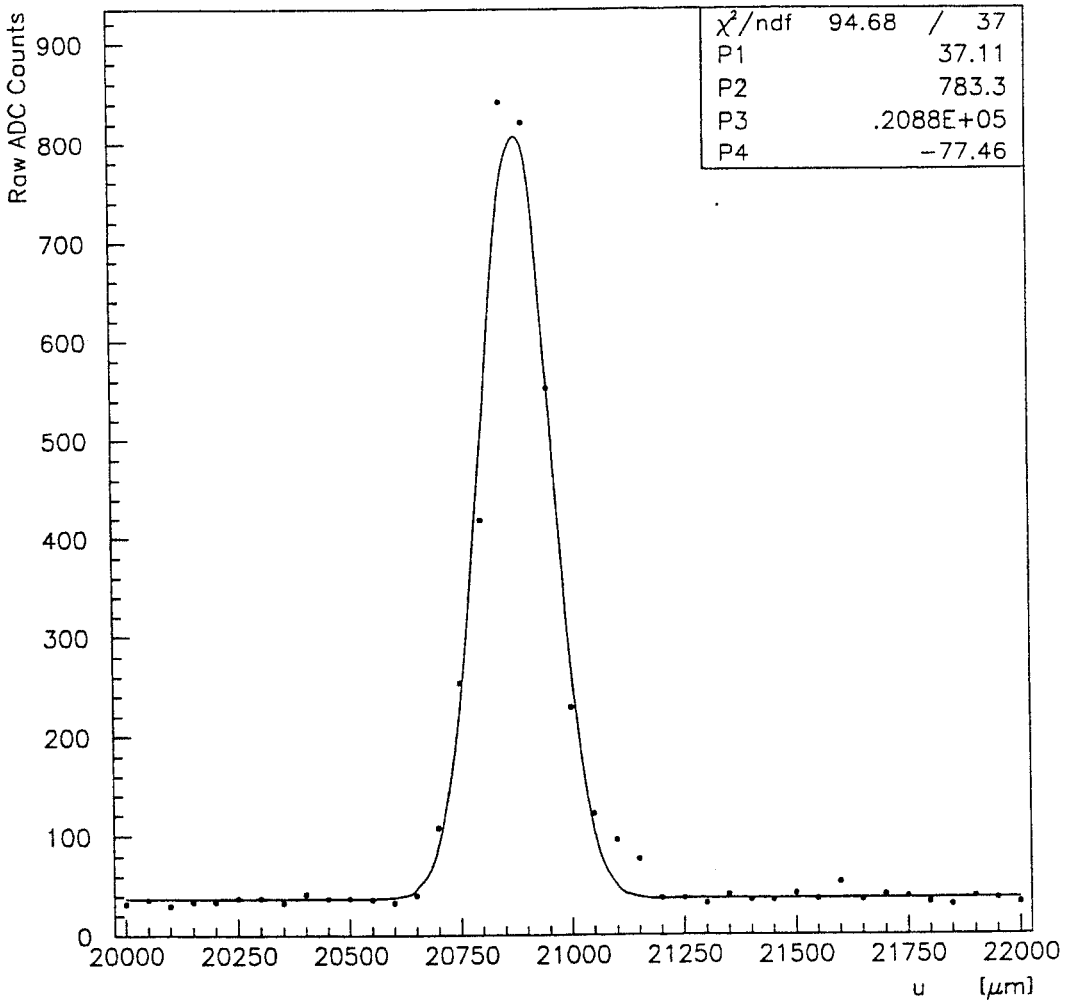

Figure 2.8: FFTB wire scan.
A plot of a wire scan performed while the "e^+ " configuration of FFTB magnet strengths was loaded. The scattering rate was monitored as a wire was rastered through the electron beam. The scattering rate varied as the wire moved through the varying electron densities.

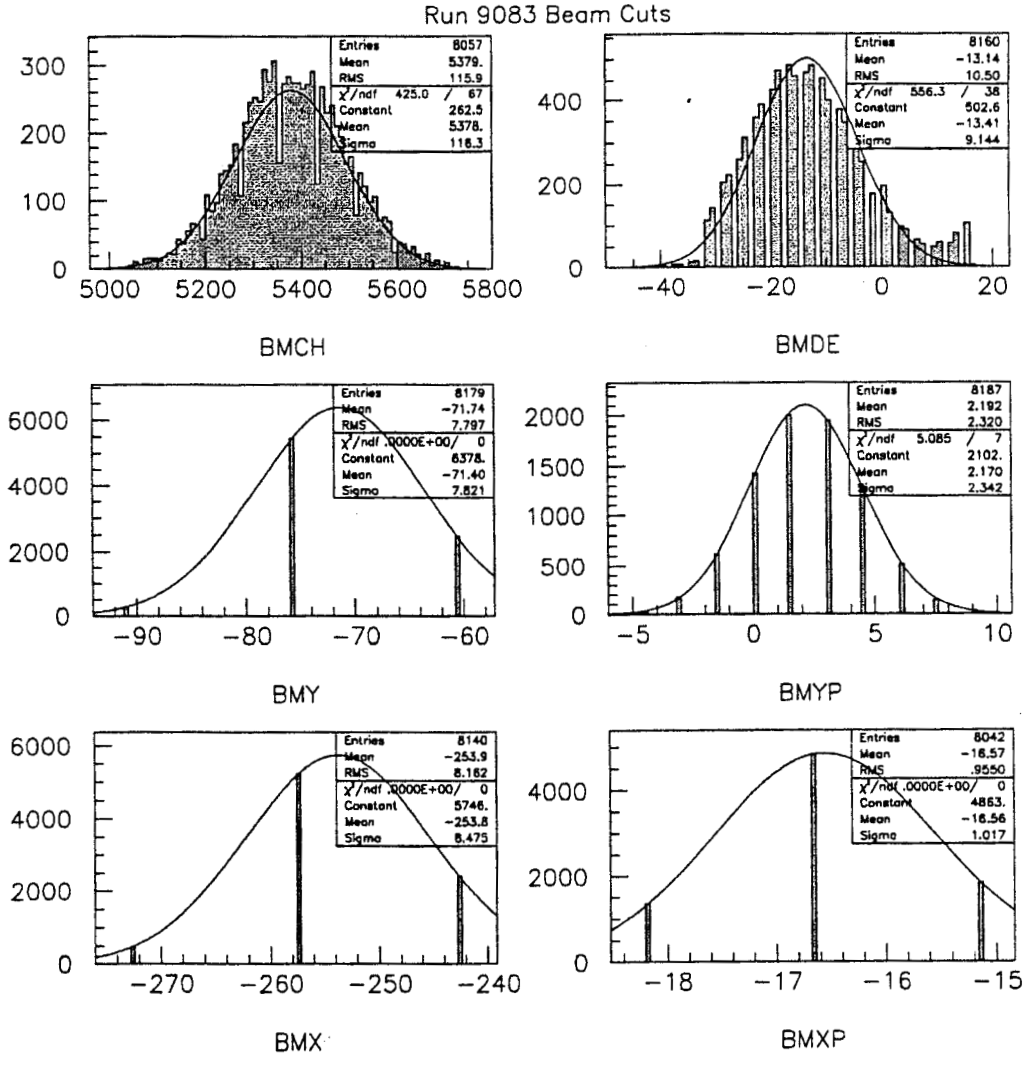

Figure 2.9: Beam Parameters for Run 9083.
These beam parameters were used to cut events for which electron bunch integrity was doubtful.

beam PC. It was calibrated using upstream toroids, which have good electronics, being unencumbered by the beam containment electronics. As such, the units of BMCH are $q_e \times 10^9$, or billion electron charges. It should be good to 2 percent or better.[28]

BMDE represents the deviation of beam energy from nominal, 46.6 GeV for FFTB running; its units are MeV. BMX and BMY represent the deviation of position from nominal, readout in microns. BMXP and BMYP represent the deviation of crossing angle from nominal, readout in microradians. BMX, BMY, BMXP, and BMYP are all measured by Beam Position Monitors.

Beam parameters jumped away from mean values for various reasons. Most notably, the temporary failure of an accelerator klystron resulted in lower e^- energy. The e^-s in a pulse traversing a tripped klystron will not be accelerated and thus emerge from the linac with energy below 46.6 GeV. Lower beam energy noticeably affected all the other parameters except beam charge since e^-s with different energies that propagate through the same beam optics get steered to different places.

Parameter	μ	σ	Lower Bound	Upper Bound
Charge	5378	116.3	5029	5727
Energy	−13.41	9.144	−40.84	14.03
y position	−71.40	7.821	−94.86	−47.94
y angle	2.170	2.342	−4.855	9.194
x position	−253.8	8.475	−279.12	−228.3
x angle	−15.56	1.017	−19.61	−13.51

Table 2.1: Beam Parameter Cuts for Run 9083.
If the value for a parameter was less than the Lower Bound or greater than the Upper Bound the event was cut. The Bounds listed in this table represent $\mu \pm 3\sigma$.

Chapter 3

The Laser System

3.1 Introduction

For the nonlinear QED studies at SLAC, we constructed a $\lambda = 1.053\mu$m laser system which delivers 2 J, 1.5 ps pulses, focused down to a 1.4 times diffraction limited, 50 μm^2 spot size. The laser system was designed and built with three primary goals: high intensity, high repetition rate, and phase stability. These goals were met by a system which combined existing technologies and techniques, including Chirped Pulse Amplification (CPA),[29, 30] active acoustooptic mode-locking[31] with electronic phase feedback,[32] and an Nd:Glass slab amplifier.[33]

The processes studied are highly nonlinear in cross section with respect to electric field strength. Diagnostics capable of measuring laser pulse energy (U_L), spot size (A_L), and pulse duration (τ_L) measurements were implemented so that the intensity and electric field amplitude could be calculated in the offline analysis.

The physics program of E–144 called for $\lambda = 1.05\mu$m (Infrared, or IR) and $\lambda = .527\mu$m (Green) running. To produce the Green light, we frequency-doubled IR laser pulses in Type II KDP crystals,[34] observing doubling efficiencies as high as 55%.

Establishing and maintaining temporal and spatial overlap of the e^- bunch and ω_0 pulse was critical to the success of E–144. Temporal overlap was more elusive than spatial overlap. Though the geometry of the experiment linked path lengths and pointing, it was possible to have spatial overlap while remaining mis-timed. Great effort was exerted to ensure "quality" collisions.

3.2 Design Principles

Experimental considerations constrained the laser system's design. The SLAC linac produces a minimum of 10 e^- bunches per second. There is a great demand for SLAC beam time. It was necessary to propose a sound experimental program when requesting beam time. Demonstrating efficient use of beam time was also necessary. For this reason, the laser system was built to produce high intensity pulses as often as possible, thus optimizing use of the e^- beam.[35] We

used an Nd:Glass slab as our final amplification stage since it can produce high energy pulses at a greater repetition rate than amplifiers of different geometry. Since high intensity, not just high energy, was needed, we used CPA so that the high energies available from the slab could be compressed in time to form a shorter, higher intensity pulse. We synchronized our laser pulse formation with the e^- bunch arrival at the interaction point with an active phase feedback system. The pulse formation and amplification sequence is depicted in Figure 3.1, the physical layout of the laser system is depicted in Figure 3.2.

3.2.1 CPA

Our system uses CPA to generate high peak power pulses. In CPA,

> ...a short optical pulse is initially chirped and stretched, allowing it to be amplified...while maintaining relatively low peak power. After amplification, an optical compressor is used to restore the original short pulse width, producing a pulse with short duration and large energy.[29]

The output of our mode-locked oscillator was passed through 1 km of 9 μm diameter, single-mode optical fiber and a grating pair expander, where it was "chirped" and "stretched" from $\tau_L = 60$ ps to $\tau_L' \sim 700$ ps and from $\Delta\lambda \sim 0.2$ Å to $\Delta\lambda = 28$ Å.[36]

"Stretch" refers to change in pulselength. The pulse is stretched by positive group velocity dispersion (GVD) in the fiber. It is stretched further as it traverses a grating pair configured, through the introduction of lenses, to provide positive GVD. Due to the nonlinear index of the fiber and the geometry of the grating expander, lower frequency light travels faster than higher frequency light through the system. As a result, in a pulse that traversed the fiber–grating expansion system, there was an approximately linear variation of frequency with time.

Since the amount of stretching is proportional to the bandwidth of the pulse transformed, it was desirable to increase the bandwidth of the pulse before it was stretched. This was done in the fiber. The mechanism responsible is the

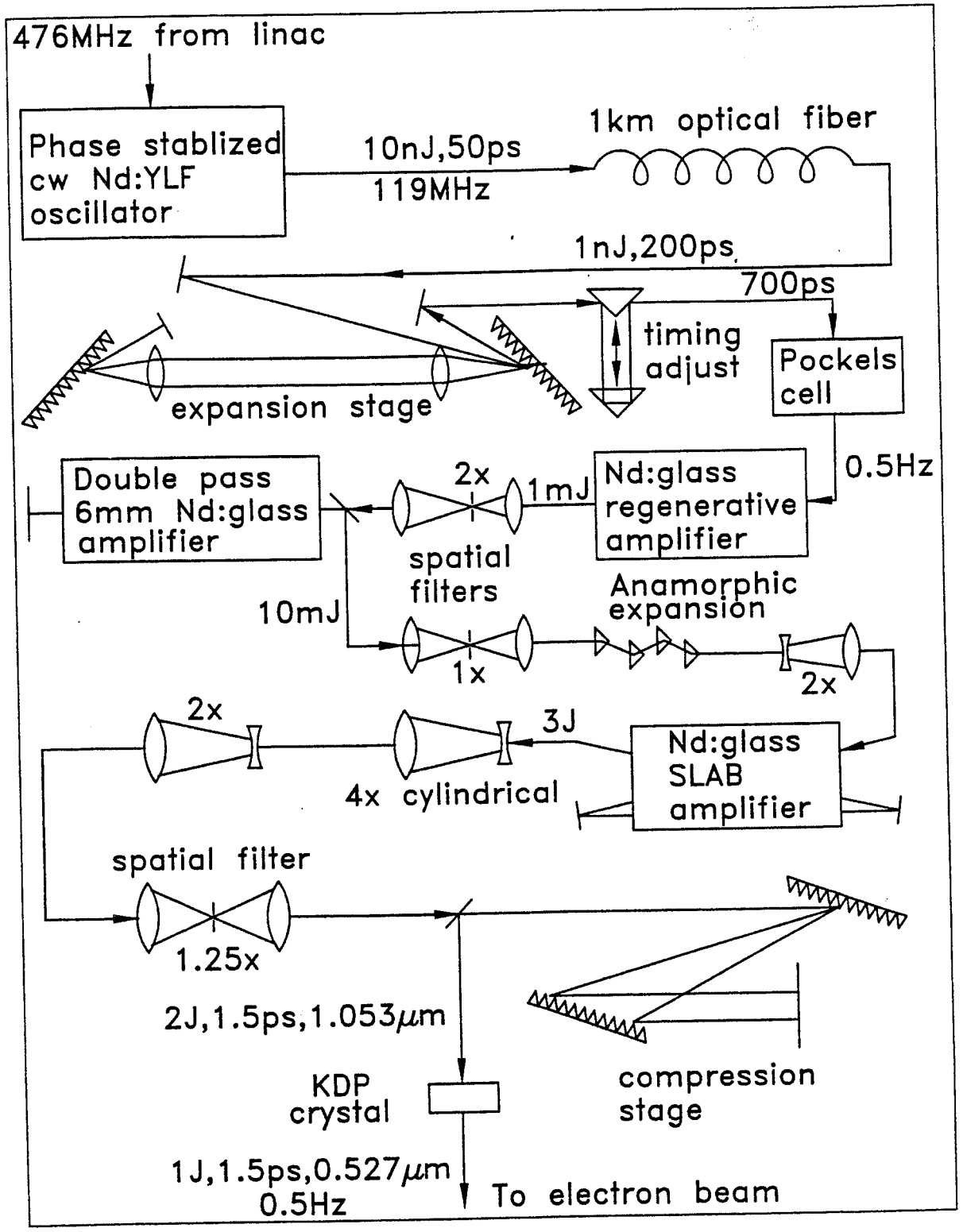

Figure 3.1: Pulse Formation and Amplification Sequence.

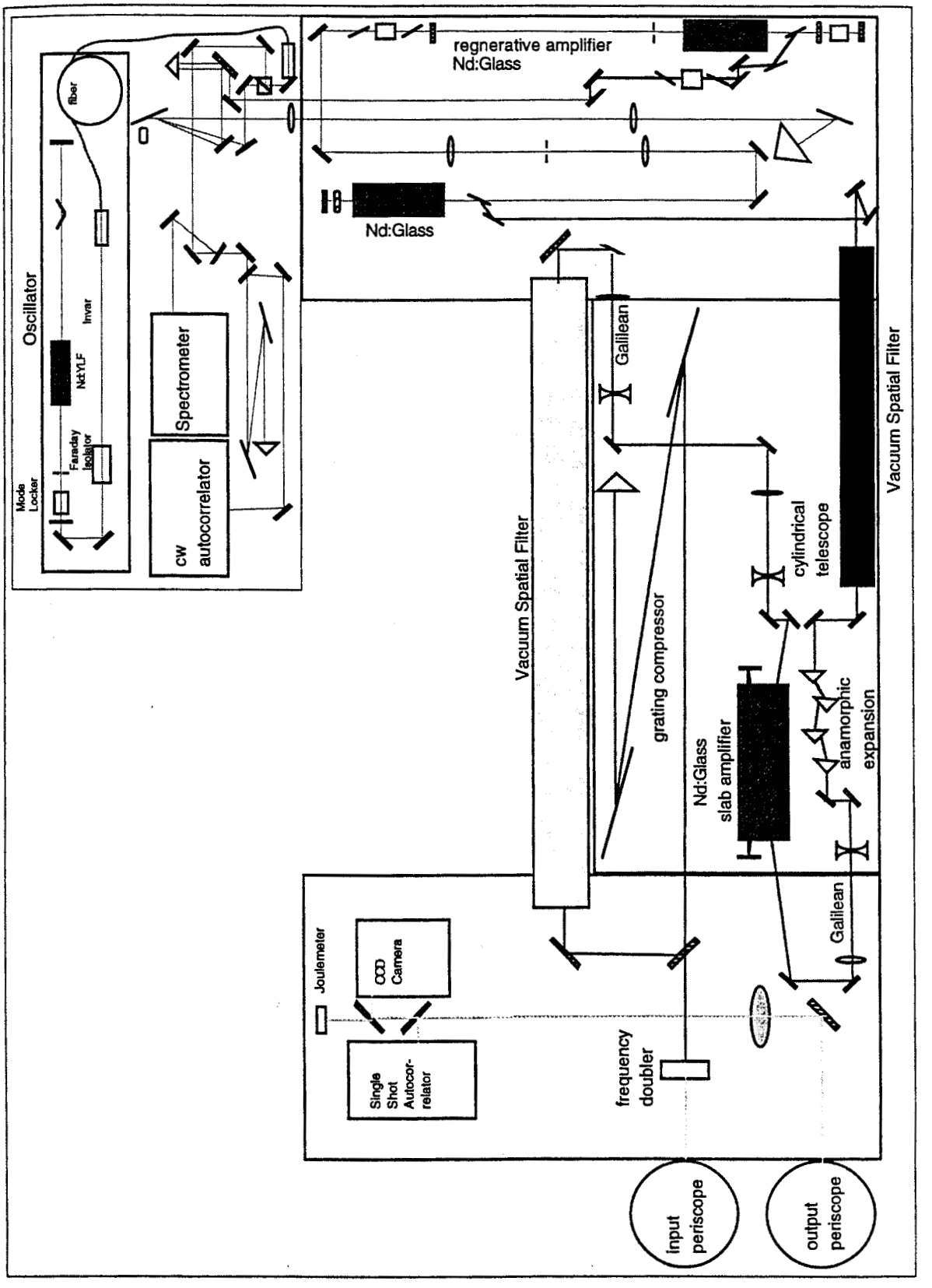

Figure 3.2: Physical Layout of Laser System.

Optical Kerr Effect. Due to the nonlinear index of refraction of the fiber, the high intensity oscillator pulses experienced self phase modulation (SPM) which imparted additional bandwidth to the propagating pulses.[37]

If the light pulse was then passed through a parallel grating compressor immediately after traversing the fiber, spaced so as to exactly compensate the negative chirp of the expansion system, it would emerge compressed to a pulselength shorter than the oscillator's.

However, the pulse is amplified before it is compressed, and in traveling through these amplifiers has both its phase and amplitude structures distorted. While system designs strive to minimize such distortions, they are still manifest to some extent and ultimately keep the pulsewidth above the bandwidth limit of the unamplified pulse.

The bandwidth limit of pulse compression can be understood by considering the gratings as performing Fourier transforms of the pulse. The expander changes a short pulse into a chirped pulse where the different frequency components are spread out in time while the compressor performs an inverse Fourier transform. If the bandwidth of the chirped pulse is reduced, the inverse transform will result in a longer pulse than we had prior to expansion.[38]

Bandwidth can be lost many ways. Gain narrowing, wherein the bandwidth of the laser transition in an amplifying media is narrower than that of the injected pulse, is the primary mechanism that limits the compressibility of Nd:Glass amplified pulses.[39] Every pass through an Nd:Glass amplifier narrows the bandwidth of our pulse. The amplitude of the frequency components in the "wings" will decrease relative to the amplitudes of the frequency components near the gain center.

Bandwidth can also be lost when gain centers are mismatched. If the frequency of maximum gain of an amplifier overlaps badly with the maximum amplitude frequency component of a seed pulse, the pulse spectrum will be narrowed. Gain narrowing also corrupts the inverse Fourier transform by distorting the linearity of the relative delay of the various frequency components.

3.2.2 Slab Geometry Amplifiers

Many high peak power lasers use optically pumped solid-state materials doped with laser-active ions as their amplifying media. These materials are susceptible to thermal effects that limit the average power and degrade beam quality. The thermal effects in an amplifier depend significantly on the geometry of the amplifying medium. Slab geometry minimizes the effects of thermal distortions. This allows higher repetition rate operation with greater beam quality than would other geometries (rod) of the same volume.

Neodymium lasers are the most common solid-state lasers. Crystals or glasses are doped with Nd^{3+} ions and pumped with optical radiation. The pump source can be flashlamp light or even other lasers. In our system, the pulse formation stage is built around an Nd:YLF rod, the three successive amplifiers are Nd:Glass-based. All four stages of our system are flashlamp pumped.

Nd:Glass has a linewidth suitable for CPA. A chirped pulse can be amplified in Nd:Glass and retain enough bandwidth to be compressible down to the picosecond level. Big boules of high quality Nd:Glass are easily (inexpensively) grown, and so for high peak-power applications, the active material dimensions of an Nd:Glass amplifier can be large. Unfortunately, Nd:Glass has low thermal conductivity. It takes a long time for heat to "flow" out of glass into coolant circulating through a heat exchanger. This limits the repetition rate of glass-based, flashlamp pumped amplifiers since such pumping causes a large amount of heat to be deposited in the glass. The heat is deposited in the lasing medium because the energy difference between an absorbed and emitted photon, the quantum defect, is transferred to the host lattice and because the host medium directly absorbs portions of the pump spectrum not overlapping the pump lines, converting ultraviolet and some infrared bands into heat.

> Thermal effects in laser rods are brought about by a combination of heat generation due to absorption of pump radiation and heat flow due to cooling processes. Heating and cooling of laser material leads to a nonuniform temperature of the rod, which results in a distortion of the laser beam due to a temperature- and stress- dependent variation of the index of refraction. The type of optical distortions

> which occur in a laser rod as a result of a nonuniform temperature distribution are thermal lensing and thermally induced birefringence due to the photoelastic effect of thermal strains. In addition, optical distortions can arise as a result of an elongation and bending of the rod.[40]

Optical distortions in a material result both from its temperature gradients and its thermal stresses. Since, in a rod, these effect will be radial, we can represent the index of refraction

$$n(r) = n_0 + \Delta n(r)_T + \Delta n(r)_S \tag{3.1}$$

This radially varying index causes focusing of pulses propagating through laser rods, an effect known as "Thermal Lensing." Thermal stress induces birefringence is solid-state media. Thermal Birefringence will alter the polarization of a wave in a material. This increases transmission losses in the laser system since the reflectivity/transmissivity of diffraction gratings, Brewster plates and windows, doubling crystals, and Pockels cells [41] used as electrooptic shutters are all polarization dependent.

Slab geometry allows faster cooling and so thermal gradients in the amplifying material are minimized. The deleterious effects of the scarce remaining thermal gradients are largely avoided due to the path of propagation through the slab. Each "bounce" of a beam between polished surfaces by total internal reflection (TIR) in a zigzag path compensates for the distortion from the index of refraction variation with temperature introduced at the previous bounce, resulting in zero net deflection. If the beam is polarized in the p-plane, reflection loss is minimized, depolarization is avoided, and distortion from thermal stress in the slab is minimized. This self compensation for thermal distortion allows pumping power in the slab up to the thermal fracture limit [42].

3.2.3 Spatial and Temporal Overlap

It is important to maintain spatial and temporal overlap of the laser pulses and electron bunches. The laser pulse area at the focus is $\sim 50\mu m^2$, whereas the electron bunch area is significantly larger. A Mach-Zender Interferometer

monitors the pointing of the laser. The FWHM lengths of the pulse and bunch are 1.5 and 3.0 ps respectively. Temporal overlap of the laser pulses with the electron bunches that are generated $\sim$ 4km away is achieved by driving a low Q, intracavity mode locker synchronously with the accelerating rf.[43, 44]

The laser was synchronized to the linac via an electronic phase feedback system. The linac e^- bunches arrive at IP1 at a fixed, or slowly varying, time with respect to the phase of the 2.856 GHz SLAC drive rf. In an acoustooptically mode-locked laser oscillator, a similar relationship is found. Pulses are emitted relative to the zero crossing of the rf input to the mode-locker driver. By using a subharmonic of the rf that drives the linac's accelerating klystrons, we were able to launch laser pulses with a fixed delay relative to the e^-s arrival time. Special electronics were used to provide phase feedback to the mode-locker, locking the phase of the laser pulse train to that of the linac.[45]

3.3 Operation

3.3.1 The Oscillator

In the laser system, pulse formation begins in the Oscillator, mode-locked in order to produce ultrashort laser pulses.[46] 476 MHz, which is the 6th subharmonic of the SLAC master rf, propagates to the laser room from sector 30 of the linac in a 600m, low attenuation, temperature stabilized optical fiber. This signal is decoded, divided down to 59.5MHz, and sent into a Lightwave Technologies stabilizer. The stabilizer output is fed into the module which drives the acousto-optic mode locker crossed by the lasing axis of our Nd:YLF Oscillator. Figure 3.3 is a block diagram of the phase feedback system.

The mode-locker sinusoidally varies the Q of the resonator which contains a cw arc lamp pumped Nd:YLF rod restricted, by opposing Brewster plates, to lasing at $\lambda = 1.053\mu$m. When rf is applied to the transducer attached to a crystal located in the cavity, light traversing the crystal is Bragg diffracted except during the rf's zero crossings.

> From a time-domain viewpoint it is then reasonable to think that the laser may begin to oscillate in the form of a short pulse which

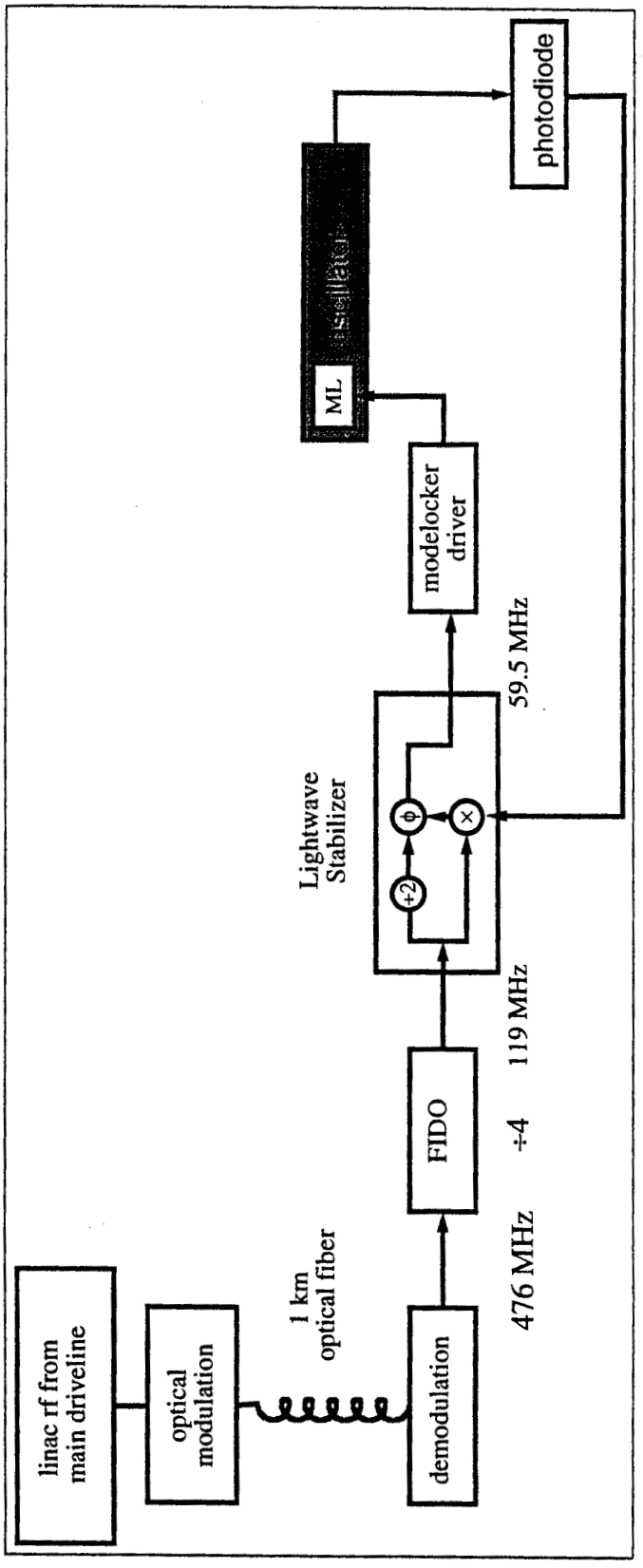

Figure 3.3: The Synchronization Scheme.

> circulates around inside the laser cavity, passing through the modulator on each round trip just at the instant when the modulator transmission is at its maximum...[47]

If the cavity length, L, is matched to the driving frequency, ν_{rf}, such that

$$\nu_{rf} = \frac{c}{4L}, \tag{3.2}$$

a pulse train will form, with pulses being emitted at the rate $2\nu_{rf}$ =119 MHz.

A fraction of the output pulse train emerging from the fiber is split off and sent into diagnostics, including a spectrometer, a cw autocorrelator,[48] and, most importantly, a photodiode integrated into the phase feedback system. The photodiode signal and the 59.5MHz are fed into a phase comparator. Feedback to maintain a constant phase difference locks the phase of the laser pulses relative to the e^- bunch, except for jitter occurring at rates above the 1 kHz sample rate of the phase comparator.[49, 50] Figure 3.4 shows a photodiode's response to the oscillator's pulse train. Figure 3.5 shows the spectrum of the chirped and stretched oscillator pulses.

3.3.2 The Regenerative Amplifier

The oscillator output is sent through a fiber/grating expansion stage where it is chirped and stretched. A 1nJ pulse is selected from the 119MHz pulse train and used to seed a Nd:Glass regenerative amplifier (regen). A pinhole in the regen cavity suppressed all but the TEM_{00} resonator modes. A single 1 mJ pulse is selected from the train transmitted through the cavity's 50% output coupler. Figure 3.6 shows a photodiode's response to the regenerative amplifier's pulse train.

3.3.3 The Rod Preamplifier

The selected pulse is sent through a 1.5:1 air spatial filter and, in twice traversing a second Nd:Glass rod amplifier (2-Pass), is boosted to 15 mJ; high spatial frequency components are removed in a 1:1 vacuum spatial filter. The polarization of the pulse from the regen is set so that it will be transmitted through, not reflected off, a Brewster plate. It traverses the 2-Pass. Emerging

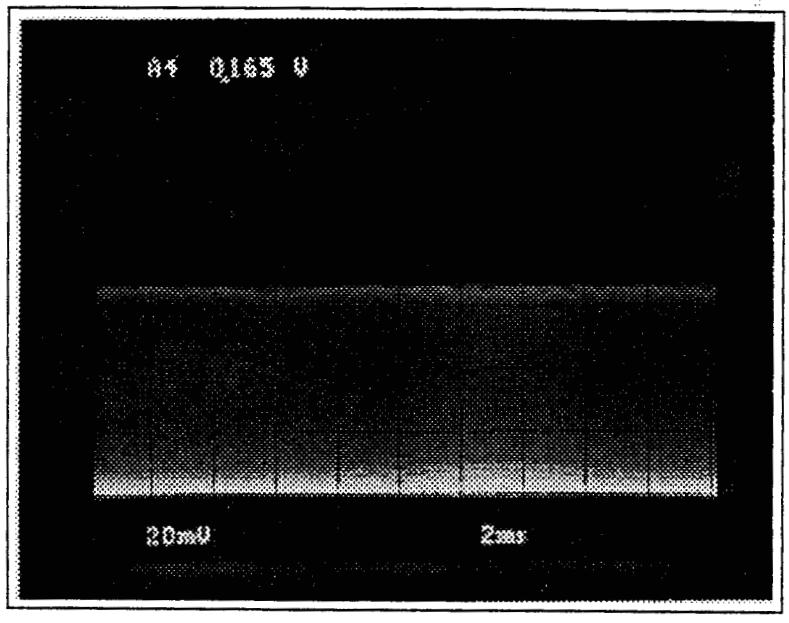

Figure 3.4: Oscillator Pulse Train.

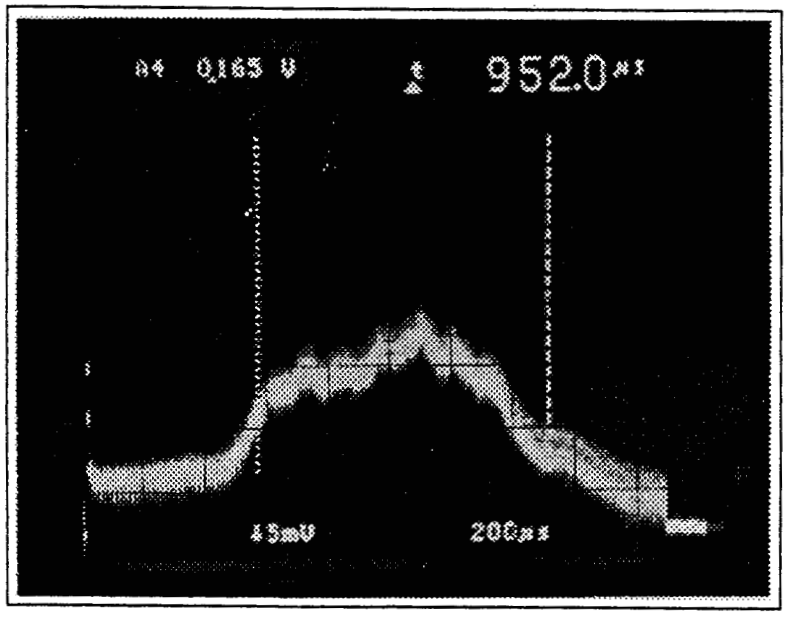

Figure 3.5: Chirped Pulse Spectrum.

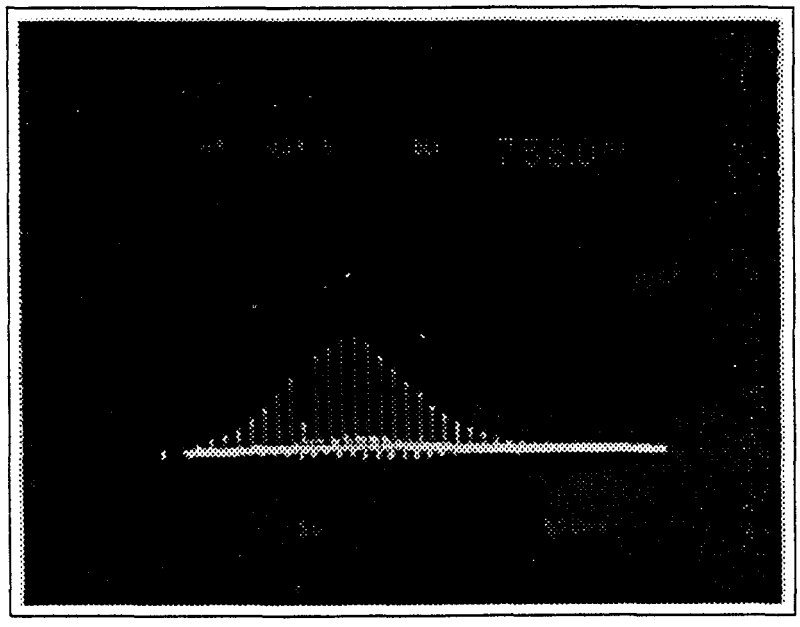

Figure 3.6: Regenerative Amplifier Pulse Train.

from the 2-Pass its polarization is rotated by a quarter wave, then it reflects off a zero degree mirror and has its polarization rotated another quarter wave before reentering the 2-Pass. Emerging from the 2-Pass it again encounters the Brewster Plate. Now however, its polarization will result in reflection, not transmission. The reflected light bounces off a second Brewster plate. Any light depolarized in the 2-Pass is removed by the Brewster plates. The depolarization losses are smallest in the center, and along the axis parallel and orthogonal to the Brewster plates' preferred direction.

3.3.4 The Slab Amplifier

The flashlamp pumped Nd:Glass Slab Amplifier (slab) that serves as the system's final amplifier, delivers 1 terawatt pulses at a 0.5 Hz repetition rate, with good focusability. Emerging from the spatial filter, the pulse is steered through a set of four prisms which expand the horizontal width of the pulse by a factor of ~ 4.4. The elliptical beam is further expanded in a 2:1 Galilean telescope before being sent into the 1.1×6.5cm clear aperture of the Nd:Glass slab. Figure 3.7 shows the anamorphic beam expander and slab amplifier. The pulse traverses the slab three times in a bow tie pattern making 12 bounces per

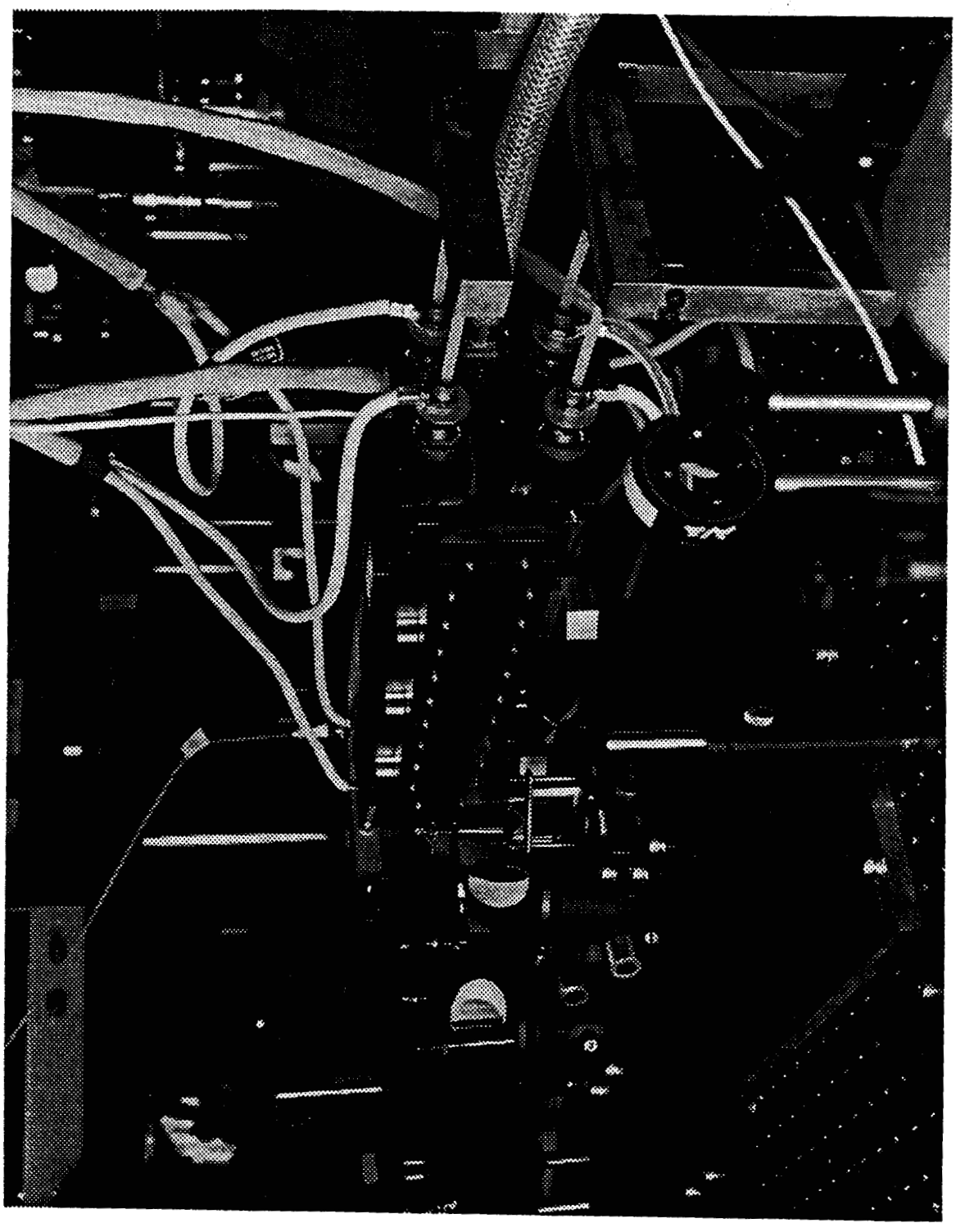

Figure 3.7: Photograph: Anamorphic Beam Expander and Slab Amplifier.

pass, 8 of which occur in the slab's 20.3cm pumped length. Small signal gains on the order of 600 have been measured, and 15 mJ pulses have been amplified to over 3.5 J. Figures 3.8 and 3.9 depict slab output for varied pumping conditions.

The slab output is recircularized by a pair of cylindrical lenses. It is further up-collimated in a second Galilean telescope and a second vacuum spatial filter before being sent into the grating pair compressor, set in a double pass configuration.[51] The vacuum spatial filters, slab amplifier, holographic diffraction gratings, and supporting optics appear in Figure 3.10. The compressed pulse is steered by the gratings into the beam transport line, depicted in Figure 3.11.

For operation in the green, the doubler is inserted just prior to the beam transport line. The $\sim$ 10m transport line steers the beam through the radiation shielding to the interaction point, depicted in Figure 3.12. An off-axis paraboloid (OAP) focuses the pulse into the interaction region. A second off-axis paraboloid recollimates the beam and directs it back to the laser room where it enters a diagnostic line. The OAP focusing scheme is depicted in Figure 3.13

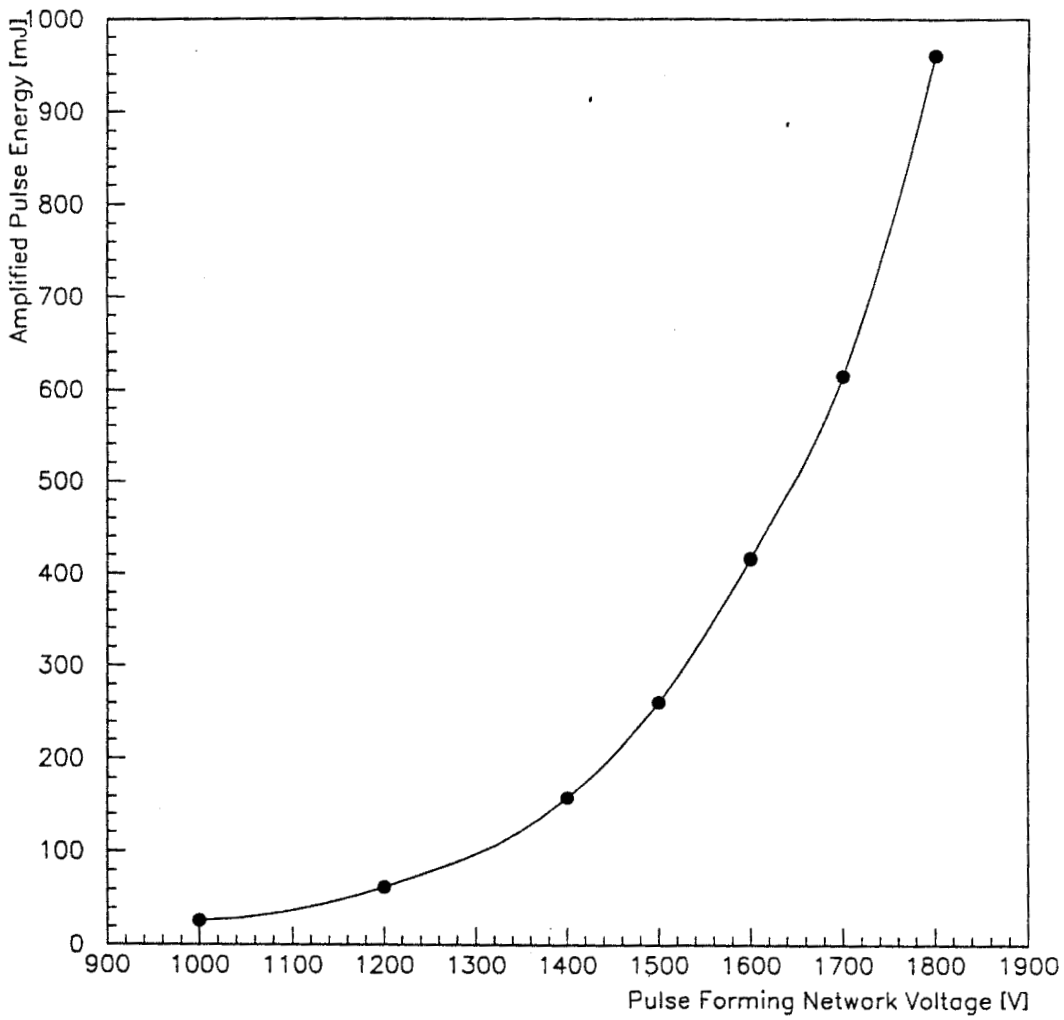

Figure 3.8: Slab Output versus PFN Voltage.
The energy measured after triple-pass amplification of a very low energy pulse in the slab versus the Pulse Forming Network (PFN) voltage. The average output of the passive (unpumped) slab for these measurements was 2.86 mJ.

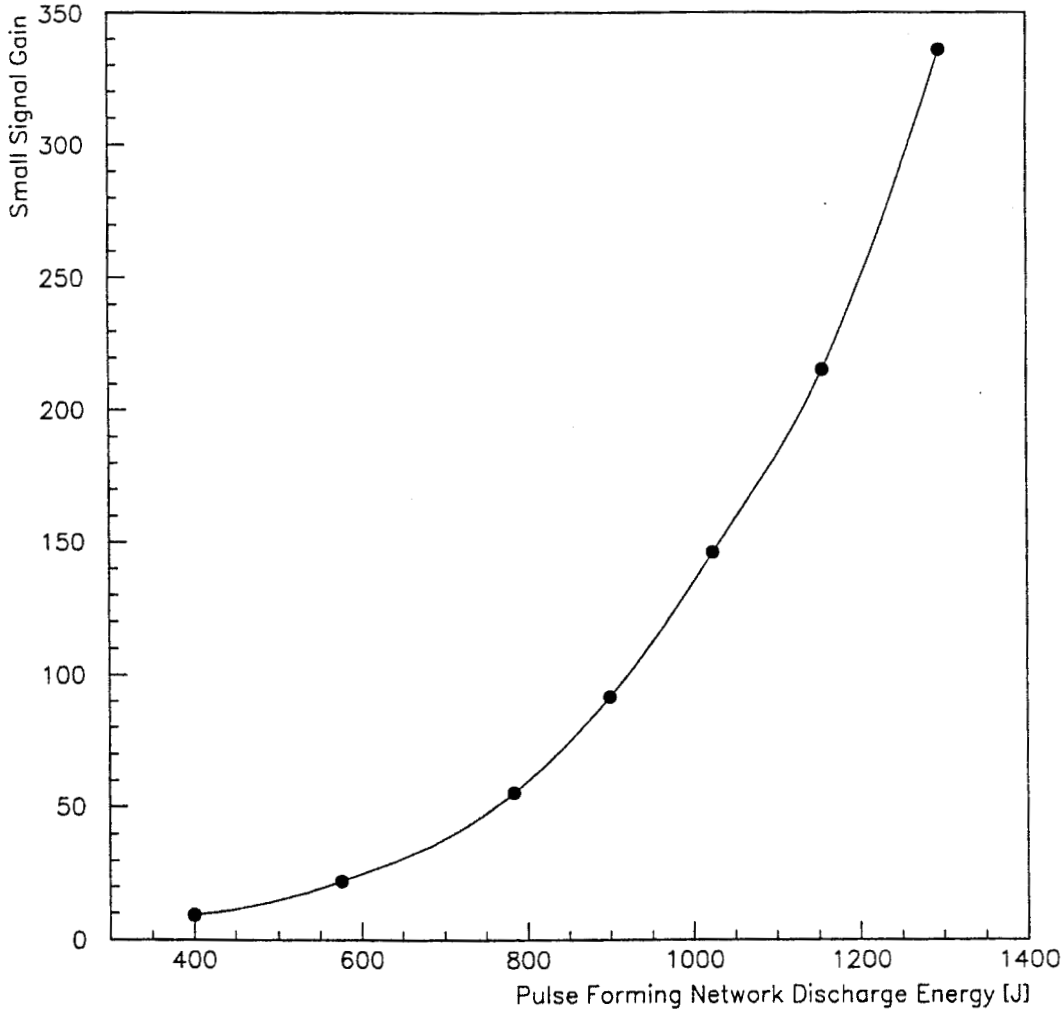

Figure 3.9: Slab Gain versus PFN Energy.
The gain measured after triple-pass amplification of a very low energy pulse in the slab versus the Pulse Forming Network (PFN) voltage. The gain here is defined as the amplified pulse energy divided by the average output of the passive slab. The average output of the passive (unpumped) slab for these measurements was 2.86 mJ.

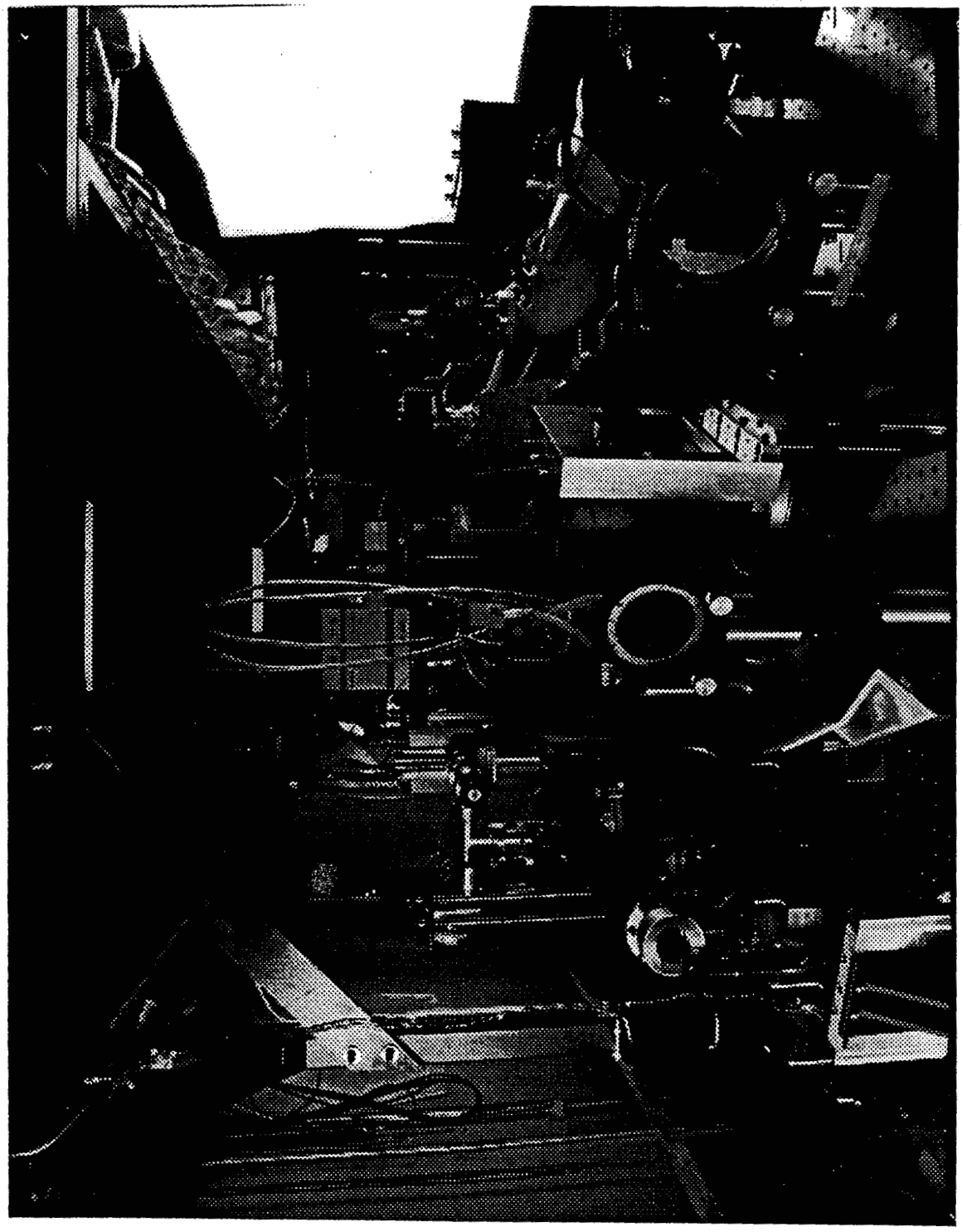

Figure 3.10: Photograph: The Third Optical Table.

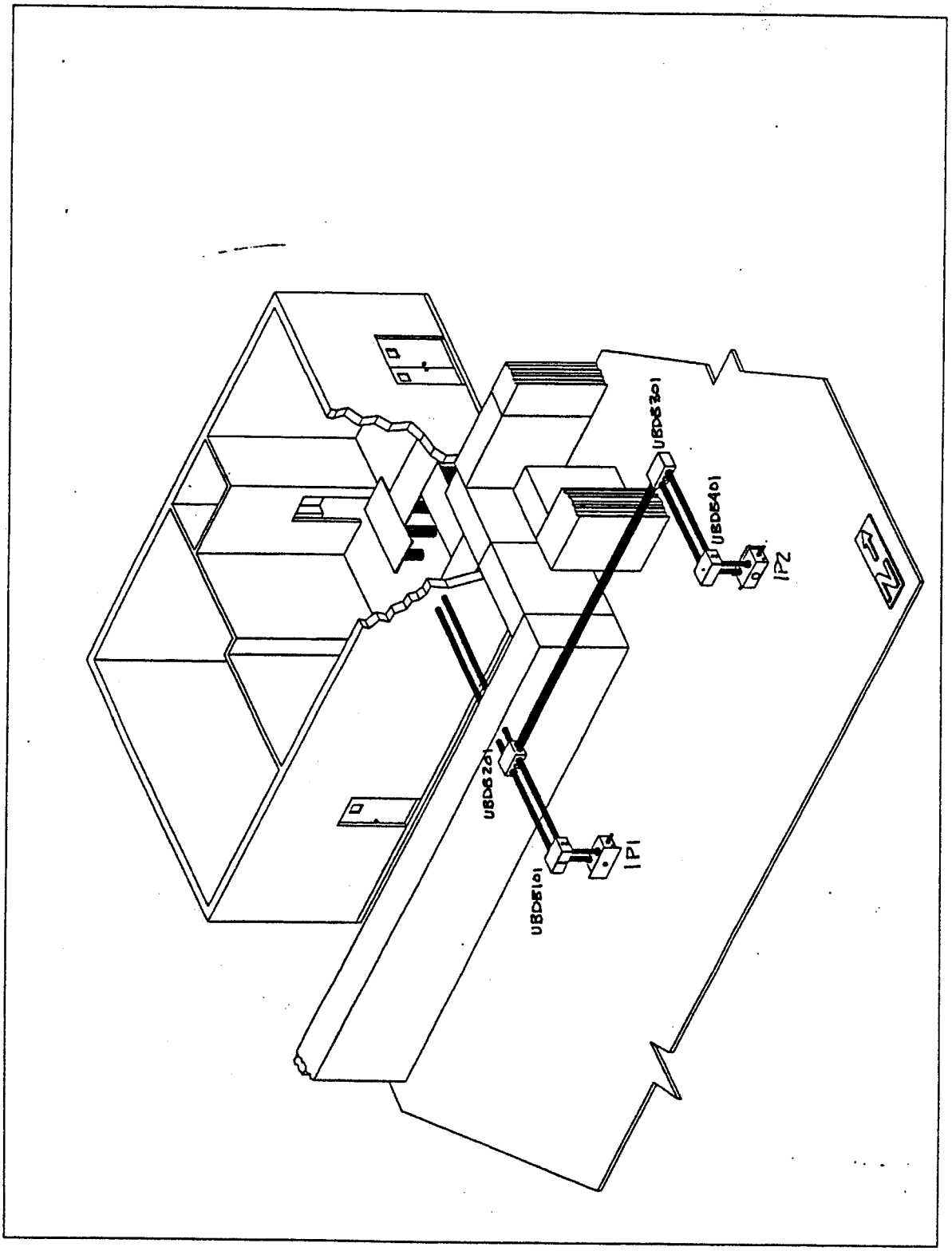

Figure 3.11: Layout of Beam Transport.

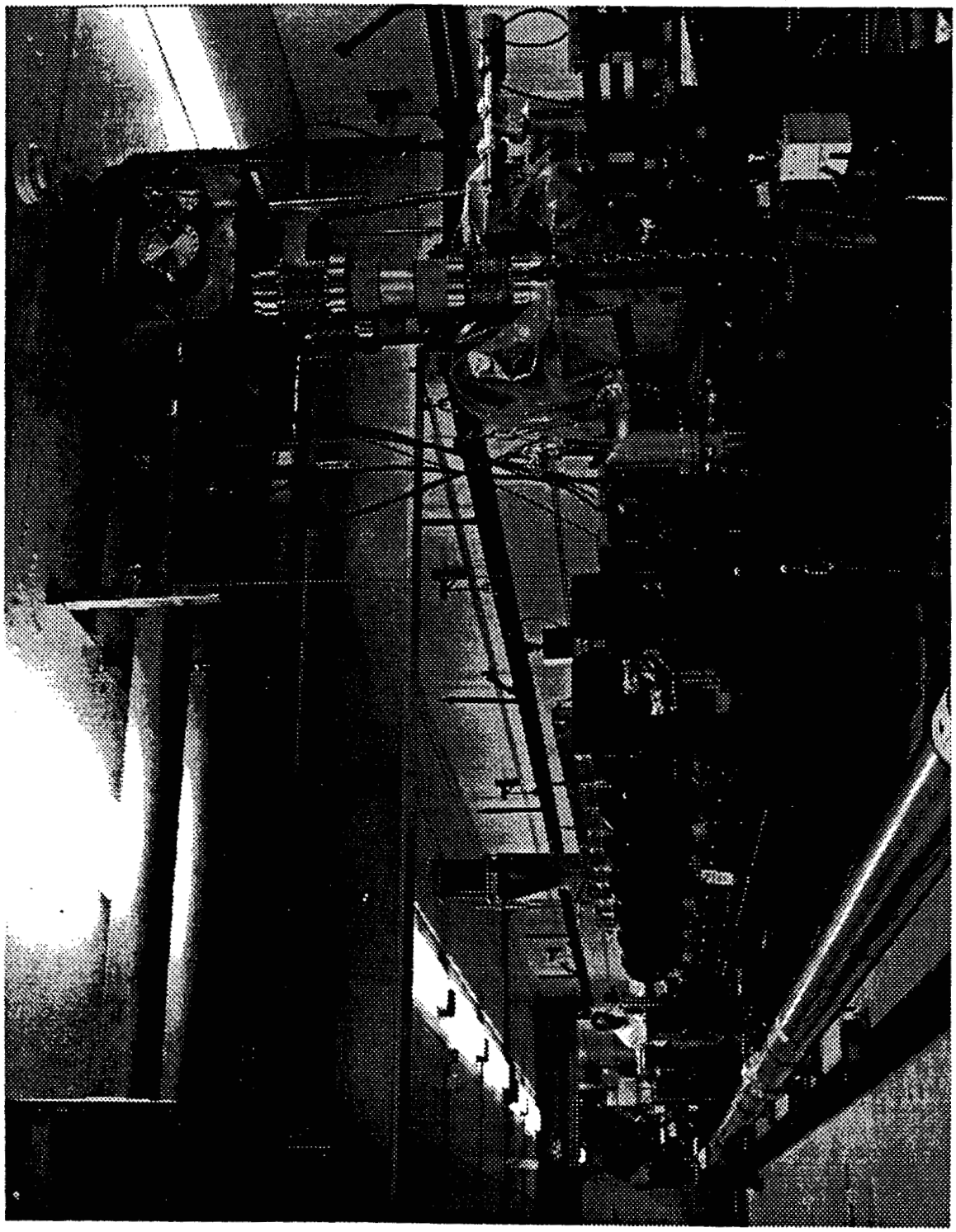

Figure 3.12: Photograph: Beam Transport and Interaction Point.

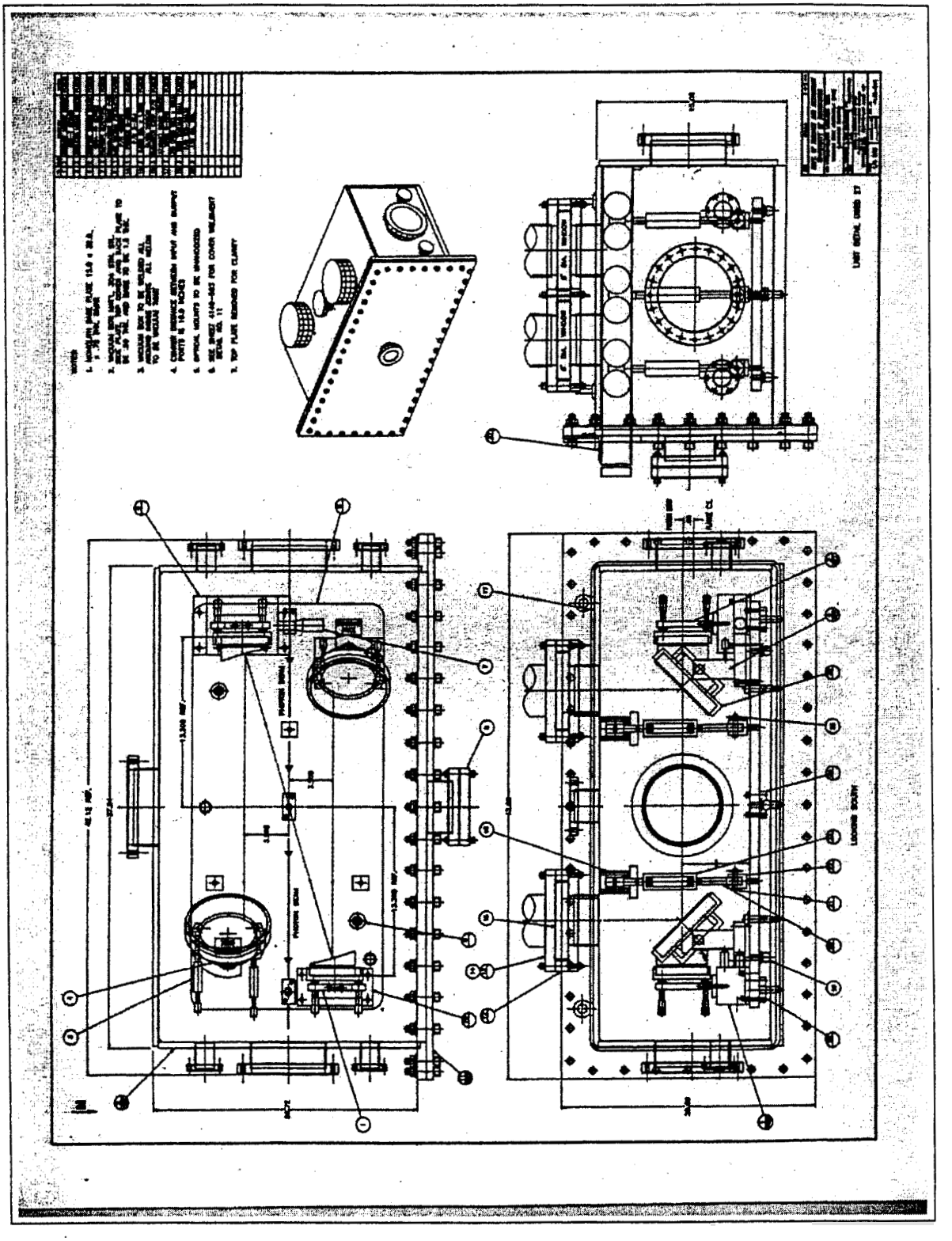

Figure 3.13: Detail Drawing of Interaction Point.

3.4 Diagnostics

The diagnostic line contains a pyroelectric Joulemeter, a CCD camera (from which a real-time fit to the focussed pulse intensity profile derives the effective focal spot area), and single shot autocorrelators sensitive to $\lambda = 1.053\mu$m and $\lambda = 527$nm light. These energy, spot size, and pulselength measurements can be combined, ignoring calibration and measurement errors, to give the pulse intensity

$$I[\mathrm{W/cm^2}] = \frac{\cdot U_L[\ \mathrm{mJ}]}{(\tau_L[\ \mathrm{ps}])\,(A_L[\mu\mathrm{m}^2])} \times 10^{17} \frac{[\ \mathrm{ps}][\mu\mathrm{m}^2][J]}{[\mathrm{s}][\mathrm{cm}^2][\ \mathrm{mJ}]}. \tag{3.3}$$

3.4.1 Energy

One channel of an HP 546001A Oscilloscope was dedicated to measuring the peak voltage attained by the output of a Molectron J50-LP pyroelectric Joulemeter illuminated by some fraction of a laser pulse. The J50-LP converted optical energy into heat, which then generated measurable current in its pyroelectric element. This signal was integrated in a capacitive load, creating a voltage, the peak value of which was directly proportional to the radiant energy absorbed by the detector. Three different detectors were used, all were calibrated by Molectron Detector, Inc. Their responsivities were all on the order of 8 mV/mJ. The test equipment and standards used in this calibration were traceable to the National Institute of Standards and Technology (NIST). The noise level quoted by the manufacturer is of the order of 16 μJ. We measured pulse energies on the order of hundreds of mJ, so the energy resolution of this detector was limited by the ADC resolution, not by fluctuations of the detector's response. High energies were digitized with less precision, sampling error for 750 mJ was on the order of 1 mJ.

Prior to the integrating of the single-shot autocorrelator into the DAQ, the second channel of the scope was used to read out a second J50-LP. This probe was located behind one of the steering mirrors that directed the slab output into the second vacuum spatial filter. The mirrors were not 100% reflective, so a fraction of the incident pulse leaked through. The pulse was, at this point, still IR. We set up a measurement where the primary probe measured only Green, while the secondary probe measured leakage IR for the same pulse. The ratio of

these two measurements was proportional to the conversion efficiency, and so we had an online, real-time measurement of η_{SHG}. We adjusted crystal orientation while monitoring η_{SHG} and were thus able to optimize conversion efficiency.

3.4.2 Pulse Duration

Photodiode response times are so long that they cannot be used to measure the 1.5 ps duration of our laser pulses. So, to measure τ_L, after our compression gratings we used two other devices, a streak camera and a single shot autocorrelator. The idea behind both is to transform pulse duration into a spatial profile of large enough scale for convenient, precise measurement.

In a streak camera, light is incident on a screen, liberating electrons. The electrons move towards a detector through a time varying electric field. The total amount of deflection will be a function of when the electron was knocked loose from the screen. By measuring the spatial profile of the deflected electrons with a CCD array, one can reconstruct dN/dt from dN/dx. The photocathode of the camera that we used was sensitive to Green, so we could measure pulselengths for either wavelength. However, the camera was poorly suited to interface with the E-144 DAQ due to long dead times between measurements and software incompatibilities. Fortunately, autocorrelators are faster and, once operational, were easier to integrate into the data stream.

Second harmonic generation will be discussed in greater detail in section 3.6. For now it is enough to say that in certain crystals, two lasers photons can combine to form a single photon with twice the energy, half the wavelength, and that the effect is roughly proportional to the square of the pulse intensity.

In our single-shot autocorrelator, a beam splitter sends equal fractions of a pulse out along separate arms of equal length. These pulses intersect in a crystal, and second harmonic light is generated. Kinematics dictate that the produced second harmonic light will propagate along the bisector of the fractions crossing angle. The SHG light is only produced where the pulses coincide both spatially and temporally. Thus, the amount of SHG light will be a function of overlap and pulselength. This scheme is depicted in figure 3.14.

The autocorrelator trace was directed onto a linear CCD array. The

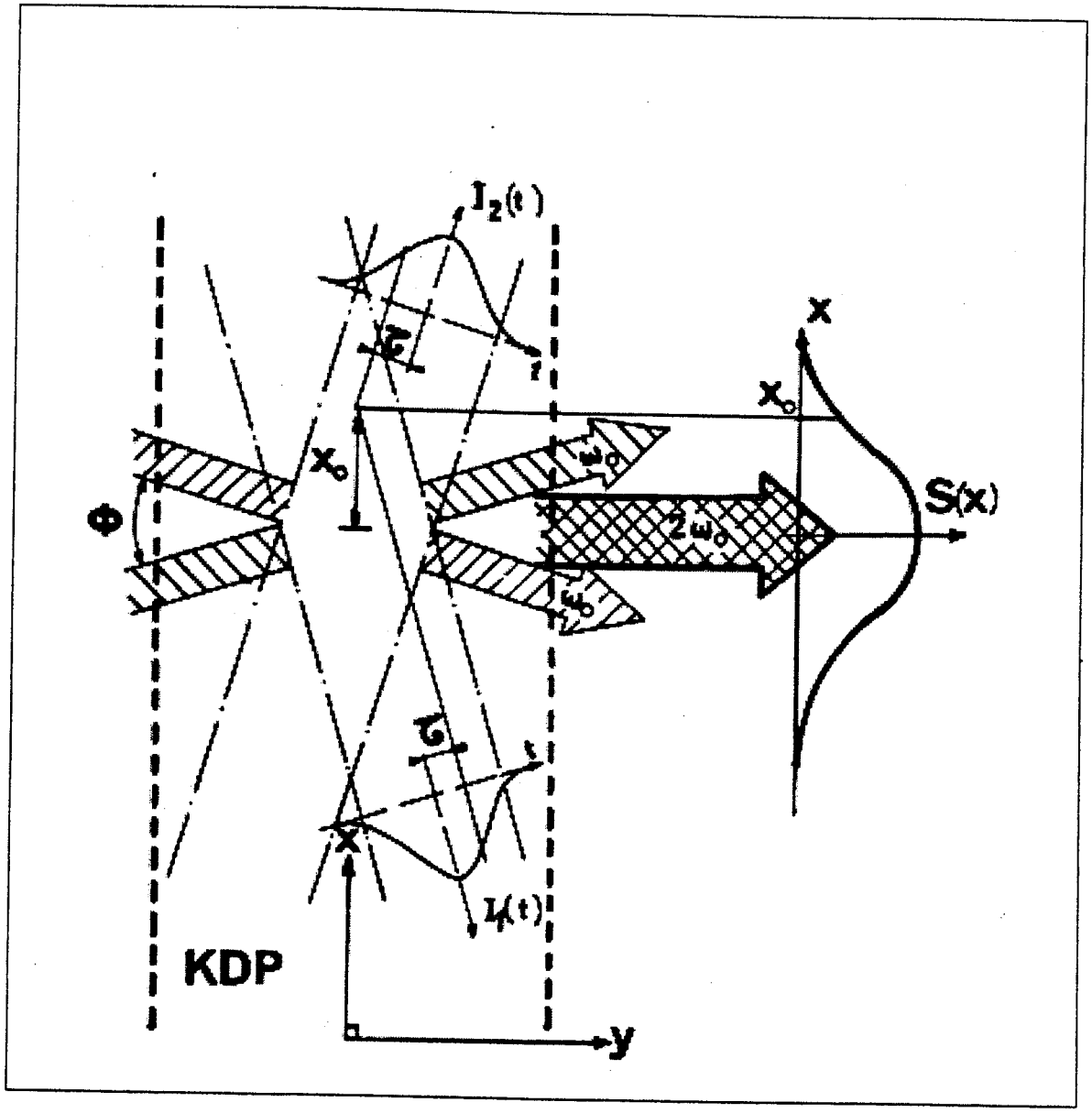

Figure 3.14: Single Shot Autocorrelation Schematic [52].
In our scheme, $S(x)$ was imaged by a linear CCD array.

waveform output by this array was digitized in an oscilloscope and read out via PC. The trace was sent to a generalized least squares fitting routine.[53] The fit function was

$$V(t) = a_1 * \exp\left(-\frac{t-a_2}{a_3}\right) + a_4 + a_5 * t - a_6 * \tanh\left(a_7 * (t-a_8)\right); \qquad (3.4)$$

This function was selected to model a gaussian centered on a Heaviside step function. This step function was added to correct for a step appearing in the voltage offset of the wings of the trace. Figure 3.15 shows the autocorrelation trace for a 500 mJ, 1.51 ps, 50μm^2 pulse recorded in the March 1995 run

3.4.3 Spot Size

A lens system was used to image the focused pulses onto the CCD camera. The collimated pulses returning from the interaction point were focused with a $f = 420$ cm lens. The intensity profile at the focus of this lens is referred to as an equivalent target plane (ETP) profile. The target in this case is the electron bunch. The intensity profile formed at the focus of the lens is considered equivalent (though magnified) to that formed by the OAPs in the interaction point. Measuring the spot size at the lens focus gives the IP1 spot size times a geometrical factor. As depicted in Figure 3.16, the focus of the "ETP Lens" was magnified onto a two dimensional array of pixels by a 5× microscope objective. The CCDs were read out by a PC, and the intensity profile was written to the data stream.

I have used the following definitions to describe laser propagation. The electric field amplitude $\mid \mathcal{E}(\vec{r}) \mid$ of the pulses is given by

$$\mid \mathcal{E}(\vec{r}) \mid = \frac{\mathcal{E}_0}{\sqrt{2}} \exp\left(\frac{-r^2}{2\sigma^2}\right). \qquad (3.5)$$

The intensity profile $I(r)$ of the pulses is given by

$$I(r) = c\epsilon_0 \mid \mathcal{E}(\vec{r}) \mid^2 = \frac{c\epsilon_0}{2}\mathcal{E}_0^2 \exp\left(\frac{-r^2}{\sigma^2}\right) = I_0 \exp\left(\frac{-r^2}{\sigma^2}\right). \qquad (3.6)$$

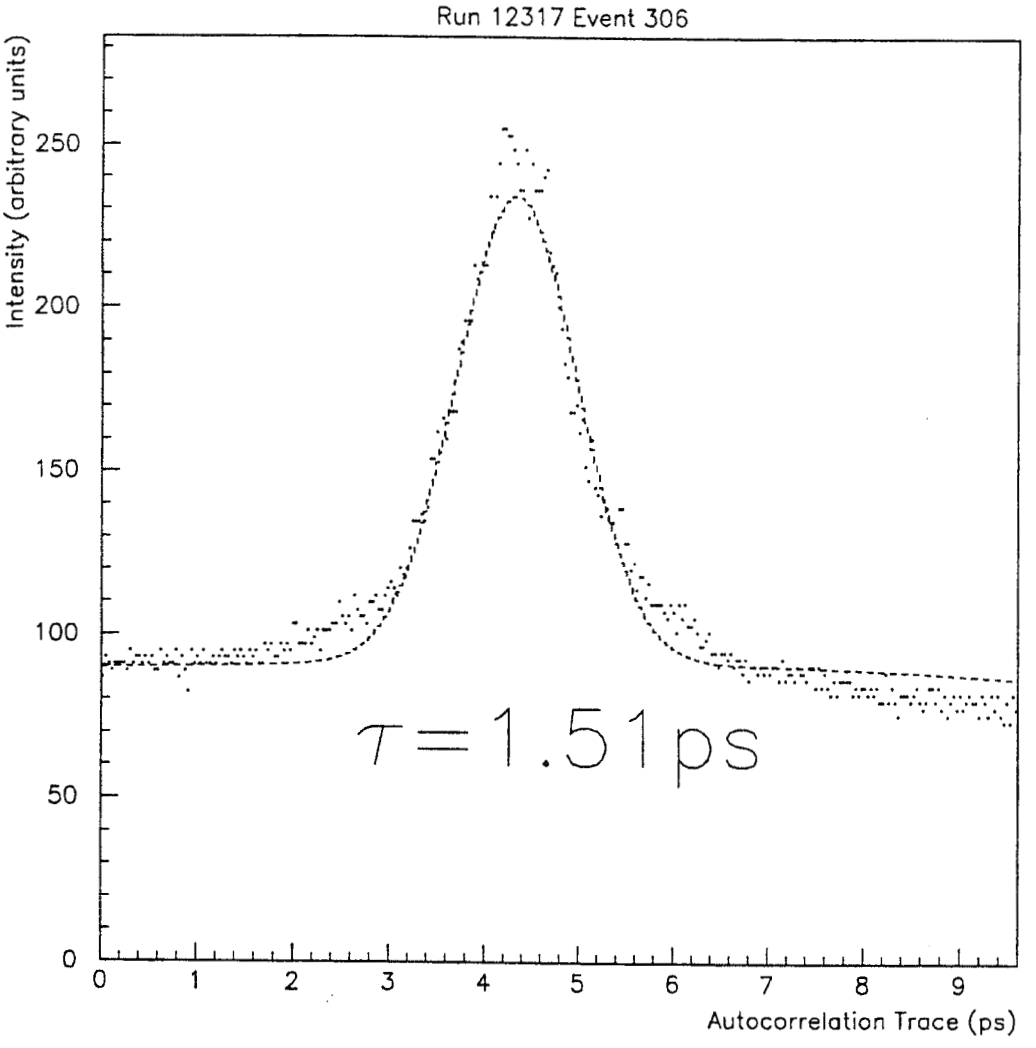

Figure 3.15: Laser Pulse Autocorrelation Trace.

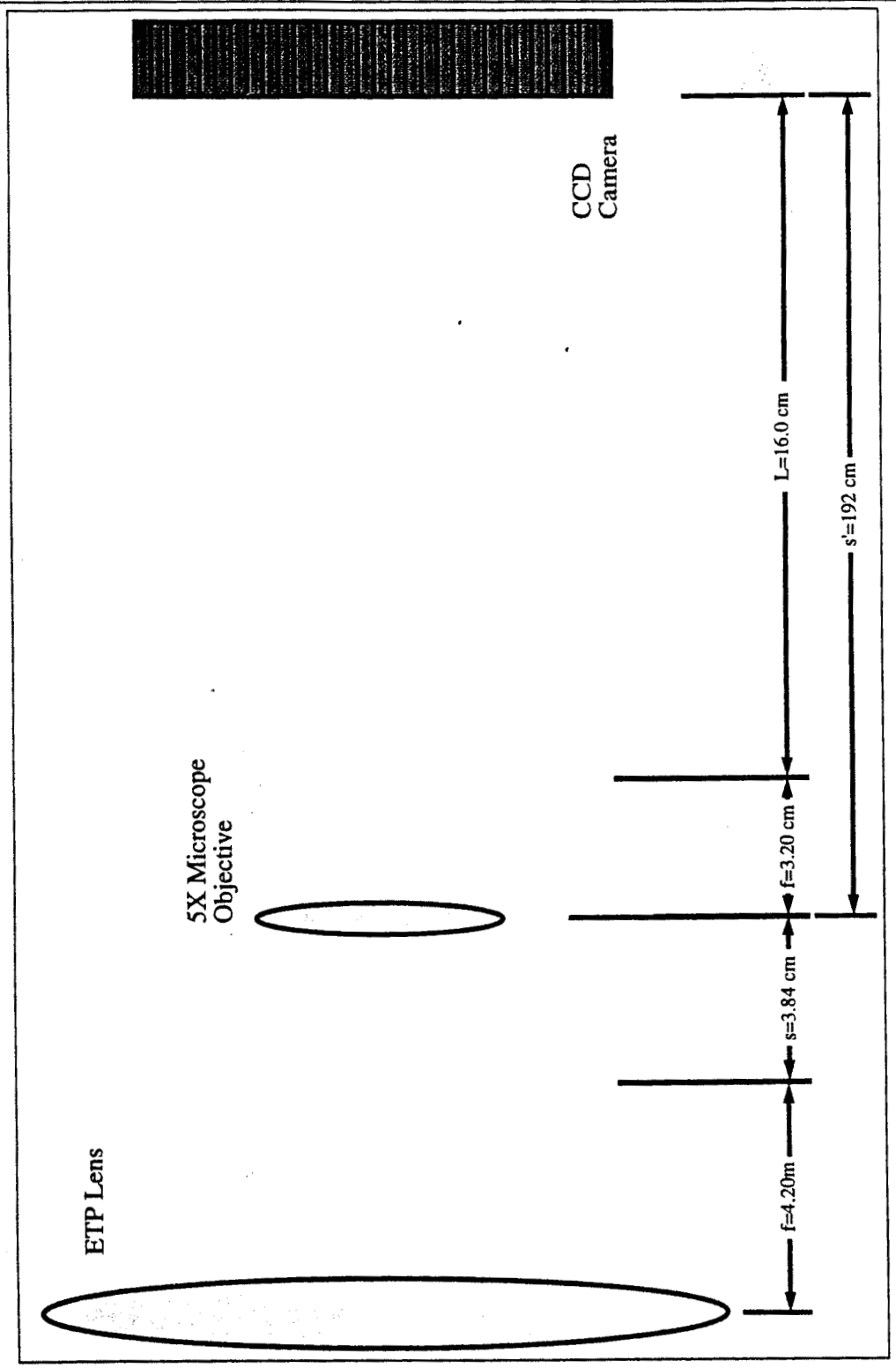

Figure 3.16: Equivalent Target Plane Measurement Setup.
The collimated beam returning from the interaction point was focused with a $f = 420$ cm lens. The resulting focus was imaged onto the plane of CCD pixels by a microscope objective.[54] The pixels were read out by a PC, and the TEM_{00} intensity profile written to the data stream.

The waist, w_0, is the radius r such that

$$I(w_0) = I_0 \exp(-2), w_0 = \sqrt{2}\sigma \tag{3.7}$$

This definition matches that used by [55] and [56]. The effective focal spot area of a pulse is found by integrating the intensity,

$$A_L = \int_{\phi=0}^{2\pi}\int_{r=0}^{\infty} I(r)\, r\, dr\, d\phi = 2\pi \int_{r=0}^{\infty} \exp\left(-\frac{(r)^2}{(\sigma)^2}\right) r\, dr = 2\pi w_0^2 = \pi\sigma^2. \tag{3.8}$$

A gaussian beam, propagating in free space, will spread according to

$$w(z) = w_0 \left(1 + \left(\frac{\lambda z}{\pi w_0^2}\right)^2\right)^{1/2}, \tag{3.9}$$

where w_0 is the waist at $z = 0$. The smallest waist $w_0(0)$ of a Gaussian beam focused by a lens or mirror is given by

$$w_0(0) = \frac{f\lambda}{\pi w_0(f)}, \tag{3.10}$$

where $w_0(f)$ is the waist at the focusing optic, λ is the wavelength of the focused light, and f is the focal length of the lens. The Rayleigh range, defined as the distance over which the beam radius increases by a factor of $\sqrt{2}$, is given by

$$z_R = \frac{\pi(w_0(0))^2}{\lambda}. \tag{3.11}$$

The CCD camera was an EDC-1000HR. It had 244 rows of 753 pixels. Each pixel was 11.5 μm wide and 27.0 μm high, giving the 8.6955 $\times$ 6.588 mm array an overall area of $\sim$ 57 mm^2. Each pixel was digitized with 8 bit resolution, and read out by a PC. The subsection of the array containing the spot was selected and copied to the Back End PC. The pixel reading the largest value was designated the spot center.

The row and column containing this pixel were copied into local arrays, which were then fed into a fitting routine. This routine performed a generalized

least-squares fit to the function

$$I(r) = a_1 \exp\left(-\frac{(r-a_2)^2}{(a_3)^2}\right) + a_4 \tag{3.12}$$

Figure 3.17 shows the focal spot profile for a 500 mJ, 1.51 ps, 50μm^2 pulse recorded in the March 1995 run.

A "dark frame" was captured before every run. The laser beam was blocked prior to the first spatial filter so that an image captured during a laser shot would "see" background associated with flashlamp light. This dark frame was subtracted from each laser image during stand alone operation. The subtraction was disabled during interactive running. The a_4 term in Equation 3.12 was introduced to absorb a uniform offset due to unsubtracted background light.

The scan depicted in Figures 3.18, 3.19, and 3.20 was performed by scanning the location of the CCD camera along the direction of pulse propagation, measuring the spot waists at various z positions. Each data point represents a 10-shot average. Waists were only introduced into the average when the fit converged. Near the focus plane, z_0, approximately 100% of the fits converged. However, as the distance from z_0 increased, past 2–3 z_R, fits tended to diverge. There were two reasons for this phenomenon. The far-field intensity profile of the focus was not as smooth as the near-field intensity profile. Also, for images captured near z_0, the absolute intensity at the CCD camera was higher than the absolute intensity for images captured in the wings. This meant that background had a greater influence on images taken away from focus. This effect was somewhat mitigated through the use of neutral density filters, however filters introduced an entirely new set of image aberrations and so a balance was struck.

For stable convergence of the Levenberg-Marquardt method of nonlinear least squares, it is useful to adopt a fit function that varies rapidly with respect to the fit parameters and the data. For such functions, the fit parameters spend less time wandering around in flat topological valleys. The waist of a Gaussian beam varies with z according to Equation 3.9. Near the focus, the waist doesn't change rapidly. The functional behavior can get lost in fluctuations. So it is desirable to weight that region less than the wings, where the waist changes

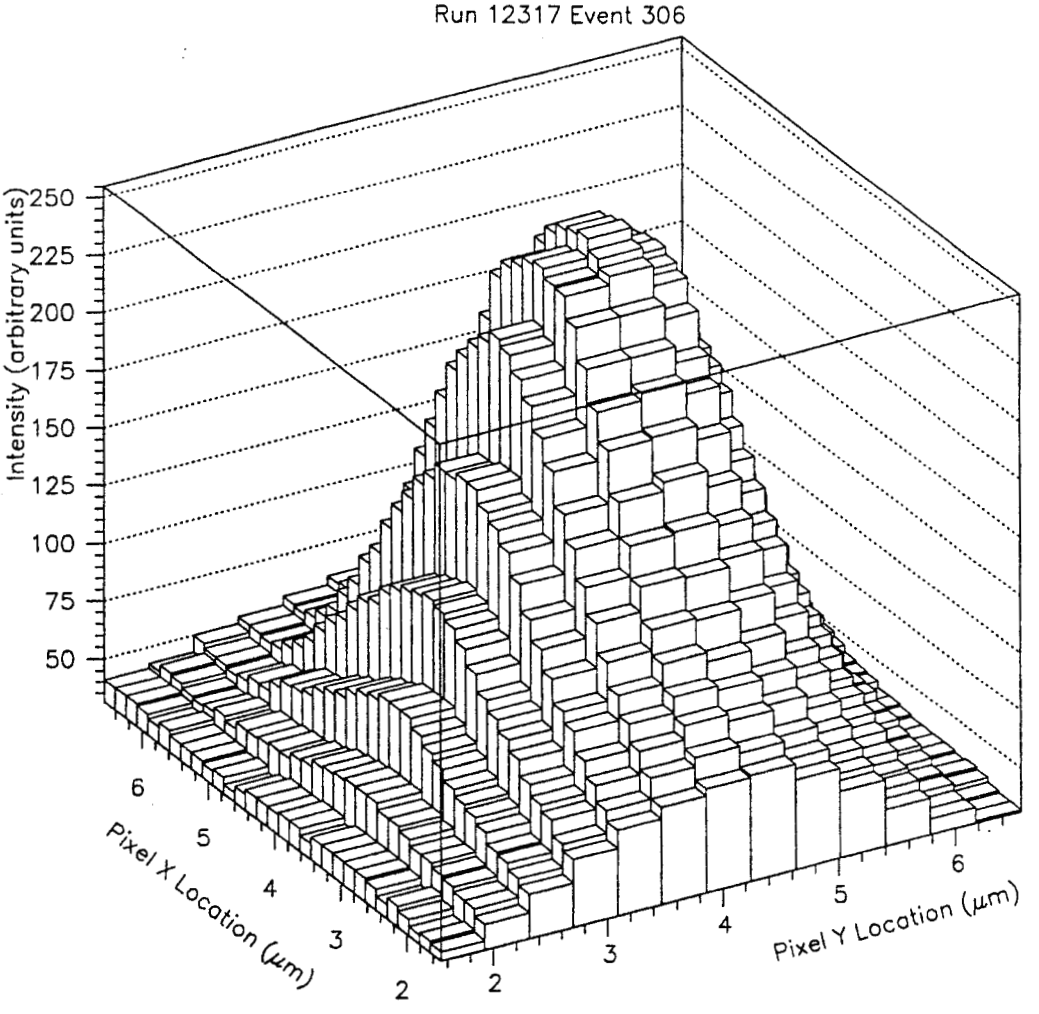

Figure 3.17: Laser Pulse Intensity Profile.
This image was taken during IR running. The pulselength was 1.5 ps. The energy was 500 mJ. The spot size was 50 μm^2.

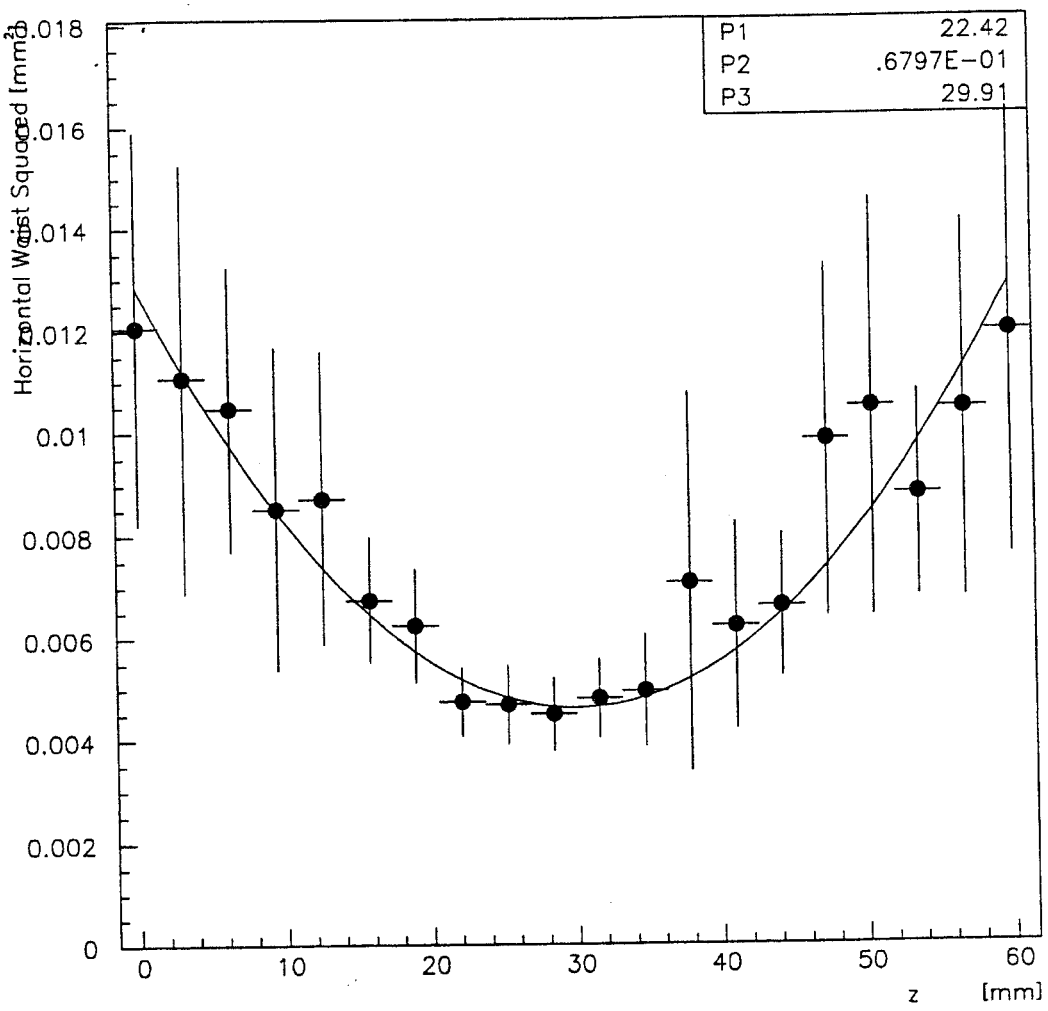

Figure 3.18: Horizontal Waist Scan.

more rapidly. This weighting can be done by squaring the data values and the function being fit.[57, 58]

$$(w(z))^2 = w_0 \left(1 + \left(\frac{z}{z_R}\right)^2\right), \tag{3.13}$$

This particular focal scan revealed both astigmatism and ellipticity. z_0^y was located at $z = 7.8cm$, while z_0^x was located at $z = 29.9cm$. The ellipticity was due to the nonunity magnification ratio between the anamorphic beam expander ($\sim 4.4\times$) and the recircularizing cylindrical telescope ($\sim 4.0\times$). The astigmatism was eliminated by correcting the collimation of the beam though adjustment of the separation of the lenses in the cylindrical telescope.

3.5 Laser Performance

The available laser parameters were written to the data stream during runs. During the September 1994 FFTB Run, the primary Green energy and Leakage IR energy measurements were available. For the runs presented in Chapter 5, the spot size was also available. The IR single-shot autocorrelator was not integrated into the DAQ until the March 1995 FFTB Run. The Green autocorrelator will be integrated into the DAQ for the December 1995 FFTB Run.

Figure 3.21 shows a variety of energy distributions, the data displayed is from Run 9083, a run presented in Chapter 5. The IR energy incident on the doubling crystal and the Green energy emerging from the doubling crystal are displayed in the top plots. The conversion efficiency distribution and the conversion efficiency as a function of incident IR energy are displayed in the bottom plots. The average spot size for this run was $\sim 60\ \mu m^2$. Figure 3.22 shows area and pulselength distributions from Run 12310 which was conducted during the March 1995 FFTB Run. The doubling crystal was not used during this run, so the IR autocorrelator was functional. The average energy for this run was ~ 500 mJ. Figure 3.23 shows η and Υ distributions for Run 9083, a run presented in Chapter 5. Energy and spot size measurements were available for most events. For the calculations of η and Υ, a pulselength of 2.5ps was used. In

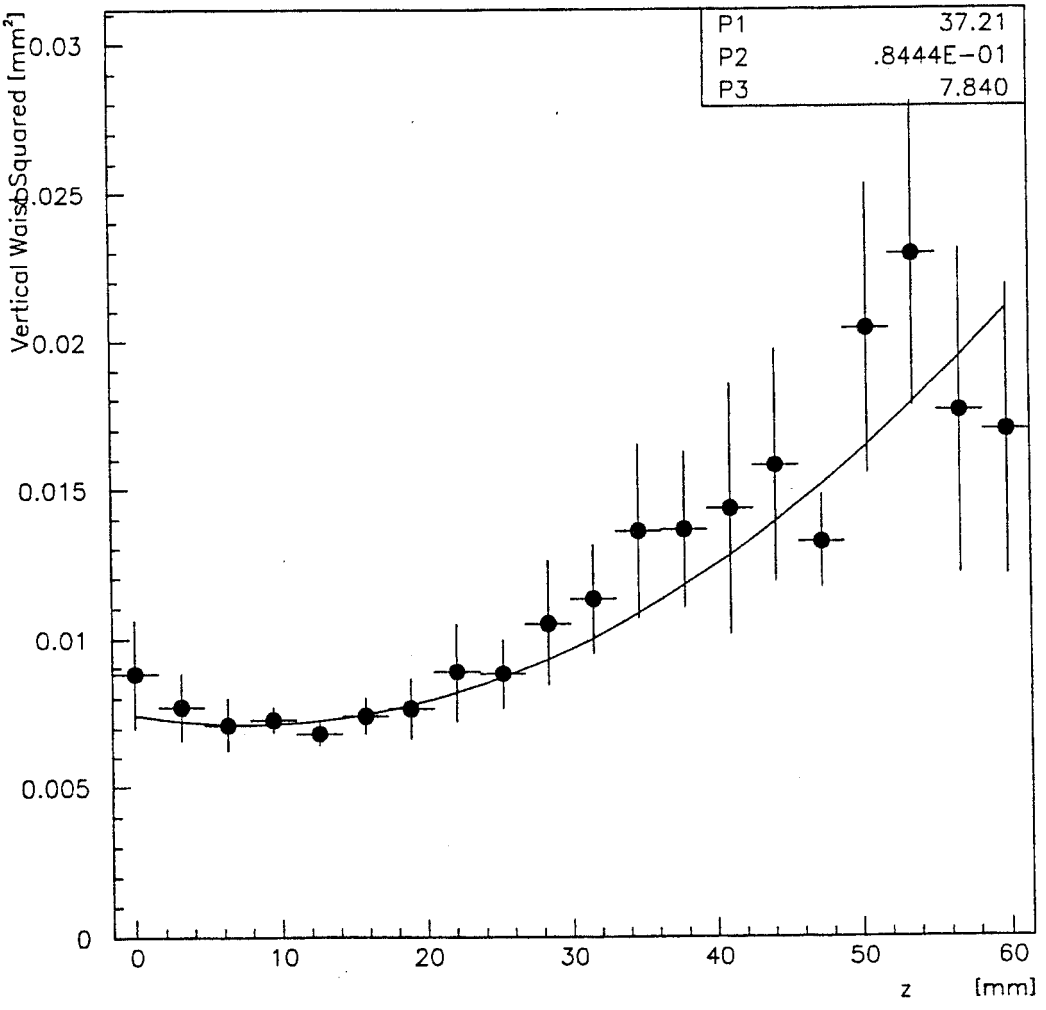

Figure 3.19: Vertical Waist Scan.

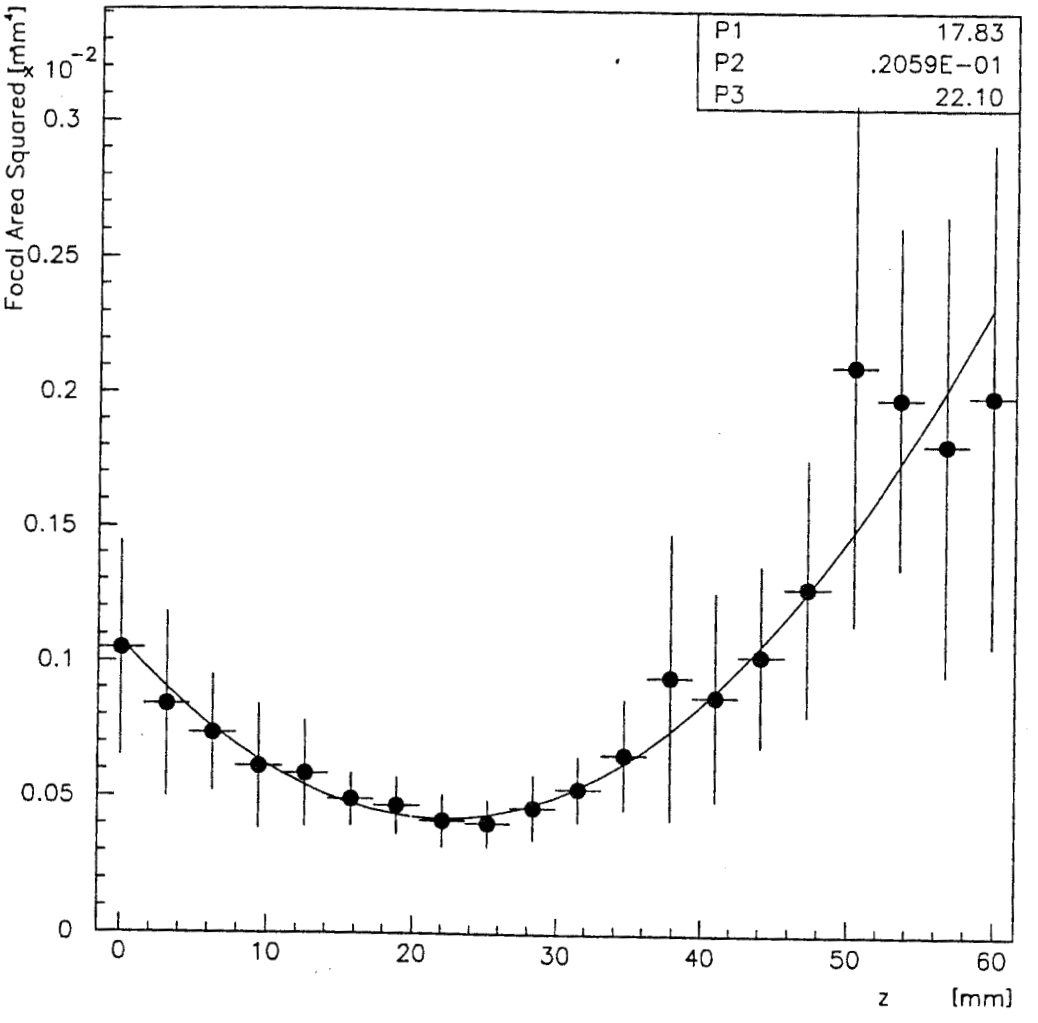

Figure 3.20: Spot Size Scan.

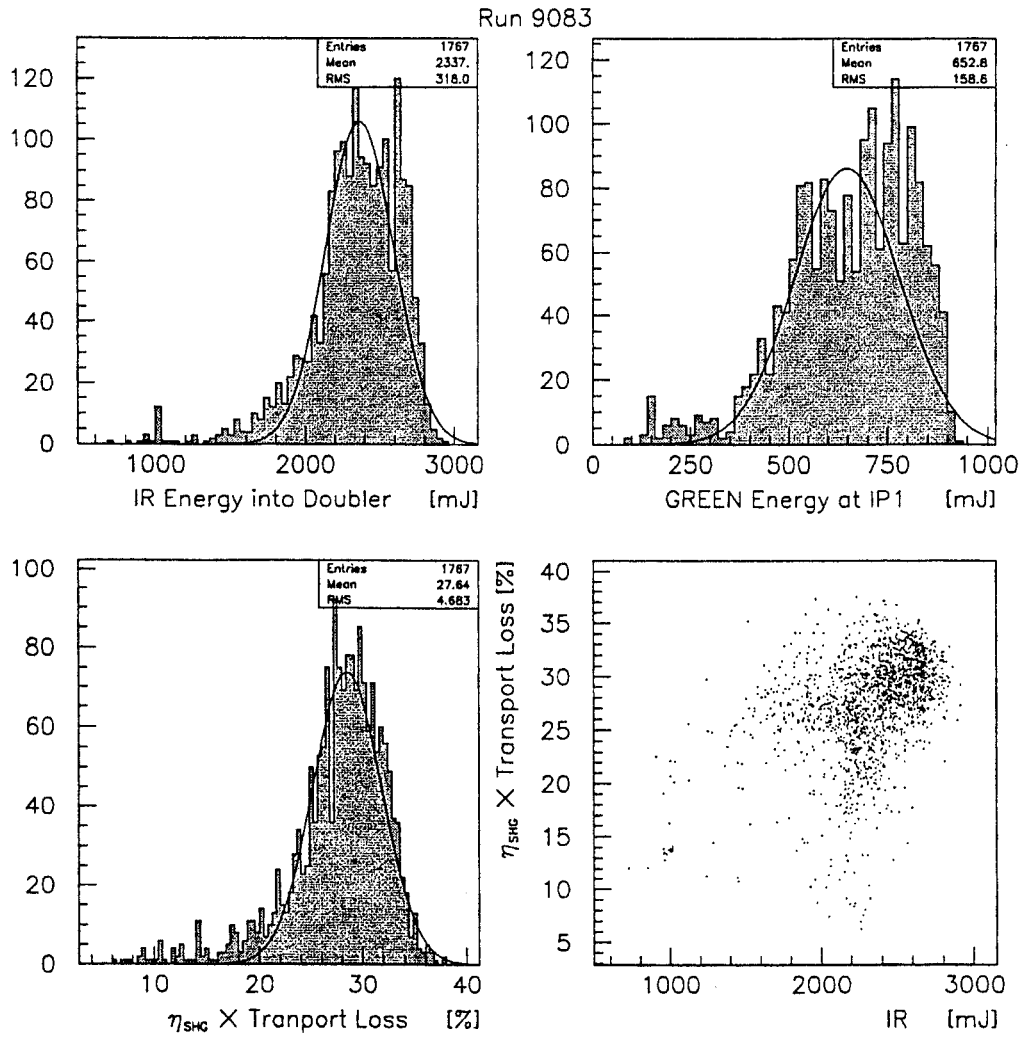

Figure 3.21: Run Averaged: Green, IR, η_{SHG} ≡Green/IR, and η_{SHG} versus IR. The IR energy incident on the doubling crystal and the Green energy arriving at the interaction point (IP1) are displayed in the top plots. The conversion efficiency times the transport loss distribution and the conversion efficiency times the transport loss as a function of incident IR energy are displayed in the bottom plots. The average spot size for this run was $\sim 60\ \mu m^2$

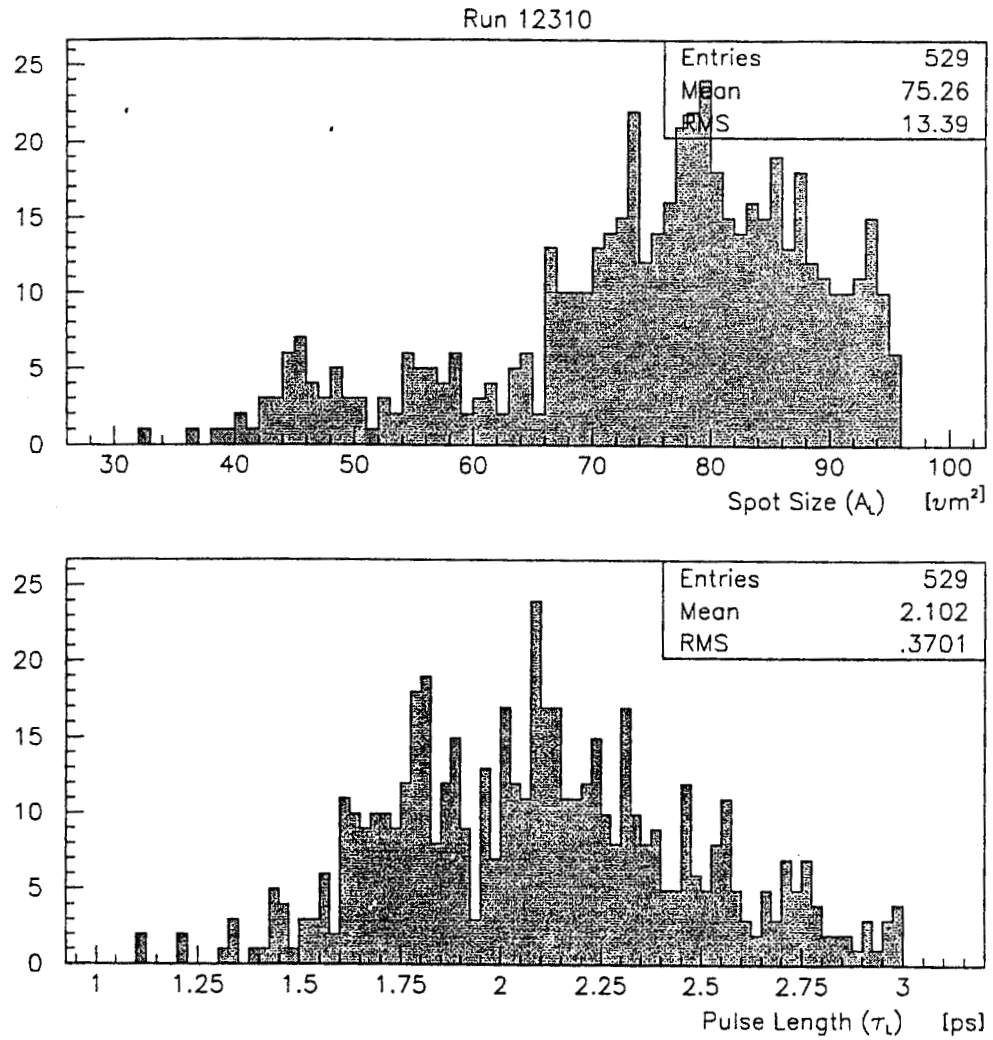

Figure 3.22: Run Averaged: area (A_L), pulsewidth (τ_L).
Run 12310 was conducted during the March 1995 FFTB Run. The doubling crystal was not used during this run, so the IR autocorrelator was functional. The average energy for this run was $\sim$ 500 mJ.

terms of U_L, A_L, and τ_L,

$$\eta = 3.18\sqrt{\frac{U_L}{A_L \tau_L}}, \tag{3.14}$$

and

$$\Upsilon = 2.64\sqrt{\frac{U_L}{A_L \tau_L}}, \tag{3.15}$$

where U_L is in Joules, A_L in square microns, and τ_L in picoseconds.

3.6 Second Harmonic Generation

Type II potassium dihydrogen phosphate (KH_2PO_4 or KDP) crystals are used for frequency doubling the slab output, we have observed efficiencies as high as 55%.

3.6.1 Motivation

Though energy is lost in the frequency doubling process, Green running is preferable for probing e^+ production. There are two reasons why. First of all, Green can be focussed down to a smaller spot size, if no significant phase errors are introduced to the wavefront by the KDP. This is important in the multiphoton regime; as shown in Figure 1.8, the rates of the nonlinear QED processes we are probing increase exponentially with intensity. So the intensity, or photon density, will be higher for Green running than for IR running. Recalling Equation 3.8, we see that for Green and IR pulses with Gaussian Intensity profiles having the same waist before the focusing optic, w_0, the focal spot areas will be different by a factor of $(\lambda_{IR}/\lambda_{Green})^2 = 4$. However, if one assumes the Green pulse was produced by doubling a Gaussian IR pulse of waist ${w_0}^\omega$, at an intensity where η_{SHG} varies linearly with power, then the waist of the Green pulse $w_0^{2\omega} = \sqrt{2}{w_0}^\omega$. The central, higher intensity region of the IR pulse will be converted more efficiently than the wings, resulting in a Green pulse with waist smaller than the IR. Focusing the frequency-doubled pulse of waist $w_0^{2\omega}$ yields $A_{IR}/A_{Green} = 2$. We ran intensities in the crystals up high enough that η_{SHG} saturated. Thus $w_0^{2\omega} \geq \sqrt{2}{w_0}^\omega$, but $w_0^{2\omega} \leq {w_0}^\omega$.

Even without the benefit of tighter focusing, the higher energy Green photons would be preferable to IR photons for e^+ production. Since the Green

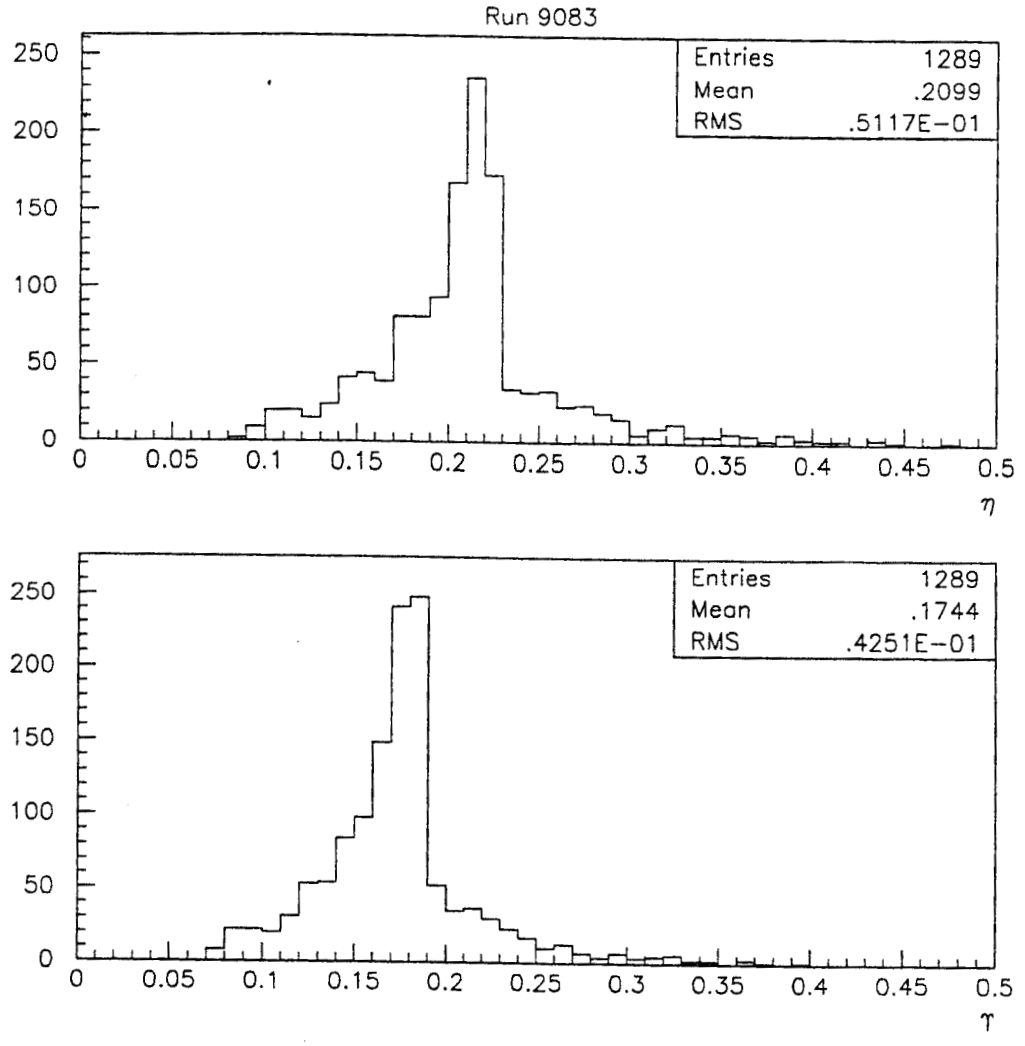

Figure 3.23: Run Averaged: η, Υ.
Energy and spot size measurements were available for most events. For the calculations of η and Υ, a pulselength of 2.5ps was used.

photons are twice as energetic as the IR photons, only half as many Green as IR laser photons are required to conserve relativistic energy and momentum in the same pair production process.

3.6.2 Conversion Efficiencies

"Doubling" occurs when laser light traverses certain nonlinear optical crystals.[59, 60] The doubled light can be treated as a wave of frequency $2\omega_0$ that arises as part of the polarization response of a crystalline medium to an incident electric field of frequency ω_0. Alternately, it may thought of as the process wherein two photons of energy $\hbar\omega_0$ are absorbed by a birefringent crystal which then emits one photon of energy $2\hbar\omega_0$. In both cases, the phase matching angle governs the fraction of ω_0 light converted into $2\omega_0$light. The ratio of energy in the doubled pulse to the energy of the incident pulse is the "conversion efficiency,"

$$\eta_{SHG} \equiv \frac{U_{2\omega_0}}{U_{\omega_0}}. \tag{3.16}$$

In a symmetric crystal, the polarization response is invariant under rotations. The restoring force on a lattice electron displaced by the inducing wave will be the same for all angles. But in an asymmetric crystal, the restoring force will depend on the direction of the displacement which depends on the direction of the electric field, or polarization, of the wave. If the polarization of the incident electric field is matched to lattice axes correctly, the $2\omega_0$component in the polarization response can be maximized.

3.7 Synchronization

The spatial and temporal overlaps of laser pulse and e^- bunch were subject to instantaneous jitter and long term drift. The long term drifts were compensated for by x,y,and time scans. The Compton scattering rate is proportional to the overlap of the pulse and bunch. In x or y scans, the Compton scattering rate was measured while the IP1 box position was rastered along one of the two axis orthogonal to the beam line at IP1. In time scans, the Compton scattering rate was measured while the optical delay line was rastered. CCM1 was a Cerenkov detector that measured incident particle flux, i.e.

Compton scattered γs . During PCAL analysis, events with laser energy under 200 mJ were cut. The ratio of gamma rays to laser energy was evaluated. If this ratio for a given event was below a threshold, poor overlap was assumed and the event was cut.

The time jitter of the laser pulses relative to the electron bunches was measured to be less than 1.5 ps. The jitter reported is derived from bunch/pulse collision data. An optical delay line, stepped with picosecond resolution, is used to temporally scan the laser pulse through the electron bunch. Since the bunch and pulse lengths are known, deconvolving the interaction rate (measured as a function of optical delay) gives a measure of the instantaneous jitter. Repeated time scans give information about long term drift. Figure 3.24 shows the scattering rate as a function of optical delay introduced into the laser pulses' path. The step size could be set with resolution on the order of 10fs. Coarse timing overlap was established by comparing the output of a photodiode with ringing cavity output. Appropriate lengths of cable were added in the line between the linac subharmonic generator and the modelocker driver.

In this manner, overlap was established at the nanosecond level; the limit of the available cable lengths. Time differences still discernible on the scope were corrected for with timing scans. Δt was converted into path length. This delay, minus half the scan range, was added by moving the stage holding the corner cube. A move of Δz of the stage corresponded to $\Delta t = 2\Delta z/c$, because of the geometry of the system. The range was then scanned. In the unusual situation wherein no signal was found in the scan range, a different, adjacent region was scanned.

Once the t_0 of overlap was identified, a finer scan over a much smaller time span was performed. Typically at 45 to 60 ps range was scanned in 1.5 to 3.0 ps steps. A gaussian fit to the rate versus Δz plot gave z_0, the stage was moved to this position for "physics" runs. Δx and Δy scans were also performed. Δy was vertical, and while important, it was stable. So y scans were infrequent. The x position mattered, it changed time as well. Figure 3.25 shows the scattering rate as a function of both x and t. Plot a represents the single photon Compton scattering rate, plot b represents the two photon nonlinear Compton scattering

rate.

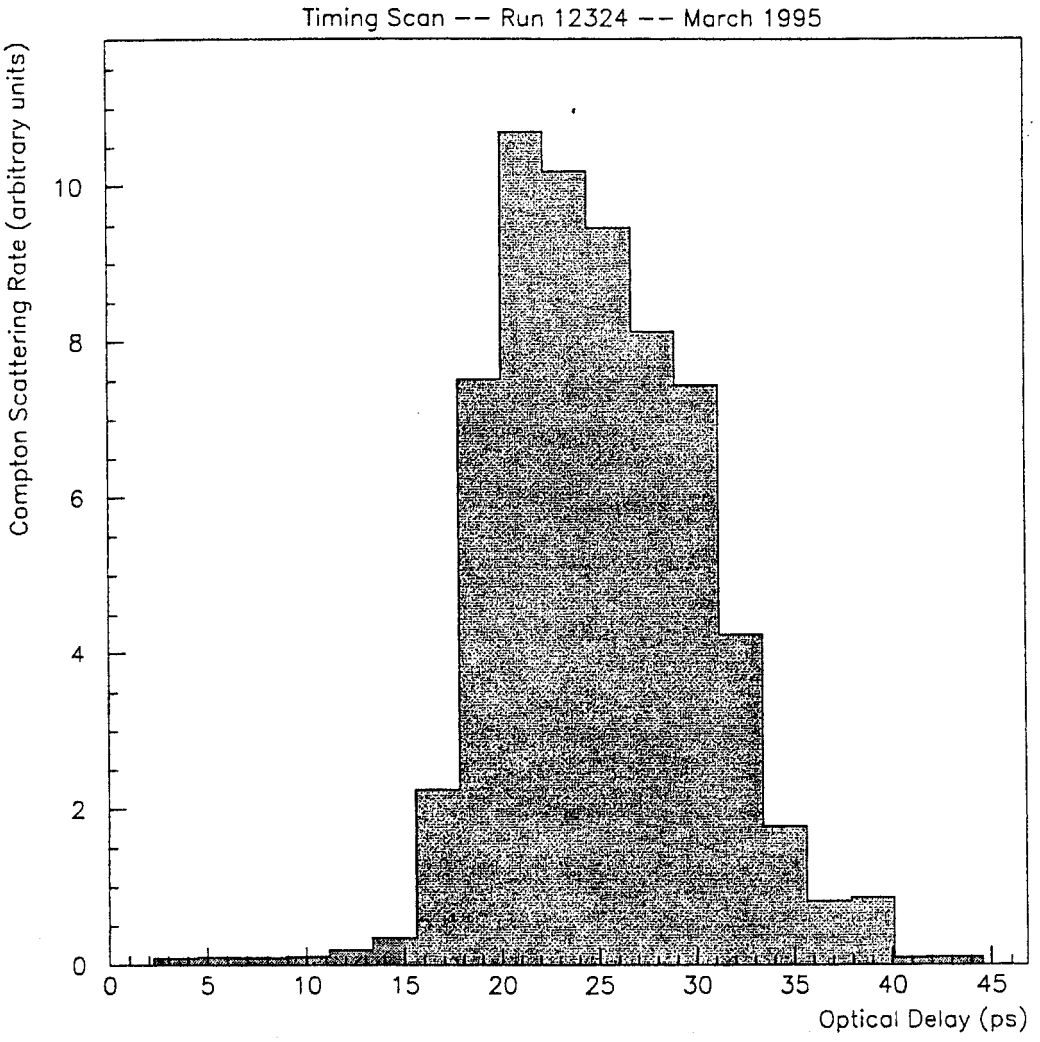

Figure 3.24: Scattering Rate versus Optical Delay.
The γ flux was proportional to the convolution of the laser pulselength with the electron bunch length. The convolution depended on the temporal overlap of the pulse and bunch. By measuring the scattering rate while scanning an optical delay line, the optimal timing overlap could be found.

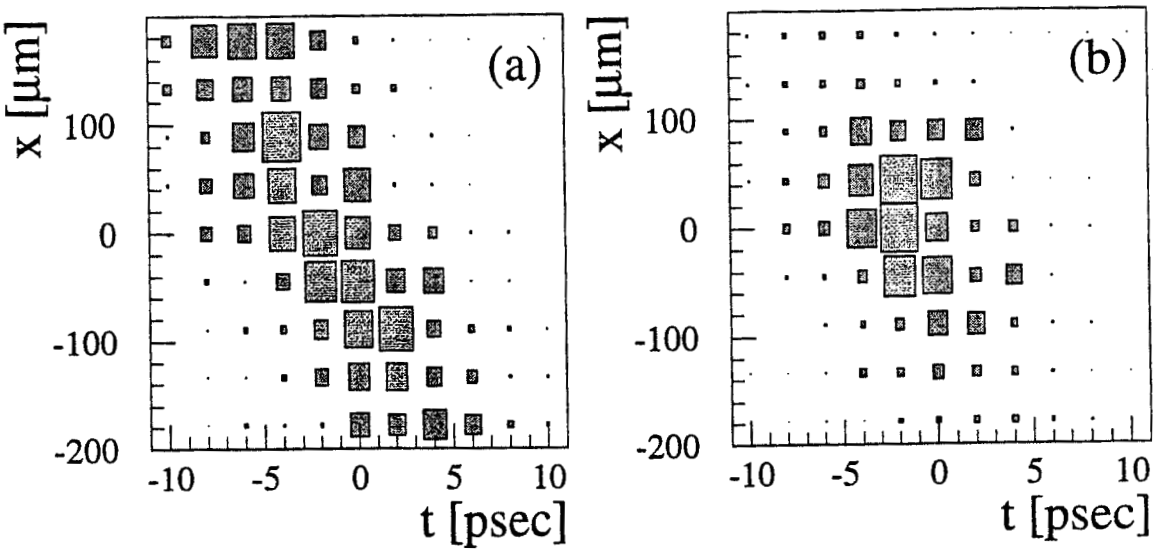

Figure 3.25: XT Scan.
Scattering rates were measured as the optical delay and x position of IP1 were rastered. The plots show scattering rates as a function of IP1 x-coordinate and optical delay. Plot (a) shows the linear Compton signal (CCM1), plot (b) shows the n=2 Compton signal (ECAL) for an xt-scan performed during the March 1995 FFTB Run.).[61]

Chapter 4

Data Analysis

4.1 Introduction

I have conducted data analysis, accumulating evidence of Multiphoton Breit-Wheeler Pair Production. This evidence takes the form of positron flux above background found in electron bunch/laser pulse collision events. The agreement of observed and simulated positron energy spectra is corroborating evidence.

I started the analysis by characterizing the calorimeter, quantifying PCAL's response to positrons arriving from IP1. The particle flux into PCAL was very low. The vast majority of events were discarded since for them PCAL measured little or no energy. Events in which PCAL did measure significant energy were subjected to a series of cuts designed to cull background e^+s . The plinth of the completed analysis was the off-momentum e^+ cut. Candidate events were screened for compatibility with the position reconstruction algorithm. Points of incidence were reconstructed where possible. Corrections were made to the EMAP(y) look-up table using e^+s produced in an Al foil located at IP1. The off-momentum e^+s were cut from the pulse/bunch collision data using the corrected EMAP(y).

4.2 Calibration Data

The positrons used to perform the characterization were generated at the bunch/pulse collision point by a combination of bremsstrahlung and pair production initiated by high energy e^-s traversing an Aluminum (Al) foil placed in the FFTB beam line in IP1. Since the electron bunches encountered the Al foil at the same place where electron bunches encountered laser pulses, the foil positrons originated at the same point as Multiphoton Breit-Wheeler positrons.

The foil data was accumulated in parasitic runs. During FFTB runs, the beam from the linac was directed into the FFTB line. During parasitic runs, the beam from the linac was directed into a different beam line. A secondary beam was generated in the linac from profile tails of the electron beam. Collimators were used to "scrape" the electron beam, removing electrons spatially distributed outside of the desired bunch transverse contour. The scraped electrons made Bremsstrahlung γs in the collimators. The γs propagated into a

stainless steel plate, electrons and positrons were produced. The resulting secondary beam of electrons was coupled into the FFTB. The secondary beam was propagated down the FFTB beam line. It struck and Al foil placed in IP1. The charged particles produced through a combination of Bremsstrahlung and pair production were deflected in the field of the dump magnets. The bunches in secondary beams contained fewer electrons than bunches in primary beams. The energy of secondary beam electrons was lower than that of primary beam electrons.

4.3 The Processing of Raw Data

The runs were analyzed in stages. The data files on the hard disk were copied onto a UNIX platform. I did my analysis in this environment.[62] In the first stage of analysis, all events in a run were skimmed. E0LX events were identified and average pedestal values for various detectors were calculated. As explained in Section 2.3, the bit following **E** represents the state of the e^- bunch, 1 indicates the presence of an e^- bunch, 0 indicates the absence of an e^- bunch, and X indicates either or both. The bit following **L** represents the state of the laser pulse, 1 indicates the presence of a ω_0 pulse, 0 indicates the absence of a ω_0 pulse, and X indicates either or both. The "pedestal" of a detector is its signal in the absence of external stimuli. When the detector is used for a measurement, the "true" value of the signal is found by subtracting the average pedestal from the detector's reading. In the second stage of analysis, all events in the were processed into a HBOOK Column-Wise-Ntuple (CWN).[63] The E1LX events underwent pedestal subtraction before being written to disk.

E0L0 and E0L1 triggers were recognized by the DAQ so that data bias introduced by nonuniformities amongst calorimeter cells and channels of the electronics could be minimized. Calorimeter readings from E0L0 and E0L1 events provided quantitative information about detector pedestals since, for such events, the e^- bunch was dumped before it ever entered the FFTB . With no e^- bunch in the FFTB, neither beam background nor ω_0–e^- collisions were sources of detector signal. Figure 4.1 shows the distribution of the pedestals of a cell for an entire physics run.

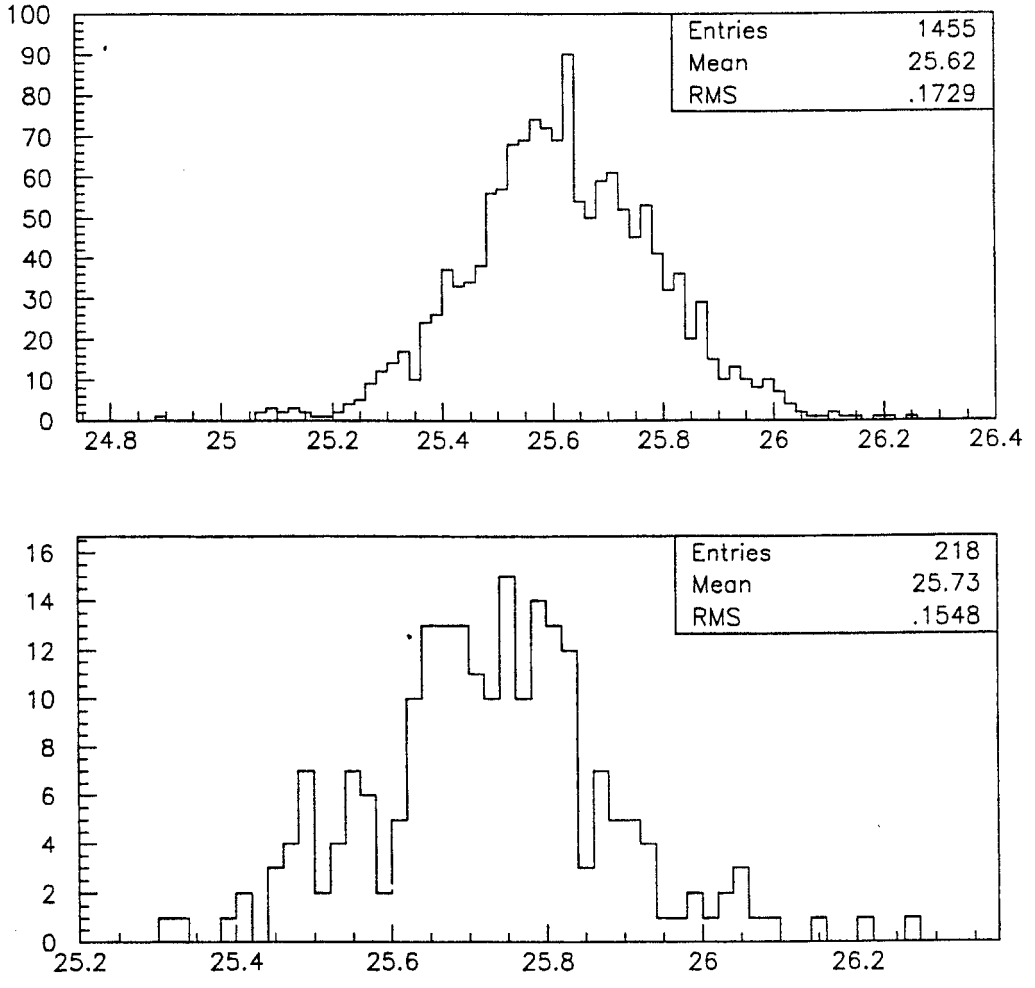

Figure 4.1: Raw PCAL Pedestals.
The pedestals acquired during Run 9083 from the cell in the 16th row of the 2nd column of the 1st segment of PCAL . The values in the top plot are from the E0L0 events. The values in the top plot are from the E0L1 events.

4.4 The Minimization of Calorimeter Fluctuations

At this point, it is useful to define:

PCAL $_{i,j,k}$ The energy, in GeV, measured by the cell located in row j and column k of segment i.

$\mathbf{E}^{CC}_{i,j}$ PCAL $_{i,j,1}$+PCAL $_{i,j,2}$ The summed energy of the inner pads (k=1,2) in row j of segment i.

$\mathbf{E}^{OC}_{i,j}$ PCAL $_{i,j,0}$+PCAL $_{i,j,3}$ The summed energy of the inner pads (k=0,3) in row j of segment i.

CC The center cells, columns 1 and 2, also known as center pads (CP).

OC The outer cells, columns 0 and 3, also known as outer pads (OP).

Figure 4.2 illustrates the division of cells in PCAL .

Subtracting the average pedestal from each event will remove the average bias from the collected data set, but there is a further procedure that was implemented to reduce fluctuations for individual events. In an idealized detector, the pedestal signals would be uncorrelated. In the absence of signal, pedestal readings would just fluctuate about their mean values, their readings independent of those of their neighbors. PCAL is not an idealized detector. There is row-wise signal correlation or "coherent noise." Figure 4.3 demonstrates this correlation in a plot of $E^{CC}_{i,j}$ versus $E^{OC}_{i,j}$ energy for the Laser Off Pedestal Events of Run 9083.The pedestal level of the center pads is directly proportional to that of the outer pads. Since no "physics" positrons could reach the outer pads, the outer pad readings for E1LX events were essentially pedestals.

Through the parameterization of the pedestal level in the center pads as a function of the pedestal level in the outer pads, an event-by-event CC correction was developed for "physics" events. The center pad pedestal value can be calculated from the outer pad pedestal reading, and subtracted from the center pad reading to yield the corrected, or "true physics" signal. The outer pads can

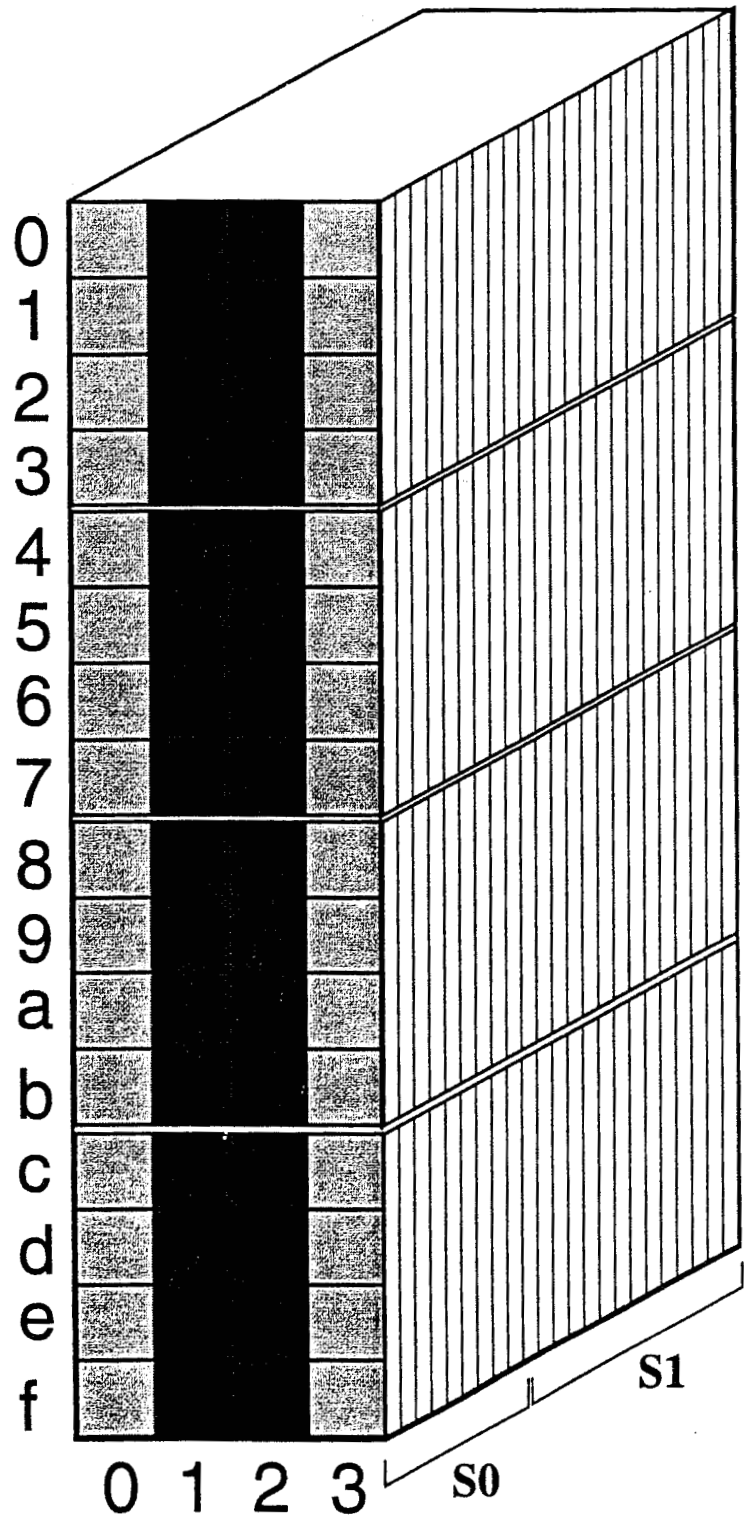

Figure 4.2: PCAL Schematic.
There are 16 rows of 4 columns. There are twenty three layers. Signals from the front 9 layers are summed and referred to Segment 0 or S0. Signals from the remaining 14 layer are summed and referred to as Segment 1 or S1.

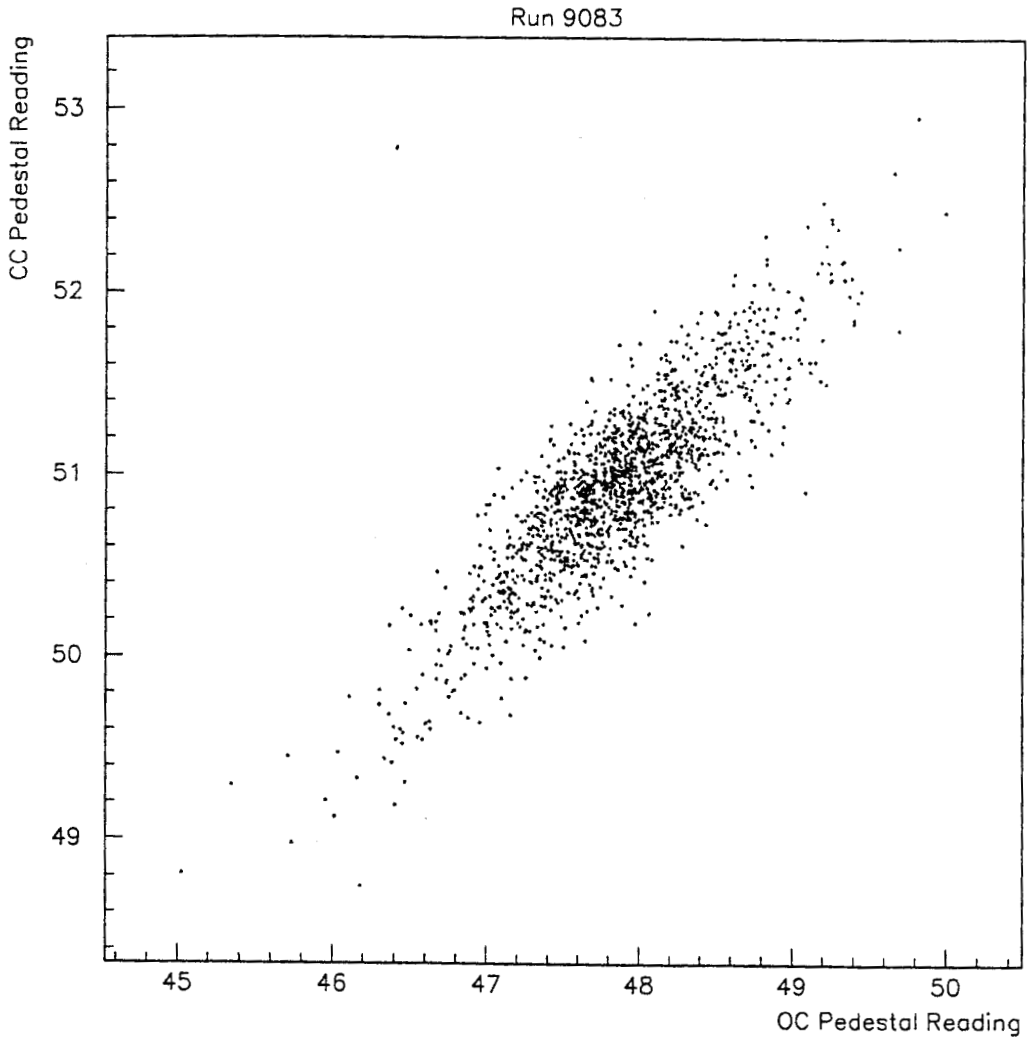

Figure 4.3: Calorimeter Coherent Noise: $E_{i,j}^{CC}$ versus $E_{i,j}^{OC}$, row f, segment 1. This plot show Outer Cell pedestals readings versus Center Cell energy readings. For collision events, an appropriate multiple of the Outer Cell reading was subtracted from the Center Cell reading. This reduced "instantaneous" pedestal fluctuations, yielding a corrected Center Cell energy.

be considered pedestals even during E1LX events despite the presence of e^- bunches in the FFTB because of the geometry of the calorimeter. The beam line is approximately 0.5 mm from the center of the PCAL rows. The shower level from a e^+ incident between the center pads has fallen to approximately 1% before reaching the out edges of the center cells. Even for a hit 5 mm towards an edge from the center, the shower height at the edge is only 5%. Examination of OC levels revealed only two contaminated runs, runs that had OC signal in excess of 1 GeV. These runs were discarded.

The parameterization was accomplished in the following manner. For fifty values of m, spaced equidistant in the range $[0.25, 1.75]$, the rms of $\mathcal{E}_{i,j}$ from Equation 4.1 was evaluated for all events with $E^{CC}_{i,j} < 5$ GeV.

$$\mathcal{E}_{i,j} \equiv \text{PCAL}\ (j,i,1) + \text{PCAL}\ (j,i,2) - m\,(\text{PCAL}\ (j,i,0) + \text{PCAL}\ (j,i,4)) \quad (4.1)$$

Figure 4.4 depicts the parameterization for row f, segment 1, during laser off events of Run 9083. For all rows, the rms varied smoothly with m and had a minimum within the range $0.25 \leq m \leq 1.75$. The minimum value was identified, and the corresponding m and

$$b \equiv \langle \mathcal{E}_{i,j} \rangle \quad (4.2)$$

were used for energy corrections.

The above method of parameterization was selected using the following reasoning. Suppose a center cell collects energy $E^{CC}_{i,j}$. The instantaneous pedestal fluctuation for the cell is $\delta E(t)^{CC}_{i,j}$. An event that should read $E_{i,j}$ reads

$$E^{CC}_{i,j} + \delta E(t)^{CC}_{i,j}.$$

$E^{CC}_{i,j}$ will naturally form a distribution

$$E^{CC}_{i,j} \pm \Delta E^{CC}_{i,j},$$

but in the presence of pedestals it will be further smeared, going to

$$E^{CC}_{i,j} \pm \Delta E^{CC}_{i,j} + \delta E(t)^{CC}_{i,j}.$$

Subtracting

$$m_{i,j} \times E^{OC}_{i,j},$$

yields

$$E^{CC}_{i,j} \pm \Delta E^{CC}_{i,j} + \delta E(t)^{CC}_{i,j} \Rightarrow E^{CC}_{i,j} \pm \Delta E^{CC}_{i,j} + \delta E(t)^{CC}_{i,j} - m * E^{OC}_{i,j}.$$

For a certain $m_{i,j}$,

$$\delta E(t)^{CC}_{i,j} \sim m_{i,j} \times E^{OC}_{i,j},$$

and the distribution

$$E^{CC}_{i,j} \pm \Delta E^{CC}_{i,j} + \delta E(t)^{CC}_{i,j} - m_{i,j} \times E^{OC}_{i,j} = E^{CC}_{i,j} \pm \Delta E^{CC}_{i,j}.$$

If

$$b \equiv \langle E^{CC}_{i,j} \pm \Delta E^{CC}_{i,j} \rangle \neq 0$$

I subtracted

$$\langle E^{CC}_{i,j} \pm \Delta E^{CC}_{i,j} \rangle$$

to get $E_{i,j}$. Figure 4.5 is a plot of CC energy versus OC energy, after OC subtraction. The width of this pedestal distribution is spread over ~ 1 GeV while the uncorrected distribution was spread over ~ 5 GeV.The m and b differ for laser on and laser off events. It has been observed that pedestals are different for laser off and laser on events. As such I calculated

$m_{i,j}$ The OC subtraction factor for row i, segment j.

$b_{i,j}$ The OC offset subtraction term for row i, segment j.

$E_{i,j}$ The corrected CC energy for row i, segment j.

$$E_{i,j} \equiv E^{CC}_{i,j} - m_{i,j}E^{OC}_{i,j} - b_{i,j} \tag{4.3}$$

for both "laser on" (L1) and "laser off" (L0) events. Table 4.1 lists the parameters selected for Run 9083.

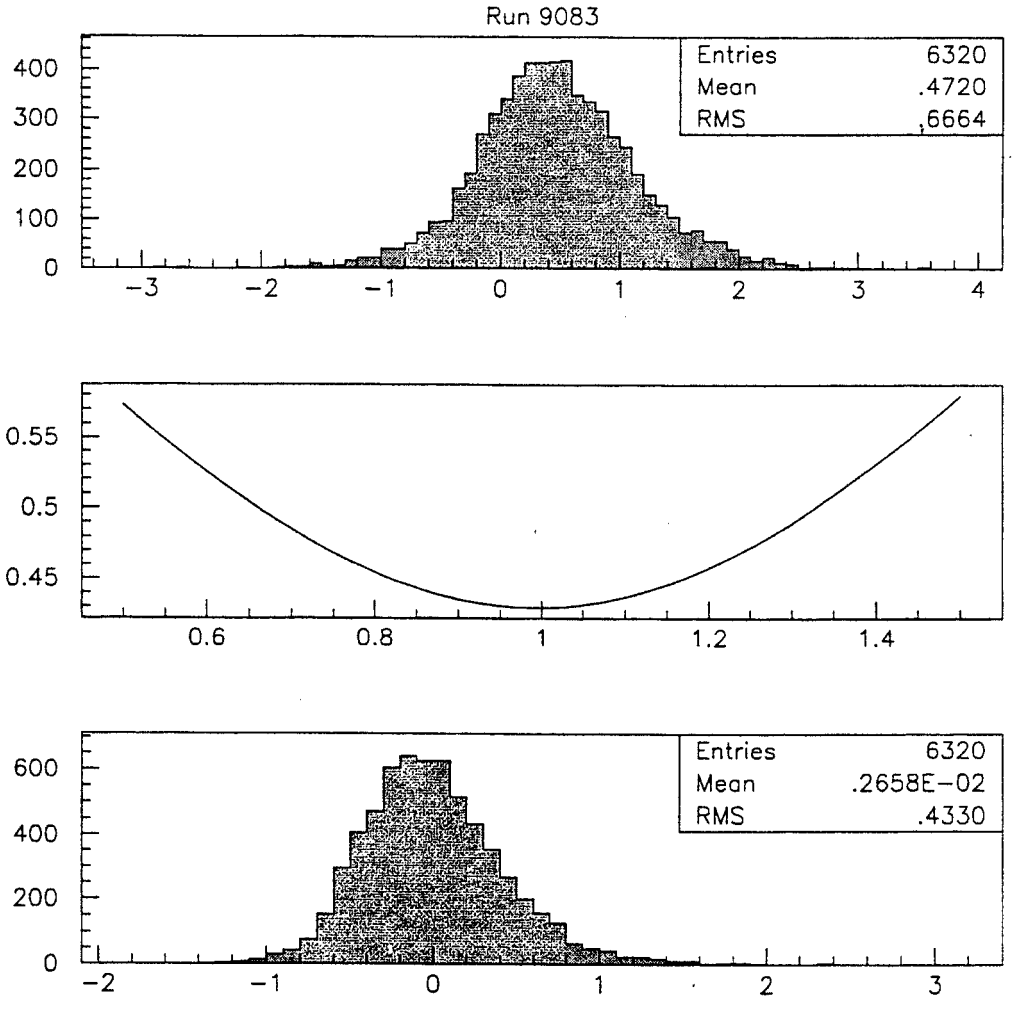

Figure 4.4: The Coherent Noise Parameterization Process.
The top plot shows the signal in segment 0 of row f. Note the rms, and the nonzero mean. The middle plot is a graph of rms values as a function of OC factor. The bottom plot shows the signal in segment 0 of row f, minus the m of the middle plot's minimum times the OC signal, minus the mean corresponding to m of the middle plot's minimum.

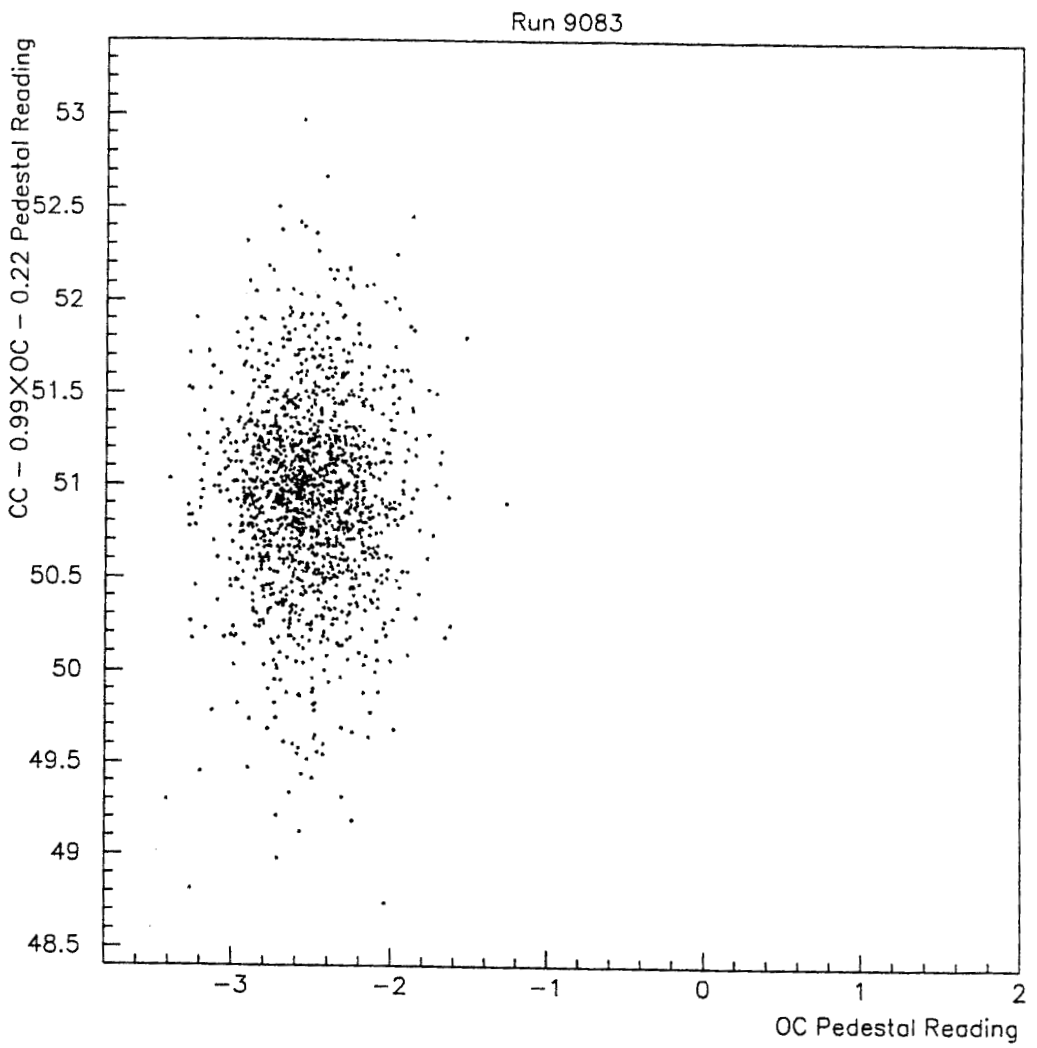

Figure 4.5: Corrected Calorimeter Signals: OC Energy versus CC Energy − 0.99OC Energy − 0.22.
This plot shows the effects of Center Cell energy correction via the subtraction of a fraction of Outer Cell energy. This is the same data shown in Figure 4.3. The energy spread of the measurements has been reduced by a factor of five.

	Laser Off					Laser On			
j	$m_{0,j}$	$b_{0,j}$	$m_{1,j}$	$b_{1,j}$		$m_{0,j}$	$b_{0,j}$	$m_{1,j}$	$b_{1,j}$
f	.709	.732	.985	.217		.587	.707	.954	.327
e	.862	.630	1.015	.062		.801	.610	.985	.156
d	.832	.522	.985	.057		.770	.496	.954	.181
c	.893	.471	1.015	.063		.862	.409	.985	.169
b	.740	.420	.832	.083		.679	.387	.862	.124
a	.770	.377	.862	.077		.770	.315	.893	.086

Table 4.1: Laser Off and On Slopes and Offsets for rows a-f, segments 0 and 1, Run 9083.

4.5 Position Reconstruction

In order to implement the cut of off-momentum e^+s , it was necessary to select a position reconstruction algorithm. Prior to explaining these algorithms it is useful to adopt some abbreviations.

ETOT$_j$ The total energy of the event in segment j,

$$\mathrm{ETOT}_j \equiv \sum_{i=a}^{f} E_{i,j} \tag{4.4}$$

$F_{i,j}$ The fraction of ETOT$_j$ deposited in row i, segment j.

$$F_{i,j} \equiv \frac{E_{i,j}}{\mathrm{ETOT}_j} \tag{4.5}$$

EMAX$_{i,j}$ The largest $E_{i,j}$

I_j The index, i, of EMAX$_{i,j}$.

ECL$_j$ The cluster energy, the energy of I_j, and its neighbors.

$$\mathrm{ECL}_j \equiv \begin{cases} E_{e,j} + E_{f,j} & \text{if } I_j = f \\ \sum_{i=I_j-1}^{I_j+1} E_{i,j} & \text{if } b \le I_j \le e \\ E_{a,j} + E_{b,j} & \text{if } I_j = a \end{cases} \tag{4.6}$$

y_R The reconstructed y position.

y_0 The y coordinate of the real point of impact.

A cluster is defined as the row containing the largest fractional energy plus the row above and the row below. When row f contained the largest fractional energy, the cluster consisted of rows e and f. When row a contained the largest fractional energy, the cluster consisted of rows a and b.

There are two position reconstruction algorithms I considered using, both involve calculating the first moment of the spatial distribution of the shower energy deposited in lateral segments. The center of gravity X of the amplitudes from the PCAL cells is calculated using

$$X = \frac{\sum_i w_{i,j} x_i}{\sum_i w_{i,j}}, \tag{4.7}$$

where the x_i are the cell center coordinates and the $w_{i,j}$ depend on the choice of algorithm. For vertical reconstruction, the x_i are given by Tables 4.2 and 4.3. For horizontal reconstruction, the x_i are at -24 mm, -8 mm, 8 mm, and 24 mm for columns 0–3 respectively. In one method, fractional weighting of each individual detector cell's fraction of the total measured energy was used. In this case,

$$w_{i,j} = \frac{E_{i,j}}{ETOT_j}. \tag{4.8}$$

In the other method, logarithmic weighting[64] was used, here

$$w_{i,j} = \max\left\{0, \left[W_0 + \ln\left(\frac{E_{i,j}}{ETOT_j}\right)\right]\right\}. \tag{4.9}$$

W_0 is a free parameter, in our case $W_0 = 4.0$. This value was derived from Monte Carlo studies of the E-144 calorimeters.[27, 65]

The fractional weighting is a less computationally intensive algorithm. However, it fails to take into account the exponential shower shape caused by real e^+s and when particles hit near cell edges, the position reconstruction error grows. The logarithmic weighting accounts for the exponential falloff of the shower profile. To illustrate the difference, showers were simulated in PCAL . The deposited energy was calculated for each row. The values thus obtained were fit with each of the techniques. Since the hits were simulated, we know the exact

y_0 of the hit. Forming the difference, $\Delta y = y_0 - y_R$, we have an estimate of the error inherent in each algorithm. Figure 4.6 is a plot of these errors. The curved trace represents Δy for the fractional weighting. This shape is referred to as the "snake curve," and is commonly seen in calorimetry.[64] The saw-toothed trace represents Δy for the logarithmic weighting. The amplitude of the error in this case is smaller than that found in the fractional weighting case. The fact that error remains is an artifact of the threshold imposed with the parameter W_0.

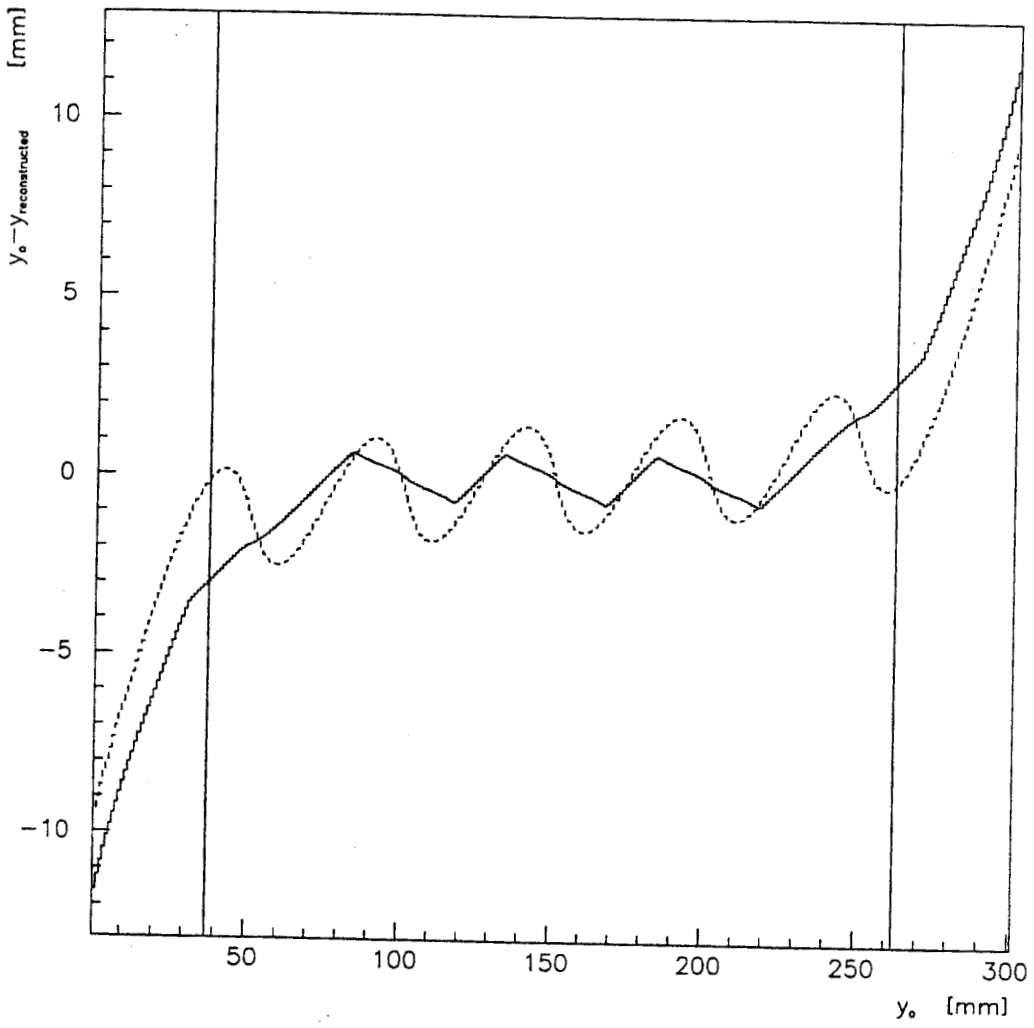

Figure 4.6: $y_0 - y_R$: Fractional and Logarithmic Weighting Schemes.
This plot shows the relative errors in reconstructed y position for Fractional (curve) and Logarithmic (saw tooth) weighting schemes.

4.5.1 The Selection of Single Peak Showers

The preceding algorithm will fail in a situation where two particles are incident upon the calorimeter in close proximity to one another. The reconstruction of a single hit position for events with two or more incident e^+s led to inaccurate, imprecise results. This can best be understood by examining Figure 4.7. It depicts a multihit event. Consider two "clean" e^+s , one incident at $x' = 20$ mm with energy $E = 15$ GeV, and the other incident at $x' = 38$ mm with energy $E = 10$ GeV. By "clean" I mean that the transverse shower profile energy measured by the calorimeter obeys the model given in Equation 2.7. The top two plots in Figure 4.7 depict the theoretical showers modeled with Equation 2.7 and the results of the fitting algorithm in the case when only one of the particles are incident. The bottom plot depicts the theoretical showers and the results of the fitting algorithm in the case when both of the particles are incident. Clearly, a way to screen out zero and multihit events was needed. Note that for y reconstruction, the sum in equation 4.7 is over the two or three rows in the cluster, and for x reconstruction, the sum is over all four columns and the raw signals are used to calculate the fractions.

Events with ETOT< 1.0 GeV were automatically considered hitless and cut. For each event the number of $F_{i,j} > 0.3$ was found where $F_{i,j}$, as defined in Equation 4.5, is the corrected CC energy divided by the total energy of the rows a–f of segment j. As such, the number of $F_{i,j} > 0.3$ is the number of rows containing more than 30% of the total energy of the rows a–f of segment j. Events with no $F_{i,j} > 0.3$ were also considered hitless. Figure 4.8 illustrates such an event. The cell dimensions were such that the transverse shower spreading induced by a single incident positron could deposit appreciable amounts of energy in at most two rows. In PCAL, the transverse segmentation causes the measured energy profile to be "granular." That is, the shower energy measured in a cell E_i^M, will be found, using the shower profile model, by integrating Equation 2.7 between lower cell boundary a and upper cell boundary b.

$$E_i^M = \frac{E_0}{2}\left(\gamma E_i^1 + (1-\gamma)\, E_i^2\right), \tag{4.10}$$

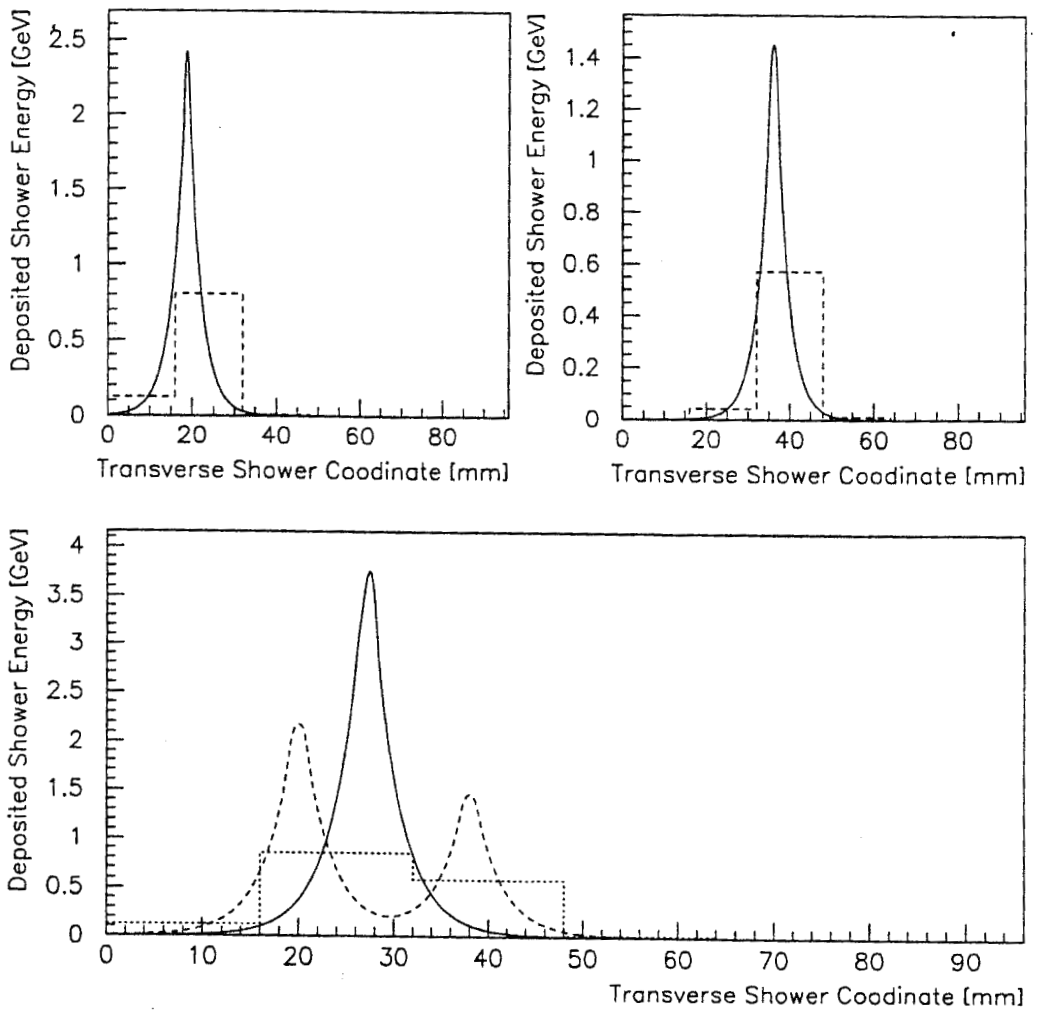

Figure 4.7: Reconstruction Algorithm Applied to Simulated Shower.

where

$$E_i^m = \begin{cases} \exp\frac{a_i - y_0}{\beta_m} - \exp\frac{b_i - y_0}{\beta_m} & y_0 < a_i \\ 1 - \frac{1}{2}\left(\exp\frac{y_0 - b_i}{\beta_m} - \exp\frac{a_i - y_0}{\beta_m}\right) & a_i < y_0 < b_m \\ \exp\frac{b_i - y_0}{\beta_m} - \exp\frac{a_i - y_0}{\beta_m} & b_i < y_0 \end{cases} \tag{4.11}$$

There are no values of y_0 for which $E_i^M/E_0 > 0.3$ for more than 2 values of i. This means that it is physically impossible for a single particle to deposit energy into more than 2 rows or 2 columns. Thus, events with more than two rows containing over 30% of the total energy were likely to constitute multihit events and consequently cut. Figure 4.9 illustrates such an event. Using similar reasoning, events with two $F_{i,j} > 0.3$ rows were vetoed if the rows were not adjacent.

Positions were reconstructed for all survivors of the single-peak cuts. Figure 4.10 illustrates such an event, a "hit." Figure 4.11 depicts the vertical shower profile of the hit depicted in Figure 4.10, and the reconstructed shower shape. The reconstruction was performed for the x and y coordinates of the hit on the face of the detector. Figure 4.15 shows y and x positions reconstructed for positrons produced at IP1 by a combination of bremsstrahlung and pair production in an Aluminum foil (foil data).

Many zero hit events survived this far, but few multihit events did. The multihit events that did survive were events wherein the hits all occurred in the same or adjacent rows. The number of hits, NHIT , in an event is defined as the cluster's energy divided by EMAP(y),

$$\text{NHIT} \equiv \frac{\text{ECL}}{\text{EMAP}(y_R)} \tag{4.12}$$

Figure 4.16 shows NHIT for foil events surviving the single particle constraints. The zero, one, two, and three hit peaks are obvious, a four hit peak is discernible. The zero hit peak is suppressed by the earlier cut of events below an energy threshold. Figure 4.17 is a zoomed view of the region $0.5 \leq \text{NHIT} \leq 1.5$. This plot can be used to calibrate the energy map. Limitations of the magnet field maps limit the accuracy to which a trajectory can be predicted. Since foil signal is guaranteed to come from IP1, a fit to the one hit peak in Figure 4.17

gives values for a cut on NHIT. This constitutes a cut of e^+s coming down the beam line with the e^- bunch. Figure 4.18 is a plot of such a cut.

The top plot in Figure 4.15 is a distribution of reconstructed y positions, y_R. There are six "spikes" evident, located at y =67.3, 83.3, 99.3, 115.3, 132.8, and 148.8 mm. These spikes correspond to row centers. The bottom plot in Figure 4.15 represents reconstructed x positions. There are two spikes evident, located at x =-8.0 and 8.0 mm. Such spikes are artifacts of the reconstruction algorithm. W_0 was chosen to minimize the "spike" to "shoulder" ratio. Spikes formed at row centers as a result of artificial weighting. Showers which deposited energy such that only one pad satisfied Equation 4.9 were automatically reconstructed at the pad center.

A study of W_0 was performed to minimized analysis artifacts in analyzed data. For idealized showers, Figure 4.12 depicts the reconstruction error as a function of y_0 for several values of the parameter W_0. As we increase W_0, the amplitude of the error diminishes within certain boundaries. As W_0 grows, the errors fall, but the region of valid reconstruction shrinks. A balance must be struck. Outside of this region, shower energy leaks out the edges of the calorimeter enough to skew reconstruction. As an example, consider $W_0 = 5.0$, and $W_0 = 9.0$. The threshold energy is $\exp(-4.0)$ times lower for $W_0 = 9.0$. and so many more rows actually contribute to the reconstruction. In the center of an infinite detector this would be great, but near the edges of a finite detector, it causes error to be introduced.

Foil data was used to select the W_0 used in the reconstruction.

Row	y_L [mm]	y_H [mm]	y_C [mm]	E_L	E_H	E_C	ΔE
a	156.8	140.8	148.8	5.97	6.87	6.42	0.90
b	140.8	124.8	132.8	6.87	7.97	7.41	1.10
c	123.3	107.3	115.3	8.05	9.53	8.75	1.48
d	107.3	91.3	99.3	9.53	11.45	10.42	1.92
e	91.3	75.3	83.3	11.45	14.06	12.64	2.66
f	75.3	59.3	67.3	14.06	17.87	15.78	3.81

Table 4.2: Cell Characteristics, September 1994.

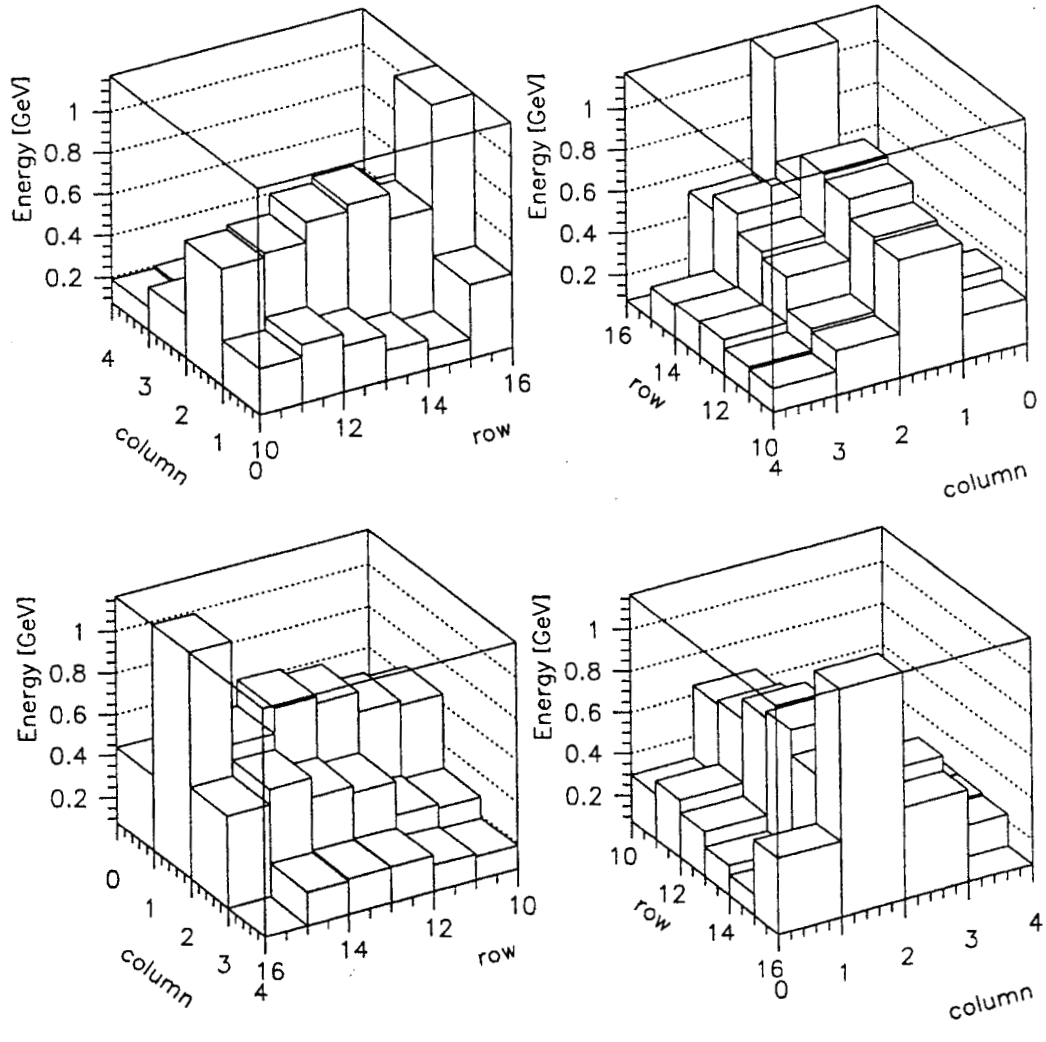

Figure 4.8: Foil Data: s0+s1, rows a-f, columns 0-4, "hitless".

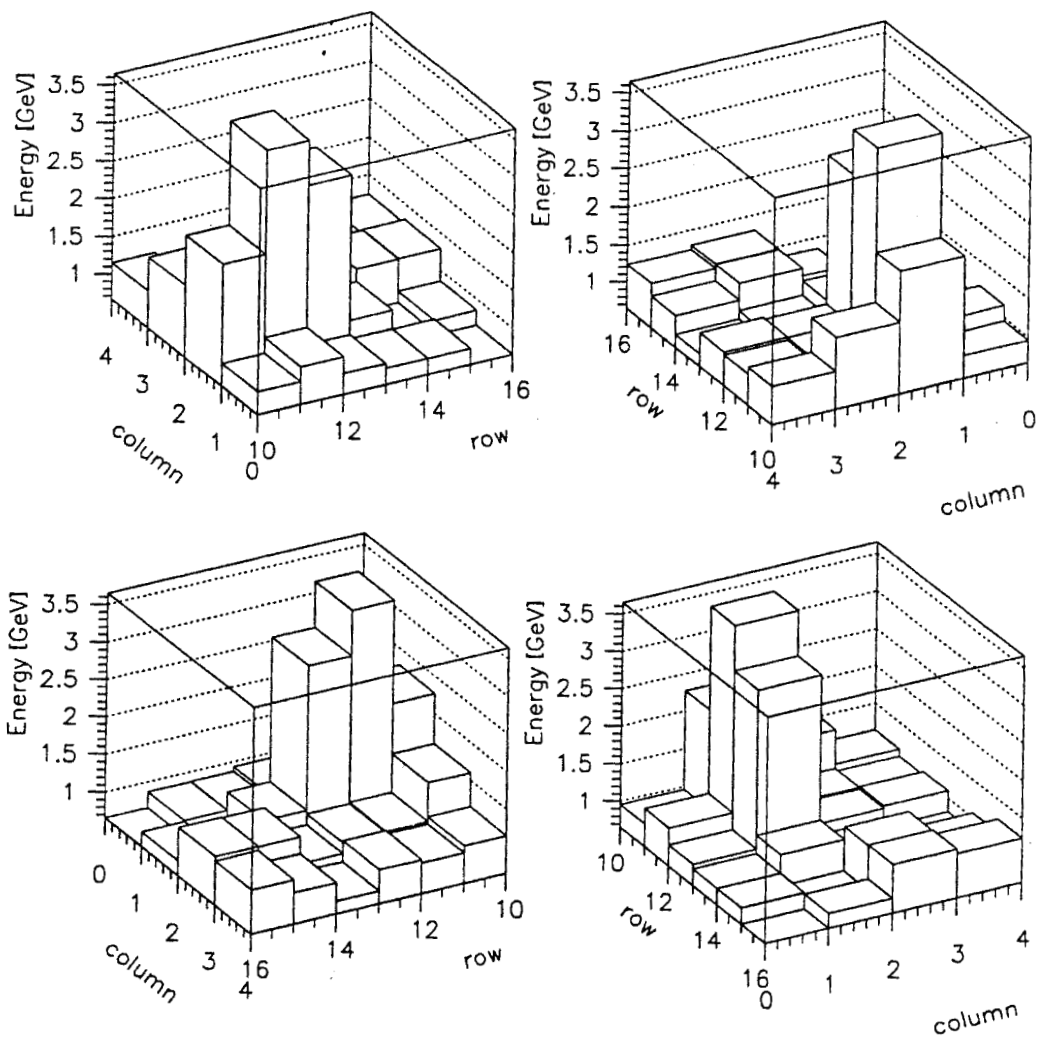

Figure 4.9: Foil Data: s0+s1, rows a-f, columns 0-4, "multihit".

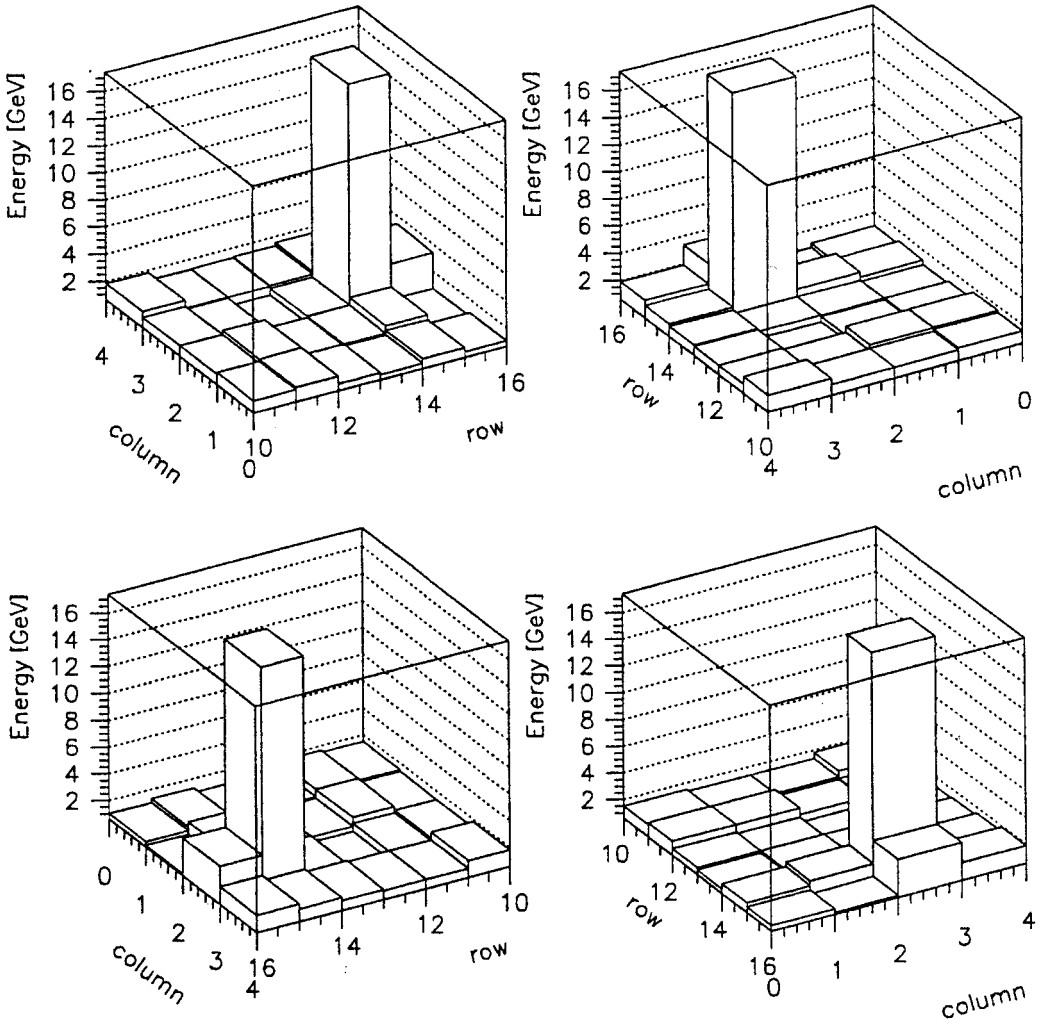

Figure 4.10: Foil Data: s0+s1, rows a-f, columns 0-4, "hit".

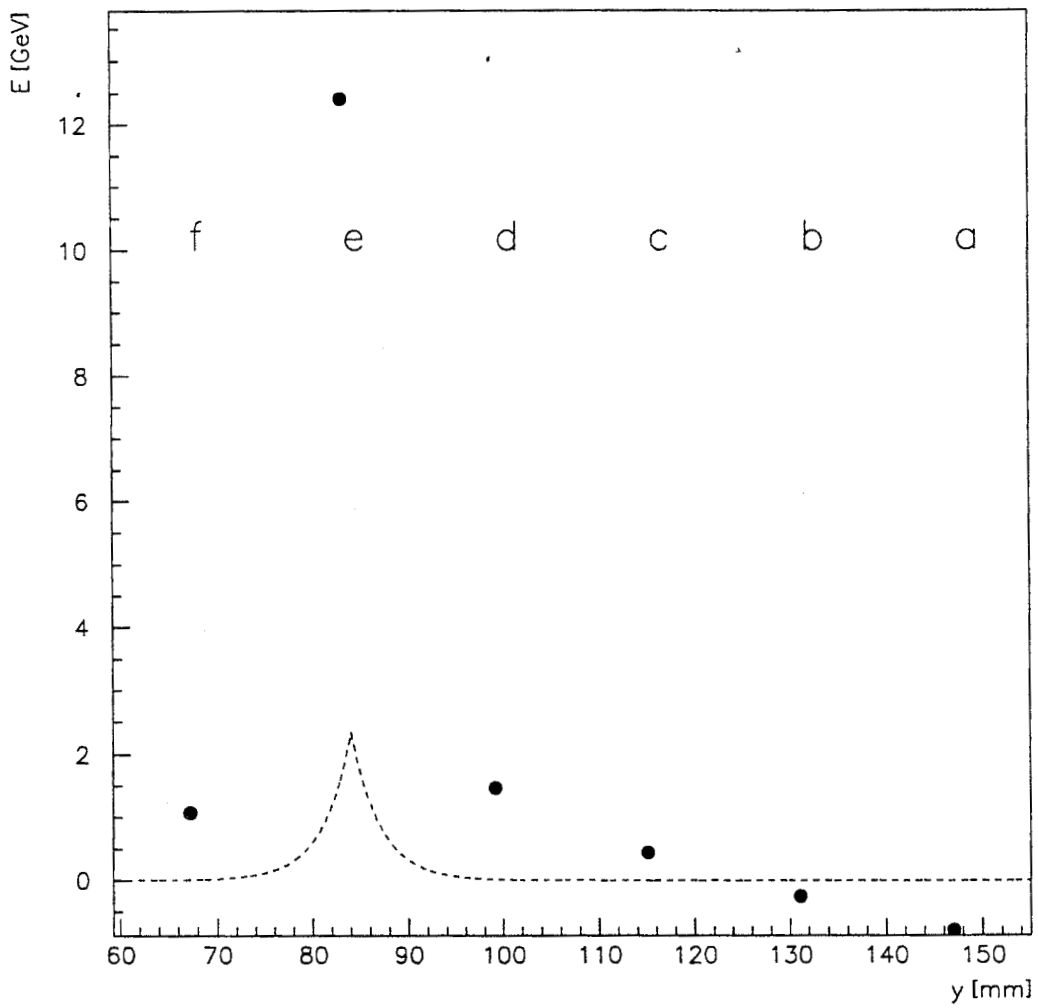

Figure 4.11: The transverse shower profile of the "hit" depicted in Figure 4.10. The histogram is a plot of $E_{0,j} + E_{1,j}$ for $a \leq j \leq f$. The dashed curve represents the simulated shower shape for a e^+ incident at the position reconstructed using the above algorithm to be $y = 84.0$ mm.

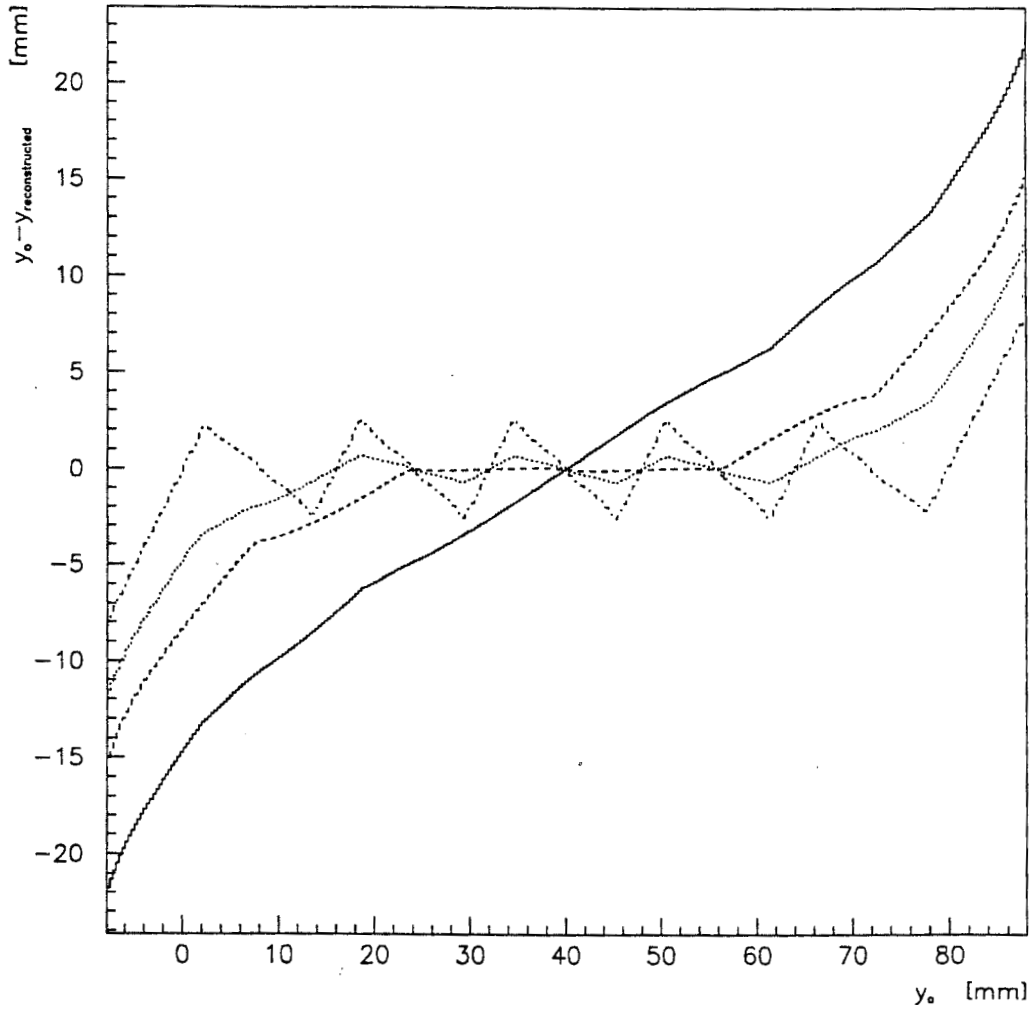

Figure 4.12: $y_0 - y_R$: Fractional and Logarithmic Weighting, Varied W_0.

Row	y_L [mm]	y_H [mm]	y_C [mm]	E_L	E_H	E_C	ΔE
a	152.8	136.8	144.8	6.18	7.10	6.64	0.92
b	136.8	120.8	128.8	7.10	8.29	7.70	1.19
c	119.3	103.3	111.3	8.42	9.97	9.20	1.55
d	103.3	87.3	95.3	9.97	12.04	11.01	2.07
e	87.3	71.3	79.3	12.04	14.92	13.48	2.88
f	71.3	55.3	63.3	14.92	19.18	17.05	4.26

Table 4.3: Cell Characteristics, March 1994.

Figures 4.13 and 4.14 show the reconstructed y distributions for several values of W_0. The value of W_0 was set to 4.5 in light of this plot, since the spikes were minimized.

The shower centers in both x and y were reconstructed. Monte Carlo studies predict a position resolution on the order of 1.5 mm for the $E144$ calorimeter. Figure 4.15 shows distributions of x and y positions for hits.

Calculations were carried out so that an optimal NHIT interval for each value predicted by the kinematic mapping program existed. Histograms were filled according to the following criteria: $0.5 <$ NHIT < 1.5, and $y_{map} - 1.5$ mm $< y < y_{map} + 1.5$ mm. Gaussians were fitted to these histograms, and for each y_{map}, σ and μ were stored. Figure 4.19 is a plot of σ and μ versus y_{map}. Figure 4.20 is a plot of a cut where for each value of y, $\mu(y) - 1\sigma(y) <$ NHIT $< \mu(y) + 1\sigma(y)$. The area bounded by 71.3 mm $< y <$ 144.8 mm $\mu(y) - 1\sigma(y) <$ NHIT $< \mu(y) + 1\sigma(y)$ is 204.407 GeV mm.

4.6 The Development of "Hit" Constraints

The foil positrons were used to characterize IP1 positrons. Backgrounds came in the form of "beam positrons." Using the distributions of several kinematical traits of IP1 positrons I was able to cut many background positrons. Many traits were studied. Cuts based on y_R, the x_R distribution, the $\Delta x \equiv x_R^{S0} - x_R^{S1}$ distribution, the $\Delta y \equiv y_R^{S0} - y_R^{S1}$ distribution, the S0%=ECLS0/(ECLS0+ECLS1) distribution, and the

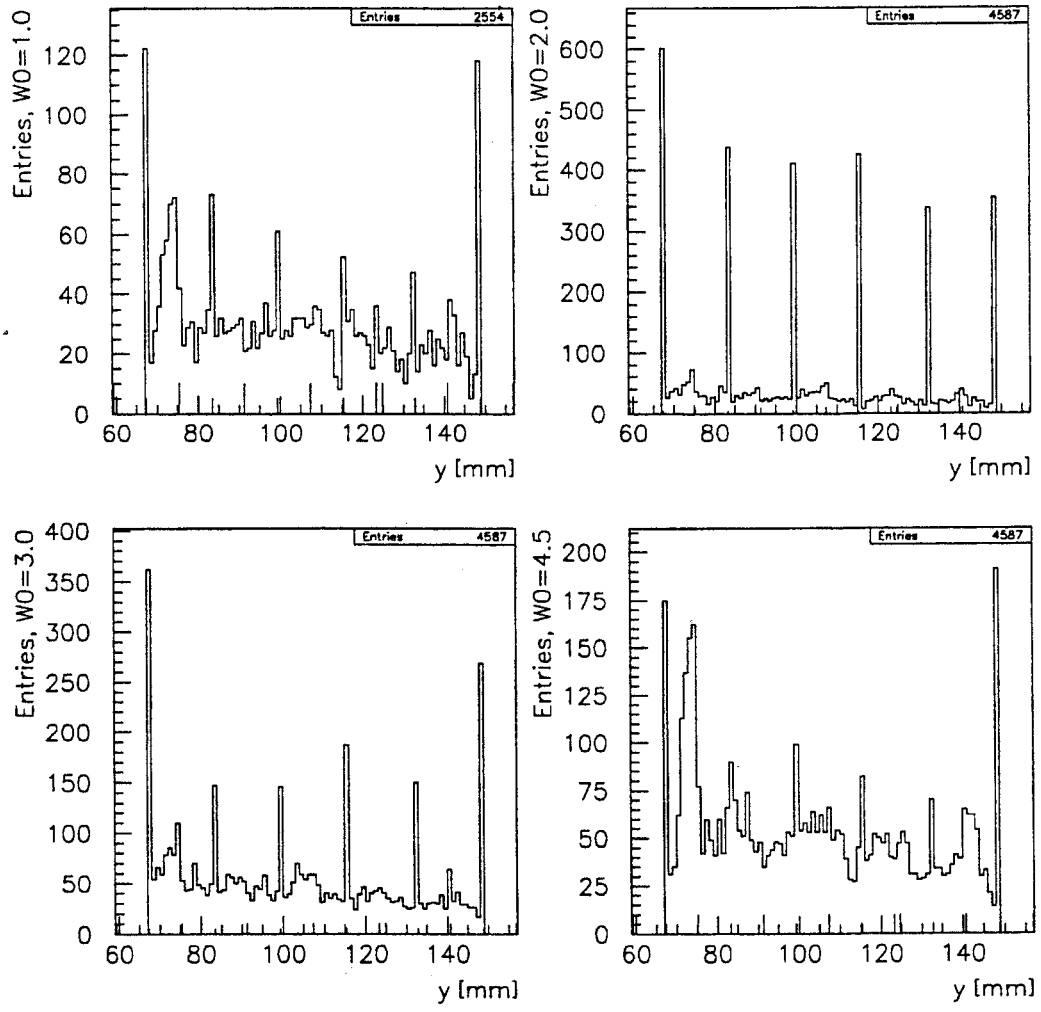

Figure 4.13: Foil Data: y_R, Logarithmic Weighting, Varied $W_0 \leq 4.5$.

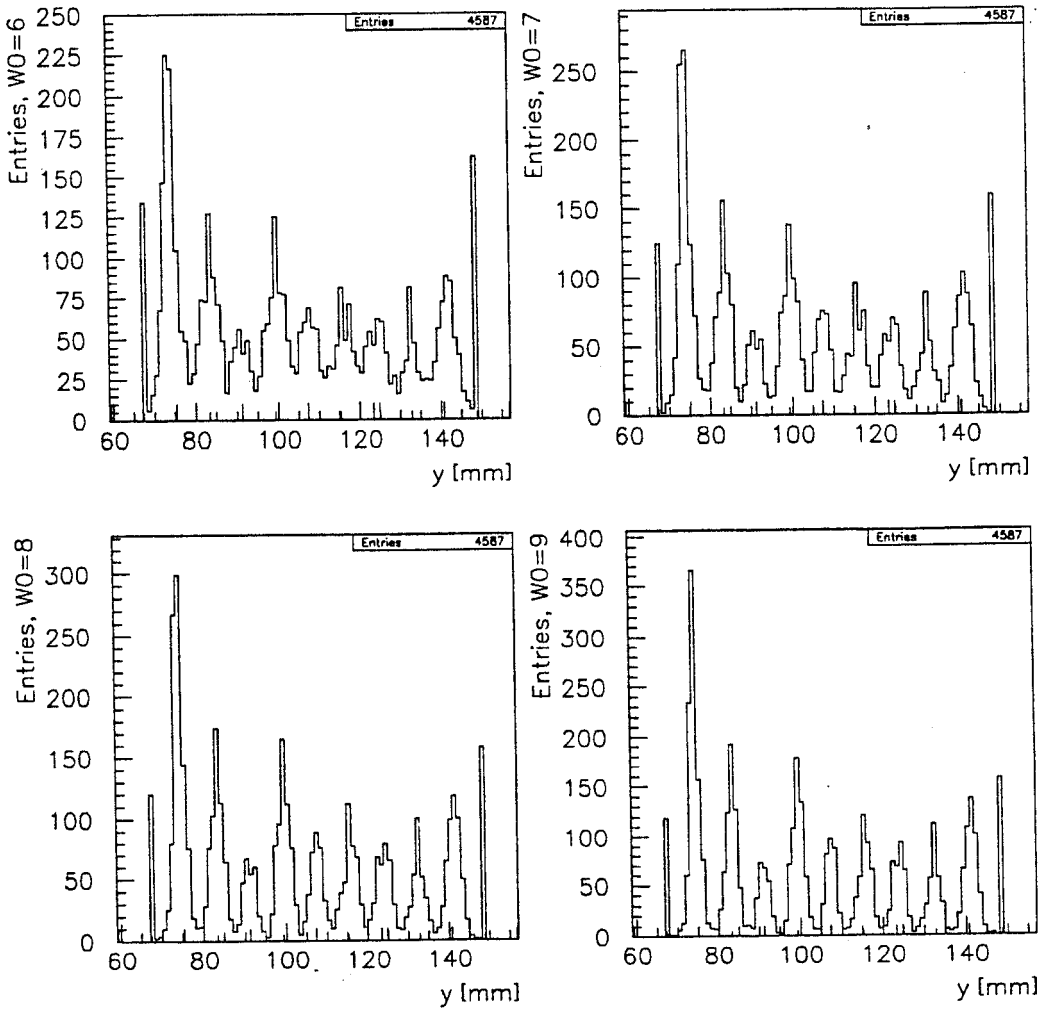

Figure 4.14: Foil Data: y_R, Logarithmic Weighting, Varied $W_0 > 4.5$.

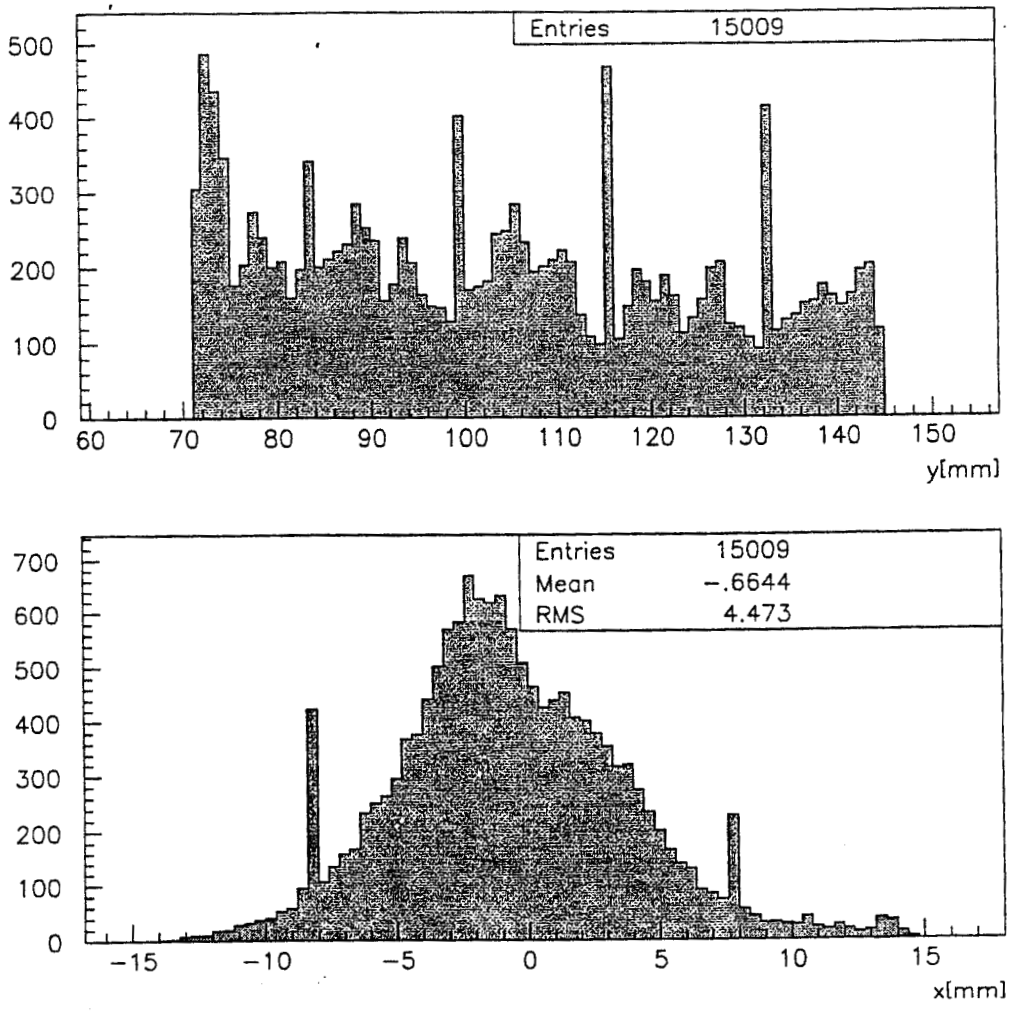

Figure 4.15: Foil Data: y_R and x_R.

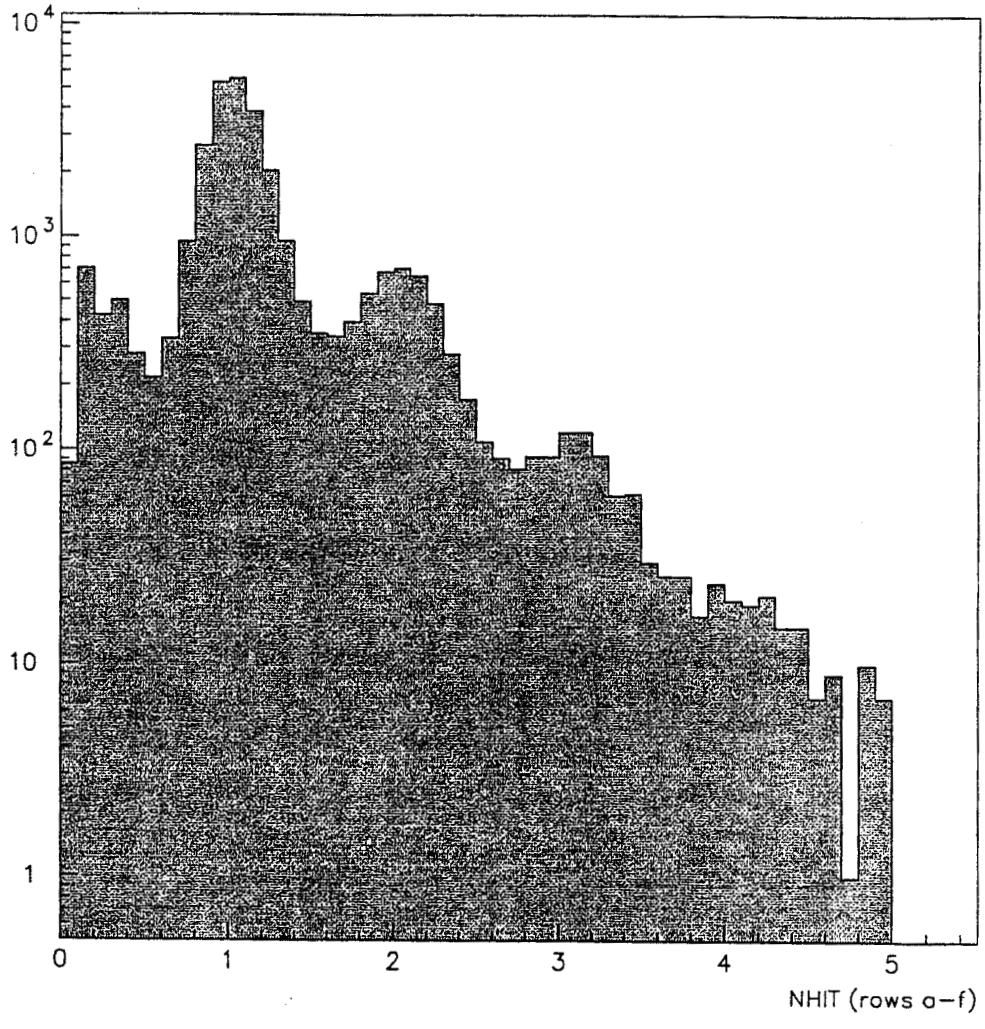

Figure 4.16: The distribution of NHIT within 0 <NHIT < 5 for 71.3 mm< y < 144.8 mm.

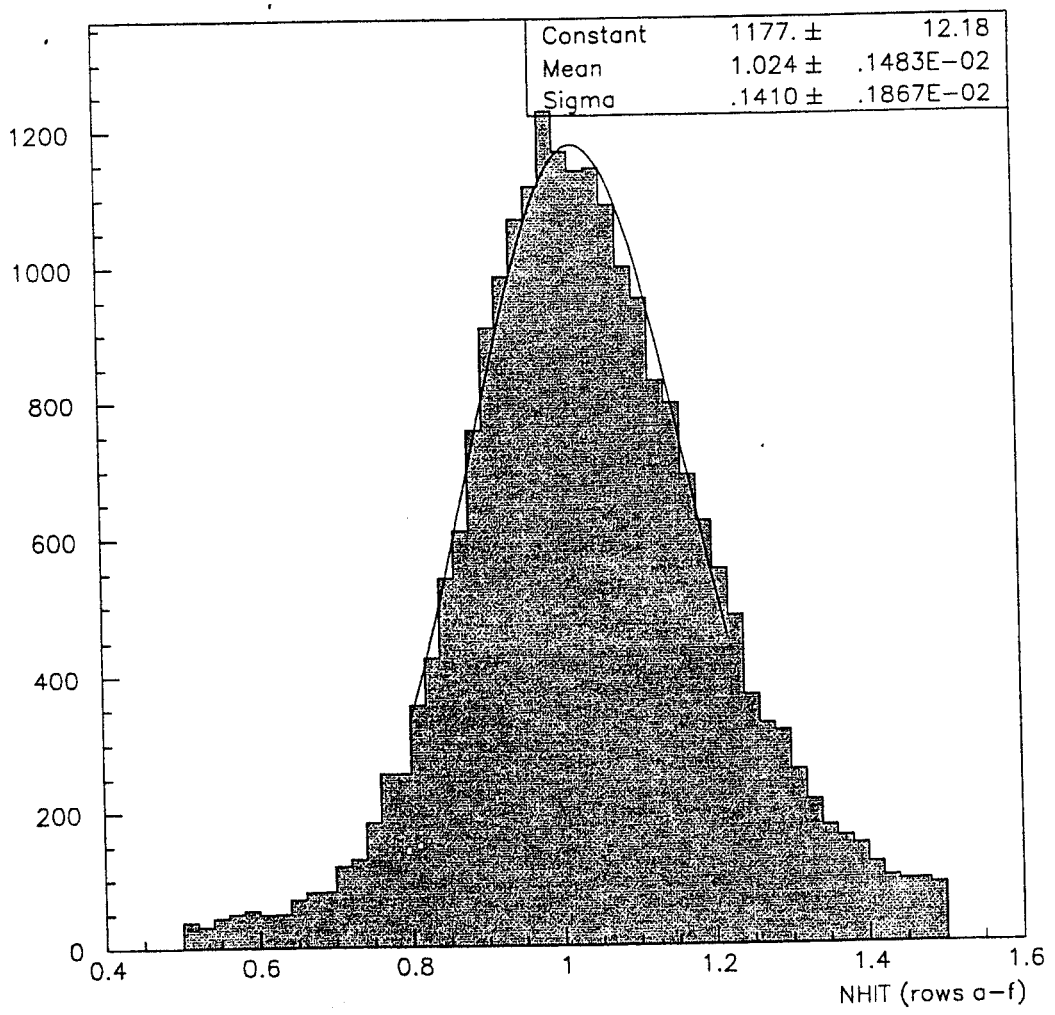

Figure 4.17: The distribution of NHIT within 0.5 <NHIT < 1.5 for 71.3 mm< y < 144.8 mm.

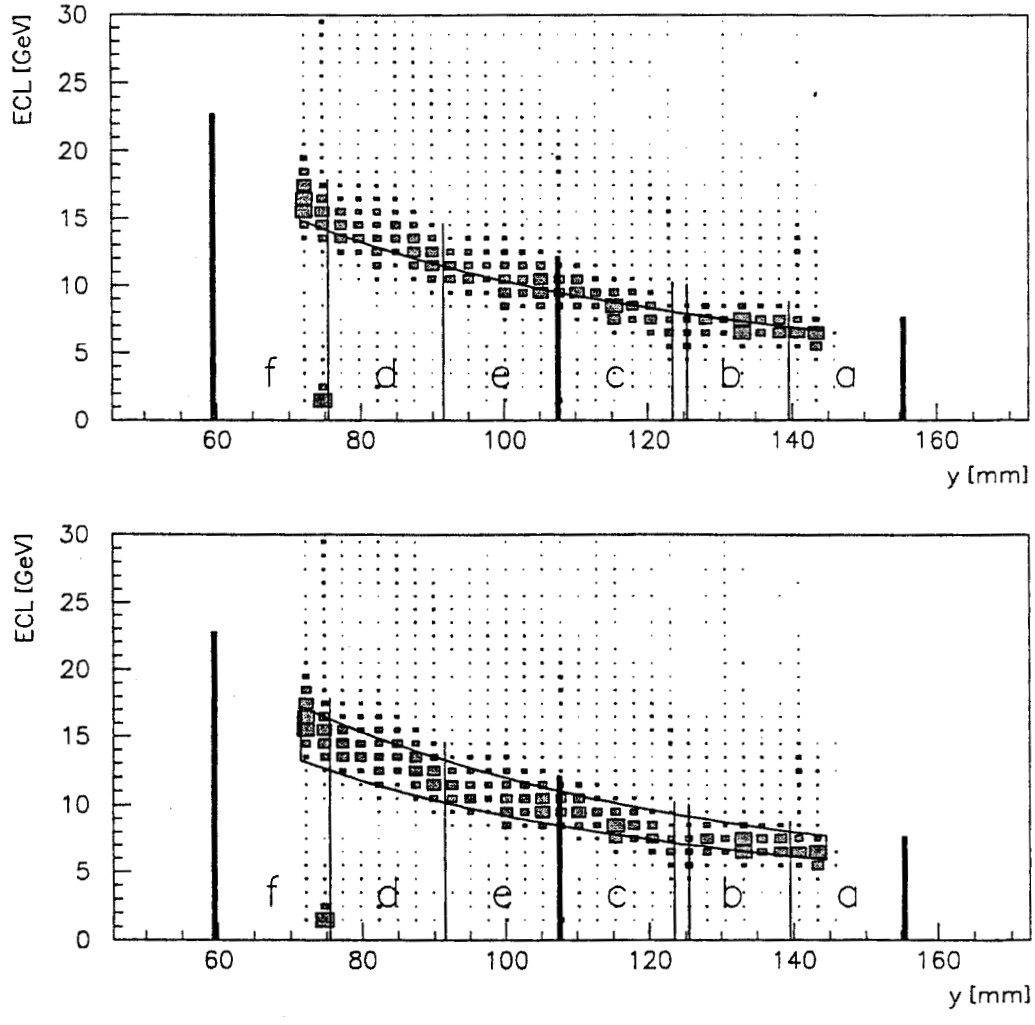

Figure 4.18: Cluster energy versus reconstructed y position for 71.3 mm$< y <$ 144.8 mm. The line in the top plot represents the mean from Figure 4.17 times the map energy. The band in the bottom plot represents the region bounded by EMAP$\times\mu \pm .834\sigma$ from Figure 4.17.

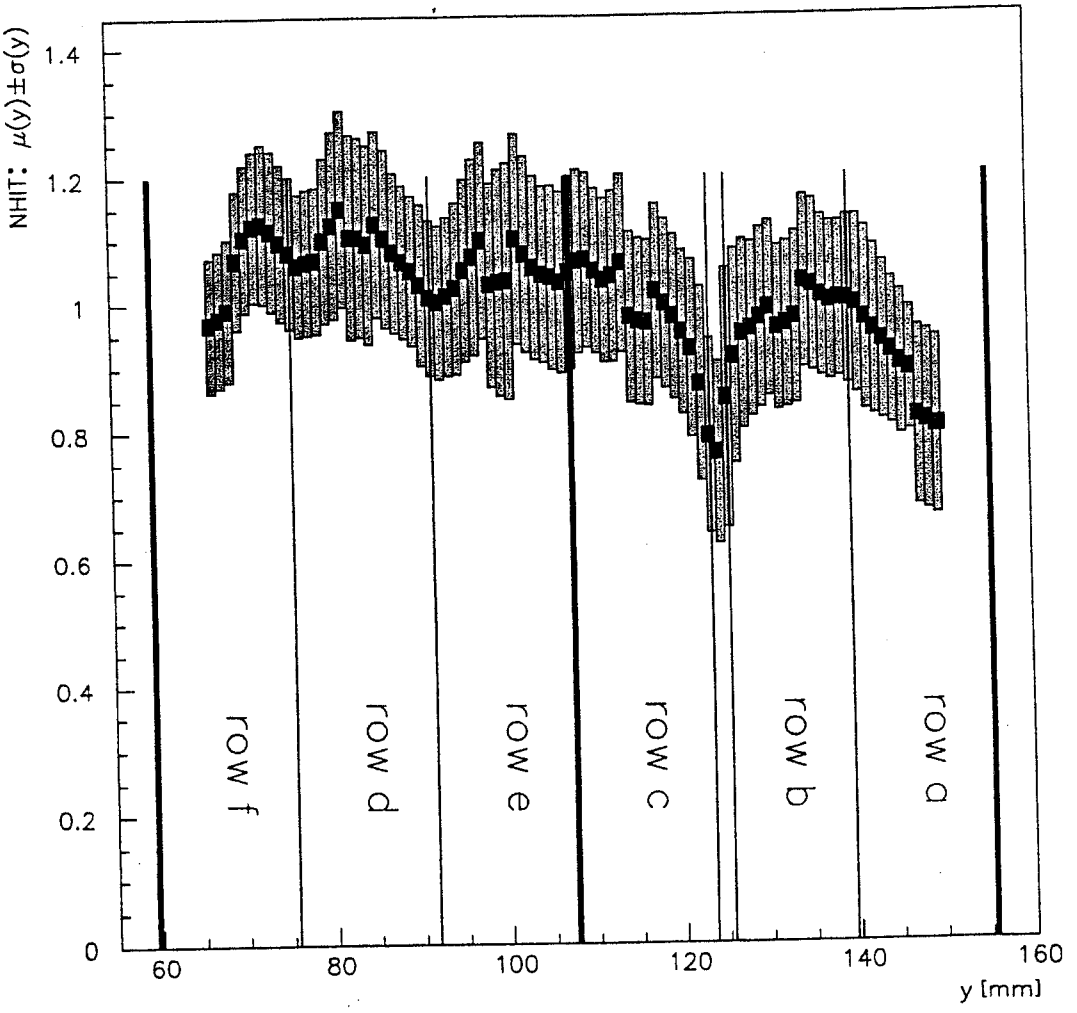

Figure 4.19: Mean NHIT $\pm\sigma$ versus reconstructed y position for 59.3 mm$< y <$ 156.8 mm.

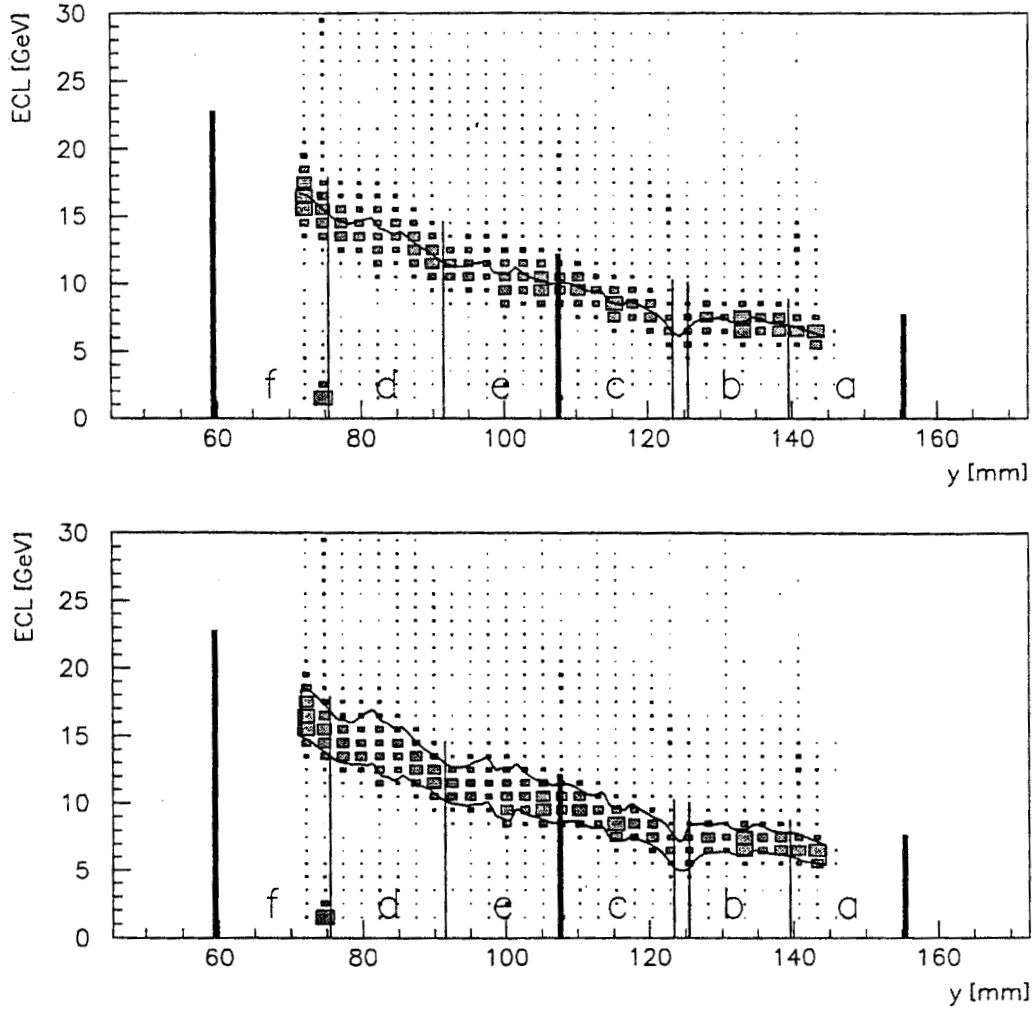

Figure 4.20: Cluster energy versus reconstructed y position for 71.3 mm$< y <$ 144.8 mm. The line in the top plot represents the means from Figure 4.19 times the map energy. The band in the bottom plot represents the region bounded by EMAP$\times\mu \pm 1\sigma$ from Figure 4.19.

S1%=ECLS1/(ECLS0+ECLS1) distribution are mentioned in this thesis. Figure reffig:yandxposition shows the y_R and x_R distributions for the foil positrons. Figure reffig:yandxdelta shows the Δy and Δx distributions for the foil positrons. Figure reffig:sharing shows the S0% and S1% distributions for the foil positrons.

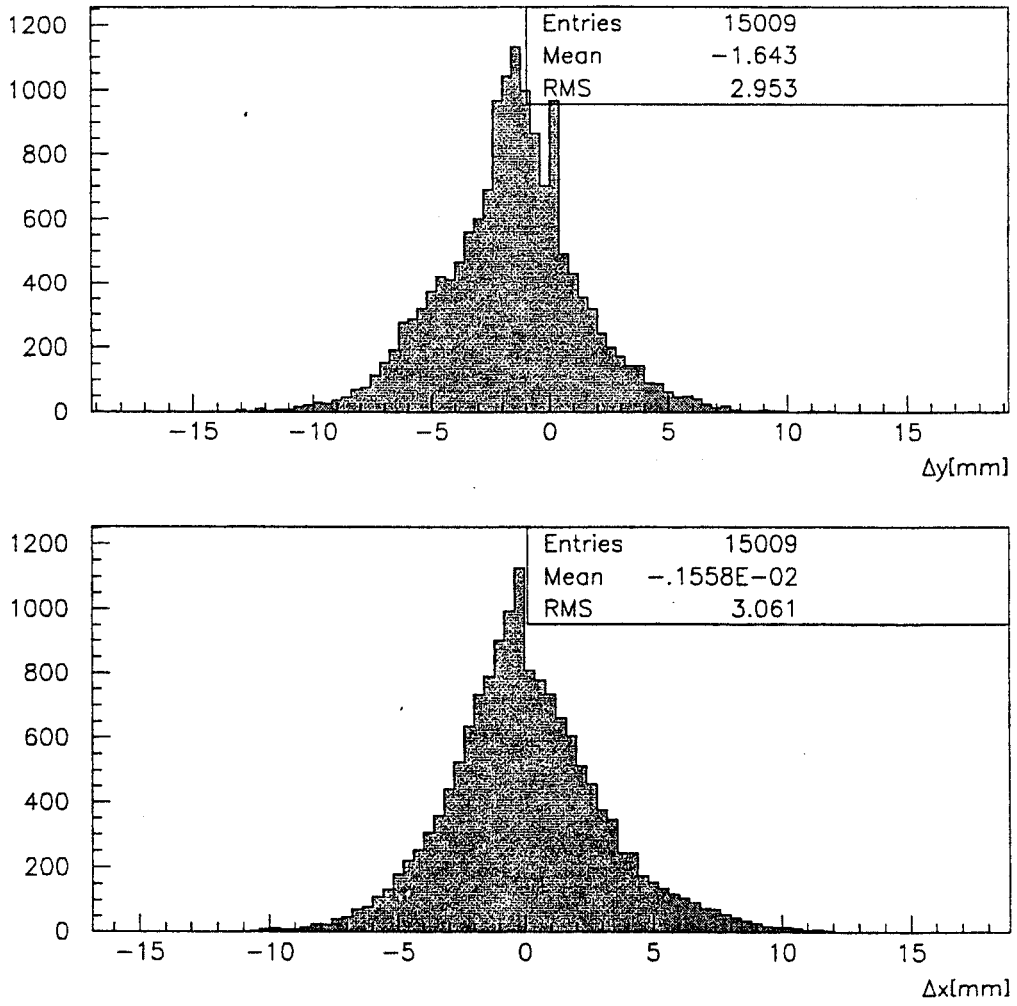

Figure 4.21: Foil Data: Δy_R and Δx_R.
The distribution of Δy and Δx for foil positrons. A positron originating at IP1 must be rising, it must have a larger y in segment 1 than in segment 0. A positron originating at IP1 must go straight downstream, it must have the same larger x in segment 0 and 1.

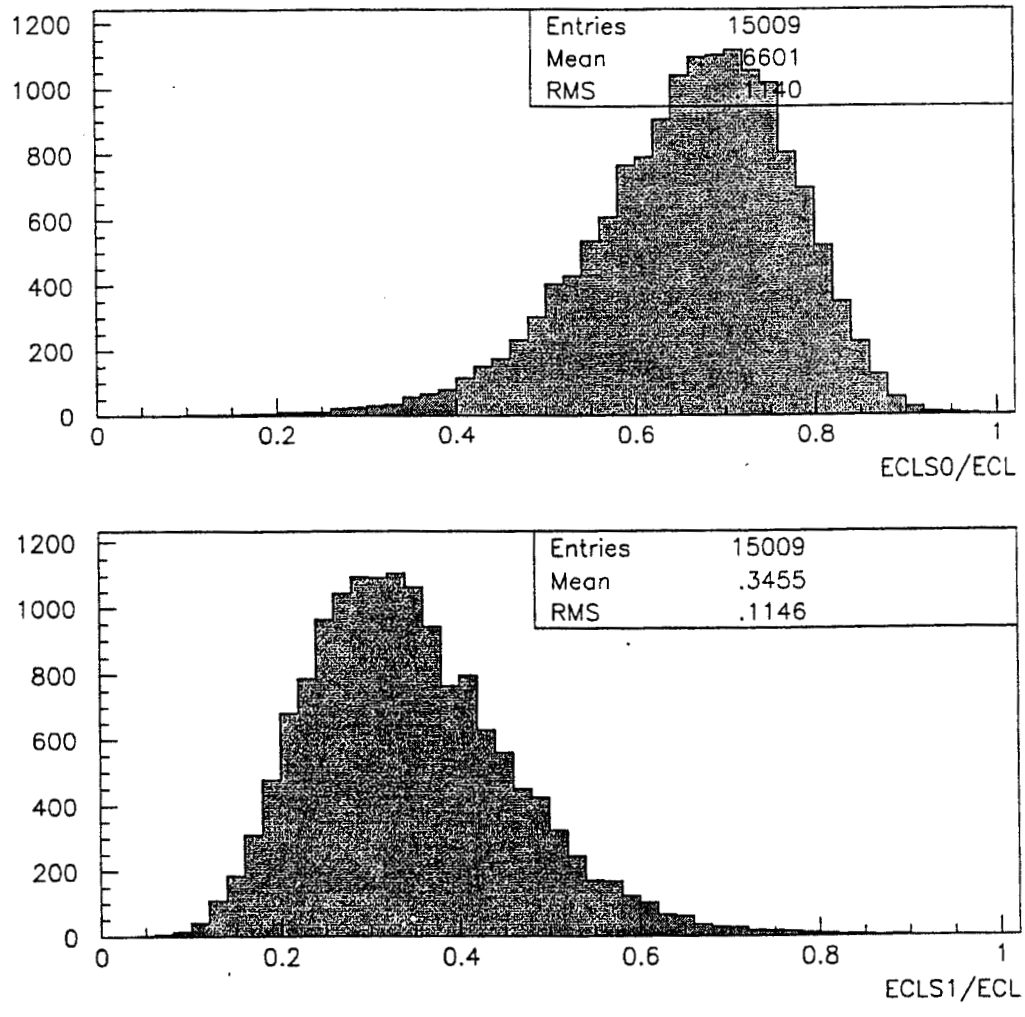

Figure 4.22: Foil Data: Shower Sharing.
PCAL was designed to collect 50% of the shower in each segment. The shower fraction of a segment is found by dividing the cluster energy of that segment by the total cluster energy.
S0%=ECLS0/(ECLS0+ECLS1)
S1%=ECLS1/(ECLS0+ECLS1).

Chapter 5

Results and Conclusions

During the September 1994 FFTB run, the laser system produced its highest intensity Green pulses to date. These pulses were brought into collisions with electron bunches. Evidence of multiphoton Breit-Wheeler pair production has been found.

Much of the bunch/pulse collision data analysis was identical to that performed on the foil data, from the calculation of corrected center pad energies to the reconstruction of shower centers. Once Ntuples of Breit-Wheeler candidates were filled, cuts were applied to suppress background positrons. These cuts were largely derived from the observed characteristics of foil positrons. This chapter details the effects of various cuts and the characteristics of detected positrons. The rate is calculated for e^+ production, and the energy spectrum of the candidates is shown. The agreement of simulation results with these observations is described.

Detailed candidate characteristics are set forth for the very highest intensity runs, and a subset of same. From both groups of events, statistically significant positron production above background was extracted. If the events from the last two runs are removed, in response to deteriorating collision conditions, the statistical significance exceeds the 99% level!

5.1 Collision Quality Control

Events accumulated during physics runs were subjected to cuts that were unavailable for foil runs. As mentioned before, the foil data was accumulated during parasitic running, a running mode in which bunch arrival is sporadic. Since the FFTB beam parameter detectors' performance is degraded when the bunch rate falls below 10Hz, electron beam diagnostics weren't available for foil runs. So no beam cuts could be made on foil data. Beam cuts can be made for physics run data. A beam/pulse overlap cut must also be applied to physics runs since the rate for every process depends on the degree of coalignment and synchronization of the e^-s and ω_0s.

In section 4.4, I stated that during foil runs, outer pad signals were essentially pedestals, since the e^+s produced in the foil collisions did not extend into outer columns. A similar statement can be made for γ/ω_0 collisions. I

plotted outer pad energies for all events of all the runs, and found outer pad signals above 5 GeV in less than 2% of the events. I examined outer pad energies for the events containing the Breit-Wheeler candidates, and found no outer pad signals above 5 GeV.

Great effort was made to ensure temporal overlap of the bunch and pulse. While the average overlap was good, instantaneous jitter degraded the event rate. Evidence of this jitter, and its consequences emerges from the linear Compton scattering rate. Temporal jitter results in variation of the flux of produced γs when pulses of equal energy (U_L) collide with electron bunches of equal charge, length, transverse area, and energy. The ratio of γ flux to U_L provides a good measure of the bunch/pulse overlap. Events where the bunch "missed" the pulse, for which the γ flux was low, were cut.

Table 5.1 lists the runs included in the "highest intensity to date" set; and gives the number of triggers in each. The runs included are 9077, 9079, 9081, 9082, 9083, 9089, and 9090. Event-by-event parameter values were placed in "Control Plot" histograms for each run.

5.2 Laser Pulse - Beam Bunch Collision Data

PCAL was located as close to the beam line as possible. Collision simulations indicated that the significant range of the Breit-Wheeler e^+ energy spectrum would run from 6–26 GeV, reaching a maximum near 14 GeV.[66] The highest energy positrons experienced the smallest deflections, remaining very close to the beam line. The beam pipe made it impossible to move PCAL into the path of all the produced positrons. The highest energy portion of the spectrum went underneath PCAL .

The energy corresponding to the bottom edge (y=59.3 mm) of the bottom row (f) of PCAL was 17.9 GeV. A 17.9 GeV positron produced at IP1 with initially downstream momentum would be deflected traversing the dump magnets. It would be 59.5 mm above the beam line by the time it reached the plane containing the front surface of PCAL. It would strike the bottom edge of the row of PCAL closest to the beam line (f). Therefore, 17.9 GeV is the highest energy observable in PCAL for Breit-Wheeler candidates.

Run Number	Triggers: Total	Triggers: Passed BC	Triggers: E1L0	Triggers: Passed OC	Triggers: Failed OC	Trigger Ratio
9077	4762	3733	2902	552	279	5.26
9079	4907	3866	2991	633	242	4.73
9081	4835	3777	2937	629	211	4.67
9082	4985	3774	2932	739	103	3.97
9083	9982	7832	6104	1289	439	4.74
9089	9953	7560	5862	1383	315	4.24
9090	9969	7666	5954	1190	522	5.00
Totals:						
'77-'83	29471	22982	17866	3842	1274	4.65
'89-'90	19922	15226	11816	2573	837	4.59
'77-'90	49393	38208	29682	6415	2111	4.63

Table 5.1: The 9000s: Triggers
The column labeled "Triggers: Total" contains the total number of triggers in the run. The sum includes Pedestal, Laser Off, and Laser On events. The column labeled "Triggers: Passed BC" contains the total number of Laser On and Laser Off events that survived the beam cuts. The column labeled "Triggers: E1L0" contains the total number of Laser Off (E1L0) events that survived the beam cuts, E1 indicates a bunch was present, L0 indicates no pulse was present. The column labeled "Triggers: Passed OC" contains the total number of Laser On (E1L1) events that survived the beam cuts and the overlap cut, E1 indicates a bunch was present, L1 indicates a pulse was present. The column labeled "Triggers: Failed OC" contains the total number of Laser On (E1L1) events that passed the beam cuts but failed the overlap cut. The column labeled "Trigger Ratio" contains ratio of E1L0 triggers to Passed OC triggers. Event rates from Laser Off and Laser On samples must be normalized using this ratio before being compared.

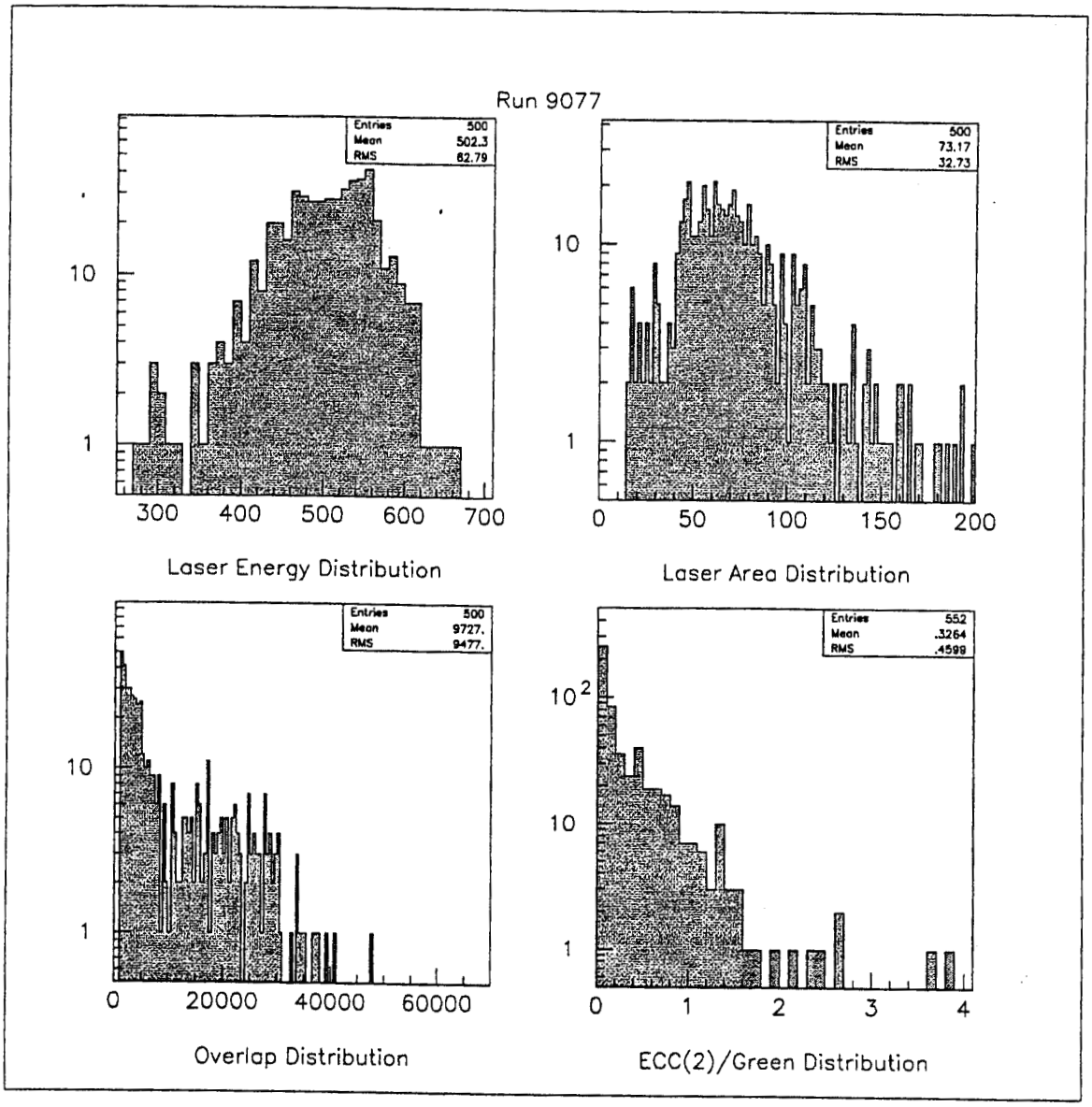

Figure 5.1: Run Data: Run 9077 Control Plot.
The distribution in the top left corner contains laser pulse energies. The top right corner contains laser spot sizes. The lower left corner contains the ratio of γ flux to laser pulse energy used in the overlap cut. The lower right corner contains the signal from another calorimeter versus laser pulse energy.

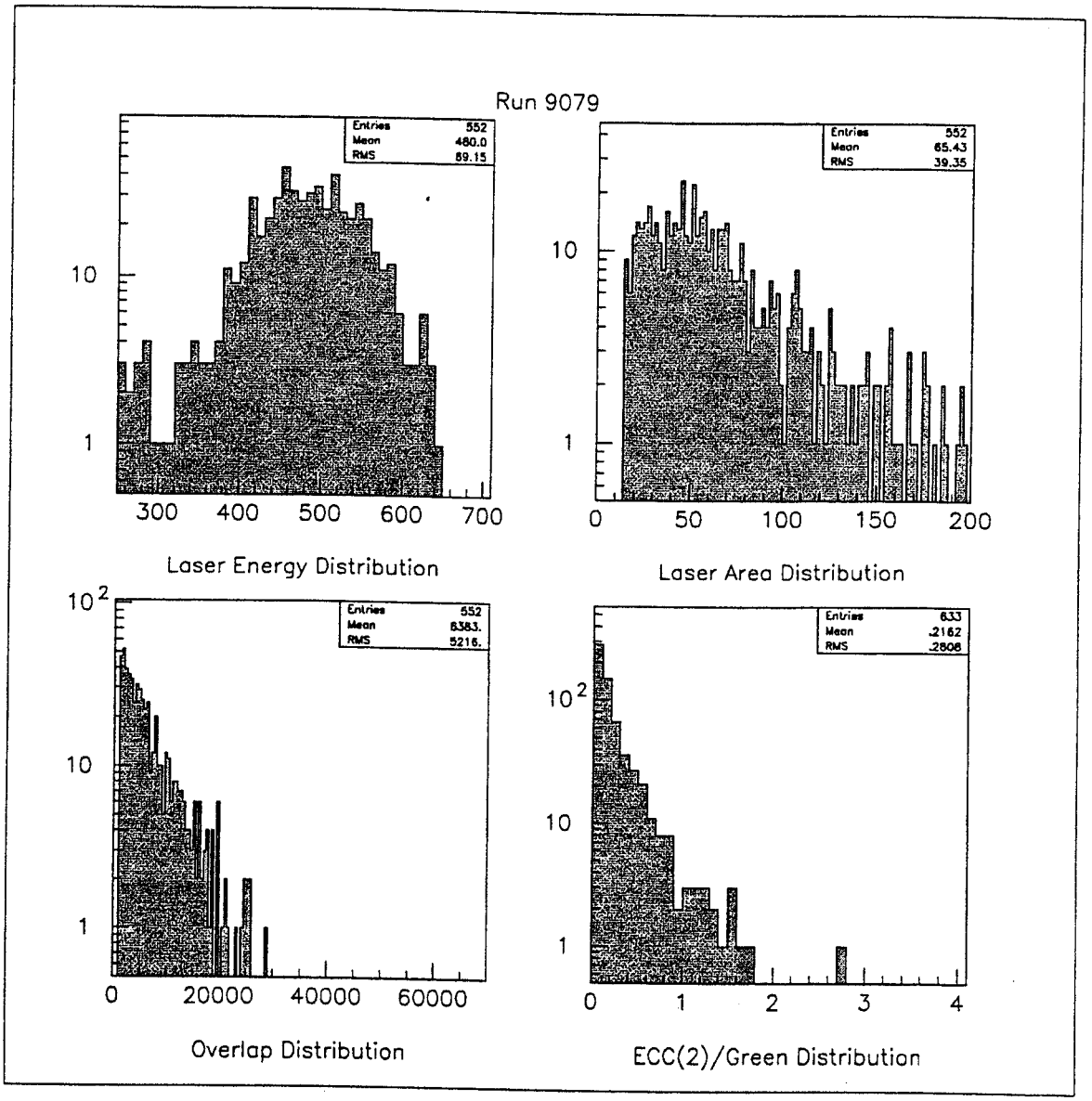

Figure 5.2: Run Data: Run 9079 Control Plot.
The distribution in the top left corner contains laser pulse energies. The top right corner contains laser spot sizes. The lower left corner contains the ratio of γ flux to laser pulse energy used in the overlap cut. The lower right corner contains the signal from another calorimeter versus laser pulse energy.

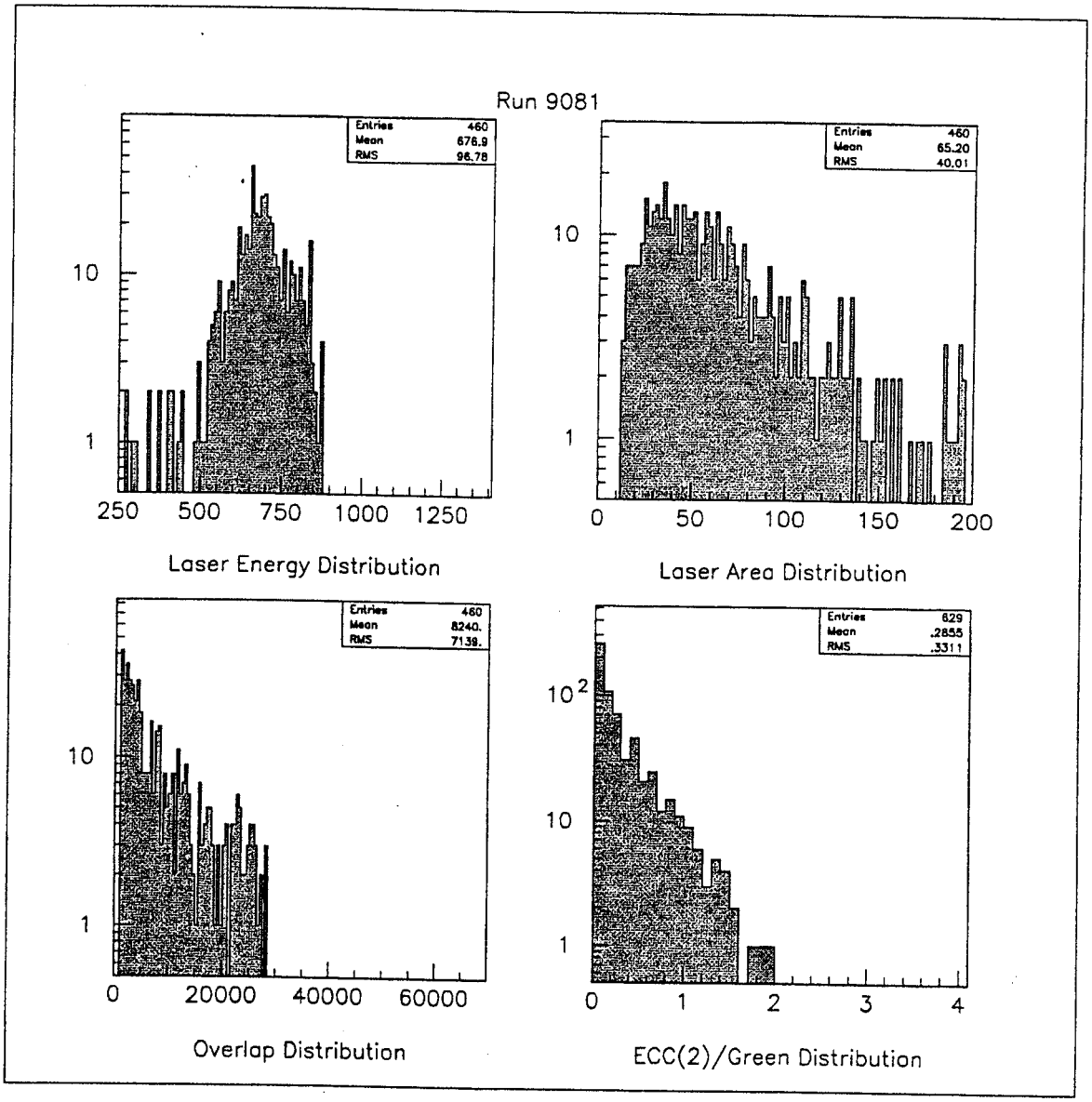

Figure 5.3: Run Data: Run 9081 Control Plot.
The distribution in the top left corner contains laser pulse energies. The top right corner contains laser spot sizes. The lower left corner contains the ratio of γ flux to laser pulse energy used in the overlap cut. The lower right corner contains the signal from another calorimeter versus laser pulse energy.

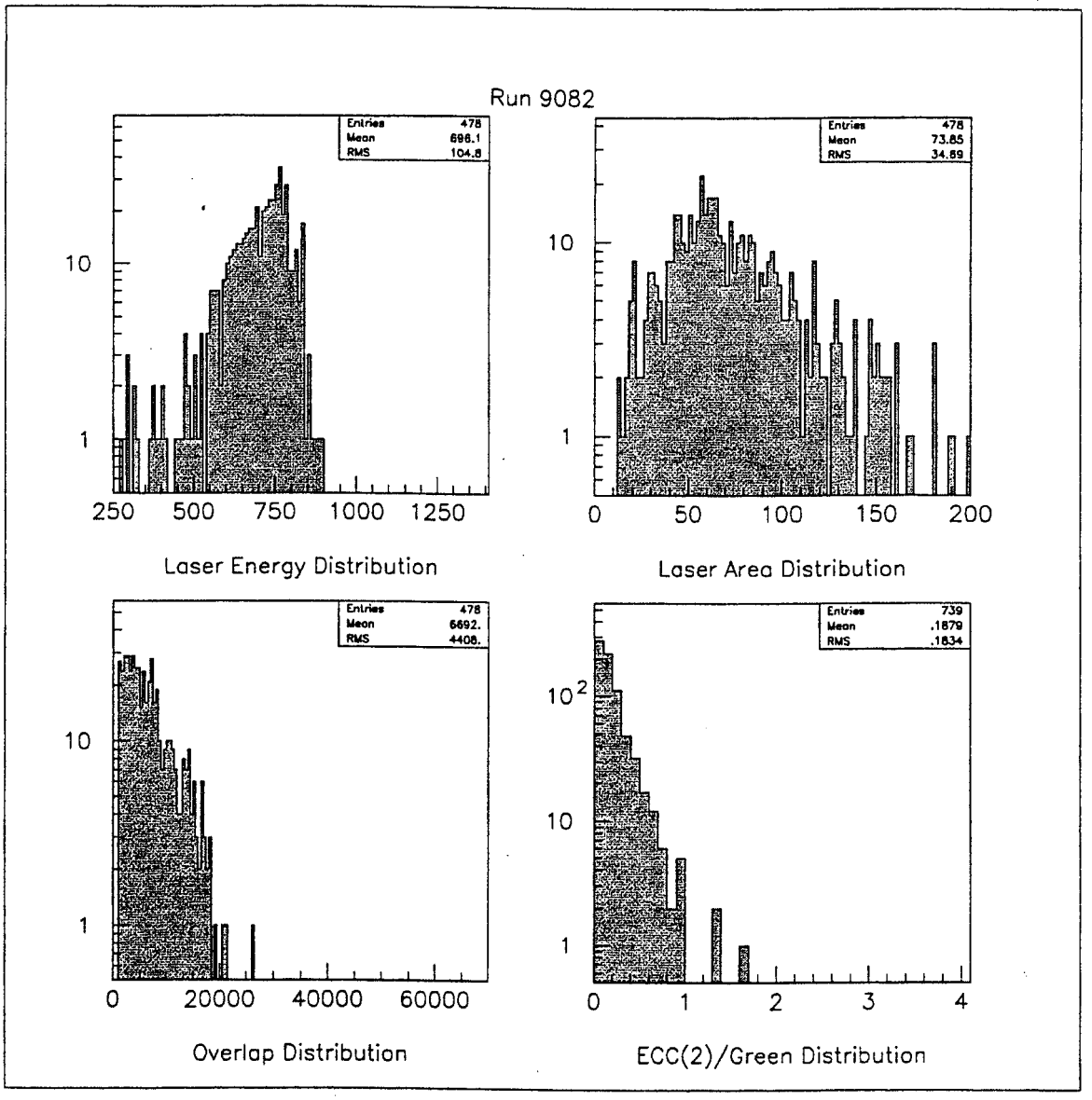

Figure 5.4: Run Data: Run 9082 Control Plot.
The distribution in the top left corner contains laser pulse energies. The top right corner contains laser spot sizes. The lower left corner contains the ratio of γ flux to laser pulse energy used in the overlap cut. The lower right corner contains the signal from another calorimeter versus laser pulse energy.

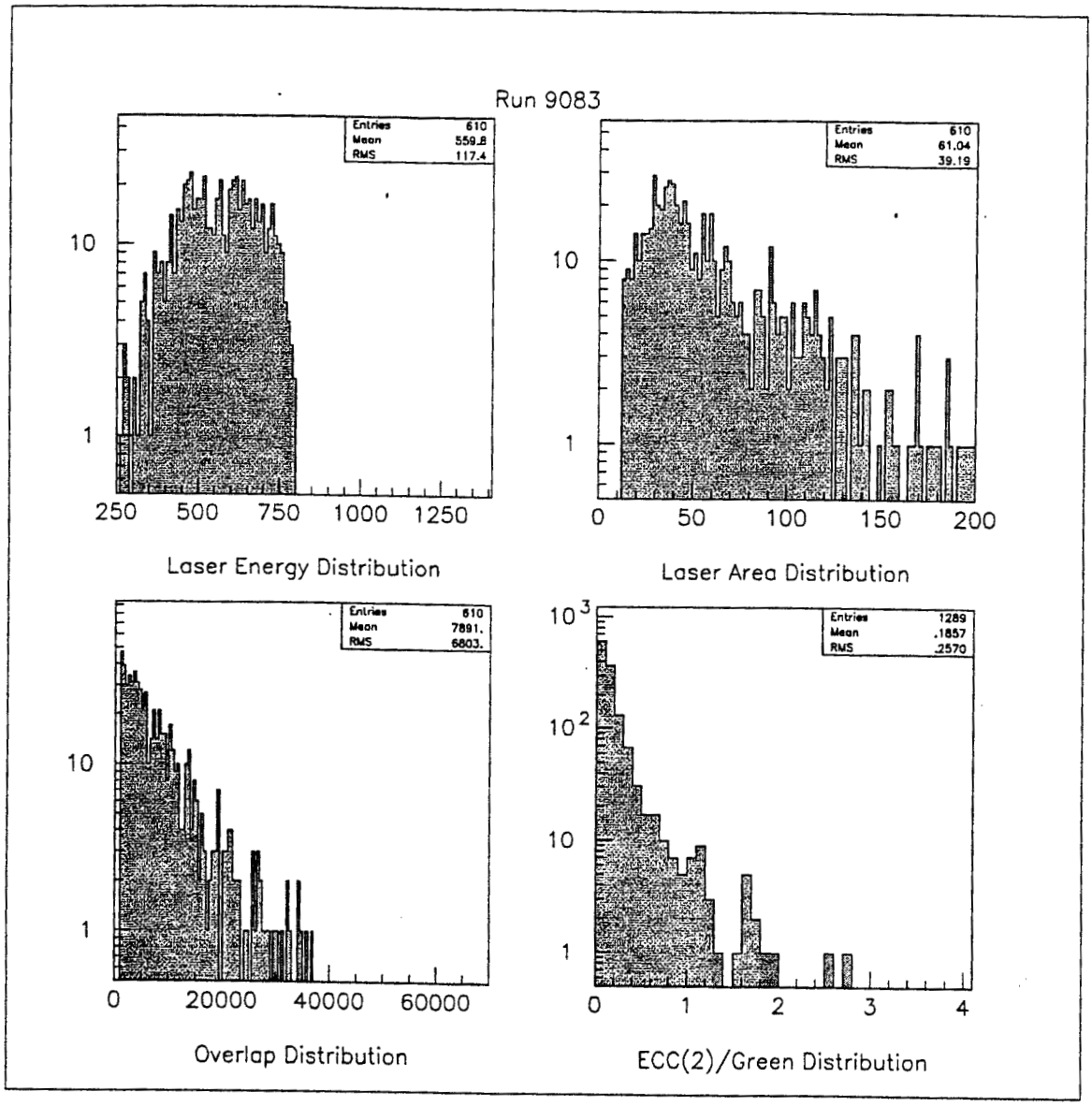

Figure 5.5: Run Data: Run 9083 Control Plot.
The distribution in the top left corner contains laser pulse energies. The top right corner contains laser spot sizes. The lower left corner contains the ratio of γ flux to laser pulse energy used in the overlap cut. The lower right corner contains the signal from another calorimeter versus laser pulse energy.

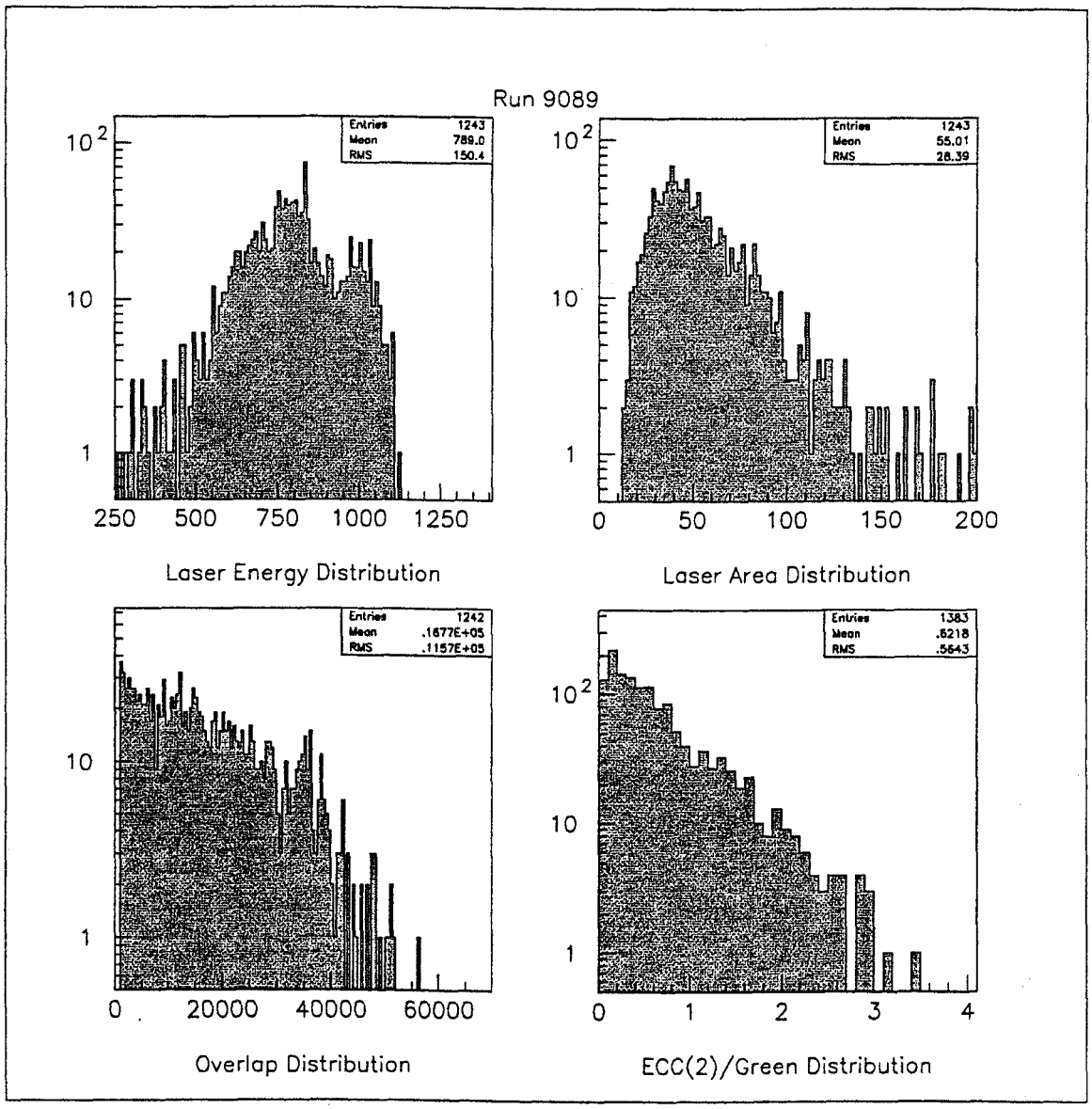

Figure 5.6: Run Data: Run 9089 Control Plot.
The distribution in the top left corner contains laser pulse energies. The top right corner contains laser spot sizes. The lower left corner contains the ratio of γ flux to laser pulse energy used in the overlap cut. The lower right corner contains the signal from another calorimeter versus laser pulse energy.

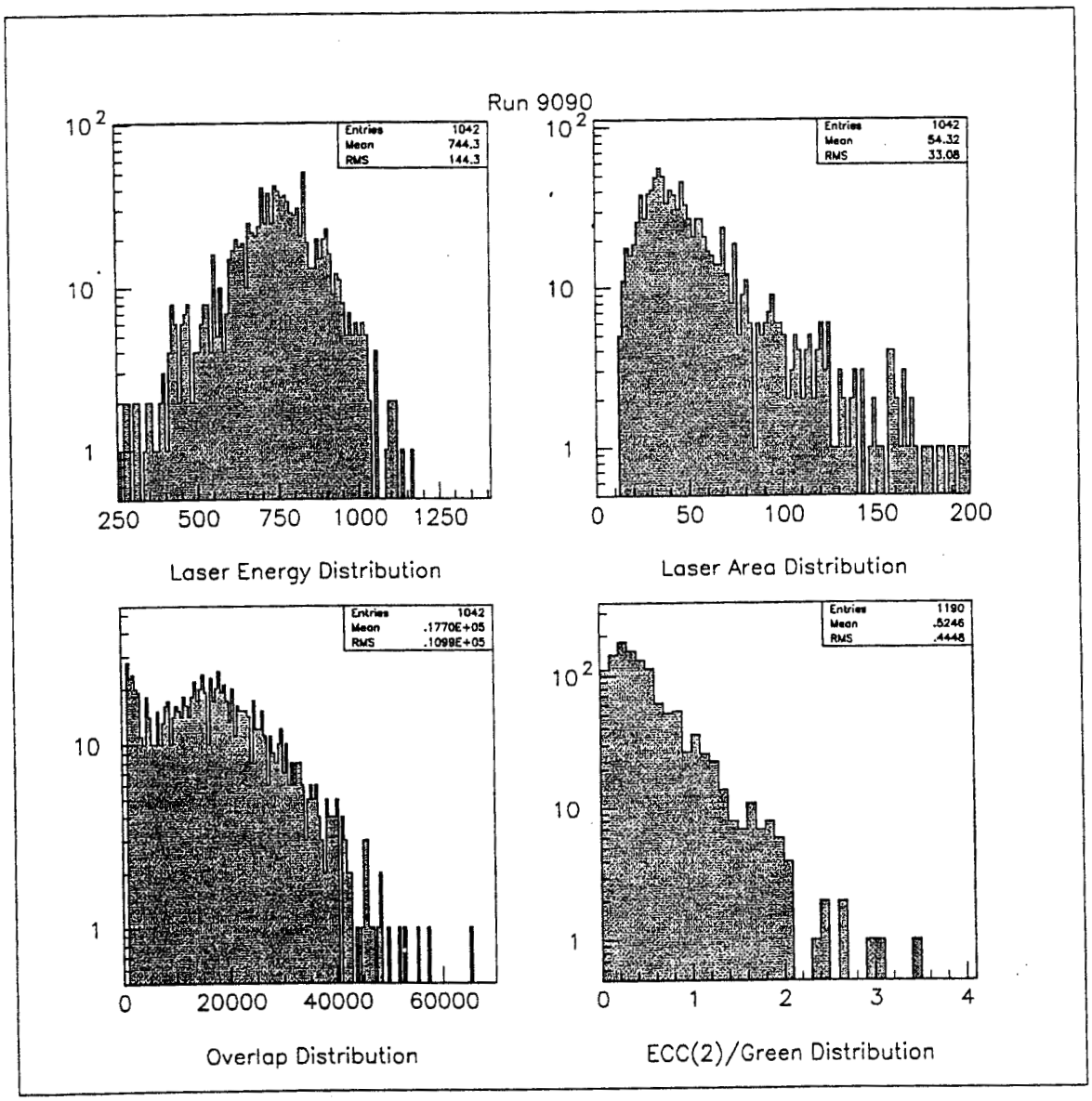

Figure 5.7: Run Data: Run 9090 Control Plot.
The distribution in the top left corner contains laser pulse energies. The top right corner contains laser spot sizes. The lower left corner contains the ratio of γ flux to laser pulse energy used in the overlap cut. The lower right corner contains the signal from another calorimeter versus laser pulse energy.

The energy corresponding to the top edge (y=156.8 mm) of the top row (a) used in PCAL was 6.0 GeV. A 6.0 GeV positron produced at IP1 with initially downstream momentum would be deflected traversing the dump magnets. It would be 156.8 mm above the beam line by the time it reached the plane containing the front surface of PCAL. It would strike the top edge of row a of PCAL. Therefore, 6.0 GeV is the lowest energy observable in the section of PCAL used for detecting Breit-Wheeler candidates.

The geometrical energy acceptance of PCAL, then, ranges from 6.0–17.9 GeV. Not all of this range is usable, however. Because a and f were edges, showers there required special consideration. During an event, if a hit occurs close to the edge of a cell, a fraction of the shower energy leaks across the cell's boundaries. For the bottom edge of row f and the top edge of row a, this fraction is lost as the shower spills out the bottom and top of the PCAL. This leads to skewed fractional and total energy readings, which corrupt the position reconstructed for the event. Automatic cuts were implemented to mitigate the effects of cell edges on data.

Events reconstructed to within 12 mm of an outer edge of PCAL were cut. This corresponded to -20 mm $< x <$ 20 mm and 71.3 mm $< y <$ 144.8 mm for the September 1994 FFTB run, reducing the energy acceptance such that it effectively ranged from 6.6–14.9 GeV.

Cuts on candidates were derived from the foil distributions shown in Chapter 4. Distributions of Δx, Δy, x, y, S0%, and S1% were formed from the Laser Off candidates. These distributions were compared to those from very clean ($\mu_0 - 0.1\sigma_0 <$ NHIT $< \mu_0 + 0.1\sigma_0$) foil data. Since the foil data "came" from IP1, cutting background to make its distributions agree more closely with those of the foil removes non-IP1 positrons. Examination of these distributions revealed cut values that significantly reduced the background rate.

The mean value of x_R for the foil data was -0.66 mm. This reflects the slight horizontal offset of PCAL. Were PCAL lowered directly into the beam path, the bunches would impact slightly to the left of the split between columns 1 and 2, the center columns. Examination of the top plot of Figure 5.11 shows mismatched distribution centers. The Laser Off (solid line) distribution center

lies to the right of the foil distribution center (dashed line). Table 5.5 shows the results of cutting around the mean of the foil plot, quantifying the background reduction effected via the x cut.

Figure 5.8 is a plot of energy versus reconstructed vertical deflection y_R for the laser on and laser off events of the runs listed in Table 5.1 (The 9000s). The entries in the Laser Off plot are, of course, all backgrounds. They are concentrated around a curve that is above EMAP(y). Another way of seeing this is by examining Figure 5.9. The center of the

$$\text{NHIT} \equiv \frac{\text{ECL}}{\text{EMAP}(y_R)} \tag{5.1}$$

distribution for the foil data lies at $\mu_0 = 1.024$. Cutting the Laser On events around EMAP(y), I eliminated a large fraction of the off-momentum e^+s. The $\mu(y)/\sigma(y)$ approach discussed in Section 4.6 added complexity without reducing the background level further than the more general μ_0/σ_0 technique. It was abandoned.

Two cases are set forth in Table 5.2. In one, a symmetric cut about μ_0EMAP(y) was selected. In the other, the upper and lower bounds were lowered. Setting the cut boundaries such that

$$\mu_0 - 2\sigma < \text{NHIT} < \mu_0 + \sigma/2, \tag{5.2}$$

or

$$0.742 < \text{NHIT} < 1.095 \tag{5.3}$$

was intended to cut an even higher fraction of the off-momentum positrons. In lowering the upper bound, however, too much of the "signal" region was cut. The ideal NHIT cut, of many tested, was

$$\mu_0 + \sigma < \text{NHIT} < \mu_0 + \sigma, \tag{5.4}$$

or

$$0.883 < \text{NHIT} < 1.165. \tag{5.5}$$

NHIT		Rows d–f		Rows a–c	
$NHIT_{Low}$	$NHIT_{High}$	Laser Off Candidates	Laser On Candidates	Laser Off Candidates	Laser On Candidates
0.742	1.095	17(3.7)	9	28(6.0)	12
0.883	1.165	20(4.3)	13	23(5.0)	4

Table 5.2: Cut Results: NHIT
The mean μ_0 of NHIT was 1.024. The σ_0 of NHIT was 0.141. The top row contains the results of the cut defined in Equation 5.2. The bottom row contains the results of the cut defined in Equation 5.4. In the Laser Off columns, the value in parentheses is the number of candidates observed in the Laser Off events divided by the Trigger Ratio.

The mean value of Δy for foil data was -1.64 mm. This reflects the rising trajectories of IP1 positrons that traversed the dump magnets, since

$$\Delta y \equiv y_R^{S0} - y_R^{S1}, \tag{5.6}$$

where y_R^{Sn} is the reconstructed y position for segment n. Segment 0 is the front segment so if $y_R^{S0} < y_R^{S1}$, the positron is climbing as expected. As seen in Table 5.3, the cut on Δy eliminated equivalent fractions of the Laser On and Laser Off distributions. A three rms cut was left in place to eliminate greatly deviant candidates, but no tight Δy cut was used.

The mean value of Δx for foil data was -0.02 mm. This reflects the lack of an x component in the trajectories of IP1 positrons that traversed the dump magnets, since

$$\Delta x \equiv x_R^{S0} - x_R^{S1}, \tag{5.7}$$

where x_R^{Sn} is the reconstructed x position for segment n. Segment) is the front segment so if $x_R^{S0} = x_R^{S1}$, the positron has not x motion as expected. As seen in Table 5.4, the cut on Δx eliminated equivalent fractions of the Laser On and Laser Off distributions. A three rms cut was left in place to eliminate greatly deviant candidates, but no tight Δx cut was used.

The y distribution of the foil positrons could not be used to develop a cut. The energy dependence of the rate for the processes generating positrons in the

foil has a roughly $1/k$ dependence, where k denotes the momentum of the outgoing positron. The energy dependence of the rate for multiphoton Breit-Wheeler pair production does not go as $1/k$. Since the y distribution is essentially a transform of dN/dk, the y distribution for the foil cannot be used as a cut to improve the y distribution for the Laser On candidates. In the top plot of Figure 5.10, the solid line indicates Laser Off candidates and the dashed line represents the foil candidates. In the bottom plot of Figure 5.10, the solid line indicates Laser On candidates and the dashed line represents the foil candidates. The y distribution of the foil candidates is fairly flat. The Laser On and Laser Off distributions have the most candidates in the high energy (small y_R) region. I stated that dN/dk for the foil positrons should go roughly as $1/k$. This dependence is verified in Appendix A.

The segments of PCAL were configured so that approximately equal amounts of the longitudinal shower would be deposited in each segment. The shower percentages

$$\text{S0\%} \equiv \frac{ECLS0}{ECL}, \text{ and S1\%} \equiv \frac{ECLS1}{ECL} \tag{5.8}$$

are measures of this sharing. Here ECLS0 is the cluster energy from the front segment and ECL is the cluster energy summed over both segments, as defined in Section 4.4. The mean of the S0% distribution for foil was 0.66. The rms of the S0% distribution for foil was 0.11. The mean of the S1% distribution for foil was 0.35. The rms of the S0% distribution for foil was 0.12. As seen in Tables 5.6 and 5.7, the cuts on S0% and S1% eliminated equivalent fractions of the Laser On and Laser Off distributions. So neither an S0% nor an S1% cut was used.

The cuts,

$$71.3 \text{ mm} < y_R < 144.8 \text{ mm},$$

$$-5.1 \text{ mm} < x_R < 3.8 \text{ mm (1 rms)},$$

$$0.883 < \text{NHIT} < 1.165 \ (1\,\sigma),$$

$$-9.2 \text{ mm} < \Delta x < 9.2 \text{ mm (3 rms), and}$$

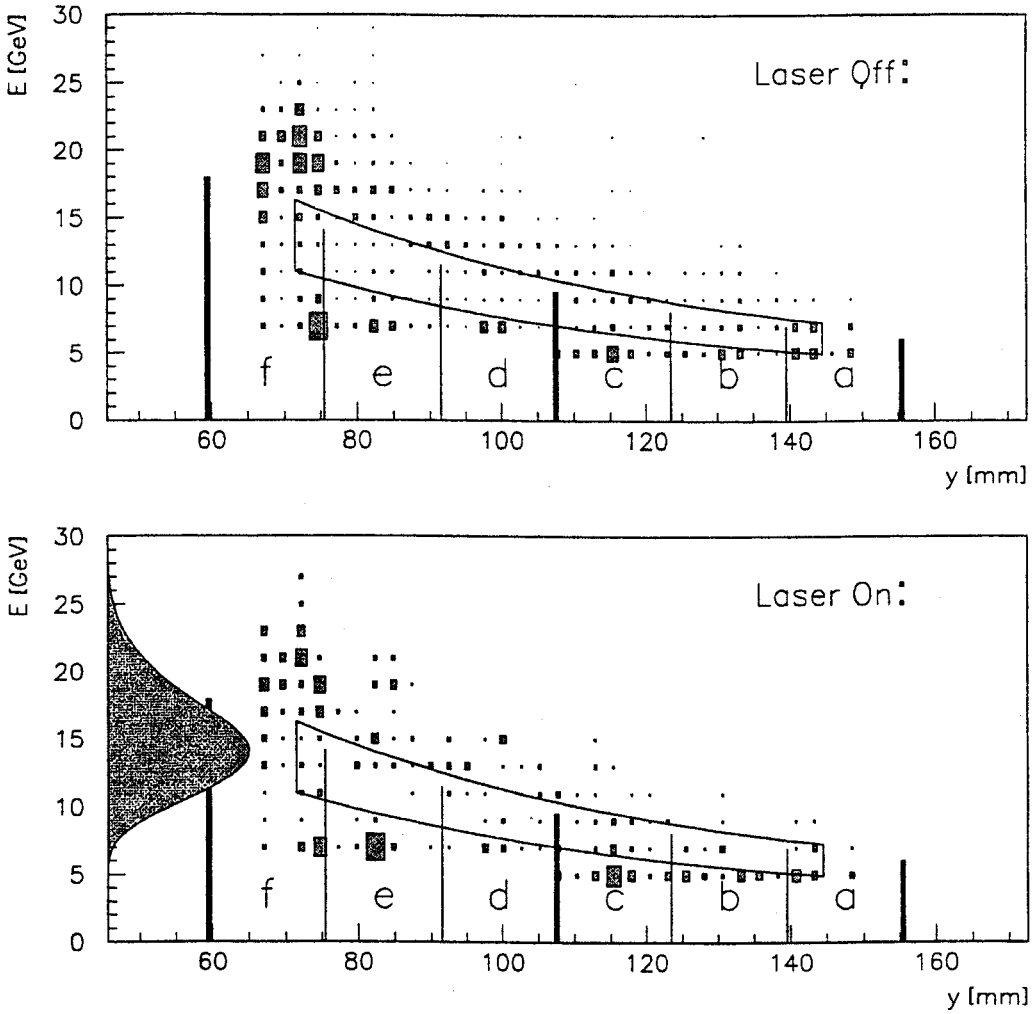

Figure 5.8: Cluster energy versus reconstructed vertical deflection, y_R for 71.3 mm$< y <$ 144.8 mm. The line in the top plot represents the mean from Figure 4.17 times the map energy. The band in the bottom plot represents the region bounded by EMAP$(y) \times \mu \pm \sigma$ =EMAP$\times(1.024) \pm (0.141)$, taken from Figure 4.17

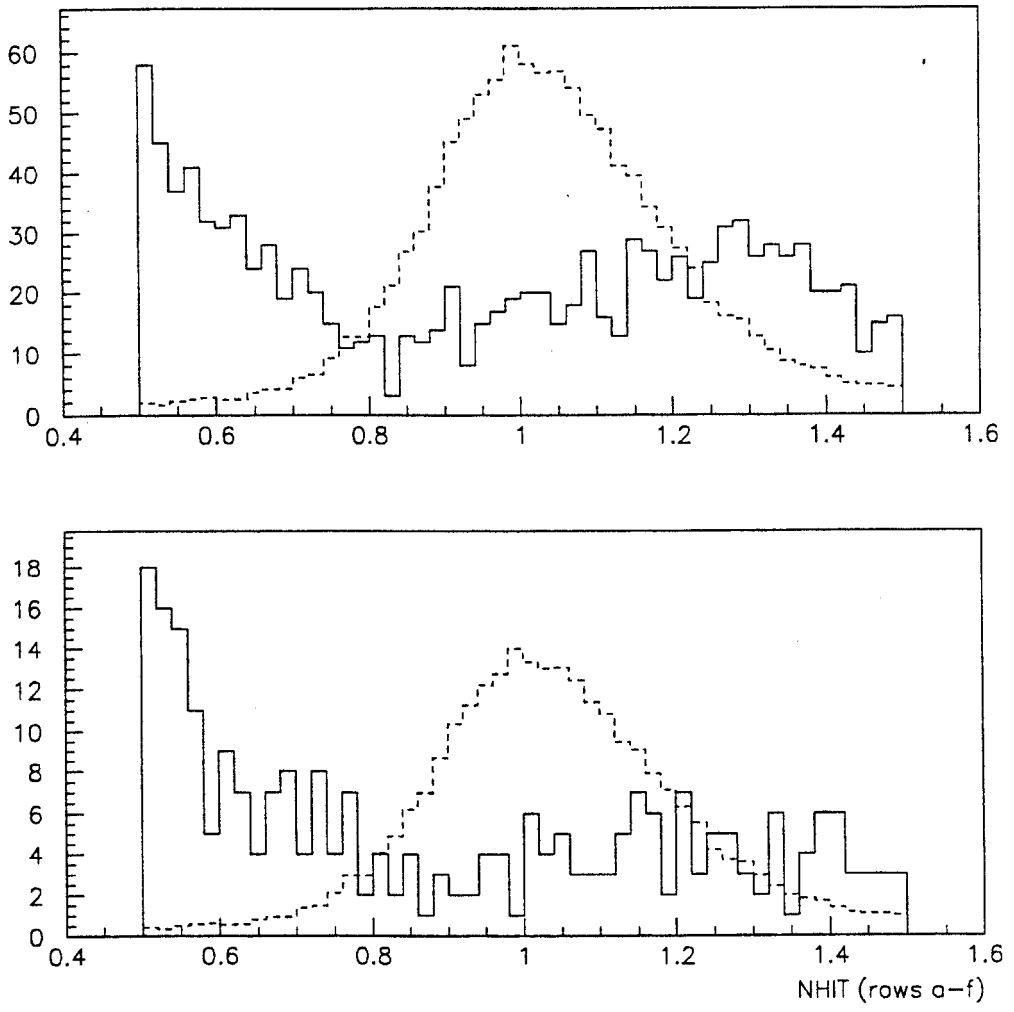

Figure 5.9: The distribution of nhit.
The dashed line in both plots represents the distribution for foil positrons. The solid line represent the distributions for Laser Off and Laser On positrons in the top and bottom plot respectively.

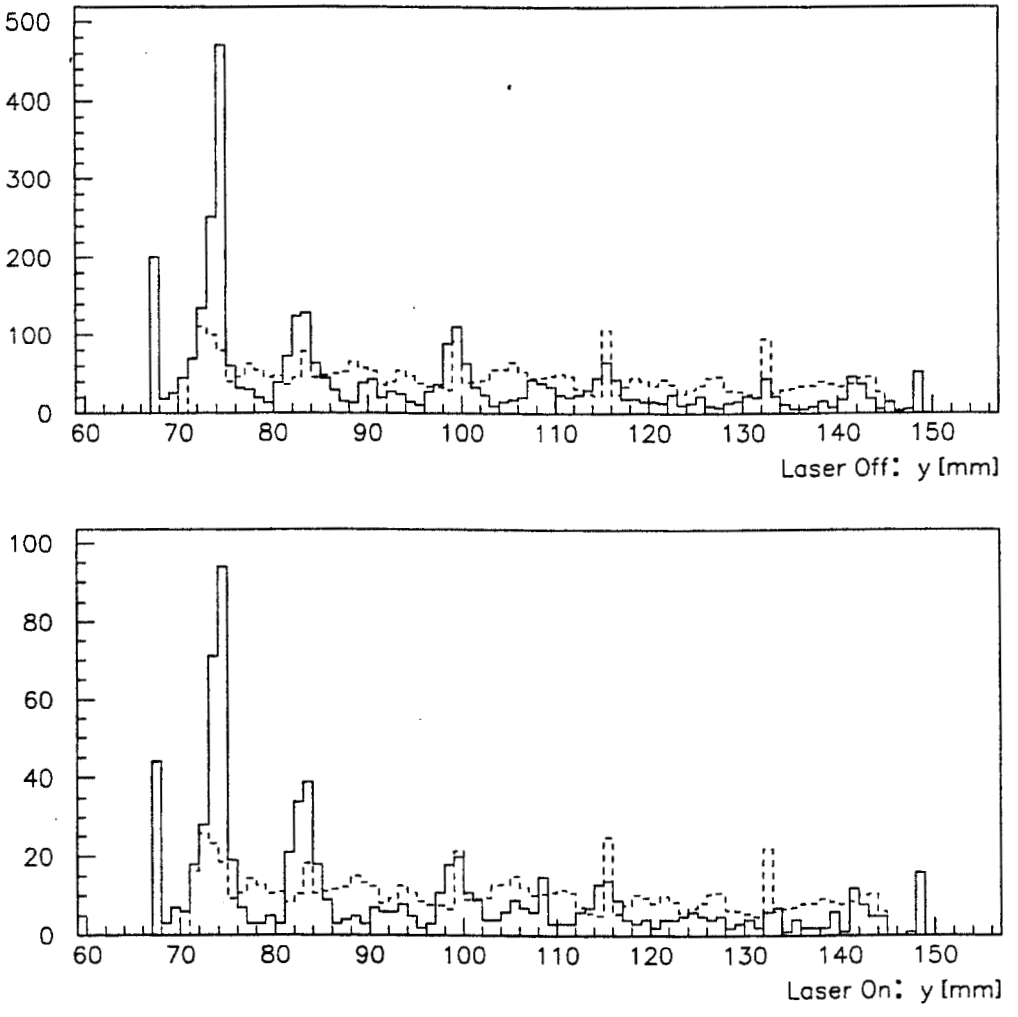

Figure 5.10: The distribution of y.
The dashed line in both plots represents the distribution for foil positrons. The solid line represent the distributions for Laser Off and Laser On positrons in the top and bottom plot respectively.

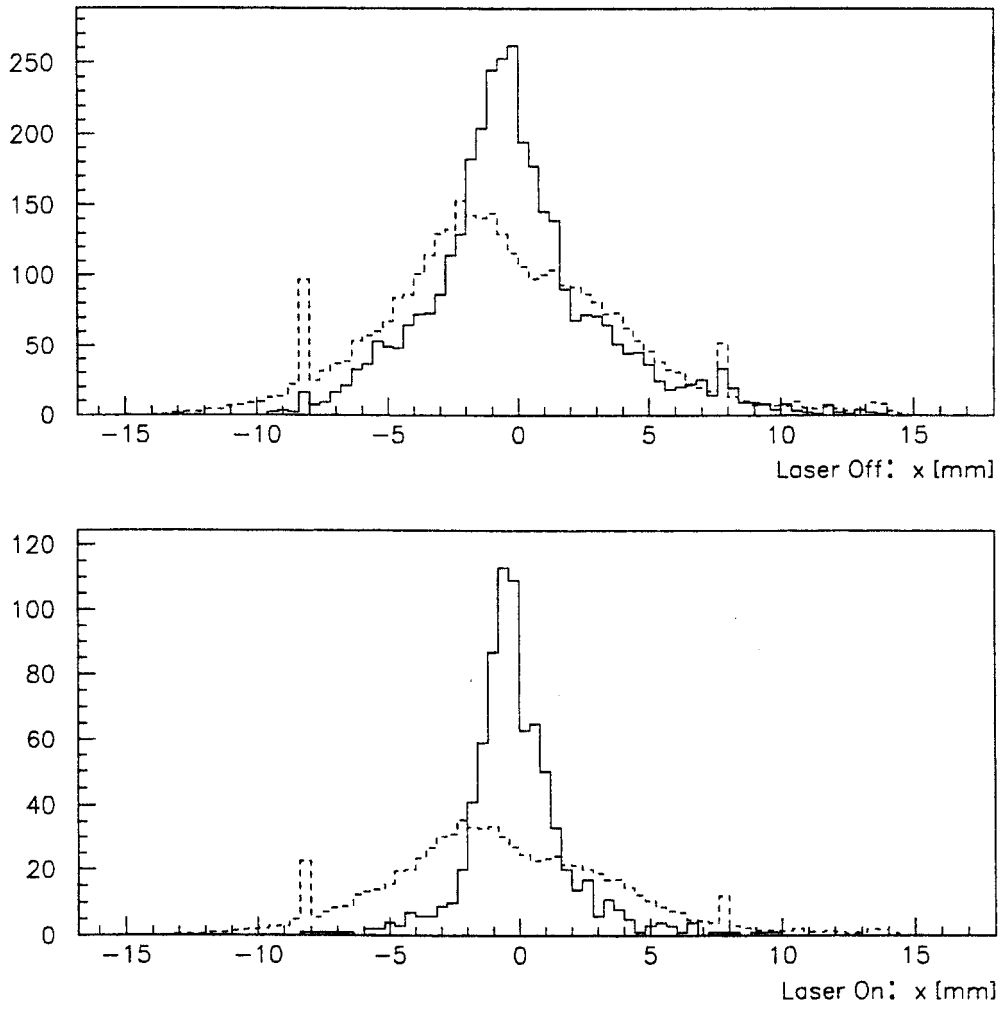

Figure 5.11: The distribution of x.
The dashed line in both plots represents the distribution for foil positrons. The solid line represent the distributions for Laser Off and Laser On positrons in the top and bottom plot respectively.

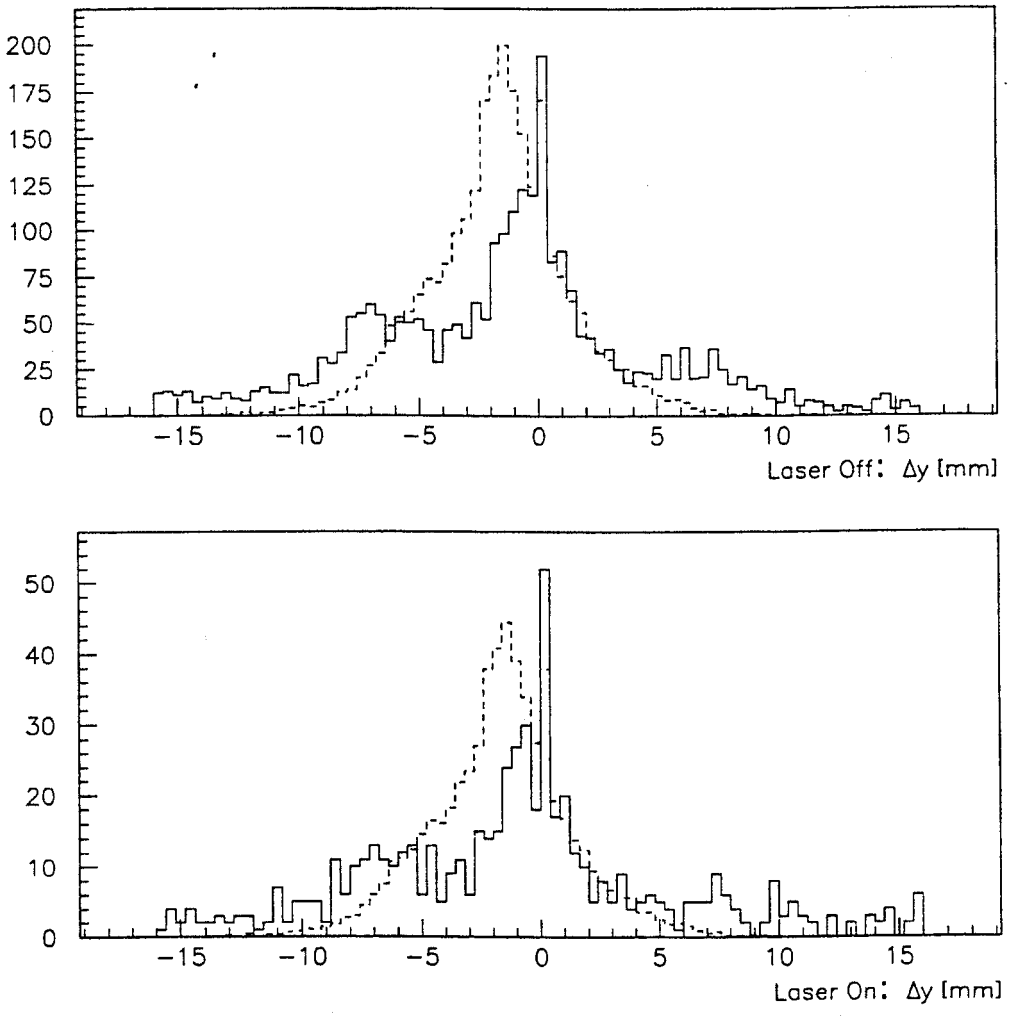

Figure 5.12: The distribution of Δy.
The dashed line in both plots represents the distribution for foil positrons. The solid line represent the distributions for Laser Off and Laser On positrons in the top and bottom plot respectively.

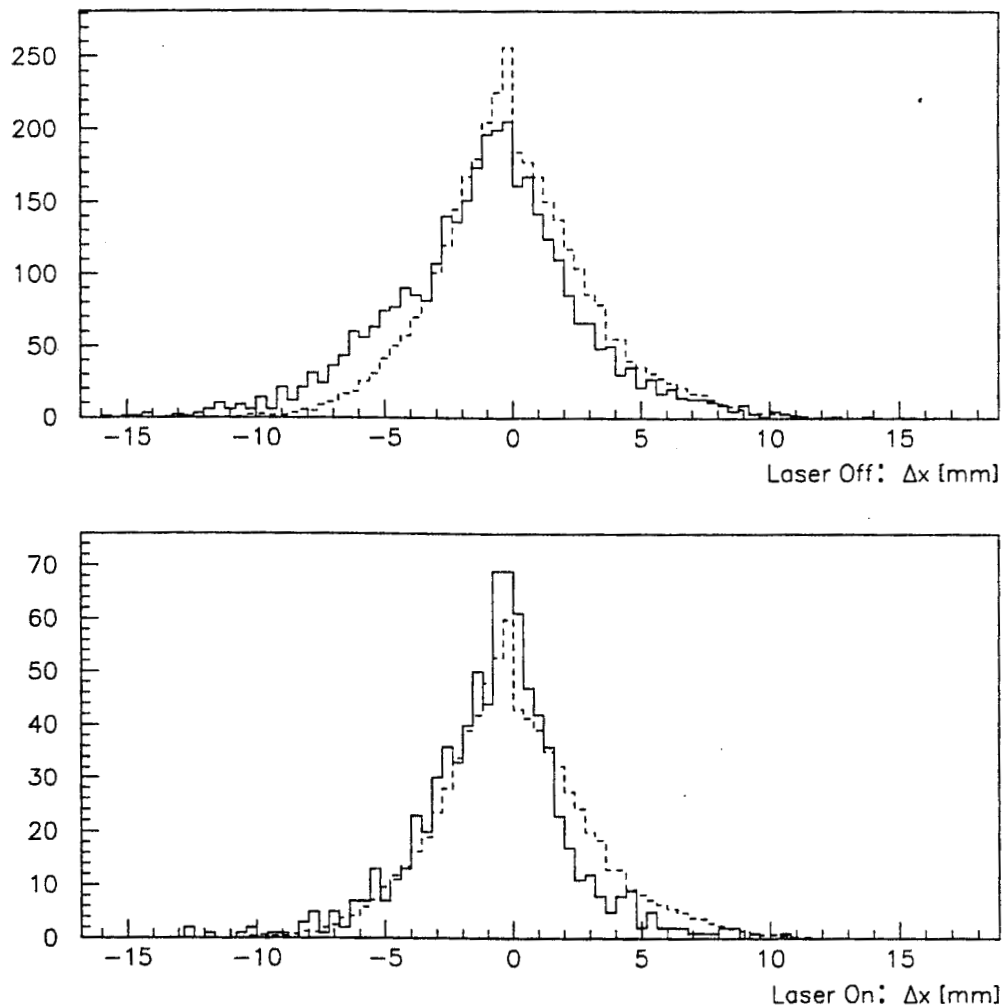

Figure 5.13: The distribution of Δx.
The dashed line in both plots represents the distribution for foil positrons. The solid line represent the distributions for Laser Off and Laser On positrons in the top and bottom plot respectively.

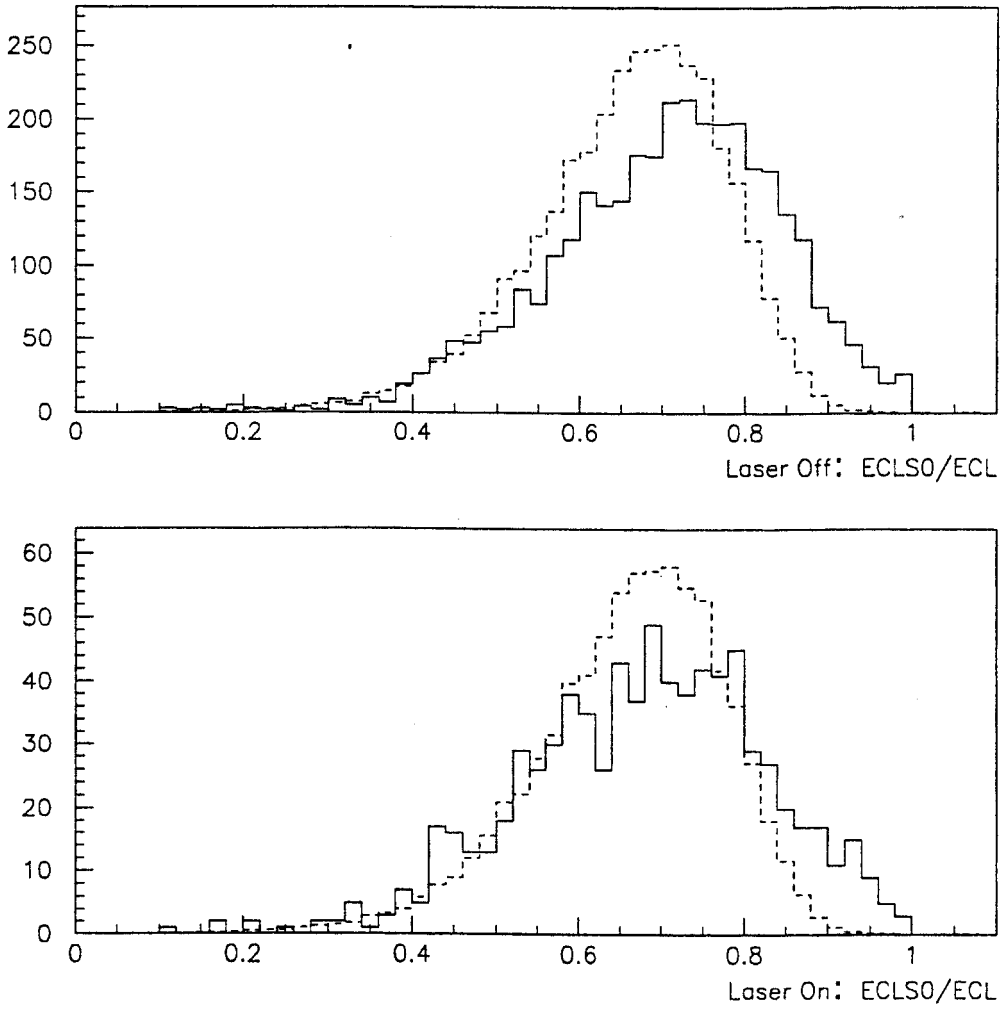

Figure 5.14: e^- / ω_0 Collision Data: The distribution of S0%.
The dashed line in both plots represents the distribution for foil positrons. The solid line represent the distributions for Laser Off and Laser On positrons in the top and bottom plot respectively.

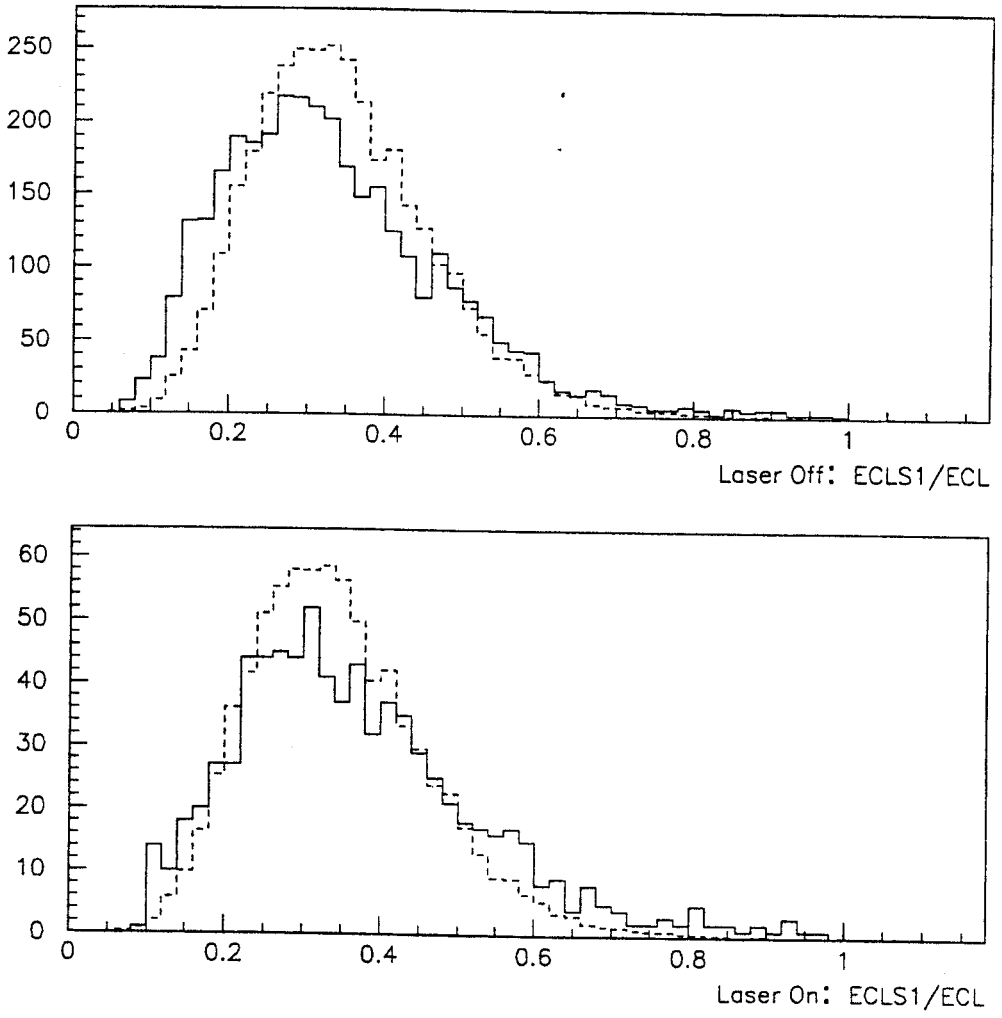

Figure 5.15: e^- / ω_0 Collision Data: The distribution of S1%.
The dashed line in both plots represents the distribution for foil positrons. The solid line represent the distributions for Laser Off and Laser On positrons in the top and bottom plot respectively.

Δy		Rows d–f		Rows a–c	
Δy_{Low} [mm]	Δy_{High} [mm]	Laser Off Candidates	Laser On Candidates	Laser Off Candidates	Laser On Candidates
−10.5	7.2	59(13)	23	60(13)	8
−7.6	4.3	54(12)	21	52(11)	7
−4.6	1.3	39(8)	12	35(8)	5

Table 5.3: Cut Results: Δy.
The mean of the foil distribution of Δy was -1.64 mm, the rms was 2.95 mm. The boundaries in the first row are for the mean plus or minus three times the rms. The boundaries in the second row are for the mean plus or minus two times the rms. The boundaries in the third row are for the mean plus or minus one times the rms. In the Laser Off columns, the value in parentheses is the number of candidates observed in the Laser Off events divided by the Trigger Ratio.

Δx		Rows d–f		Rows a–c	
Δx_{Low} [mm]	Δx_{High} [mm]	Laser Off Candidates	Laser On Candidates	Laser Off Candidates	Laser On Candidates
−9.2	9.2	62(13)	25	62(13)	9
−6.1	6.1	57(12)	23	58(13)	9
−3.1	3.0	41(9)	16	41(9)	4

Table 5.4: Cut Results: Δx.
The mean of the foil distribution of Δx was -0.02 mm, the rms was 3.06 mm. The boundaries in the first row are for the mean plus or minus three times the rms. The boundaries in the second row are for the mean plus or minus two times the rms. The boundaries in the third row are for the mean plus or minus one times the rms. In the Laser Off columns, the value in parentheses is the number of candidates observed in the Laser Off events divided by the Trigger Ratio.

x		Rows d–f		Rows a–c	
x_{Low} [mm]	x_{High} [mm]	Laser Off Candidates	Laser On Candidates	Laser Off Candidates	Laser On Candidates
−14.1	12.8	60(13)	25	62(13)	9
−9.6	8.3	42(9)	21	57(12)	9
−5.1	3.8	20(4)	13	27(6)	4

Table 5.5: Cut Results: x.
The mean of the foil distribution of x was -0.66 mm, the rms was 4.47 mm. The boundaries in the first row are for the mean plus or minus three times the rms. The boundaries in the second row are for the mean plus or minus two times the rms. The boundaries in the third row are for the mean plus or minus one times the rms. In the Laser Off columns, the value in parentheses is the number of candidates observed in the Laser Off events divided by the Trigger Ratio. In the Laser Off columns, the value in parentheses is the number of candidates observed in the Laser Off events divided by the Trigger Ratio.

S0%		Rows d–f		Rows a–c	
$S0\%_{Low}$	$S0\%_{High}$	Laser Off Candidates	Laser On Candidates	Laser Off Candidates	Laser On Candidates
0.32	1.00	61(13)	24	66(14)	8
0.43	0.89	59(13)	23	57(12)	7
0.55	0.77	45(10)	14	30(7)	6

Table 5.6: Cut Results: S0%≡ECLS0/ECL.
The mean of the foil distribution of S0%≡ECLS0/ECL was 0.660, the rms was 0.115. The boundaries in the first row are for the mean plus or minus three times the rms. The boundaries in the second row are for the mean plus or minus two times the rms. The boundaries in the third row are for the mean plus or minus one times the rms. In the Laser Off columns, the value in parentheses is the number of candidates observed in the Laser Off events divided by the Trigger Ratio.

S1%		Rows d–f		Rows a–c	
$S1\%_{Low}$	$S1\%_{High}$	Laser Off Candidates	Laser On Candidates	Laser Off Candidates	Laser On Candidates
0.00	0.69	61(13)	24	66(14)	8
0.12	0.57	58(13)	23	57(12)	7
0.23	0.46	44(10)	15	30(7)	6

Table 5.7: Cut Results: S1%≡ECLS1/ECL.
The mean of the foil distribution of S1%≡ECLS1/ECL was 0.346, the rms was 0.115. The boundaries in the first row are for the mean plus or minus three times the rms. The boundaries in the second row are for the mean plus or minus two times the rms. The boundaries in the third row are for the mean plus or minus one times the rms. In the Laser Off columns, the value in parentheses is the number of candidates observed in the Laser Off events divided by the Trigger Ratio.

$$-10.5 \text{ mm } < \Delta y < 7.2 \text{ mm (3 rms)},$$

were used. Applied to Runs 9077–9083, these cuts revealed 13 Laser On candidates in 3842 triggers when 20 Laser Off candidates in 17866 triggers indicated a background signal of ~ 4 positrons. When Runs 9089 and 9090 were included in the same, the same cuts cuts revealed 17 Laser On candidates in 6415 triggers when 50 Laser Off candidates in 29682 triggers indicate a background signal of ~ 11 in Runs 9077–9090. The results on a run-by-run basis are given in Table 5.8.

5.3 dN/dE of Positrons: Experiment and Theory

5.3.1 Relative Rate

The number of positrons in the "Laser On" samples is larger than the numbers in the normalized "Laser Off" samples. Consider the set of Runs 9077–9083. After cuts, there were 13 positrons found in the collection of 3842 E1L1 triggers that passed the overlap cut. There were 20 positrons found in the collection of 17866 E1L0 triggers. These positrons were backgrounds. In the 3842 E1L1 triggers, we expect to have seen 20*3842/17866~4 positrons due to background. We saw 9 positrons above this level.

Run	Trigger	Rows d–f		Rows a–c	
Number	Ratio	L0	L1	L0	L1
9077	5.26	4(1)	1	1(1)	1
9079	4.73	4(1)	3	6(1)	0
9081	4.67	4(1)	1	4(1)	0
9082	3.97	3(1)	2	6(2)	3
9083	4.74	5(1)	6	6(1)	0
9089	4.24	14(3)	2	13(3)	3
9090	5.00	16(3)	2	15(3)	2
Totals:					
'77–'83	4.65	20(4.3)	13	23(4.9)	4
'89–'90	4.59	30(6.5)	4	28(6.1)	5
'77–'90	4.63	50(10.8)	17	51(11.0)	9

Table 5.8: Cut Results: Individual Runs
In the Laser Off columns, the value in parentheses is the number of candidates observed in the Laser Off events divided by the Trigger Ratio.

5.4 Statistical Significance

The statistical significance of this observation can be found by treating these measurements as Poisson processes.[67] We saw 20 background events in 17866 Laser Off triggers. This corresponds to

$$X' = 20 * 3842/17866 \sim 20/4.65 \sim 4.3, \tag{5.9}$$

background events in 3842 Laser On triggers. We saw 13 events in 3842 Laser On triggers. The likelihood that a background level X fluctuated to produce n observed positrons is given by a Poisson distribution

$$p(n;X) = \frac{X^n \exp(-X)}{n!}. \tag{5.10}$$

The probability the X will fluctuate to produce n_0 or more positrons is given by

$$p(n \geq n_0; X) = \sum_{n=n_0}^{\infty} \frac{\exp(-X)X^n}{n!} = \left(1 - \sum_{n=0}^{n_0-1} \frac{\exp(-X)X^n}{n!}\right). \tag{5.11}$$

In Runs 9079–9083, I found 13 Laser On events and 20 Laser Off positrons. Approximating X with $X' = 4.3$, Equation 5.11 yields $p(n \geq 13; X') = 5.4 \times 10^{-4}$. In Runs 9079–9090, I found 17 Laser On events and 50 Laser Off positrons. Approximating X with

$$X' = 50 * 6415/29682 \sim 50/4.63 \sim 10.8, \tag{5.12}$$

Equation 5.11 yields $p(n \geq 17; X') = 4.9 \times 10^{-2}$.

Now $X' \rightarrow X$ only as the number of E1L0 triggers goes to infinity. In that regard, using X' in Equation 5.11 is not strictly correct. I selected X' differently, thereby deriving a much more correct likelihood estimate. X' was selected by maximizing the joint probability distribution that represents the sequence of events where exactly m events occur in one measurement and n or more occur in the next. The parameter α is the Trigger Ratio, introduced to ensure that proper weight was given to the observed background.

$$\begin{aligned} p(n|m \geq m_0) &= \frac{\exp(-\alpha X)(\alpha X)^n}{n!} \sum_{i=m_0}^{\infty} \frac{\exp(-X)X^i}{i!} \\ &= \frac{\exp(-\alpha X)(\alpha X)^n}{n!} \left(1 - \sum_{i=0}^{m_0-1} \frac{\exp(-X)X^i}{i!}\right) \end{aligned} \tag{5.13}$$

Equation 5.13 was maximized by numerically calculating the root of

$$\frac{d}{dX}\left(\frac{\exp(-\alpha X)(\alpha X)^n}{n!}\left(1 - \sum_{i=0}^{m_0-1} \frac{\exp(-X)X^i}{i!}\right)\right) = 0 \tag{5.14}$$

For Runs 9079–9083, $p(20|n \geq 13; X', \alpha \sim 4.65)_{\max} = 2.3 \times 10^{-4}$ occurred for $X' \sim 6.0$. The measured signal excess for Runs 9077–9083 was at least, 13-6=7. For Runs 9079–9090, $p(50|n \geq 17; X', \alpha \sim 4.63)_{\max} = 4.3 \times 10^{-3}$ occurred for $X' \sim 12$. The measured signal excess for Runs 9077–9090 was at least 17-12=5. Figures 5.16 and 5.17 are plots of Equations 5.13 and 5.14 for the 9077–9083 and 9077–9090 cases respectively.

5.5 dN/dE: Observed and Theoretical

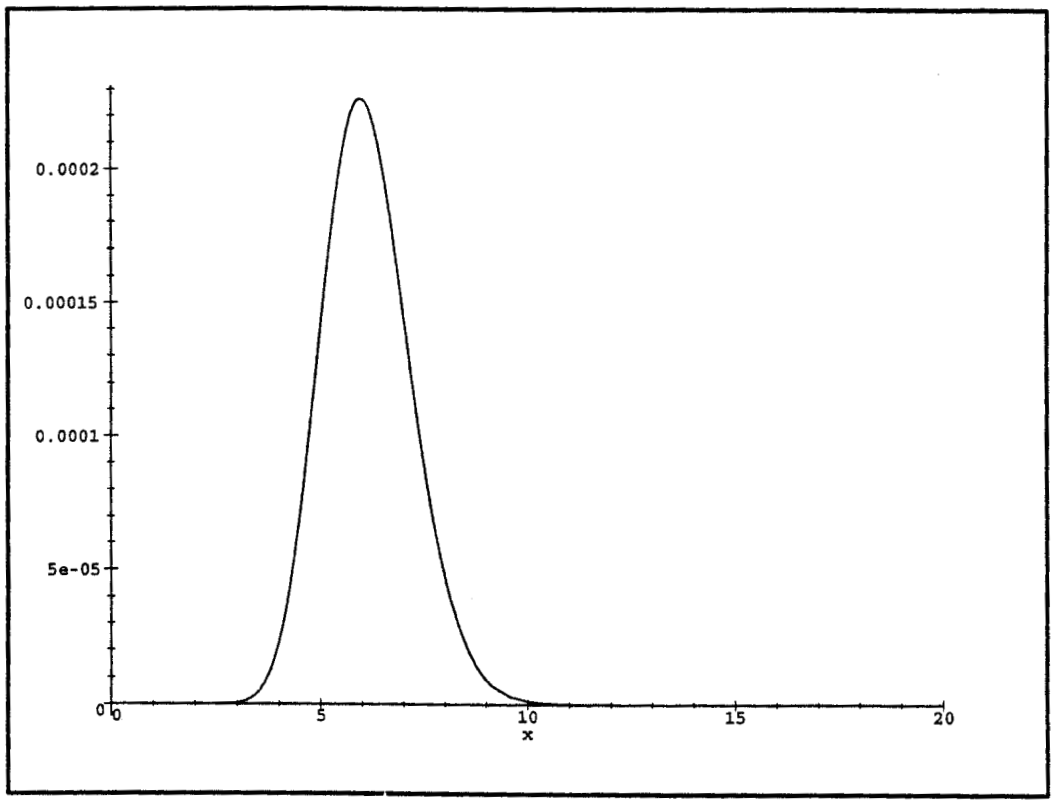

Figure 5.16: Joint Probability Density Function $P(m' = 20|n \geq 13; X)$.
A plot of the function $P(m' = 20|n \geq 13; X)$ as a function of X. This represents the case where 13 positrons were detected in 3842 Laser On events and 20 positrons were detected in 17866 Laser Off events. The function maximum occurs at $X \sim 6.0$.

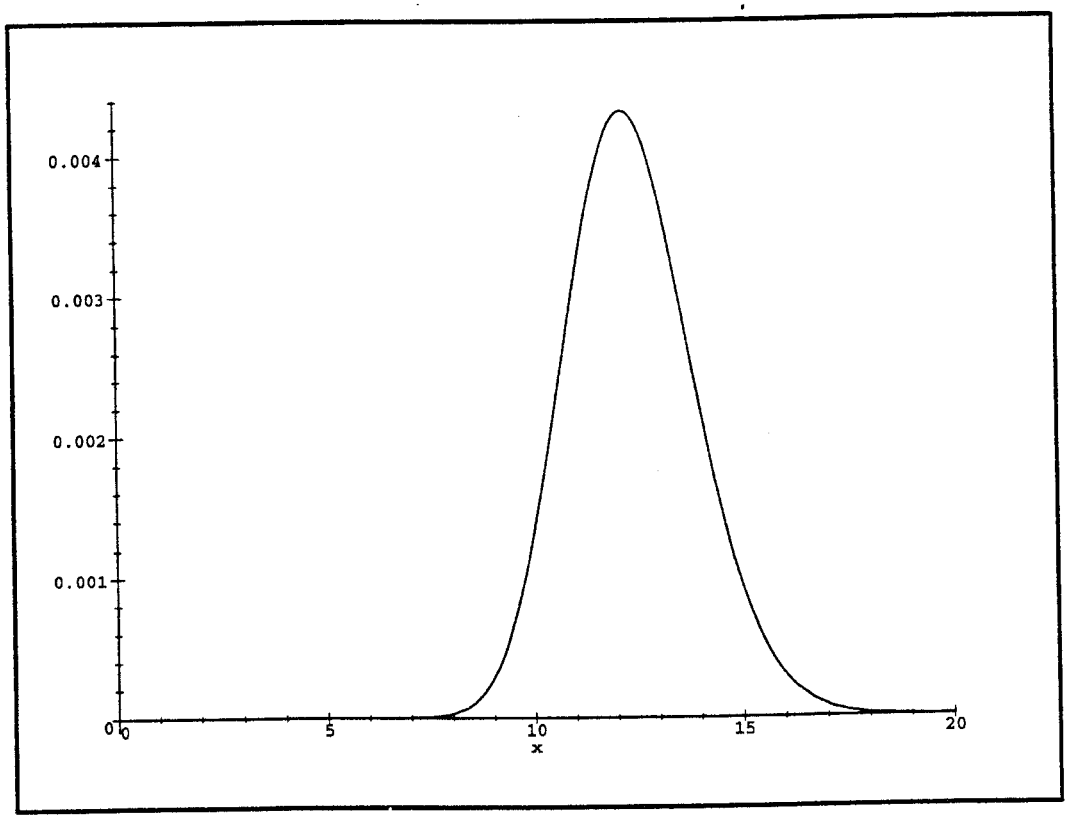

Figure 5.17: Joint Probability Density Function $P(m' = 50|n \geq 17; X)$.
A plot of the function $P(m' = 50|n \geq 17; X)$ as a function of X. This represents the case where 17 positrons were detected in 6415 Laser On events and 50 positrons were detected in 29682 Laser Off events. The function maximum occurs at $X \sim 12$.

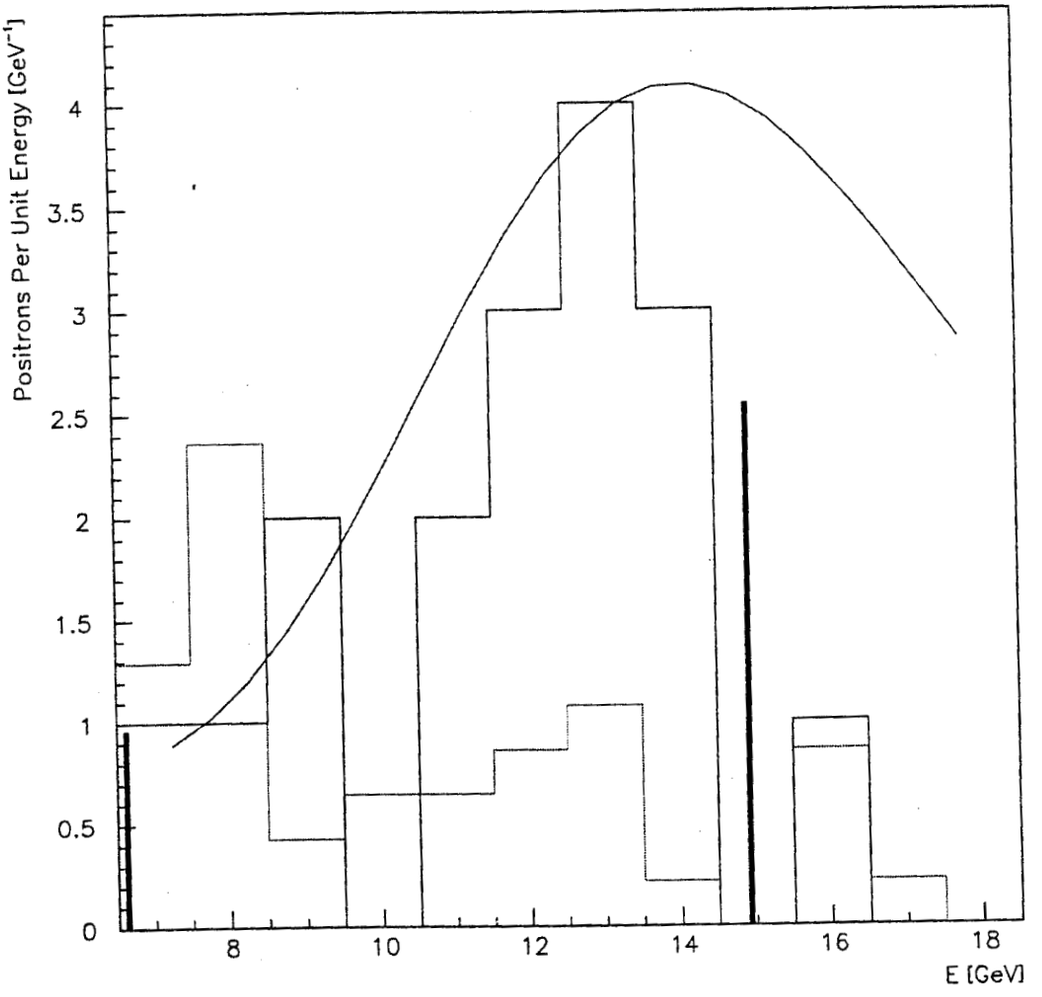

Figure 5.18: dN_e/dE_e: Runs 9077–9083.
This figure shows the energy spectrum of the positrons detected in Runs 9077–9083. The solid-bordered histogram represents the Laser On positrons. The dashed-bordered histogram represents the Laser Off positrons, scaled to the same number of triggers as the Laser On positrons. The curve represents the shape of the spectrum calculated by the event simulation program. The thick vertical lines represent the energy boundaries imposed by the 71.3 mm $< y_R <$ 144.8 mm constraint.

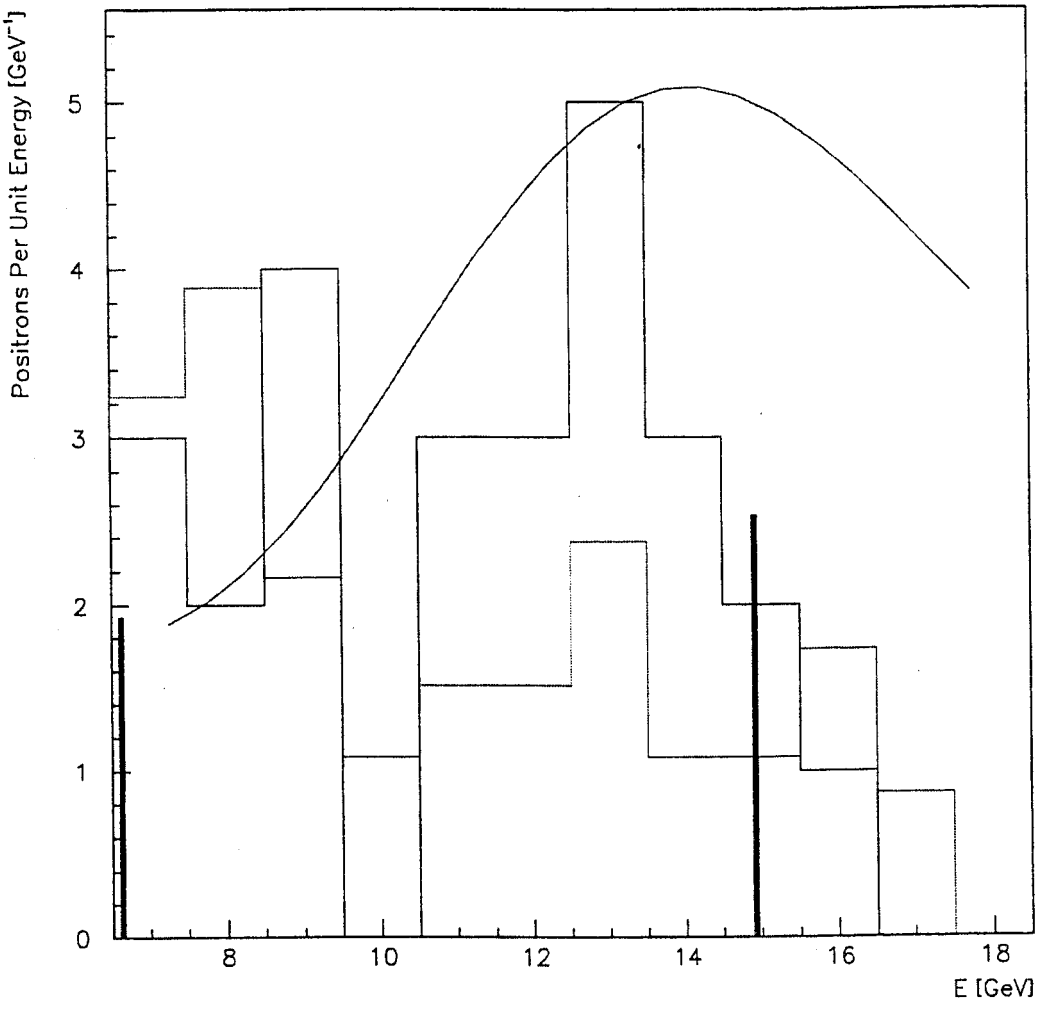

Figure 5.19: dN_e/dE_e: Runs 9077–9090.
This figure shows the energy spectrum of the positrons detected in Runs 9077–9090. The solid-bordered histogram represents the Laser On positrons. The dashed-bordered histogram represents the Laser Off positrons, scaled to the same number of triggers as the Laser On positrons. The curve represents the shape of the spectrum calculated by the event simulation program.The thick vertical lines represent the energy boundaries imposed by the 71.3 mm $< y_R <$ 144.8 mm constraint.

5.5.1 Absolute Rate

The absolute rate can be estimated in the following fashion. The multiphoton Breit-Wheeler cross section is highly nonlinear with respect to laser intensity. So it would be wrong to calculate the rate for a single set of laser parameters and assume it represents the average rate for the entire ensemble. Ideally one would calculate the rate for each laser event and then average over the entire ensemble. However, calculating the rate for every event is not practical. Simulating a bunch/pulse collision for a single set of laser and beam parameters takes approximately 6 Pentium hours. Calculating a rate for each event in a set of 5000 E1L1 events would take over 3 years. A balance was struck.

Figure 5.20 contains a plot of the parameter Υ. The average rate for the data set was calculated using representative values of Υ. The Υ distribution was divided into 8 equal width bins. The bins, B_i were defined according to:

$$B_1 \equiv \left[\overline{\Upsilon} - 3\Upsilon_{RMS}, \overline{\Upsilon} - 2\Upsilon_{RMS}\right] = [0.01, 0.07]$$

$$B_2 \equiv \left[\overline{\Upsilon} - 2\Upsilon_{RMS}, \overline{\Upsilon} - 1\Upsilon_{RMS}\right] = [0.07, 0.13]$$

$$B_3 \equiv \left[\overline{\Upsilon} - 1\Upsilon_{RMS}, \overline{\Upsilon}\right] = [0.13, 0.18]$$

$$B_4 \equiv \left[\overline{\Upsilon}, \overline{\Upsilon} + 1\Upsilon_{RMS}\right] = [0.18, 0.24]$$

$$B_5 \equiv \left[\overline{\Upsilon} + 1\Upsilon_{RMS}, \overline{\Upsilon} + 2\Upsilon_{RMS}\right] = [0.24, 0.30]$$

$$B_6 \equiv \left[\overline{\Upsilon} + 2\Upsilon_{RMS}, \overline{\Upsilon} + 3\Upsilon_{RMS}\right] = [0.30, 0.36]$$

$$B_7 \equiv \left[\overline{\Upsilon} + 3\Upsilon_{RMS}, \overline{\Upsilon} + 4\Upsilon_{RMS}\right] = [0.36, 0.41]$$

$$B_8 \equiv \left[\overline{\Upsilon} + 4\Upsilon_{RMS}, \overline{\Upsilon} + 5\Upsilon_{RMS}\right] = [0.41, 0.47]$$

, where $\overline{\Upsilon} = 0.18$ and $\Upsilon_{RMS} = 0.06$. The event simulation program does not take Υ as an input parameter. Rather, it takes laser pulse energy (U_L), focal spot area (A_L), and FWHM pulse duration (τ_L). From this it calculates an intensity and subsequently an Υ. So the average laser energy and focal spot area were calculated for each of the Υ bins. These values were fed to the simulation program, which yielded a rate. These values were used to calculate an average

rate. The rate calculated for a bin was weighted with the fraction of entries in the bin. Table 5.9 gives the values used. Table 5.10 gives the program results, before and after the weighting with the fraction of entries was performed.

Summing up the values from column 3 of Table 5.10 yields an average of 4.5×10^{-4} in PCAL per laser shot. In the simulation runs, 1.0×10^9 was used as the number of electrons per bunch. In the actual collisions, there were 5 times more electrons. In the 3842 bunch/pulse collisions of Runs 9077–9083, the calculated rate yields $4.5 \times 10^{-4} \times 5 \times 3842 \sim 9$ PCAL positrons. In the 6415 bunch/pulse collisions of Runs 9077–9090, the calculated rate yields $4.5 \times 10^{-4} \times 5 \times 6415 \sim 14$ PCAL positrons.

There are some other rate factors not yet included in calculated rate. By cutting on positron characteristics we exclude possibly real signal present outside our cut band. 44% of the candidate distribution was excluded by the 1 rms x cut. 38% of the remaining distribution was excluded by the 1 σ NHIT cut. The 3 rms Δx cut and the 3 rms Δy cut did not exclude and appreciable portion of the remaining distribution. The excluded region was found using Figures 5.21 and 5.22. The figures were generated in a effort to quantify the signal loss due to cuts. A very tight NHIT cut (0.1 σ) was applied to the foil positrons. Then successively tighter cuts on a single parameter were applied. The number of surviving positrons was recorded for differing multiples of σ or rms. The observed cut efficiencies are similar to those given by integrating the area of a gaussian outside the cut band.The jitter of the electron beam bunches relative to the laser pulses degraded collision quality. This was only minimally corrected by the overlap cut. It is estimated that at least 50% of the pulses did not collide with bunches. The calculated rates was corrected using these efficiency values; they were multiplied by 0.56 (x cut), 0.62 (NHIT cut), 0.99 (Δx), and 1.0 (Δy).

The resulting values are compared to the measured signal excess in Table 5.11. Given the exponential dependence of the Multiphoton Breit-Wheeler pair production rate on Υ and the presence of significant background in the data, differences between expected and predicted rates were not unexpected.

Bin	Entries	Υ_L	Υ_C	Υ_H	$\langle U_L \rangle$ [mJ]	$\langle A_L \rangle$ [μm^2]
B_1	15	0.01	0.04	0.07	380	180
B_2	653	0.07	0.10	0.13	540	125
B_3	1445	0.13	0.15	0.18	597	71.1
B_4	1056	0.18	0.21	0.24	692	44.8
B_5	495	0.24	0.27	0.30	692	30.4
B_6	169	0.30	0.33	0.36	743	22.4
B_7	48	0.36	0.39	0.41	792	17.2
B_8	13	0.41	0.44	0.47	867	14.5

Table 5.9: Parameters for Average Rate Calculation.
The fraction of entries in the Υ Bin is defined as the number of entries (column 2) in the bin divided by the total number of entries in the histogram (The sum of the column 2 entries equals 3894).

Bin	Rate_{PCAL}	Rate_{Total}	$\langle\text{Rate}\rangle_{PCAL}$	$\langle\text{Rate}\rangle_{Total}$
B_1	2.6E-08	4.4E-08	1.0E-10	1.7E-10
B_2	8.6E-07	1.4E-06	1.4E-07	2.4E-07
B_3	1.3E-05	2.2E-05	5.0E-06	8.3E-06
B_4	1.7E-04	2.8E-04	4.5E-05	7.6E-05
B_5	1.3E-04	1.1E-03	8.3E-05	1.4E-04
B_6	2.9E-03	4.8E-03	1.2E-04	2.1E-04
B_7	9.1E-04	1.5E-02	1.1E-04	1.0E-04
B_8	2.5E-05	4.2E-02	8.3E-05	1.4E-04

Table 5.10: Average Rate Calculation Results.
The first column contains the Υ Bin ID. The second contains the calculated rate per laser shot observable by PCAL . The third contains the total calculated rate. The fourth contains the calculated rate observable by PCAL times the fraction of entries in the Υ Bin. The fifth contains the total calculated rate times the fraction of entries in the Υ Bin.

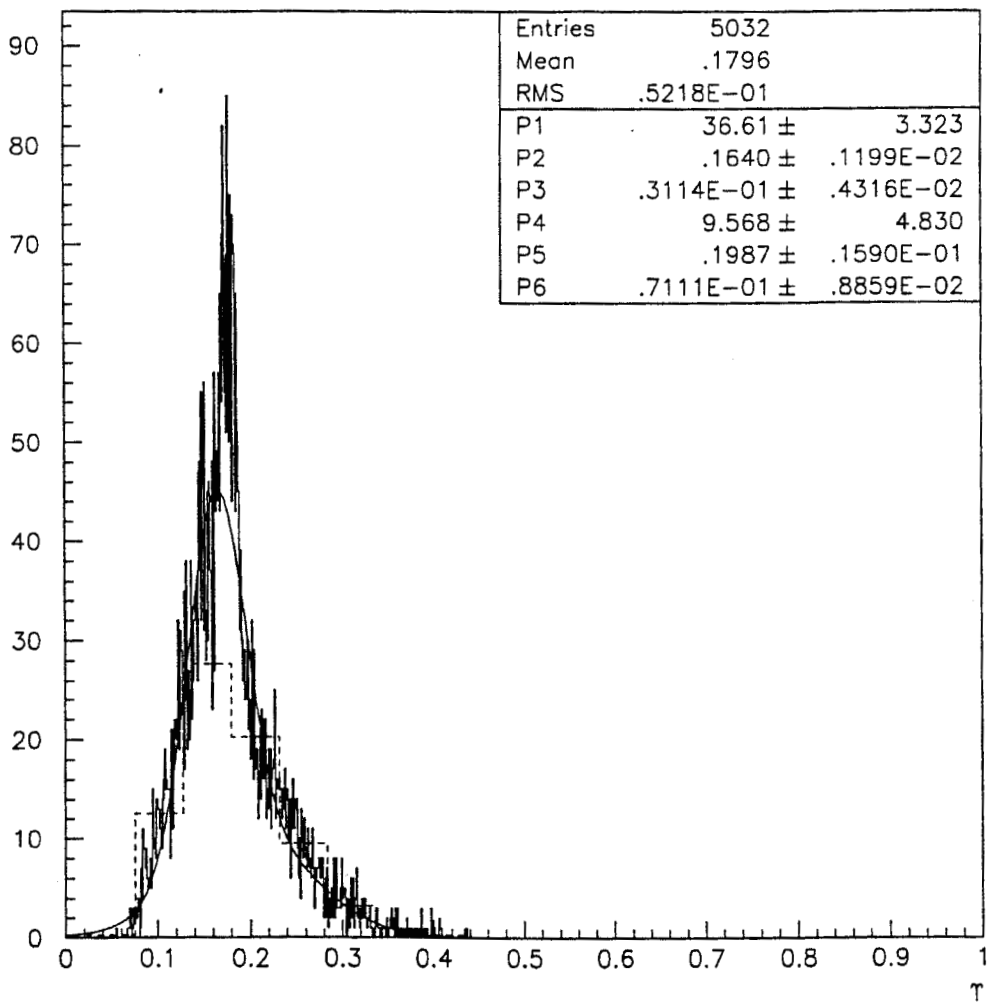

Figure 5.20: Υ Distribution.
This is the Υ distribution representing all the laser pulses in Runs 9077–9090 that passed beam and overlap cuts as discussed in Section 5.1. The dashed-bordered histogram represents the bins used to generate Tables 5.9 and 5.10.

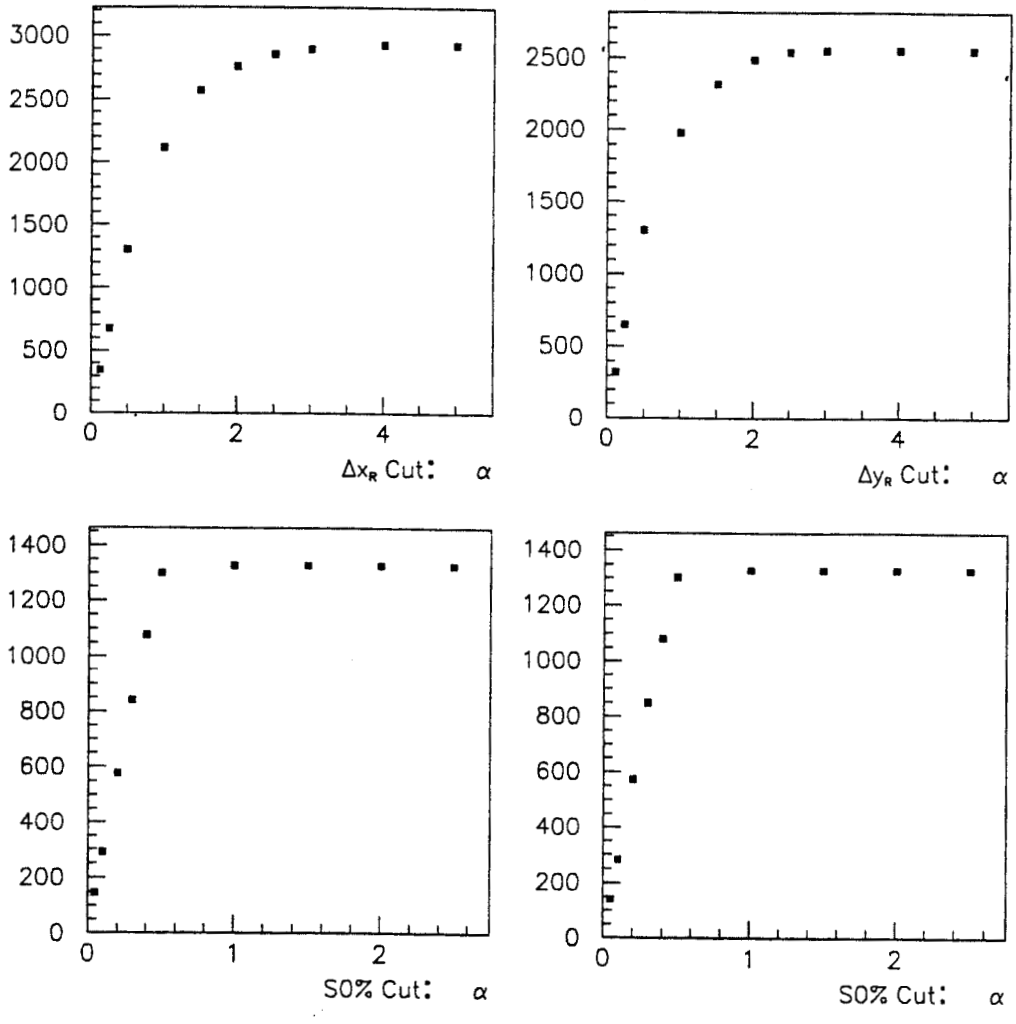

Figure 5.21: Cut Efficiencies: Δx_R, Δy_R, S0%, S1%.
A 3 rms cut on Δx removed 1% of the foil positrons. A 3 rms cut on Δy removed less than 1% of the foil positrons. S0% and S1% cuts were not used.

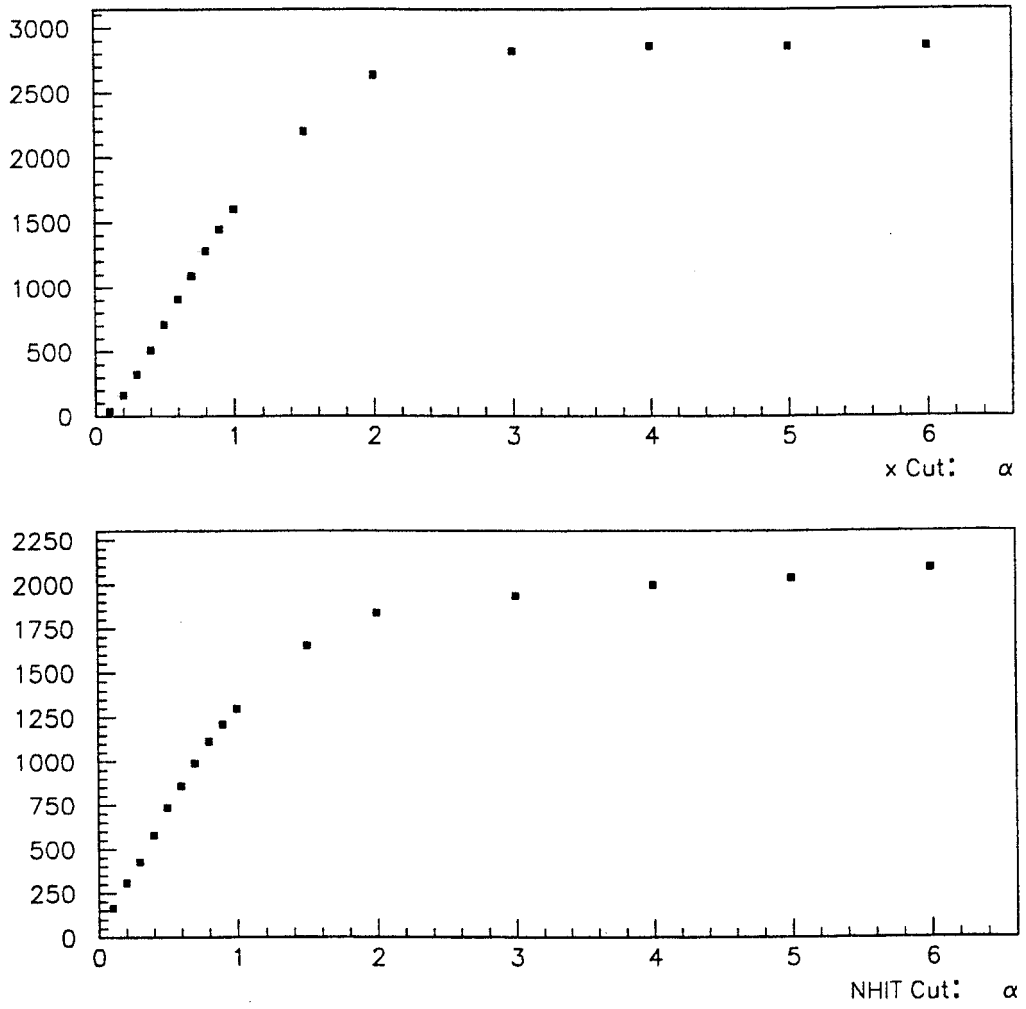

Figure 5.22: Cut Efficiencies: x_R, nhit.
A 1 rms cut on x_R removed 44% of the foil positrons. A 1 σ cut on NHIT removed 38% of the foil positrons.

Positrons Above Background		
Runs	Observed	Predicted
9077–9083	7 ± 2.9	1.5
9077–9090	5 ± 1.2	2.4

Table 5.11: Absolute Rate: Observed and Predicted .
The second column contains the observed signal above background. The error was calculated by subtracting the background count from the signal plus background count and dividing the difference by the standard deviation of the background count,
$7 \pm (13 - 6.0)/\sqrt{6.0} = 7 \pm 7/\sqrt{6.0} \sim 7 \pm 2.9$,
$5 \pm (17 - 12)/\sqrt{12} = 5 \pm 5/\sqrt{12.0} \sim 5 \pm 1.2$.
For this calculation I used the X' background values found by solving Equation 5.14.
The third column contains the predicted signal, corrected for detection efficiency.

Bibliography

[1] C. Bula et al. Observation of Nonlinear Effects in Compton Scattering. In preparation for submission to Physical Review Letters.

[2] G. Breit and J. Wheeler. Collision of Two Light Quanta. *Physical Review*, 46:1087–1091, December 1934.

[3] Howard R. Reiss. Production of Electron Pairs from a Zero-Mass State. *Physical Review Letters*, 26(17):1072–1075, April 1971.

[4] Adrian C. Melissinos. *Experiments in MODERN PHYSICS*, chapter 6: Scattering Experiments, pages 226–279(252). Academic Press, New York, 1966.

[5] Richard H. Milburn. Electron Scattering by an Intense Polarized Photon Field. *Physical Review Letters*, 10(3):75–77, February 1963.

[6] W. Greiner et al. *Quantum Electrodynamics*, volume 4 of *Theoretical Physics Text and Exercise Books*. Springer-Verlag, New York, 1992.

[7] C. Bula et al. *Proposal for a STUDY OF QED AT CRITICAL FIELD STRENGTH In Intense Laser-High Energy Electron Collisions At The Stanford Linear Accelerator Center*, October 1991.

[8] A.I. Nikishov and V.I. Ritus. Pair Production by a Photon and Photon Emission by an Electron in the Field of an Intense Electromagnetic Wave And In A Constant Field. *Soviet Physics JETP*, 25(6):1135–1142, December 1967.

[9] I.I. Goldman. Intensity Effects in Compton Scattering. *Physics Letters*, 8(2):103–106, January 1964.

[10] A.I. Nikishov and V.I. Ritus. Nonlinear Effects in Compton Scattering and Pair Production Owing to Absorption of Several Photons. *Soviet Physics JETP*, 20(3):757–759, March 1965.

[11] J. Schwinger. The Quantum Correction in the Radiation by Energetic Accelerated Electrons. *Proceedings of the National Academy of Sciences*, 40:132, 1954.

[12] A.I. Nikishov and V.I. Ritus. Quantum Processes in the Field of a Plane Electromagnetic Wave and in a Constant Field. *Soviet Physics JETP*, 19(2):529–541, August 1964.

[13] Lowell S. Brown et al. Interaction of Intense Laser Beams with Electrons. *Physical Review*, 133(3A):A705–A719, February 1964.

[14] N. Narozhnyi et al. Quantum Processes in the Field of a Circularly Polarized Electromagnetic Wave. *Soviet Physics JETP*, 20:622, 1963.

[15] Joan M. Winters et al. SLAC-I-040-20200-001-1.2. http://www.slac.stanford.edu/grp/ad/addo/grp_pages/beamlines.html, August 1st 1995.

[16] Peter G. Tenenbaum. The Final Focus Test Beam. *Beam Line*, 25(1):2–6, Spring 1995.

[17] V. Balakin et al. Focusing of Submicron Beams for TeV-Scale e^+e^- Linear Colliders. *Physical Review Letters*, 74(13):2479–2482, March 1995.

[18] David C. Carey. *The Optics Of Charged Particle Beams*, volume 6 of *Accelerators And Storage Rings*. harwood academic publishers, New York, 1987.

[19] J.D. Jackson. *Classical Electrodynamics*, chapter 12, pages 571–617. John Wiley & Sons, New York, second edition, 1975.

[20] D.O. Caldwell et al. *Techniques of High Energy Physics*, volume V of *Interscience Monographs And Texts In Physics And Astronomy*. Interscience Publishers, Inc., New York, 1961.

[21] S.C. Berridge et al. Beam Test of the SLD Silicon-Tungsten Luminosity Monitor. *IEEE Transactions On Nuclear Science*, 37(3):1191–1198, June 1990.

[22] S. Pensotti et al. Large-Area Silicon Detection in Hadronic Sampling Calorimetry. *Nuclear Instruments and Methods in Physics Research*, A(257):538–542, 1987.

[23] Richard Fernow. *Introduction to experimental particle physics*, page 260. Cambridge University Press, New York, 1986.

[24] Particle Data Group. Review of Particle Properties. *Physical Review D*, 50(3):1251–1267(1254), 1994.

[25] C. Bula et al. ECAL Calibration. http://www.slac.stanford.edu/exp/e144/plots/plots.html, November 1st 1995.

[26] G. Barbiellini et al. ENERGY RESOLUTION AND LONGITUDINAL SHOWER DEVELOPMENT IN A Si/W ELECTROMAGNETIC CALORIMETER. *Nuclear Instruments and Methods in Physics Research*, A235:55–60, 1985.

[27] Konstantine Shmakov. Monte Carlo study of E144 ECAL Calorimeter.Reconstruction of position. E-144 Internal Memo., July 1994.

[28] September 26th 1995. Glenn Horton-Smith, Electronic Correspondence.

[29] P. Maine et al. Generation of Ultrahigh Peak Power Pulses by Chirped Pulse Amplification. *IEEE Journal of Quantum Electronics*, 24(2):398, February 1988.

[30] M. Pessot et al. 1000 times Expansion/Compression of Optical Pulses for Chirped Pulse Amplification. *Optics Communications*, 62(6):419–421, June 1987.

[31] Charles V. Shank. *Ultrashort Laser Pulses and Applications*, volume 60 of *Topics in Applied Physics*, chapter 2: Generation of Ultrashort Optical Pulses, pages 5–34. Springer-Verlag, New York, January 1988.

[32] M.J.W. Rodwell et al. Reduction of timing fluctuations in a mode-locked Nd:YAG laser by electronic feedback. *Optics Letters*, 11(10):638–640, October 1986.

[33] CONFERENCE ON LASERS AND ELECTRO-OPTICS. *A High-Energy, Short-Pulse, Multiwavelength, Slab-Geometry Nd:Phosphate Glass Laser Source.* Optical Society of America, April 1989.

[34] Teresa Wilson et al. Second and Third Harmonic Generation of 1.054μ Radiation Using Picosecond Pulses. University of Rochester Report UR-1271, August 1992.

[35] David C. Brown. *High-Peak-Power Nd:Glass Laser Systems*, volume 25 of *Springer Series in Optical Sciences*, chapter 8: The Design of High-Peak-Power Nd:Glass Laser Systems, pages 236–257. Springer-Verlag, New York, January 1981.

[36] Charles Bamber et al. 0.5 Hz, Phase-Stabilized Terawatt Laser System with a Nd:Glass Slab Amplifier for Nonlinear QED Experiments. University of Rochester Report UR-1428, June 1995.

[37] Orazio Svelto. *Principles of Lasers*, chapter 8: Laser Beam Transformation, pages 411–455. Plenum Press, New York, third edition, 1989. Translated from Italian and edited by David C. Hanna.

[38] Y.-H. Chuang et al. Propagation of Light Pulses in a Chirped-Pulse-Amplification Laser. *IEEE Journal of Quantum Electronics*, 29(1):270–280, January 1993.

[39] November 21st 1995. David D. Meyerhofer, private communication.

[40] W. Koechner. *Solid-State Laser Engineering.* Springer-Verlag, New York, 1976.

[41] P. Bado et al. Multikilohertz Pockels cell driver. *Review of Scientific Instruments*, 56(9):1744–1745, September 1985.

[42] JR. William B. Jones. *Handbook of Solid State Lasers*, volume 18 of *Optical Engineering*, chapter 6: Slab Geometry Lasers, pages 581–612. Marcel Dekker, Inc., New York, 1989.

[43] M.J.W. Rodwell et al. Subpicosecond Laser Timing Stabilization. *IEEE Journal of Quantum Electronics*, 25:817, 1989.

[44] D. Cotter. Technique for Highly Stable Active Mode-Locking. In *Ultrafast Phenomena IV*. Springer-Verlag, 1984.

[45] Charles Bamber et al. E144 Timing System Evaluation. E-144 Internal Memo, June 14th 1994.

[46] P. Bado et al. Nd:YLF mode-locked oscillator and regenerative amplifier. *Optics Letters*, 12(5):319–321, May 1987.

[47] Anthony E. Siegman. *Lasers*, chapter 17: Physical Properties of Gaussian Beams, pages 1041–1103(1056). University Science Books, Mill Valley, CA, 1986.

[48] P. Laporta et al. Optimization Study of a Picosecond Rotating-Mirror Autocorrelator. *Optics Communications*, 51(2):95–99, August 1984.

[49] November 15th 1995. Theofilos Kotseroglou, private communication.

[50] Theofilos Kotseroglou. Synchronization of a High-Power Laser System and the SLAC Electron Beam. In *CONFERENCE ON LASERS AND ELECTRO-OPTICS 1995*, volume 15 of *OSA Technical Digest Series*, page 218. Optical Society of America, Washington, D.C., May 24th 1995.

[51] Edmond B. Treacy. Optical Pulse Compression with Diffraction Gratings. *IEEE Journal of Quantum Electronics*, 5(9):454, September 1969.

[52] F. Salin et al. Single-Shot measurement of a 52-fs pulse. *Applied Optics*, 26(21):4528–4531, November 1987.

[53] William H. Press et al. *Numerical Recipes in C*, chapter 15: Modeling of Data, pages 671–688. Cambridge University Press, Cambridge, second edition, 1992.

[54] Eugene Hecht. *Optics*, chapter 5: Geometrical Optics–Paraxial Theory, pages 128–210(190). Addison-Wesley Publishing Company, Menlo Park, CA, second edition, May 1990.

[55] Anthony E. Siegman. *Lasers*, chapter 17: Physical Properties of Gaussian Beams, pages 663–697. University Science Books, Mill Valley, CA, 1986.

[56] David D. Meyerhofer. Summary of Gaussian Focusing. E-144 Internal Memo., June 1994.

[57] Spring 1995. Glenn Horton-Smith, private communication.

[58] Spring 1995. Kirk T. McDonald, private communication.

[59] Amnon Yariv. *Optical Electronics.* Saunders College Publishing, San Francisco, fourth edition, 1991.

[60] Alfred Laubereau. *Ultrashort Laser Pulses and Applications*, volume 60 of *Topics in Applied Physics*, chapter 3: Optical Nonlinearities with Ultrashort Pulses, pages 35–112. Springer-Verlag, New York, January 1988.

[61] C. Bula et al. XT-Scan. http://www.slac.stanford.edu/exp/e144/plots/plots.html, November 1st 1995.

[62] The data files were processed using a program linked to libraries developed by G. Horton-Smith.

[63] CERN Application Software Group. HBOOK Reference Manual. World Wide Web, December 1993. Physics Analysis Workstation.

[64] T. Awes et al. A simple method of shower localization and identification in laterally segmented calorimeters. *Nuclear Instruments and Methods in Physics Research, Section A*, 311:130, 1992.

[65] Spring 1995. Christian Bula, private communication.

[66] Summer 1995. Collisions were simulated with the program "NUMINT" which was written by Christian Bula.

[67] Y.A. Rozanov. *Probability Theory: A Concise Course*, chapter 5: Three Important Probability Distributions, pages 54–67(56). Dover Publications, Inc., New York, 1977.

[68] H.W. Koch et al. Bremsstrahlung Cross-Section Formulas and Related Data. *Reviews of Modern Physics*, 31(4):920–955, 1959.

Appendix A

Positron Production in Al

The differential cross section for bremsstrahlung by highly relativistic e^-s in materials of arbitrary Z is given by,

$$d\sigma_{\hbar\gamma} = \frac{4\,Z^2 r_e^2 \alpha}{E_\gamma}\left(\ln\left(183\,\sqrt[-3]{Z}\right)\left(1+\frac{E_r^2}{E_e^2}-\frac{2}{3}\frac{E_r}{E_e}\right)+\frac{1}{9}\frac{E_r}{E_e}\right)dE_\gamma \qquad \text{(A.1)}$$

where Z is the atomic number of the material E_e is the incident electron energy, $E_r = (E_e - E_\gamma)$ is the recoil electron energy, $E_\gamma = \hbar\gamma$ is the outgoing γ energy, r_e is the classical electron radius, and α is the fine-structure constant.[68] Figure A.1 is a plot of Equation A.1.

Wire scanners were located at various places in the FFTB . These scanners were used to determine the transverse profile. Since the production of γs and e^-e^+ pairs is linear with the amount of radiator intersecting the beam, the wire diameter can be deconvolved from a plot of rate versus transverse wire coordinate, giving the transverse profile of the beam. Most of these wire scans were performed between "physics" runs. However, the data acquisition system was used to record calorimeter output during Run 9087. During this run, a 34 μm diameter wire was scanned across the e^- beam, measuring a 45.86μm bunch width. Since the wire was being scanned, there was a continuously varying thickness of Al in the e^- 's path. According to the standard tables, wire scanner WS6B is 11.440 meters upstream of IP1. It is 0.503 meters downstream of the Orsay monitor, and 0.226 meters upstream of the entrance to the first

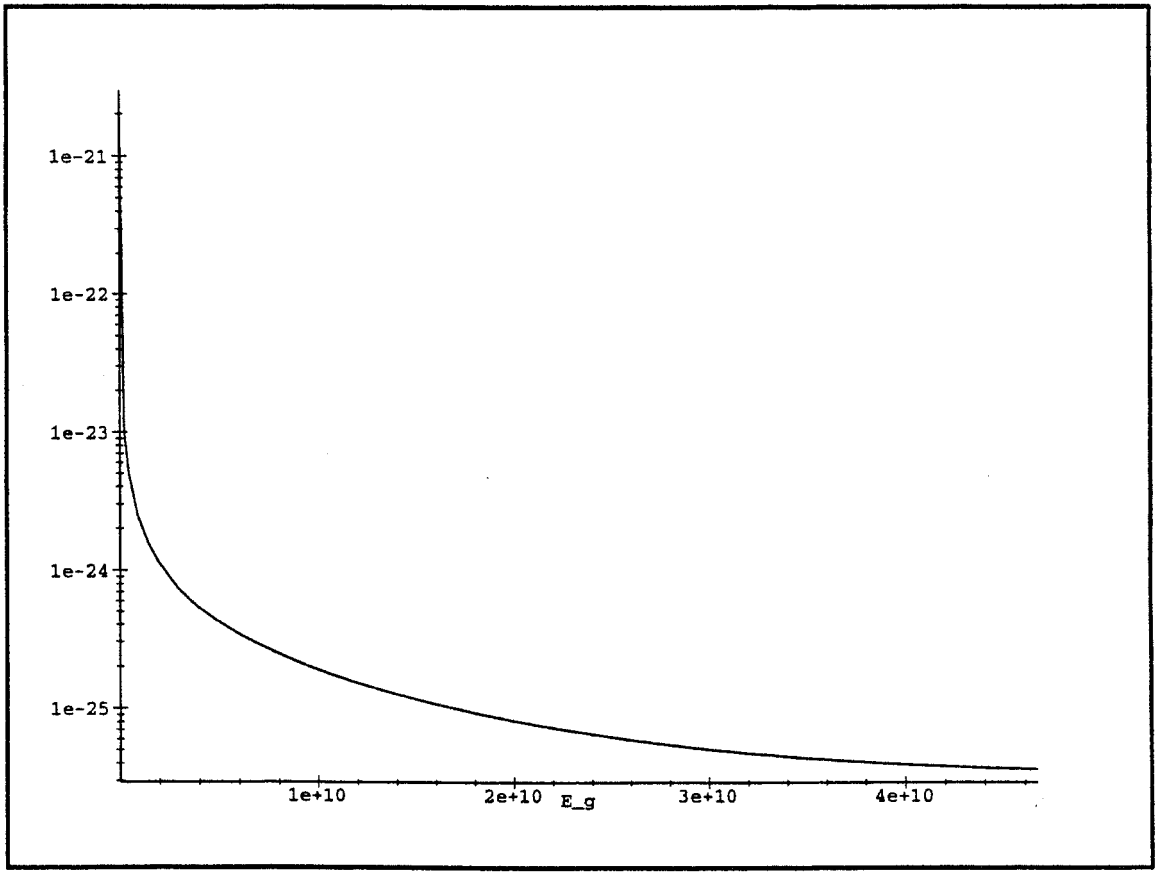

Figure A.1: $d\sigma_{\hbar\gamma}$ versus $\hbar\gamma$ for e^+ production in Al.
This is a plot of Equation A.1 for $Z = 13$,$E_e = 46.6$ GeV, and $dE_e = 1.0$ GeV.

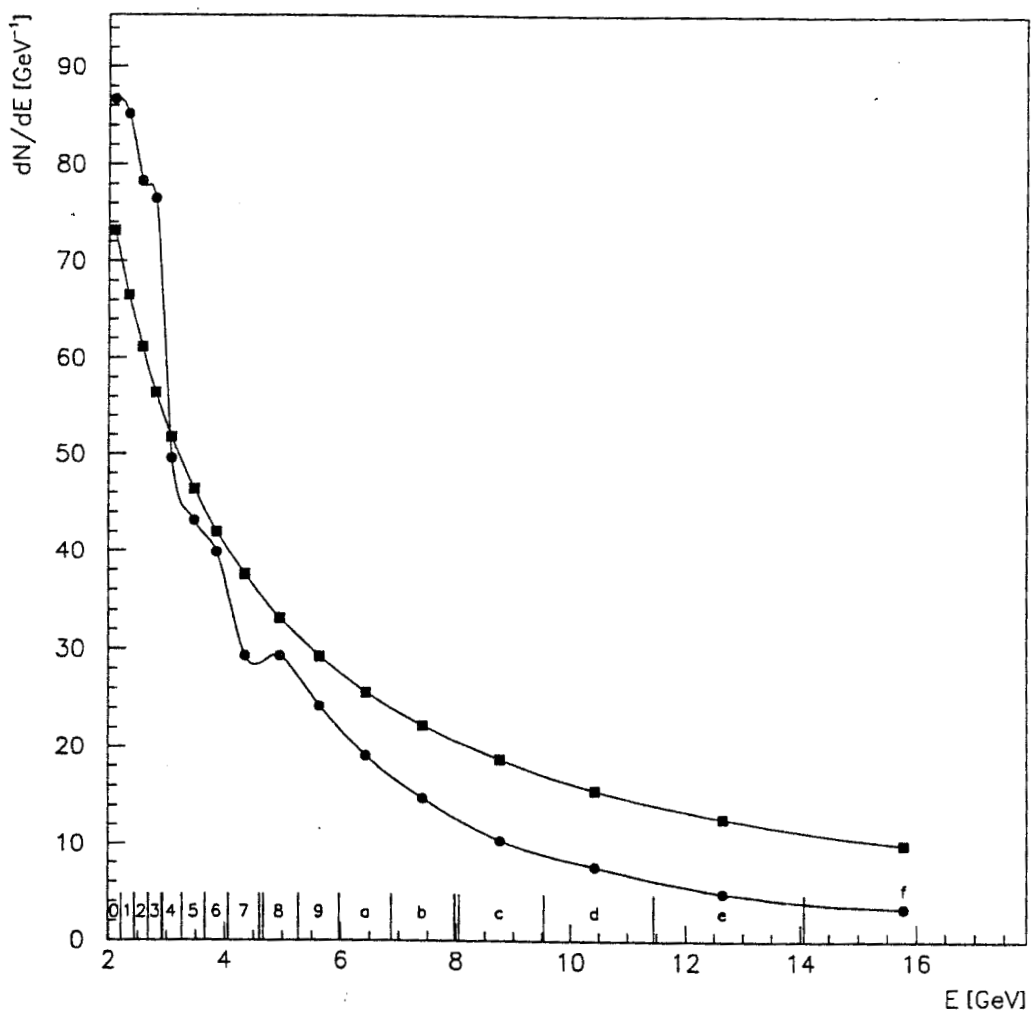

Figure A.2: This is a plot of dN/dE as a function of E for e^+ production in Al. A wire was inserted into the electron beam $\sim$ 6m upstream of IP1.

dump-line quadrupole magnet (QP1A).

Figure A.2 shows dN/dE versus E for e^+s produced during this run. Here E refers to the energy of a positron produced through a combination of bremsstrahlung and pair production in the Al. There is good agreement between the observed spectrum and the theoretical one. The motion of the wire amounts to a constantly varying, unmeasured radiator thickness, therefore it is not possible to say anything meaningful about the absolute rate. But, all the e^+ measured in a given event were produced in the same thickness of material. So within each event, dN/dE should be proportional $d\sigma/dE$.

There was a large e^+ flux during this run. This made the position reconstruction cut unfeasible. Cutting multihit events would introduce extra energy-dependent bias into the dN spectrum. Theoretically, the e^+ production rate goes roughly as E^{-1}. Higher rates are predicted for lower energies. For cells of equal energy acceptance, then, the probability of multiple hits is increased. Some of this is mitigated because of the dispersion of the spectrometer, inasmuch as the acceptance of rows was smaller for lower energies.

But change in acceptance was not matched to dN/dE, so a different, energy independent cut was needed. I simply divided the energy measured in each row by its kinematic map energy (described in Section 2.2). This gave me, roughly, the number of incident positrons. I made a histogram of this ratio for each row, and fit a Poisson distribution to each histogram. This gave me N as a function of E. Then I divided N by the acceptance ΔE of the row. This result approximates dN/dE as a function of E. There were 3553 triggers in Run 9087. The average beam charge was 5.3×10^9 q_e.

Appendix B

Event Simulation

Collision simulations were conducted. Log files were produced, containing the input parameters and calculated event rates.

```
INF: Input Parameters for Laser:
INF: ---------------------------
INF: Wavelength of Laser Photons :        0.527 [um]
INF: Ratio A_eff(0)/A_diff_limit :        1.335
INF: Ratio Sigma(x)/Sigma(y)     :        1.000
INF: Crossing Angle (Laser,-Beam):       17.000 [Deg]
INF: Energy of Laser Pulse       :        0.741 [Joule]
INF: f-Number of focusing optics :        6.000
INF: FWHM(t) of Laser Intensity  :        2.500 [psec]
INF: Delay of Laser wrt Beam     :        0.000 [psec]
INF: X-Offset of Laser wrt Beam  :        0.000 [um]
INF: Y-Offset of Laser wrt Beam  :        0.000 [um]
INF:
INF: Input Parameters for Electron Beam:
INF: -----------------------------------
INF: Energy of Electrons         :       46.600 [ GeV]
INF: Nr of Electrons in Bunch    :   1.000E+009
INF: Sigma(x) of Electron Density:      100.000 [um]
INF: Sigma(y) of Electron Density:       30.000 [um]
INF: FWHM(t)  of Electron Density:        5.000 [psec]
```

```
INF:
INF: Calculated Laser Parameters:
INF: --------------------------
INF: Energy of Laser Photons      :        2.353  [eV]
INF: Total Nr of Photons          :   1.965E+018
INF: Rayleigh Range               :       24.156 [um]
INF: Eff Focal Spot Area          :        8.500 [um^2]
INF: 1/e Intensity Radius at Focus:        1.645 [um]
INF:
INF: Calculated Electron Beam Parameters:
INF: ------------------------------------
INF: 1.-Beta of Beam Electron     :   6.012E-011
INF: Gamma   of Beam Electron     :   9.119E+004
INF: Sigma(z) of Electron Density:   6.366E+002 [um]
INF: Peak Electron Density        :   3.325E+001 [um^-3]
INF:
INF:  NON-LINEAR QED PROCESSES
INF:  <Energy> [GeV] |    Photons    |   Electrons   |   Positrons
INF: ---------------------------------------------------------------
INF:      5.000E-001 |  8.7294E+004 |  0.0000E+000 |  0.0000E+000
INF:      1.500E+000 |  8.4779E+004 |  1.2300E-020 |  4.0431E-025
INF:      2.500E+000 |  8.2317E+004 |  1.1755E-009 |  1.0121E-013
INF:      3.500E+000 |  7.9923E+004 |  3.9853E-005 |  2.6799E-009
INF:      4.500E+000 |  7.7590E+004 |  8.0618E-003 |  1.4951E-006
INF:      5.500E+000 |  7.5365E+004 |  1.9735E-001 |  3.3419E-005
INF:      6.500E+000 |  7.3312E+004 |  1.7981E+000 |  2.2078E-004
INF:      7.500E+000 |  7.1151E+004 |  9.6950E+000 |  7.8480E-004
INF:      8.500E+000 |  6.8787E+004 |  3.4986E+001 |  1.9112E-003
INF:      9.500E+000 |  6.6592E+004 |  1.1637E+002 |  3.5883E-003
INF:      1.050E+001 |  6.4560E+004 |  2.5725E+002 |  5.5642E-003
INF:      1.150E+001 |  6.2695E+004 |  5.0602E+002 |  7.4878E-003
INF:      1.250E+001 |  6.0999E+004 |  1.7149E+003 |  9.0035E-003
INF:      1.350E+001 |  5.9512E+004 |  2.7122E+003 |  9.8792E-003
INF:      1.450E+001 |  5.8251E+004 |  3.1534E+003 |  1.0023E-002
INF:      1.550E+001 |  5.7263E+004 |  3.3373E+003 |  9.5014E-003
INF:      1.650E+001 |  5.6605E+004 |  3.4781E+003 |  8.4881E-003
```

INF:	1.750E+001	5.6336E+004	3.6703E+003	7.2092E-003
INF:	1.850E+001	5.6537E+004	9.6608E+004	5.8746E-003
INF:	1.950E+001	5.7279E+004	1.0493E+005	4.6319E-003
INF:	2.050E+001	5.8720E+004	9.3683E+004	3.5522E-003
INF:	2.150E+001	6.1011E+004	8.3243E+004	2.6438E-003
INF:	2.250E+001	6.4346E+004	7.4935E+004	1.8939E-003
INF:	2.350E+001	6.8972E+004	6.8634E+004	1.2909E-003
INF:	2.450E+001	7.5204E+004	6.3941E+004	8.2984E-004
INF:	2.550E+001	8.3435E+004	6.0539E+004	5.0055E-004
INF:	2.650E+001	9.3702E+004	5.8180E+004	2.8317E-004
INF:	2.750E+001	1.0460E+005	5.6668E+004	1.5016E-004
INF:	2.850E+001	9.5021E+004	5.5848E+004	7.4317E-005
INF:	2.950E+001	2.3651E+003	5.4862E+004	3.3815E-005
INF:	3.050E+001	1.7505E+003	5.5186E+004	1.4029E-005
INF:	3.150E+001	1.8007E+003	5.5879E+004	5.1633E-006
INF:	3.250E+001	1.7592E+003	5.6878E+004	1.6522E-006
INF:	3.350E+001	1.5099E+003	5.8131E+004	4.4525E-007
INF:	3.450E+001	9.4223E+002	5.9594E+004	9.6364E-008
INF:	3.550E+001	2.7006E+002	6.1230E+004	1.5703E-008
INF:	3.650E+001	1.2862E+002	6.3010E+004	1.7354E-009
INF:	3.750E+001	5.7734E+001	6.4908E+004	1.1491E-010
INF:	3.850E+001	1.7032E+001	6.6901E+004	3.4746E-012
INF:	3.950E+001	4.6361E+000	6.8973E+004	1.6073E-014
INF:	4.050E+001	8.6662E-001	7.1108E+004	5.5158E-018
INF:	4.150E+001	9.6160E-002	7.3292E+004	6.4335E-025
INF:	4.250E+001	4.2170E-003	7.5516E+004	0.0000E+000
INF:	4.350E+001	1.8095E-005	7.7769E+004	0.0000E+000
INF:	4.450E+001	9.4172E-012	8.0045E+004	0.0000E+000
INF:	4.550E+001	0.0000E+000	8.2336E+004	0.0000E+000
INF:	4.650E+001	0.0000E+000	8.4636E+004	0.0000E+000
INF:	4.750E+001	0.0000E+000	0.0000E+000	0.0000E+000
INF:	---	---	---	---
INF:	Total	2.0728E+006	2.0465E+006	9.5477E-002

The leftmost column in the body of the table represents the outgoing particle energy. The rightmost column in the body of the table represents the

number of positrons per laser shot within the 1 GeV bin centered on the energy listed in the leftmost column.